Experimental and *in silico* computational studies of novel nanoparticle vaccine adjuvants

Charlotte Natalie Maughan

University College London

A thesis submitted for the degree of Doctor of Philosophy in the Department of Pharmaceutics at University College London

Declaration

I, Charlotte Natalie Maughan, confirm that the work presented in this thesis is my own. Where information has been derived from other sources, I confirm that this has been indicated in the thesis.

March 2017

Abstract

This thesis applies inorganic chemistry to develop new nanoparticulate vaccine adjuvants, entities added to a vaccine to inculcate robust immunity. The **Introduction** sets out the background to this work, and the **Experimental Methods** chapter reviews the techniques applied.

Chapter 3 then reports the preparation of AlO(OH) using a continuous hydrothermal synthetic pathway – with sub-100 °C temperatures and atmospheric pressure – to produce nanoscale particles. A variety of experimental parameters was explored, and some degree of particle engineering could be achieved albeit over a narrow range of sizes and shapes. There was some evidence of particle size influencing the response of macrophages to the samples.

Chapter 4 and **Chapter 5** aim to engineer the size and shape of hydroxyapatite and zinc oxide nanoparticles, respectively, through different continuous hydrothermal processes. Several different morphologies (spheres, and mixtures of spheres/rods/platelets) could be produced. The morphology and particle size appear to affect cytokine production *in vitro*.

Chapter 6 explores layered double hydroxides (LDHs) as inorganic adjuvants. A series of materials were prepared and characterised, and the effect of changing the LDH chemical composition on adjuvanticity determined. It was found that the size of the guest anion influences the immune response. Further, computational models were developed to aid the *in silico* prediction of immunogenicity, with calculated energy values being a suitable proxy for the zeta potential.

The related hydroxy double salt (HDS) materials are investigated as adjuvants in **Chapter 7**. A series of materials was prepared and their chemical composition found to markedly effect the immune response *in vitro.* Computational models were sought with the same *in silico* aim as the LDH materials, however with limited success owing to a lack of detailed structural knowledge in the literature.

Finally, overarching conclusions and suggestions for the future outlook of this area of research are given in **Chapter 8**.

Publications from this Thesis

An invited review published in the Journal of Pharmacy and Pharmacology:

Maughan, C. N., Preston, S. G. and Williams, G. R. (2015), Particulate inorganic adjuvants: recent developments and future outlook. *Journal of Pharmacy and Pharmacology*, **67**: 426–449. doi:10.1111/jphp.12352

This paper forms the majority of **Chapter 1** and is reproduced with permission from John Wiley and Sons, Copyright Wiley Publishers 2016.

Acknowledgements

First and Foremost, I would like to thank my PhD supervisor Dr Gareth Williams for his continued support and guidance throughout my studies. Additionally, I want to thank Professor Jawwad Darr and Dr Dewi Lewis for their help and support as my secondary supervisors.

Furthermore, I would like to acknowledge and thank my UCL Impact Studentship funding for my PhD, without which I would not have been able to facilitate my research.

Thank-you to members of both the Williams and Darr laboratory groups who have helped me during my time at UCL.

Finally, I would like to thank my family and close friends for their continued support and encouragement through the difficult times.

Table of Contents

Table of Figures

Table of Tables

List of Abbreviations

Abbreviation	Definition of the Abbreviation
AD	Alzheimer's Disease
AH-MP	Aluminium oxyhydroxide Microparticle
AH-NP	Aluminium oxyhydroxide Nanoparticle
$Al(OH)_3$	Aluminium hydroxide
AlO(OH)	Aluminium oxyhydroxide
APC	Antigen Presenting Cell
ATP	Adenosine Triphosphate
BCR	B-Cell Receptor
BET	Braunauer, Emmett and Teller
BJH	Barrett, Joyner and Halenda
BMDC	Bone Marrow-derived Dendritic Cell
CaN	Calcium Nitrate
CaP	Calcium Phosphate
CCL	CC Chemokine Ligand
CCR	CC Chemokine Receptor
CD	Cluster of Differentiation
cDMEM	Complete Dulbecco's Modified Eagle Medium
CHFS	Continuous Hydrothermal Flow Synthesis
CPFS	Continuous Plastic Hydrothermal Flow Synthesis
CTL	Cytotoxic T-Lymphocytes
DAMP	Damage-Associated Molecular Patterns
DAP	Diammonium Hydrogen Phosphate
DAPI	4', 6-diamidino-2-phenylindole
DC	Dendritic Cell
DLS	Dynamic Light Scattering
DNA	Deoxyribose Nucleic Acid
ELISA	Enzyme-Linked ImmunoSorbent Assay
FITC	Fluorescein Isothiocyanate
FTIR	Fourier-Transform Infra-Red
GDIS	Graphical Display Interface for Structures
GM-CSF	Granulocyte Macrophage Colony-Stimulating Factor
GMP	Good Manufacturing Practice
GULP	General Utility Lattice Program
HA	Hydroxyapatite
HDS	Hydroxy Double Salt
HPLC	High-Performance Liquid Chromatography
HPV	Human Papilloma Virus
IFN	Interferon
Ig	Immunoglobulin
IL	Interleukin
IR	Infra-Red
IUPAC	International Union of Pure and Applied Chemistry
LDH	Layered Double Hydroxide
LPS	Lipopolysaccharide

MHC	Major Histocompatibility Complex
MØ	Macrophage
MPL-a	Monophosphoryl Lipid A
NLRP	NOD-Like Receptor Protein
NMM	Nuclear Magnetic Moment
NMR	Nuclear Magnetic Resonance
NOD	Nucleotide-Oligomerisation Domain
OD	Outer Diameter
OVA	Ovalbumin
PAMP	Pattern-Associated Molecular Patterns
PBS	Phosphate-Buffered Saline
PEG	Polyethylene Glycol
PTFE	Polytetrafluoroethylene
P-XRD	Powder X-Ray Diffraction
R^2	Correlation Co-efficient
RNA	Ribonucleic Acid
ROS	Reactive Oxygen Species
SEM	Scanning Electron Microscopy
SS-NMR	Solid State-Nuclear Magnetic Resonance
TCR	T-Cell Receptor
TGA	Thermogravimetric Analysis
Th	T-helper
TNF-α	Tumour-Necrosis Factor-alpha
UP-water	Ultrapure Water
XPS	X-ray Photoelectron Spectroscopy
ZnO	Zinc Oxide
ZP	Zeta Potential

Chapter 1 : Introduction

1.1 Immunity and Vaccination

1.1.1 Preamble

Vaccination is perhaps the most effective public health intervention of all time. It is estimated that some three million lives per year are saved as a result of vaccines. They allow infectious diseases to be controlled or even completely purged from countries: for instance, 10 Asian nations including India, Bangladesh and Sri Lanka have very recently been declared free of polio [1]. In favourable cases diseases may be eradicated, as in the case of smallpox. There exist a range of other disease prevention schemes including screen and treat (which screens an individual for a certain condition and if a positive result is obtained provides medication immediately), aggressive treatment regimens (targeting diseases through intensive courses of medication) and widespread anti-viral distribution (such as the stockpiling of oseltamivir for the swine-flu epidemic in 2009), all of which can be effective: for instance, screen and treat has successfully been used against cervical cancer [2]. However, vaccination is in general a more cost-effective and safer route for controlling the spread of disease [3]. In vaccination, we aim to expose the immune system to the infectious agent (the “antigen”; a bacterial or viral component) in a safe environment where there is minimal risk of an infection ensuing. This is akin to footballers training before a match.

Vaccination programmes can only achieve their maximum protection potential if the majority of the population are inoculated against a particular infectious disease. This concept is commonly referred to as “herd immunity”. There is a threshold percentage of the population that must be inoculated in order to contain the spread of infections; this target vaccination level is dependent on factors including infectivity of the disease and the length of the infectious period [4]. With effective herd immunity, infection rates even amongst unprotected individuals are extremely low, due to the reduced pool of susceptible hosts available for pathogen reproduction and dissemination.

1.1.2 Innate and Adaptive Immunity

The human immune system consists of two major arms: innate and adaptive. Innate immunity is triggered by evolutionary-conserved pathogen components (pattern-associated molecular patterns, PAMPs) and/or by other forms of danger, including cell stress and damage (damage-associated molecular patterns, DAMPs). The response is rapid but restricted to a relatively confined array of fixed (germline-encoded) specificities.

Adaptive immunity rests on the clonal (each cell has a single specificity) expression of T cell and B cell receptors (TCRs/BCRs). These receptors are generated with an extraordinary number of specificities (calculations suggest a theoretical diversity of *ca.* 10^{15} forms for the human αβ TCR [5], and attempts to assess actual diversity produce estimates from 2.5×10^7 to 2.5×10^8 forms [6-8]) using a mechanism which involves the somatic recombination of gene elements and the addition and deletion of nucleotides at certain junctions [9]. This diversity of specificity allows adaptive immunity to mount an exquisitely targeted attack, but cells specific for a previously unencountered threat will tend to be extremely rare: as a result, the expansion of antigen-specific T and B cells imposes a lag on the development of an effective response. This lag phase is greatly reduced in a 'memory' or 'recall' response on the second or subsequent encounter with an antigen, with greatly accelerated response kinetics being due to the persistence of memory T and B cells. These are present at increased frequencies and have lower activation thresholds than naïve (antigen-inexperienced) cells [10]. Long-lived (antibody-producing) plasma cells may also persist long after pathogen clearance, maintaining specific antibody levels [11]. To provide protection a vaccine must, therefore, generate a pool of memory B and T cells, and/or long-lived plasma cells.

The key cells involved in the innate and adaptive immune response are detailed in **Table 1.1**. Dendritic cells (DC) are the primary activators of naïve T cells [12], and as such are particularly important in the generation of an adaptive response. They also play a role in determining the nature of the T cell response [13], which, in turn, largely determines whether the adaptive response is appropriately tailored towards effectively combatting a given infection.

***Table 1.1:* A brief summary of the key cells of immunity.**

Immune cell	Description
Dendritic cell (DC)	Key antigen-presenting cell. DCs are stationed throughout the body and constantly sample their local environment. If a foreign body is detected, then the DC can migrate to the lymph nodes for presentation of antigen to naïve T cell populations.
Macrophage (MØ)	An antigen presenting cell whose main purpose is to engulf pathogens through phagocytosis.
Monocytes	A circulating phagocyte which can migrate into the tissues and differentiate into macrophages or dendritic cells.
T cell	Express T cell receptors (which recognise antigenic peptides bound to major histocompatibility complex [MHC] proteins, presented on the surface of other cells). T helper (Th) cells (typically CD4+) assist other cells in an immune response, including accelerating the maturation of B cells, and activating macrophages and cytotoxic T cells. Cytotoxic T lymphocytes (CTL, typically CD8+) destroy virally infected cells and cancerous cells.
B cell	Express B cell receptors (membrane-bound antibodies), and can differentiate into antibody-secreting plasma cells.

DCs and macrophages are antigen presenting cells (APCs), meaning that they can take up antigen from their environment and process it for presentation to T cells. Antigens taken up by DCs are partially degraded in endosomes (internal membrane-bound compartments) into fragments which are then expressed on the cell surface on major histocompatibility complex class-II (MHC-II) receptors. The resultant MHC-II/peptide complex presents antigen to CD4+ T cells.

Immature DCs that internalise antigen at the non-lymphatic exposure sites are only weakly capable of stimulating T cell activation; they first must undergo a maturation process which results in elevated surface expression of the co-stimulatory molecules CD80 and CD86 (see **Figure 1.1**). When they mature, DCs also secrete greater amounts of cytokines (**Figure 1.1**). Depending on the cytokine composition, a Th1 or Th2 response can be initiated, a process known as T cell polarisation. Th1 responses are effective against viral and intracellular infections, whilst Th2-type responses aid against extracellular bacterial and gastrointestinal nematodes [14]. The two are also known as cell-mediated (Th1) and humoral (Th2) immunity, respectively. The activation of cytotoxic T-lymphocytes (CTLs) occurs similarly, but with antigenic peptide being presented on the MHC-I receptor, and a requirement (for naïve CTLs) for "help" from Th cells.

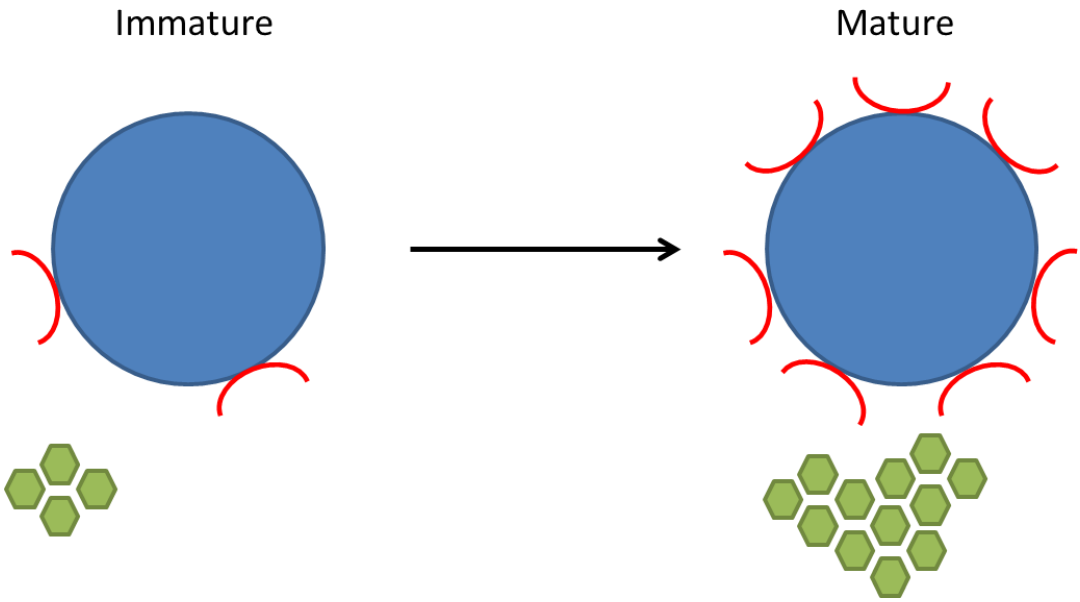

Figure 1.1: ***Schematic representation of immune cell maturation, have increased expression of cell surface markers (red semi-circles) such as CD86, CD80, and Major Histocompatibility Complex (MHC) I/II as well as increased production and subsequent secretion of cytokines such as IL-6, IL-12 and IL-1β (green hexagons).***

An ideal vaccine would stimulate a strong immune response of a class appropriate to the pathogen. For example, a Th1-type response will drive a potent CTL response and (through interferon [IFN]-γ production) promote macrophage activation, useful weapons against intracellular pathogens [10, 15]. Th2-type responses induce strong antibody responses *via* production of interleukin (IL) molecules such as IL-4, IL-5 and IL-13 [14].

Further details on the mammalian immune system are available in recently published immunology textbooks [10, 16].

1.1.3 Vaccine Types and Classifications

Vaccines may be classified by their intended purpose (prophylactic *vs.* therapeutic and immunogenic *vs.* tolerogenic); by the nature of antigen delivered (principally live attenuated, inactivated or subunit); or by the adjuvant they incorporate (discussed in **Section 1.1.4**). The role of the adjuvant is to increase the immune response induced by the administration of the antigen.

Prophylactic vaccines are given to healthy individuals to provide protection, whereas therapeutic vaccines exploit the immune system to treat a pre-existing condition. Prophylactic vaccines are universally designed to be immunogenic, whereas therapeutic vaccines include both immunogenic (*e.g.* against tumours) [17] and tolerogenic vaccines (which are intended to resolve autoimmune diseases or allergies through restoring tolerance to autoantigens/allergens) [18].

Live attenuated vaccines contain a live form of disease-causing organism that has been rendered non-virulent (unable to cause disease), typically by repeated passage *in vitro* [10]. Their main advantage is the induction of strong cellular and antibody-mediated immune responses, which can result in the inculcation of lifelong immunity to the pathogen of interest in one or two doses [19]. For instance, this is true for the viral vaccine against measles, mumps and rubella [20]. However, there is a risk of an attenuated pathogen reverting to its virulent state, in which case it may cause disease in the recipient or render them an asymptomatic carrier. This can, for instance, occur with the polio vaccine [21].

Inactivated vaccines contain chemical-, heat-, or radiation-killed pathogen; they are, therefore, safer than live attenuated vaccines in that there is no chance of the reversion to virulence provided care is taken to ensure complete inactivation. Inactivated vaccines tend to stimulate weaker (and predominantly antibody-mediated) responses than live attenuated vaccines, so most such formulations require multiple doses [22] and the use of adjuvants to induce sustained protective immunity [10].

Subunit vaccines contain defined protective component(s) from the disease-causing agent, for instance a polysaccharide viral capsid component or an immunogenic peptide [23, 24], which may be produced in recombinant form or isolated from pathogen lysate. Alternatively, DNA encoding a peptide antigen may be inoculated ("DNA vaccination") [25]. A subunit vaccine, therefore, exposes the immune system to antigen(s) without the risk of infection associated with live attenuated or (to a lesser extent) inactivated vaccines [26], providing an improved safety profile and the possibility of administration to immunocompromised recipients. A further advantage is that the defined nature of subunit antigens should permit the rational design of advanced vaccines, although this remains one of the major challenges in vaccinology [27, 28]. However, most purified antigens have limited intrinsic immunogenicity so that, as with inactivated vaccines, subunit vaccines usually need multiple doses and the incorporation of an adjuvant to induce a sufficient response [10]. Both inactivated and sub-unit vaccines tend to stimulate antibody-mediated rather than cellular immunity, though this may be a result of the adjuvants used in current vaccines [29].

A range of other vaccine types have been described, including conjugate vaccines; recombinant vector vaccines; and toxoid vaccines. These are all essentially variations on either subunit or DNA vaccines, as described above.

1.1.4 The Adjuvant

If antigens are used alone in a formulation, subunit vaccines typically have low immunogenicity. To ensure robust immunity, a second component known as an "adjuvant" needs to be added to the formulation. This helps the immune system to recognise the presence of a foreign body and acts to stimulate the immune response to it. Adjuvants are also generally needed for inactivated vaccines, but attenuated vaccines usually do not need to be adjuvanted.

An ideal adjuvant would be cheap to manufacture, safe to administer, provide life-long immunity and elicit the desired immune response (either humoral, cell-mediated, or both) [30, 31]. At the present time, very few adjuvants are licensed for use in humans: see **Table 1.2**.

***Table 1.2:** Adjuvants in vaccines currently licensed for human use [32, 33].*

EMA-approved vaccine adjuvants	FDA-approved vaccine adjuvants
MF59	
AS03	AS03
AS04	AS04
Virosomes[a]	Virosomes[a]
Aluminium-containing compounds	Aluminium-containing compounds

[a] Antigens are present as virosomes in Cervarix and Gardasil, but these vaccines also contain AS04/Alum (respectively) as adjuvants. EMA = European Medicines Agency.

By far the most widely used adjuvant is “alum”, an inorganic salt first identified as potent by Glenny in 1926 [34, 35]. However, other metal salts, such as calcium phosphate (CaP), have also been used – for instance, in diphtheria-pertussis-tetanus vaccines in France [36-38] – and there is a significant research effort underway to look at other inorganic systems. MF59 and AS03 are oil-in-water based adjuvants. Virosomes (otherwise known as virus-like particles) are nanoparticles designed to mimic the outer surface of a virus, yet not containing any RNA or DNA and hence having no virulence. AS04 is a mixture of alum and monophosphoryl lipid A (MPL-a). MPL-a is an attenuated form of lipopolysaccharide (LPS), a component of bacterial cell walls. Since it contains alum, I will touch on AS04 in the discussion that follows.

1.2 Inorganic Adjuvant Systems

1.2.1 Alum

“Alum” is used by chemists to refer to materials with the formula $KAl(SO_4)_2{\cdot}12H_2O$ or $[NH_4^+][Al(SO_4)_2]{\cdot}12H_2O$. Immunologists, in contrast, use the term “alum” to refer to all aluminium-containing adjuvants. The alum of immunologists is typically poorly defined in terms of its chemical and physical properties – it is not unusual to receive a sample from a supplier labelled “$Al(OH)_3$ solution” where a cursory visual inspection reveals it to be a suspension rather than a solution, and where a minimal characterisation suggests that there is in fact very little $Al(OH)_3$ present at all. For these reasons, alum is often referred to as “immunologist’s dirty little secret” [39].

In fact, most commonly “alum” comprises either aluminium oxyhydroxide [AlO(OH)] or aluminium hydroxyphosphate $[Al(OH)_x(PO_4)_y]$. AlO(OH) is a crystalline layered material, the surface of which comprises only hydroxyl groups. Its structure is depicted in **Figure 1.2**. In contrast, $Al(OH)_x(PO_4)_y$ is an amorphous material with both hydroxyl and phosphate groups on the particles surfaces [40].

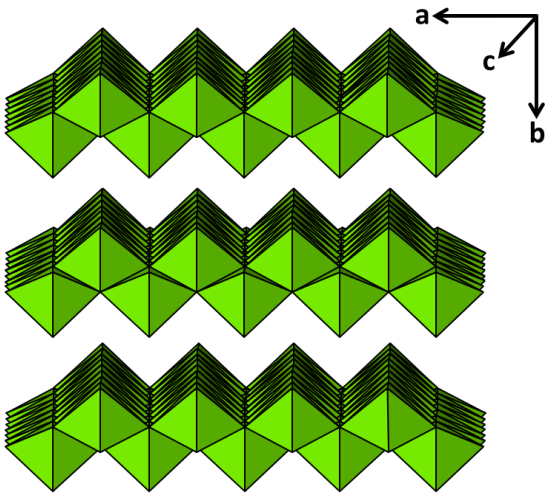

***Figure 1.2:** The structure of AlO(OH). AlO_6 octahedra are shown in green. Hydrogen atoms are omitted for clarity.*

For most of the time which has elapsed since their first use nearly 90 years ago, aluminium-containing adjuvants have been the only licensed adjuvants for use in human vaccines: only in 1997 was the first vaccine containing an alternative adjuvant licensed (in Italy) [41]. Aluminium-containing adjuvants are used in a wide variety of vaccines, such as those for diphtheria, tetanus and pneumococcal infections [33]. They promote a Th2 response, and so can be effective for targeting extracellular pathogens, but are much less useful for vaccination against intracellular pathogens and tumours.

It should be noted that the use of "Imject alum" is frequently reported in *in vivo* studies in the literature. This is chemically quite distinct from the aluminium-containing adjuvants used in human and veterinary medicine. Imject alum consists of 40 mg mL^{-1} crystalline magnesium hydroxide and 40 mg mL^{-1} amorphous aluminium hydroxide. Magnesium ions exert an effect on immune and inflammatory responses [42], and have also been shown selectively to block calcium-ion channels resulting in the inhibition of macrophage activation and an anti-inflammatory response [43]. The composition of Imject alum is such that it is not recommended for use in research aimed at elucidating the mode of action of adjuvants in licenced human vaccines [44], nor should it be used for research into the effects of aluminium oxyhydroxide or aluminium hydroxyphosphate [45].

1.2.1.1 Adsorption of Antigen to Alum

Alum and antigen are typically admixed in vaccine formulations, and it is thus vital to consider how the two components might interact to understand formulation efficacy. Antigen adsorption refers to the adhesion of antigen to the surface of an adjuvant *via* interactions between the two entities. In vaccine prophylaxis, antigen adsorption provides a means of delivering the antigen to the recipient for induction of an immune response. There are two main antigen adsorption mechanisms: electrostatic interactions and ligand exchange, both of which are discussed further below.

Crystalline AlO(OH) has a point of zero charge ranging between pH 7.7 and 9.4 [46]. Therefore, at physiological pH, it carries a positive charge. In contrast, amorphous aluminium hydroxyphosphate has a point of zero charge at around pH 4, and thus at physiological pH carries a negative charge. Seeber *et al.* provided experimental evidence for electrostatic interactions being involved in protein adsorption to alum by studying AlO(OH), $Al(OH)_x(PO_4)_y$, lysozyme and albumin [47]. Lysozyme has an isoelectric point (pI) of 11 [48], while the equivalent value for albumin is 4.8 [49]. The two proteins thus at physiological pH carry positive and negative charges, respectively. Positively charged AlO(OH) strongly adsorbed the negatively charged albumin, but no lysozyme adsorption was recorded. The inverse was shown to be true for the negatively charged $Al(OH)_x(PO_4)_y$. These results were ascribed to the different electrostatic interactions in the systems, as depicted in **Figure 1.3**.

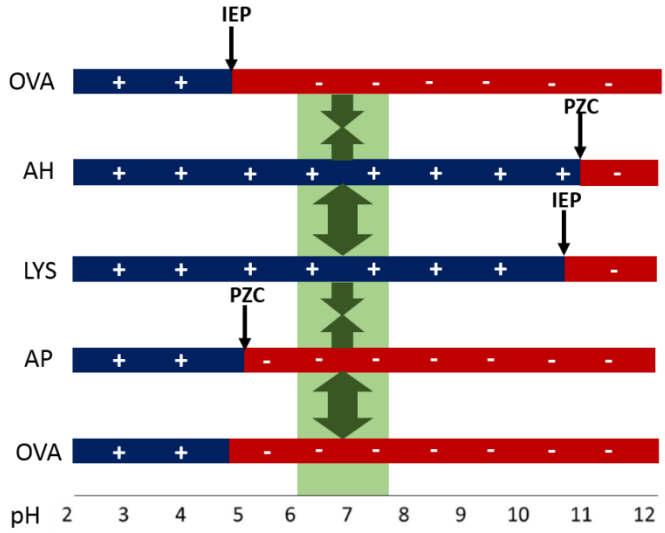

Figure 1.2: ***A schematic illustrating possible electrostatic interactions between protein antigens and Al-based adjuvants. The isoelectric point (IEP) describes proteins whilst the point of zero charge (PZC) refers to mineral adjuvants. If the antigen and adjuvant carry opposite charges at physiological pH then there will be electrostatic attractions and binding between them. OVA = ovalbumin, AH = aluminium hydroxide, LYS = lysozyme, AP = aluminium phosphate. Reproduced from ref [44]. Copyright Harm HogenEsch. 2013.***

Another mechanism of antigen adsorption is ligand exchange; this provides direct covalent bonding between the antigen and adjuvant, and thus leads to stronger antigen binding than electrostatic bonding. Ligand exchange arises if the antigen is phosphorylated because these phosphate groups can displace hydroxides bound to aluminium [50, 51]. It has been reported that antigen adsorption through either ligand exchange or electrostatic interactions can be sufficient to induce an immune response [52].

Thirty-seven years ago, Edelman postulated that adjuvanticity might be dependent on complete adsorption of antigen to the adjuvant surface [30]. Taken with the more recent results of Seeber *et al.* (discussed above) [47], this suggests that adjuvant selection should be dependent on the physiological behaviour of both the adjuvant and the antigen. Upon administration of the vaccine, it may be necessary for the adsorbed antigen to be eluted from the surface of the adjuvant in order to induce an immune response.

However, it has also been shown that particulate adjuvants can be internalised by DC [53], and hence elution may not be an absolute requirement or may occur intracellularly. Antigen elution certainly can occur, however, as demonstrated by Iyer and colleagues, who adsorbed ovalbumin and dephosphorylated α-casein antigens to aluminium hydroxide and injected the admixtures subcutaneously to BALB/c mice [54]. Their results demonstrated that both ovalbumin and dephosphorylated α-casein eluted completely upon exposure to the interstitial fluid. Seeber *et al.* have additionally proposed that citrate ions in interstitial fluids cause dissolution of the adjuvant, subsequently freeing the antigen into solution [55].

Recent studies have cast doubt on to what degree of antigen adsorption is desirable, however. Hansen and co-workers demonstrated that if the antigen is too strongly adsorbed to the adjuvant surface, the immune response can be impaired [56]. In this study, α-casein and dephosphorylated α-casein were adsorbed to aluminium hydroxide based adjuvants with different surface hydroxyl concentrations, and antibody titres in mice found to be inversely correlated with the strength of adsorption. In addition, non-adsorbed antigen has been shown to elicit an immune response *in vivo.* Romero-Mendez *et al.* tested three antigen-alum formulations containing a commercial aluminium hydroxyphosphate based adjuvant (Adju-Phos®) in mice [57]. They found that the antibody titres were similar regardless of whether the antigen was adsorbed to the Adju-Phos® or not. Results from electron microscopy highlighted that the adjuvants create porous aggregates with the non-adsorbed antigen entrapped in the pores. This was found in *in vitro* studies to allow effective antigen uptake by DC. A range of other studies have cast doubt on the need for antigen absorption onto alum, with similar antibody titres observed both with and without adsorption [53, 58, 59].

In an extreme example, Flebbe and Braley-Mullen have given antigen and alum in separate injections and found that separate injections induced higher antibody titres than the antigen administered alone [60]. However, it should be noted that other studies reported that no immune response was initiated following separate antigen/alum injections [53, 61]. More recently, some authors have suggested that it is in fact favourable to have minimal interactions between alum and the antigen for anthrax vaccination [62], and also in the hepatitis B setting [63]. One reason for this might be that antigens are thought to be less stable when adsorbed to alum than when in solution [64], because in the former setting there is an increased susceptibility to physical and chemical degradation [65, 66]. Two recent reviews discuss these challenges in detail and posit future formulation strategies to maximise vaccine efficacy [67, 68].

1.2.1.2 Activation of the Immune System by Alum-Adsorbed Antigen

Vaccines are injected at non-lymphatic sites, where antigen desorption from the surface of aluminium-containing adjuvants is thought to occur in the interstitial fluid [47, 53, 54, 57, 69, 70]. Whether desorbed or not, antigen must enter the lymphatic system in order to reach the lymph nodes and then stimulate naïve B and T cells [71]. Antigenic particles less than 30 nm in size can enter into the lymph node as free antigen; however, larger antigenic species (*e.g.* antigen adsorbed to a particulate adjuvant) must be internalised by resident DCs to be delivered to the lymph node and be presented to naïve B and T cells for induction of a primary immune response [72].

Particle size thus significantly impacts how an antigen enters the lymphatic system: this is illustrated in **Figure 1.4**. Particles of sizes 20 – 1000 nm are taken up by cells (either by DC themselves or by cells which may then be phagocytosed by DC). Antigens ranging between 1 and 30 nm can either pass through between the cellular wall of the lymphatic system for DC internalisation or pass straight into the lymph node as free antigen. All these routes ultimately deliver antigen to naïve B- and T cell populations for induction of an immune response.

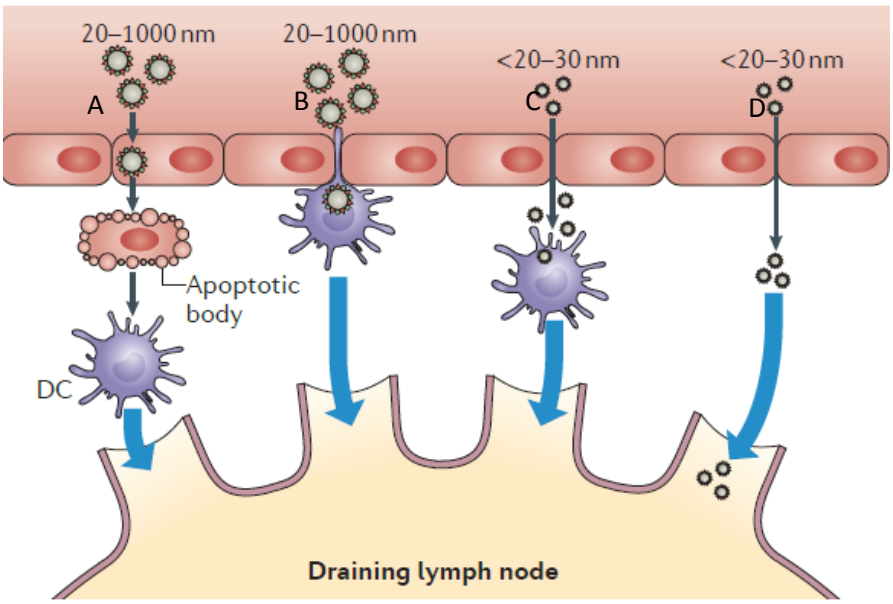

Figure 1.2: ***A schematic representation of antigen delivery to the lymphatic system depending on the size of the antigen. Reproduced with permission from ref [73]. Copyright Macmillan Publishers Ltd 2013.***

There are three key pathways in which DC may take up antigen from their local environment: macropinocytosis, receptor-mediated endocytosis and phagocytosis [74]. A schematic representation of these pathways is given in **Figure 1.5**.

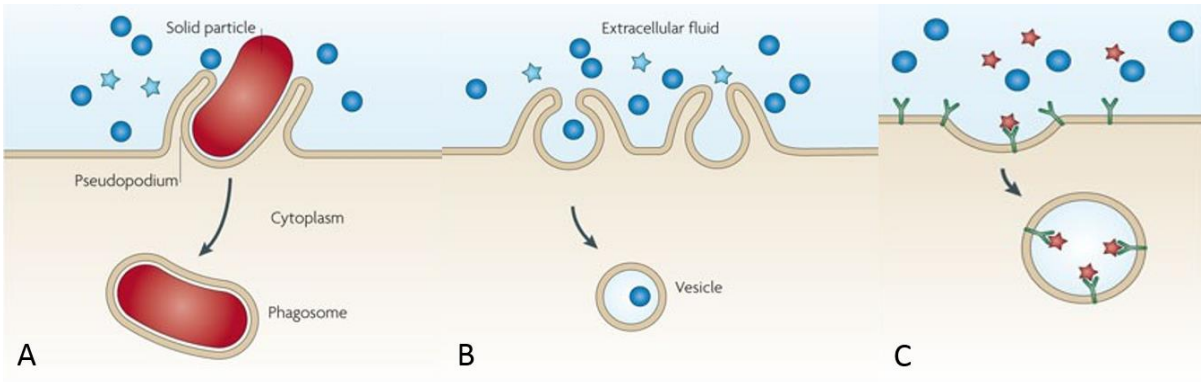

Figure 1.2: ***A schematic representation of the main pathways in which antigen may be taken up by dendritic cells. (a) Phagocytosis, in which a dendritic cell (DC) engulfs solid particles and entraps them in an intracellular vesicle; (b) Macropinocytosis, in which extracellular fluid is internalised by invaginations of the cell membrane for entrapment in a vesicle within the DC; (c) Endocytosis, a process by which cells internalise particles of size 60 - 120nm from the extracellular environment and encapsulate them in a vesicle. Reproduced with permission from ref [75]. Copyright Macmillan Publishers Ltd 2010.***

Experimental evidence supports the idea that the DC-uptake route of the antigen can affect its presentation. Burgdorf and colleagues showed that endocytosis of the model antigen ovalbumin (OVA) by DCs results in the antigen being presented on the surface by major histocompatibility complex (MHC)-I co-stimulatory molecules. This leads to the activation of CD8+ cytotoxic T cells [76]. In contrast, if the DC internalises OVA *via* micropinocytosis, then the antigen will be presented on MHC-II, causing the activation of Th cells [77].

It has been suggested that antigen-alum complexes can be more readily internalised by antigen-presenting cells than soluble antigen alone. This might cause increased interaction between the dosed antigen and the immune system [78], indicating that stronger absorption may be preferred. However, as described in **Section 1.2.1.1**, the experimental data are mixed, and it is likely that more than one mode of immune system activation is involved.

1.2.1.3 Hypothesised Modes of Action for Alum

1.2.1.3.1 The Depot Effect

"Alum" was first described in 1926 when Glenny [34, 35] used it as an adjuvant for diphtheria vaccines and hypothesised a "depot-effect" for the mode of action. In this, he proposed that the adjuvant essentially act as a reservoir, slowly releasing the antigen over a prolonged period of time and thus inculcating robust immunity. This idea went largely unchallenged for almost 70 years. Only in the last 20 years have further investigations into the detailed mechanism of action taken place. Since then, the way in which aluminium-containing adjuvants function has been much debated, with evidence supporting a range of hypotheses.

Glenny and Barr [34] used a precipitation of the diphtheria toxoid antigen with “potash alum” to slow the rate of antigen elimination from the injection site. Guinea pigs were injected with the alum-precipitated toxoid, and three days after vaccination the injection site was recovered. The tissue thereby collected was macerated and then re-injected into naïve guinea pigs. The latter animals developed an anti-toxoid response, indicating the antigen was still present in the tissue. The same reaction not observed when injection sites were recovered from a control group of guinea pigs inoculated with soluble diphtheria toxoid and transferred to a population of naïve animals. The authors concluded that there was sustained release of antigen from the alum adjuvant particles, providing prolonged exposure to the antigen and eliciting a greater immune response. This hypothesis is known as the “depot effect”. However, given that the macerated tissue must have contained alum as well as antigen, it is unclear whether this is a true depot effect or whether the adjuvant performed some other role.

Another early report also proposed a depot effect to explain the adjuvant effect of alum [79]. The authors of this work dissected nodules from diphtheria-immunised guinea pigs, ground them up in a saline solution and re-injected the resultant solution into other guinea pigs. Antibody titres collected in these experiments suggested that the antigen could potentially remain at the site of injection for up to 7 weeks. Further evidence to support the depot hypothesis comes from the fact that the $Al(OH)_x(PO_4)_y$ has been found to result in less efficacious immune responses than AlO(OH) [80]. The phosphate content of $Al(OH)_x(PO_4)_y$ results in this salt having higher solubility, and in it being eliminated more readily from the body [81], perhaps reducing the exposure time of leukocytes to the antigen and thus leading to reduced immunogenicity.

However, a more recent study provides evidence that aluminium-containing adjuvants at the injection site are dispensable for adjuvanticity just two hours after the initial administration [82]. BALB/c mice were injected with alum/OVA (alum provided by Brenntag Biosector, Frederikssund, Denmark) and the injection sites subsequently ablated. The OVA-specific antibody responses were the same in mice which underwent this ablation process as in those that did not [82]. In summary, therefore, although the depot effect may have some role to play in the adjuvanticity of alum, it appears that it is not the only factor of importance.

1.2.1.3.2 Molecular Mechanisms of Action

In recent years, a number of authors have undertaken more detailed mechanistic studies to probe the molecular immunological pathways which underlie alum adjuvanticity. Unfortunately, a range of different protocols have been employed, with a number of different types of "alum". This has resulted in inconsistent findings, and so although steps have been taken toward unravelling alum's mechanism of action our understanding remains incomplete.

In one of the first such studies, intraperitoneal injection of the model antigen OVA with Imject alum was found to induce chemoattraction of key immune cells, including monocytes, to the site of injection in BALB/c mice [83]. The recruited monocytes internalised the desorbed OVA and migrated to the draining lymph node, where they differentiated into DCs. These monocyte-derived DCs were "mature" in the sense that they had high levels of MHC-II and CD86 expression (both are cell surface markers that enable signalling between cells), and they induced the proliferation of antigen-specific T cells [83-86]. Depletion of DCs (through diphtheria toxin administration) abolished OVA/Imject alum adjuvanticity [83]; thus, DC activation *in vivo* was found to be key to the induction of the humoral immune response by aluminium-containing adjuvants. Alum has also been found to enhance macrophages' abilities to drive T cell proliferation [86]. In addition to monocyte and macrophage recruitment, alum can also accelerate differentiation of monocytes to DCs [87]. The latter have a greater capacity for antigen uptake and subsequent migration in the lymph node to prime naïve B- and T cell populations, leading to an improved immune response.

Alum administration has also been shown to stimulate the release of DAMPs, such as deoxyribonucleic acid (DNA), adenosine triphosphate (ATP) and uric acid from necrotic (dying) cells at the site of alum injection [88-91]. Such release has been proposed to be crucial for adjuvanticity since the DAMPs produced can aid the recruitment of immature DCs and subsequent T-cell activation following alum administration [83].

Flach and co-workers explored the binding of aluminium caesium sulphate dodecahydrate ("caesium alum") and Imject to the membranes of APCs [92]. Caesium alum was found to bind very strongly to DC membranes, triggering abortive phagocytosis and the internalisation of antigen alone. This resulted in antibody production and humoral immunity only (*i.e.* no cellular immunity) because the antigen was presented on MHC-II rather than MHC-I. Interestingly, strong alum binding was exhibited only by DC – and not by B-cell- or macrophage- like cell lines – indicating that DC may be the primary target for alum.

A further hypothesis for alum's mode of action concerns the activation of the nucleotide oligomerisation domain (NOD)-like receptor protein (NLRP)-3 inflammasome. This is a protein complex whose assembly is induced during the innate immune response to stimuli, including bacterial and fungal components and toxins (such as lipopolysaccharide [LPS], zymosan, and nigericin), and signatures of cellular damage or stress (including extracellular ATP and uric acid) [93]; it is depicted in **Figure 1.6**. Inflammasome complex formation begins with the oligomerisation of NLRP-3 protein units [94, 95]. Recruitment and activation of the caspase-1 enzyme then ensue. The latter can stimulate proteolytic cleavage of precursor molecules to proinflammatory cytokines; including interleukin (IL)-1β and IL-18, leading to secretion of the mature cytokines.

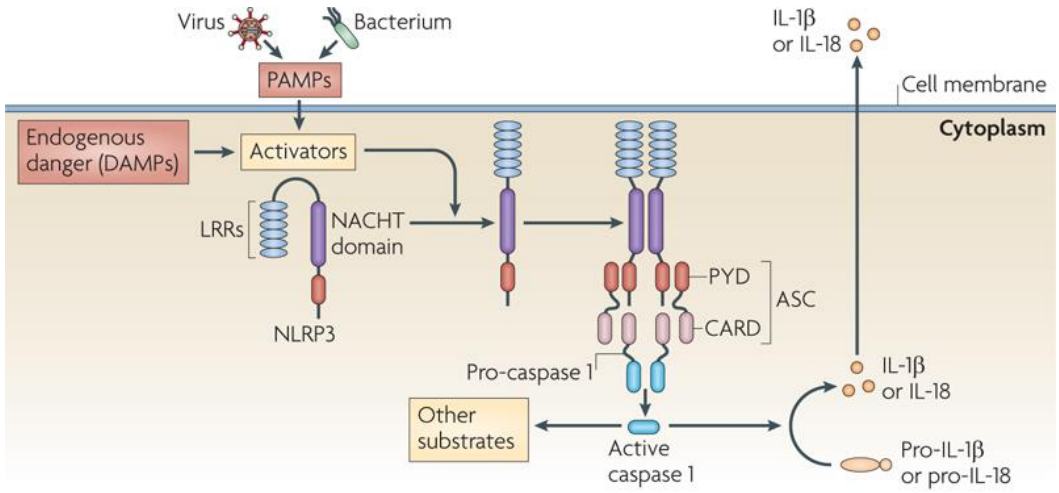

Figure 1.2: ***The mechanism of NLRP-3 inflammasome activation, in which pathogen-associated or danger-associated molecular patterns (PAMPs or DAMPs) stimulate the activation and subsequent opening-up of NLRP-3 proteins to expose their PYD domains. Oligomerisation then occurs, leading to activation of the enzyme pro-caspase 1; this in turn results in secretion of mature pro-inflammatory cytokines. Reproduced with permission from ref [94]. Copyright Macmillan Publishers Ltd 2010.***

Alum has been proposed to activate NLRP-3, but exactly how it does so remains unclear. Zhang *et al.* recently demonstrated a positive linear relationship between the surface hydroxyl content of alum and the induction of reactive oxygen species (ROS) synthesis [96], indicating that ROS stress signals may be responsible. Experimental evidence also suggests that the administration of alum can induce inflammasome activation by release of uric acid from necrotic cells [83]. Uric acid is an endogenous danger signal which causes the maturation of caspase-1, leading to the release of IL-1β and IL-18 [97, 98].

A role for the NLRP-3 inflammasome in alum adjuvanticity has not been suggested by all studies, however. While some groups [98-102] have found that aluminium-containing adjuvants act *via* inflammasome activation for induction of an immune response, others concluded experimentally that the inflammasome is in fact dispensable [83, 92, 103, 104]. A summary of the findings to date can be found in **Table 1.3**. De Gregorio *et al.* [103] concluded that the conflicting evidence for aluminium-containing adjuvants' mode of action could arise due to study-to-study variation in formulation route, antigen purity, assay and other variables. This seems reasonable, given that the aluminium adjuvants often used in research (*e.g.* Imject alum) are not the same as those used in the clinic, and thus are not recommended for mode of action studies [44, 69, 105, 106]. It seems entirely possible that this difference, coupled with variations in experimental protocol, account for the variations in mechanism suggested by the experiment work conducted to date.

Table 1.3: ***A summary of experimental findings as to whether alum's mode of action involves the activation of the NLRP-3 inflammasome.***

Authors and reference	Alum used	Vital role for NLRP-3 inflammasome?
Eisenbarth *et al*. **[99]**	Imject-Alum	Yes
Li *et al.* **[98]**	Imject-Alum Alhydrogel Adju-Phos	Yes
Li *et al.* **[100]**	Alhydrogel	Yes
Kool *et al*. **[101]**	Imject-Alum	Yes
Hornung *et al.* **[102]**	Imject alum	Yes
Flach *et al.* **[92]**	Cesium alum Imject alum "Clinical AlOH"	Dispensible
Franchi and Nunez **[107]**	"Mixture of alum"	Dispensable
Mckee *et al.* **[104]**	Imject alum Alhydrogel	Dispensable
Kool *et al.* **[83]**	Imject alum	Indirect

Several recent reviews have discussed the mechanism of action of alum in more detail than can be presented here, and the interested reader is directed to these for further information [108, 109]. A summary of the various proposed routes of action of alum is given in **Figure 1.7**.

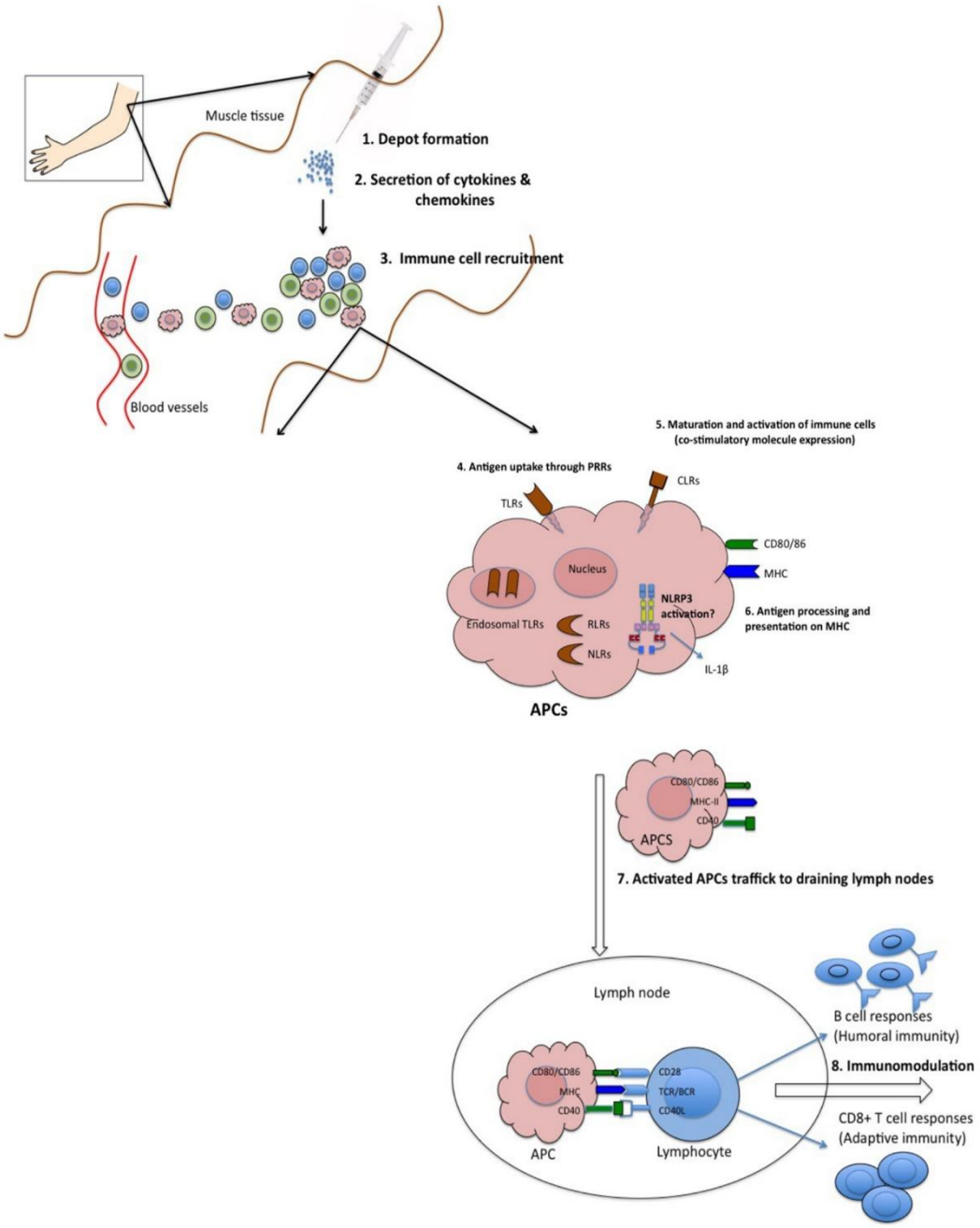

Figure 1.2: ***Possible mechanisms of action for adjuvants*** **in vivo**, ***following intramuscular injection. Abbreviations: - TLR = Toll-like receptor, CLR = C-type lectin receptor, RLR = RIG-I like receptor, NLR = NOD-like receptor, MHC = major histocompatibility complex, CD = Cluster of Differentiation, TCR = T cell receptor, BCR = B cell receptor, PRR = pattern recognition receptor. These receptors are located at different places on the cell surface with the purpose of providing a docking site for their cognate ligand on another cell to induce intracellular signalling cascades. Reproduced from ref [109]. Copyright Frontiers Media S.A 2013.***

1.2.1.4 AS04

AS04 is a new adjuvant developed by GlaxoSmithKline. It comprises a mixture of aluminium hydroxide and MPL-a [110]. The latter is an attenuated version of LPS, which is an abundant component of Gram-negative bacteria. LPS is a powerful PAMP but is considered too dangerous to use in vaccines, whereas MPL-a is less toxic [111]. Since its regulatory approval, AS04 has been used in a number of vaccines, for instance the Cervarix human papilloma virus (HPV) formulation [112]. AS04 has been reported to perform better than alum alone in a vaccine against Herpes simplex virus [113]. Like alum, AS04 stimulates cytokine production at the injection site; this results in recruitment of DCs and monocytes, and ultimately increased numbers of antigen-presenting cells in the lymph nodes [114]. A detailed discussion of AS04 lies outside the scope of this introduction, but the AS04-adjuvanted human papilloma virus (HPV) vaccine has been found to be highly effective, and an AS04 vaccine for Hepatitis B was determined to be more efficacious than one adjuvanted with alum alone [115]. AS04 is not a panacea, however: an AS04-adjuvanted vaccine against genital herpes was found to be ineffective [115].

1.2.1.5 Effect of Size and Shape of Alum Adjuvant Particles on the Immune Response

The possible influence of surface charge on adjuvant/antigen interactions is discussed above. Very recently, some authors have sought to control the particle size and shape of alum and explored how this influences its immunogenicity. Sun and co-workers synthesised a library of AlO(OH) particles of different sizes and shapes [116]. It proved possible systematically to vary the morphology and size of the particles by varying the synthesis pH: see **Figure 1.8**.

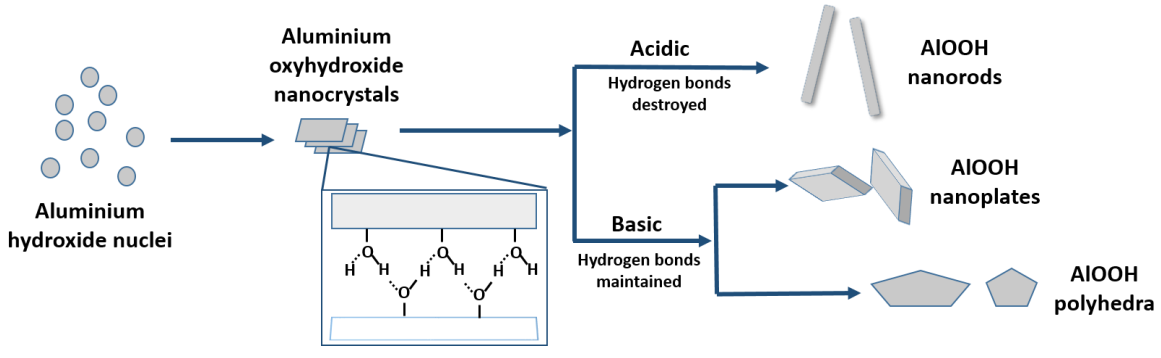

***Figure 1.2:* The variation of AlO(OH) particle morphology through synthesis pH. Adapted from ref [116]. Copyright American Chemical Society 2013.**

At pH 5, rod shaped particles were obtained, while at pH 9 polyhedra-shaped particles were collected and at pH 10, platelets. The samples were found to stimulate ROS production, a property which was ascribed to their high hydroxyl contents. They were also tested for their ability to stimulate macrophages *in vitro*: macrophage-like cells were derived from phorbol 12-myristate 13-acetate (PMA)-treatment of the THP-1 monocytic leukaemia cell line [117] and treated with different AlO(OH) materials in the presence of LPS to induce the production of pro-IL-1β [116]. The results are presented in **Figure 1.9** and show that three of the synthesised AlO(OH) rods were capable of significant NLRP-3 inflammasome activation and subsequent IL-1β production.

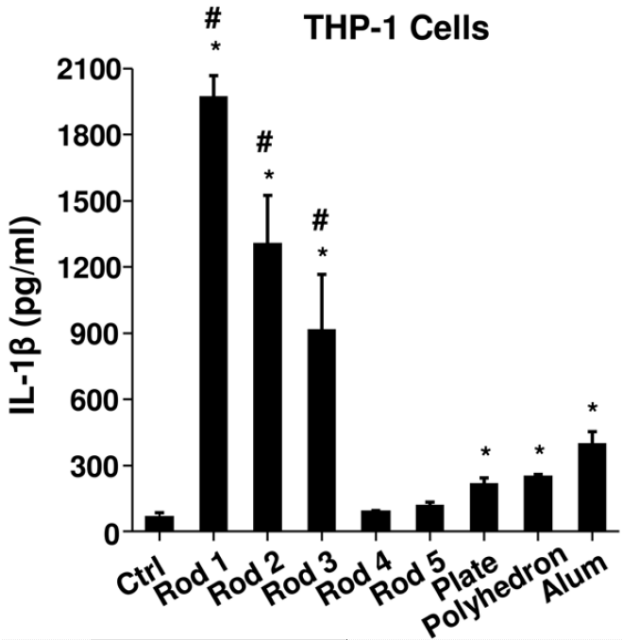

Figure 1.2: ***The production of IL-1β in response to treatment with Sun's particle-engineered alum samples and LPS. AlO(OH) samples were administered to THP-1 macrophages at 500 μg mL^{-1} for 6 hours. 500 μg mL^{-1} alum (Thermo Scientific, Pittsburgh, USA) was also dosed as a control. In water, the hydrodynamic sizes of the AlO(OH) samples are approx. as follows. Rod 1: 810 nm; rod 2: 592 nm; rod 3; 451 nm; rod 4: 434 nm; rod 5: 244 nm; plate: 93 nm; polyhedron: 333 nm; alum: 452 nm. Reproduced from ref [116]. Copyright American Chemical Society 2013.***

There was a clear influence of particle size and shape on cytokine production, with an increase in rod size causing increased secretion. While certain of the rods were effective, the platelet and polyhedra shaped particles had very poor capacity to stimulate IL-1β synthesis. With murine bone-marrow derived DC (BMDC), the rods were found to stimulate the production of IL-6 (a Th2-polarising cytokine), IL-12 (a Th1-polarising cytokine) and IL-1β. The largest rods (rods 1 and 2) were again most effective here. The production of MHC-II, CD86 and CD80 was also increased by the AlO(OH) rods, and again the larger rods are more potent (although the trend is not completely straightforward).

In vivo studies were also undertaken using OVA in C57BL/6 mice [116]. The largest rods (1 and 2, *ca.* 800 and 600 nm respectively) were compared with rod 5, with the smallest particles (244 nm), and alum. The *ca.* 600 and 800 nm rods were found to stimulate higher OVA-specific IgG1 and IgE titres than 244 nm rods or alum. The 244 nm rods did not significantly boost IgG1 production over the level induced by alum, nor did it increase IgE. Control of adjuvant particle size and shape therefore clearly has great promise for the design of vaccines with maximal efficacy.

A second and very recent study seems to confirm the importance of alum particle size and shape control. Li and co-workers explored the influence of alum particle size on the immune response inculcated *in vivo* [118]. AlO(OH) nanoparticles of size 112 nm (AH-NPs) and microparticles of size 9.3 μm (AH-MPs) were prepared. It should be noted that the AH-NPs were found to be completely amorphous by X-ray diffraction, meaning it is not possible from the data presented to confirm the chemical composition of the materials, and the AH-MPs appear to comprise a mixture of poorly-crystalline AlO(OH) and $Al(OH)_3$. Whether the two samples are chemically identical is thus unknown.

Li *et al.* observed increased OVA antigen adsorption to the AH-NPs (*cf.* the AH-MPs), as a result of the much greater surface area of the former. This concept is supported by work undertaken by Lundqvist *et al.* looking at protein interactions with polystyrene nanoparticles [119]. The AH-NPs led to a stronger anti-OVA IgG response in mice than the AH-MPs [118]. Experimental data showing this are presented in **Figure 1.10**.

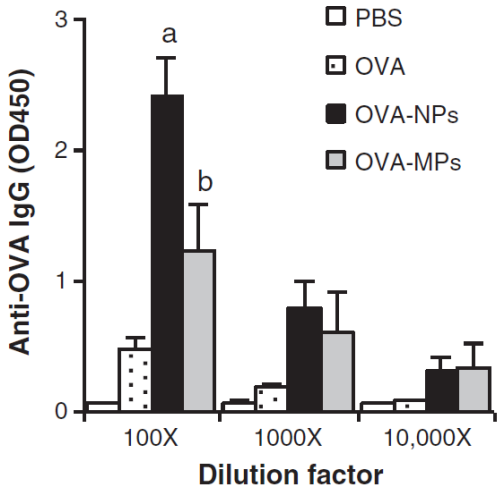

***Figure 1.2:* Total serum anti-OVA IgG levels measured on day 27 following BALB/c mice inoculation with OVA/AH-NPs or OVA/AH-MPs. A denotes p=0.001, OVA vs. OVA/AH-NPs and b p=0.02, OVA/AH-NPs vs. OVA-MPs at 100x dilution factor. Reproduced from ref [118]. Copyright Elsevier 2014.**

Similar results were obtained using the anthrax AP antigen [118]: although both the AH-MPs and NPs induced similar antibody production after one week, after 4 weeks the titres were much higher with the NPs. Internalisation of the adjuvant particles by antigen-presenting cells was also demonstrated to be much greater with the AH-NPs than the MPs, and the amount of local inflammation observed to be lower with the former.

1.2.1.6 Potential Disadvantages of Aluminium-Containing Adjuvants

A number of possible side effects from the use of alum in vaccines have been proposed. Aluminium is classed as a neurotoxin [120] and has been reported to accumulate in regions of the brain commonly affected by Alzheimer's Disease (AD) [121, 122]. However, the evidence is far from conclusive: others [123, 124] found no evidence of aluminium accumulation in AD brains. Elevated levels of aluminium hydroxide have also been connected to macrophagic myofasciitis [125-127].

Alum administration has been linked to localised effects including erythema (reddening of the skin) and granulomatous inflammation (accumulation of phagocytes causing a local inflammatory response) [128-130], although these phenomena may well be the inevitable correlates of the use of an immunostimulatory substance (*i.e.* an adjuvant) rather than being alum-specific [129]. The current consensus is that the side effects, even where undisputed, are extremely minor in comparison to the health benefits: despite the fact that alum has been the only licensed vaccine adjuvant for most of the past 80 years, persuasive evidence of widespread side effects is notable by its absence, and the FDA emphasises that it has been safely administered to humans since 1932 [131].

1.3 Layered Metal Hydroxide Anion Exchange Materials

Layered hydroxides can carry positively charged metal hydroxide layers with interchangeable charge-neutralising interlayer anions. Layered double hydroxides and hydroxy-double salts are two subdivisions of this superfamily. There is some evidence in the literature to suggest that these materials, which are structurally related to AlO(OH), can also act as adjuvants [132-135].

1.3.1 Layered Double Hydroxides

Layered double hydroxides (LDHs) have a general structural formula $[M^{z+}_{1-x}M'^{3+}_{x}(OH)_2]^{\zeta+}(A^{n-}_{\zeta/n})\cdot mH_2O$ (see **Figure 1.11**). When "z" equals 2, possible divalent metal cation species include Ca^{2+}, Co^{2+}, Fe^{2+}, Mg^{2+}, Mn^{2+}, Ni^{2+}, Zn^{2+}; and for M'^{3+}, the common trivalent metal cations are Al^{3+}, Cr^{3+}, Co^{3+}, Fe^{3+}, Ga^{3+}, Mn^{3+} and Ni^{3+}, in this situation $\zeta = x$ [136, 137]. When "z" equals 1, then M^+ is Li^+ and M'^{3+} is Al^{3+} to give $\zeta = 2x-1$. "A^{n-}" denotes the interlayer anion species; this can either be inorganic such as Cl^- and NO_3^- or organic (*e.g.* CO_3^{2-}) [138]. The value of "x" is calculated by $[M'^{3+}/(M^{2+} + M'^{3+})]$ [139] and can range between $0.1 \leq x \leq 0.5$; however, phase pure LDH structures are restricted to a tighter $0.2 \leq x \leq 0.33$ range [140] (see **Figure 1.12**).

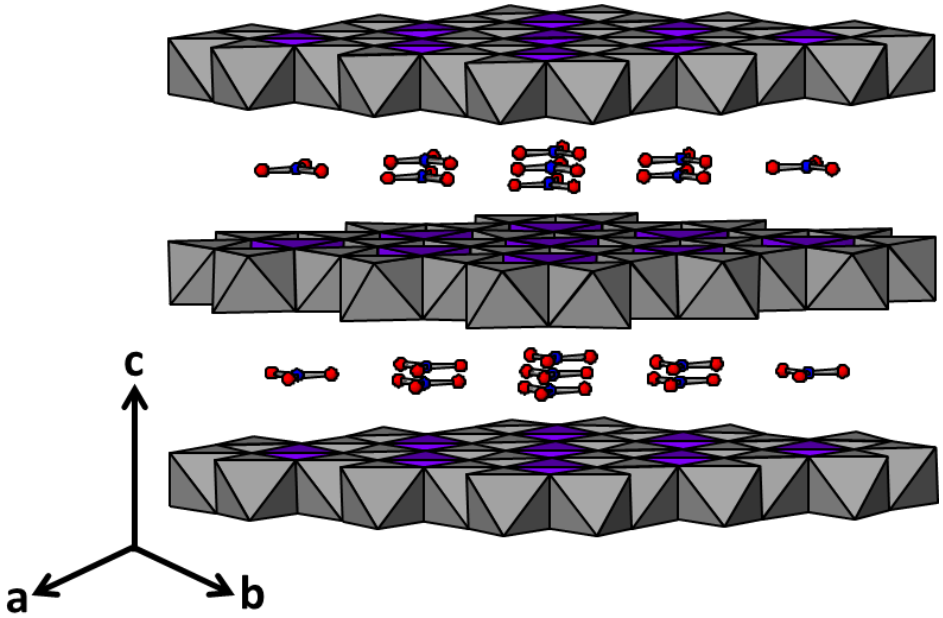

Figure 1.3: *The generic structure of a layered double hydroxide. A material of composition* $[M^{z+}_{1-x}M'^{3+}_{x}(OH)_2]^{\zeta+}(A^{n-}_{\zeta/n})\cdot mH_2O$ *is shown; grey and purple polyhedra represent* $M(OH)_6$ *and* $M'(OH)_6$ *octahedra. N atoms are shown in blue and O atoms in red. The metal cations and interlayer anions are considered to be fully ordered here (that is not always the case). Interlayer water molecules are omitted for clarity.*

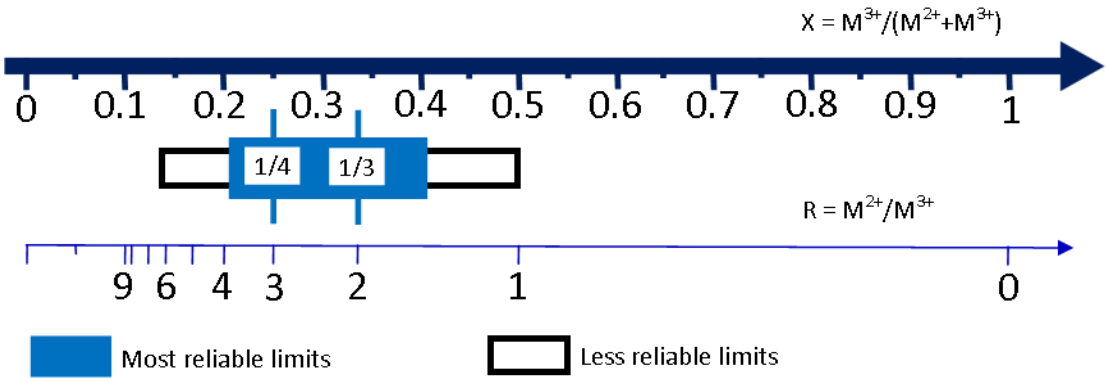

Figure 1.3: *Comparison of trivalent metal ratio "X" scale (top) and divalent vs trivalent ratio "R" (bottom) with the corresponding limits for layered double hydroxide structures. Edited from[136], Copyright 2001.*

Layers within a LDH contain metal cations of similar ionic radii co-ordinated by 6 oxygen atoms to generate either M^{2+}- or M^{3+}-$(OH)_6$ octahedra; edge-sharing results in the formation of 2-dimensional sheets. These layers are net positively charged [141]; intercalated, charge-neutralising interlayer anions balance the positive charge. LDHs exhibit a high degree of compositional flexibility by substitution of the metal cations and interlayer anions; however, ions with too small (*i.e.* Be^{2+}) or too great (*i.e.* Sc^{3+}) an ionic radius are unsuitable candidates for substitution as they are unable to octahedrally co-ordinate in the layer [142-144].

LDHs can be synthesised by a variety of different processes including co-precipitation (which sees the slow addition of a solution containing a mixture of M^{2+} and M^{3+} metal salts into water; alongside the addition of an alkaline solution for the maintenance of a constant pH-value for co-precipitation [145, 146]) and ion exchange [147].

1.3.2 Other Metal Hydroxides

There are other classes of structurally similar layered materials, such as hydroxy double salts (HDS). They contain two divalent metal cations in their hydroxide layer and have a general formula of $[(M^{2+}_aN^{2+}_b)(OH)_y]^{(2a+2b-y)+}A^{n-}_{(2a+2b-y)/n}\cdot zH_2O$. In this, M^{2+} and N^{2+} denote two different divalent metal cation species and A^{n-} represents a charge-balancing, interlamellar anion – the nature of this anionic species controls the interlayer separation [148]. The potential of HDSs as vaccine adjuvants has not been explored in detail to date, although there is some evidence to suggest that they are effective [135].

1.3.3 Immunological Applications of LDHs

Structurally, layered double hydroxides (LDHs) have strong similarities with that of aluminium oxyhydroxide [AlO(OH)] making them a suitable, inorganic adjuvant candidate. The first study to explore LDHs as adjuvants was published in 2010 by a team from Shanghai [133]. These authors synthesised three different LDHs containing Mg and Al, with nitrate as the interlayer ion: $[Mg_3Al(OH)_8]NO_3{\cdot}yH_2O$ ($Mg_3Al\text{-}NO_3$), $[Mg_2Al(OH)_6]NO_3{\cdot}yH_2O$ ($Mg_2Al\text{-}NO_3$), and $[MgAl(OH)_4]NO_3{\cdot}yH_2O$ ($MgAl\text{-}NO_3$) with particle sizes of *ca.* 60 nm. They then investigated the influence of these materials on murine DCs. The LDH particles were taken up by DCs, with maximum uptake reached after around 2h at 37 °C. The co-stimulatory molecules CD86 and CD40 (but not CD80 or MHC-II) were upregulated upon exposure to the $MgAl\text{-}NO_3$ LDH. In contrast, no such upregulation was observed with the $Mg_2Al\text{-}NO_3$ or $Mg_3Al\text{-}NO_3$ materials. Consistent results were observed for the production of cytokines by DC in response to the LDH samples: the $MgAl\text{-}NO_3$ LDH causes a significant and dose-dependent increase in the production of TNF-α and IL-12p70, while no change is seen when DCs are exposed to the other LDHs (see **Figure 1.13**).

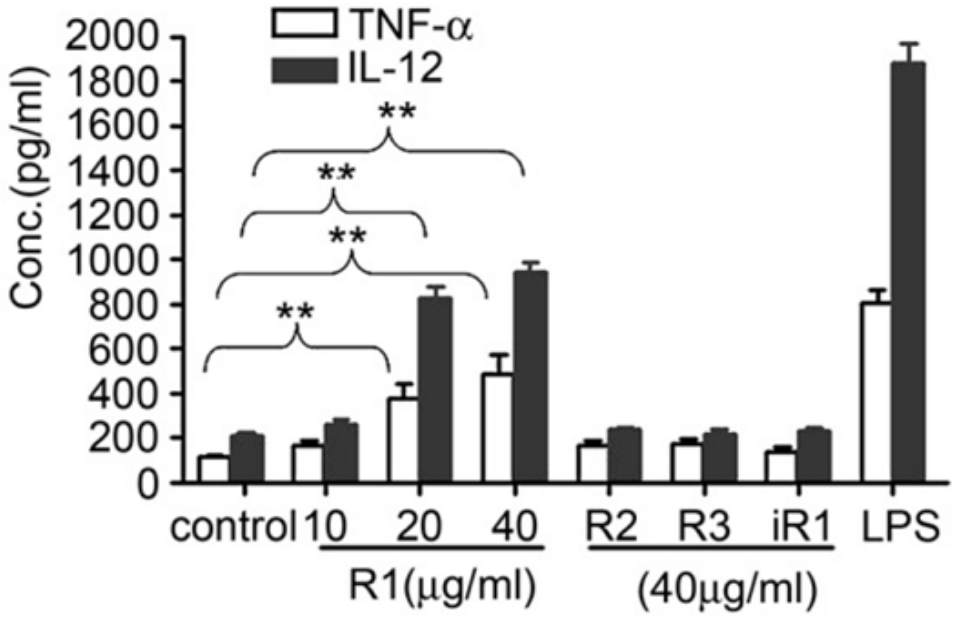

Figure 1.3:* Dendritic cell production of TNF-α and IL-12p70 after 24 hours exposure to $MgAl\text{-}NO_3$ (R1), $Mg_2Al\text{-}NO_3$ (R2) and $Mg_3Al\text{-}NO_3$ (R3), and a 1:1 physical mixture of $Mg(OH)_2/Al(OH)_3$ (iR1). ** denotes $p < 0.01$. Reproduced from ref [133]. Copyright Elsevier 2010.

The migration of DCs towards CCL21 (as assessed in transwell plates) was also seen to increase following treatment with MgAl-NO_3, but not with the other LDHs. This phenomenon was found to be CCR7 dependent [133]. It should be noted, however, that the MgAl-NO_3 material is not phase pure: $Al(OH)_3$ was observed to be present in the sample as well as the LDH. It is thus unclear to what extent the immunogenicity of this sample was due to the presence of LDH, or whether the impurity is important in this regard.

Li *et al.* have built on these early studies to explore the utility of LDHs in DNA vaccines [132]. MgAl-NO_3 was found to readily form complexes with DNA, and the resultant complex had high transfection efficiency as evidenced using a green-fluorescent protein plasmid as a reporter. When C57BL/6 mice were immunised with OVA and the DNA/LDH complex and subsequently challenged with B16-OVA melanoma cells, the complex was found to induce significant increases in serum anti-OVA IgG1 and IgG2c titres over mice immunised with DNA-alone. Survival rates were also improved by use of the LDH. IgG2c was produced in greater amounts than IgG1, suggesting that a Th-1 polarised response was being provoked. This was confirmed by the observation of an increase in IFN-γ (but not IL-4) production by splenocytes. OVA-specific CD8+ T cell activity was also increased in the presence of the LDH adjuvant [132]. Again, however, the LDH sample used shows clear signs of phase impurity.

Another study explored the potential of LDH particles as adjuvants using OVA as the dosed antigen. The LDH particles were found to induce high levels of IgG1 antibodies, comparable to alum [149], and co-delivery of CpG and OVA was found to increase IgG1 and IgG2a titres. Therefore, the composite LDH materials were shown to polarise both Th1- and Th2-type immune responses, rendering them suitable for use with a wide variety of antigens, both viral and bacterial [149].

Another advance in the use of LDHs as adjuvants was reported by Wang and co-workers in 2014 [150]. Core-shell nanoparticles of SiO_2 (core) and Mg/Al LDH (shell) were prepared (denoted SiO_2@LDH; the ratio of Mg:Al is unclear in this work). They were found to be non-cytotoxic and to protect DNA molecules from degradation when incubated with DNAse enzymes. When macrophages (RAW264.7 cell line) were exposed to the SiO_2@LDH particles, increased levels of IFN-γ, IL-12p70 and TNF-α were observed; IL-6 production was additionally enhanced at higher doses. CD86 and MHC-II were also upregulated. BALB/c mice were immunised with the SiO_2@LDH nanoparticles and hepatitis B viral DNA, which was found to result in an increase in anti-hepatitis B IgG titres.

Some of the most recent work in this area was reported by Williams and co-workers [134]. These authors exploited the fact that LDHs have huge structural and chemical diversity, and investigated the immune response to a range of LDHs both *in vitro* (using human monocyte-derived DC and macrophages) and *in vivo* (with OVA in C57BL/6 mice). A systems vaccinology approach was implemented in an attempt to ascertain whether the immune response could be correlated with the LDH physicochemical properties. This approach is illustrated in **Figure 1.14**.

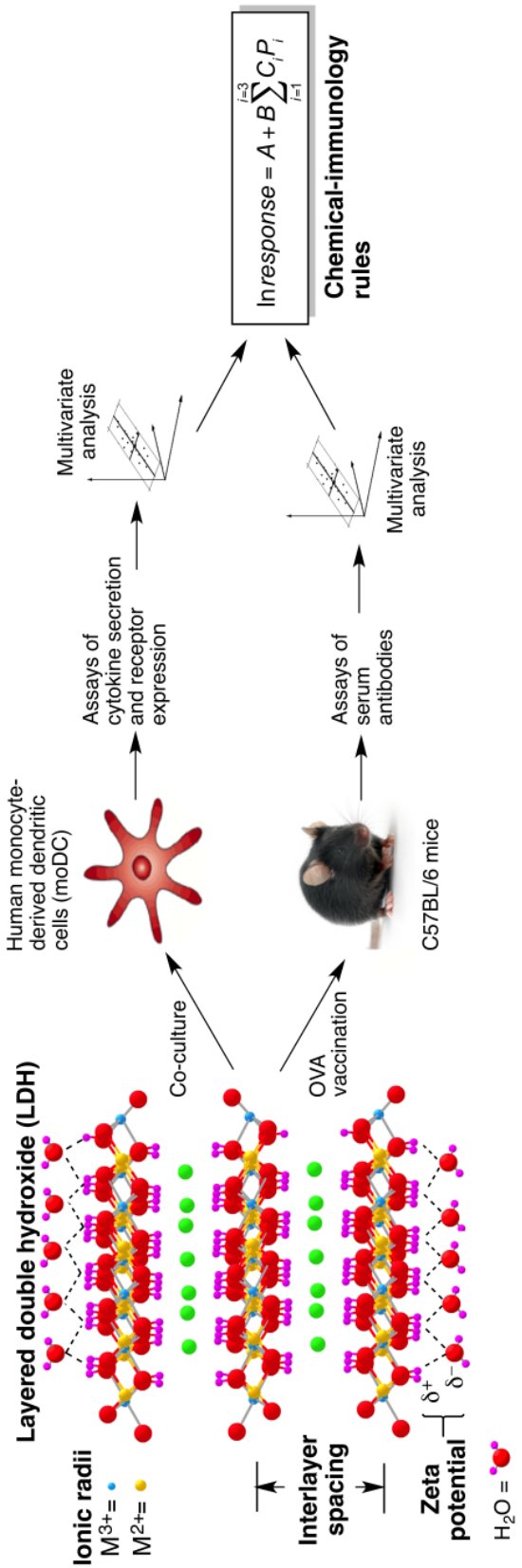

Figure 1.3: ***The systems vaccinology approach adopted by Williams*** **et al.** ***A series of layered double hydroxide materials was prepared, and the response of human dendritic cells in co-culture or of mice upon OVA vaccination quantified. The physicochemical properties of the LDHs were then considered to be causative of the immune response, and structure/property relationships elucidated. Reproduced from ref*** **[134]**. ***Copyright Rockefeller University Press 2014.***

It was observed that different LDHs promote quite distinct immune responses, with some (notably $[LiAl_2(OH)_6]_2CO_3{\cdot}yH_2O$) stimulating very significant cytokine production and co-stimulatory molecule upregulation by DC, while others ($[Mg_2Fe(OH)_6]Cl{\cdot}yH_2O$, Mg_2Fe-Cl) have almost no effect. Similarly, *in vivo* certain LDHs caused large uplifts in antibody titres, while Mg_2Fe-Cl was largely ineffective. The LDHs generally performed at least as well as Imject alum and Alhydrogel® in these assays. *In vivo*, some LDHs were found to produce greater amounts of anti-OVA IgG1 and IgE (Th-2 type antibodies) than the standard commercial adjuvants, while others ($[Mg_2Fe(OH)_6]_2CO_3{\cdot}yH_2O$ in particular) yielded high IgG2c titres, indicative of a Th1 polarised response.

Most remarkably, it was found that the immune response (both *in vitro* for DC and macrophages and *in vivo*) was very highly correlated with three of the physicochemical properties of the LDHs: the zeta potential, the interlayer spacing, and the radius of the monovalent or divalent metal cation (see **Figure 1.14**). An equation could be devised which allowed the magnitude of a particular immunological output to be calculated from these LDH properties (**Figure 1.14**). To test the robustness of this approach, the authors performed blinded trials, where they predicted the responses to two new, untested, LDHs using the mathematical model described above before performing immunological assays *in vitro*. The responses observed were found to be extremely close to those predicted mathematically as depicted in **Figure 1.15**, showing that it is possible to predict *a priori* the immune response to an LDH if its physicochemical properties are known.

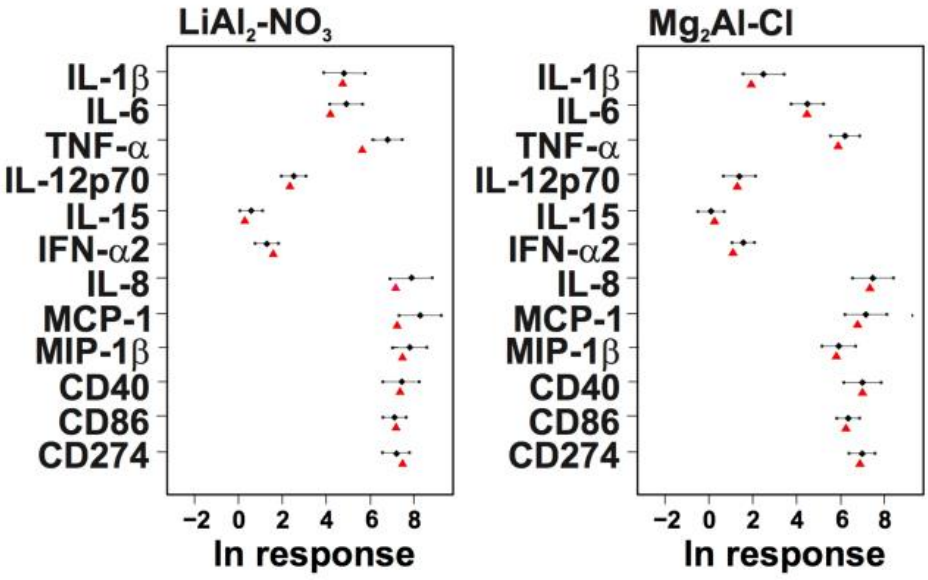

Figure 1.3: ***Data showing that the* in vitro *dendritic cell response to a layered double hydroxide can be accurately predicted from its physicochemical properties. $LiAl_2$-NO_3 = $[LiAl_2(OH)_6]NO_3 \cdot yH_2O$; Mg_2Al-Cl = $[Mg_2Al(OH)_6]Cl \cdot yH_2O$. The production of a range of different cytokines and co-stimulatory molecules was measured, with mean results shown as black squares and 95 % confidence intervals as bars. The red triangles indicate the response predicted mathematically; it is clear that these lie within the confidence intervals in the majority of cases. Reproduced from [134]. Copyright Rockefeller University Press 2014.***

These most recent results suggest that LDHs have enormous potential as bespoke adjuvants. The radii of metal ions are well documented, and interlayer spacing and zeta potential can be easily measured for a sample within a few minutes. Interlayer spacing can also be calculated *in silico*. Ultimately, *in silico* screening of thousands of possible LDHs should be possible, permitting the material required to deliver a particular immune response to be identified, and subsequently synthesised and tested *in vitro* and *in vivo*.

1.4 Alternative Inorganic Adjuvants

Although alum is by far the most commonly used adjuvant, a range of other systems have been explored for use in vaccine. These are discussed below.

1.4.1 Calcium Phosphate

Calcium phosphate (CaP) occurs naturally within the body, and its resultant biocompatibility might be expected to result in reduced immunotoxicity compared with alum, although it is reported to be haemolytic *in vitro* [151]. When compared with alum, CaP has been found to stimulate reduced immunoglobulin-E (IgE) antibody responses and elevated IgG1 production following administration of diphtheria, tetanus or pertussis toxoid antigen to mice [152]. A study in guinea pigs indicated that CaP was as potent or less potent than an Al hydroxide adjuvant for diphtheria-tetanus vaccines [153]. However, in a human trial vaccinating against the same diseases, the CaP adjuvant was found to have higher efficacy but also to lead to more adverse reactions [154]. CaP has been widely administered as a vaccine adjuvant in the diphtheria-pertussis-tetanus vaccine in France [155-157].

Detailed chemical characterisation studies of a commercially available CaP adjuvant found it to comprise not $Ca_3(PO_4)_2$ as would be intuitively expected, but instead to have the chemical formula $Ca_{10-x}(HPO_4)_x(PO_4)_{6-x}(OH)_{2-x}$ (with x varying between 0 and 2) [158] – it is thus a hydroxyapatite material. The CaP sample analysed was found to be poorly crystalline with a point of zero charge of 5.5, indicating that at physiological pH it is likely to adsorb positively charged antigens. Crystals of CaP have been shown to induce IL-1β secretion through inflammasome activation, [159] suggesting a similar mechanism of action to that proposed for alum adjuvants. However, the mechanism of CaP adjuvanticity has not been studied in detail so questions remain.

A range of studies have been performed investigating the adjuvant effect of CaP, for instance in vaccines for influenza [160] or herpes simplex [161, 162]. In the latter case, CaP yielded higher IgG2a titres than alum while provoking minimal IgE production [162]. IgG2a immunoglobulins indicate that a Th1-type immune response is elicited [163], thus targeting viral infections, whilst IgE is produced in response to allergic reactions. Therefore, a higher IgG2a titre is favourable to aid clearance of the infection in this case. In a murine model, CaP could also induce systemic immunity to herpes simplex through mucosal administration [161]. CaP has also been explored for tolerogenic vaccination, for instance to pollen extracts, [164] and in veterinary vaccines [165, 166].

In a very recent study, Olmedo *et al*. explored the response in mice to *Bothrops asper* snake venom [167]. When antigen was adsorbed onto the surface of the adjuvant, CaP was found to be superior to aluminium hydroxide adjuvant, leading to enhanced leucocyte recruitment and greater antibody responses. An alternative approach was explored in which the antigen was co-precipitated with the CaP; these samples resulted in the highest antigen loading, phagocytosis by macrophages, leucocyte recruitment and antibody response. The approach of co-precipitating antigen and CaP together is a popular one, having been used by He *et al*. in their 2002 study [161, 168] and also by Joyappa and co-workers for DNA vaccines [168]. The latter study used a DNA antigen for foot-and-mouth disease (FMD), which was incorporated into CaP nanoparticles through co-precipitation. The transfection efficiency of the resultant systems was found to be very high, and high antibody titres were also observed.

Co-precipitation of CaP with antigen has been shown by Zhou *et al*. to lead to long-lasting CD8+ T-cell responses in mice [169]. In Zhou *et al*.'s work, OVA was co-precipitated with CaP. The CaP-OVA particles were comparable to soluble OVA in terms of antibody responses, but led to high levels of IFN-γ production and a potent CTL response in mice. Combinations of CaP and protein-coated microcrystals (co-precipitated protein and amino acid or sugar formulations) have also been investigated, with CaP inclusion found to enhance phagocytosis in the J774.2 murine monocyte/macrophage cell line [170]. CaP modification also decreased the IgG1 : IgG2a ratio in NIH mice, indicating that its inclusion can help skew the immune response to the Th1 pathway [170].

Zn- and Mg-containing CaP adjuvants were reported by Wang *et al*. in 2013 [171]. The adjuvants were loaded with a hydrothermal extract of a human tubercle bacillus and explored for cancer immunotherapy. The authors hypothesised that the inclusion of Zn and Mg would enhance the adjuvanticity of the CaP materials, owing to the ability of Zn to enhance the activity of antigen-presenting cells and Mg's role in macrophage modulation. *In-vitro* Granulocyte macrophage colony-stimulating factor (GM-CSF) production by macrophage-like cells was increased by the inclusion of zinc or magnesium, and certain of the systems were found to have enhanced anti-tumour activity. Flagellin-functionalised CaP nanoparticles have also been reported and shown effectively to activate the innate immune system [172].

The influence of CaP particle size and shape has also been explored. Crystalline needle-like particles were proposed to elicit a greater immune response than that achieved with spherical nanoparticles, with smaller particle sizes preferred [173].

1.4.2 Zinc Oxide

Zinc oxide (ZnO) is a non-toxic entity commonly used as a dietary supplement. It could thus be an ideal biocompatible adjuvant candidate [174]. There is a small body of literature in which ZnO nanoparticles have been explored as potential adjuvants.

Matsumura and colleagues inoculated BDA/1J mice with the model antigen OVA and 1–3 mg of ZnO, and then sacrificed the animals 21 days after immunisation [175]. The addition of ZnO was found to significantly increase the production of anti-OVA IgG1 and IgE antibodies compared with mice injected with phosphate buffered saline (PBS) alone. An increase in OVA-specific splenocyte proliferation was discovered with higher doses (3 mg) of ZnO. Enhanced splenocyte production of IL-4, IL-5 and IL-17 was also observed 21 days after inoculation (although no statistical tests were presented). In contrast, ZnO did not yield an uplift in IgG2a production nor of IFN-γ production. The authors thus concluded that ZnO provokes a Th2-type response, similar to alum adjuvants. In the experiments reported, ZnO was found to perform approximately on a par with the Imject alum used as a control (it is worth restating here that Imject alum is not the same as the alum used in clinical vaccines, and can be less effective in stimulating an immune response [106]; exactly how ZnO compares with commercially used alums is thus not known). It was postulated that a small amount of dissolution may occur, resulting in Zn^{2+} being present in solution. This has previously been found to cause IL-4 production by T cells [176].

A second study was performed by Roy *et al*. in 2014 [174]. These authors used nano-sized ZnO (<50 nm) and also immunised mice (BALB/c) with ZnO and OVA. The results were largely in agreement with those of Matsumura *et al*.: OVA-specific IgG1 and IgE levels were significantly enhanced when ZnO was co-administered with OVA (see **Figure 1.16**). Studies on splenocytes revealed that the use of ZnO resulted in increased IL-2, IL-4, IL-6 and IL-17 production, while IL-10 and TNF-α production declined. In the presence of ZnO, increased numbers of eosinophils and mast cells were detected in the lungs and spleen, and macrophages and B cells were shown to mature to a greater extent. T-cell proliferation was also observed. These data further support the stimulation of a Th2 response when ZnO is used as an adjuvant.

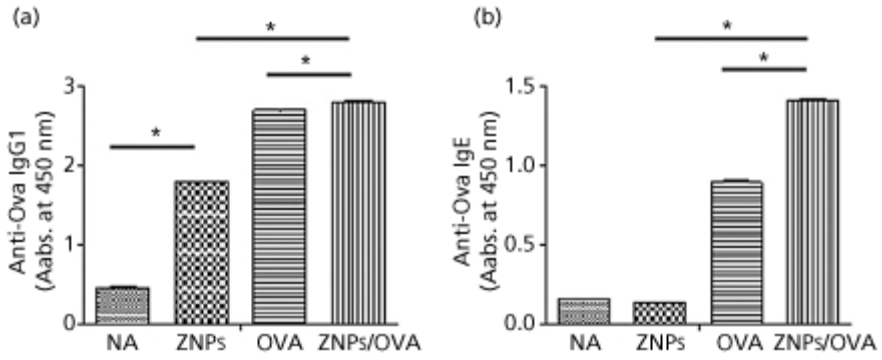

Figure 1.3: ***Serum antibody levels of anti-OVA (a) IgG1 and (b) IgE by BALB/c mice immunised with 0.25 mg of ZnO nanoparticles (ZNPs) and 100 µg OVA. NA represents a negative control. An increase in production of both antibodies can be seen when ZnO is used as an adjuvant with OVA. * denotes $p < 0.05$. Taken with permission from Roy et al [174] Copyright Oxford University Press 2014.***

1.5 Aims of this Thesis

This work aims to fill some of the key gaps in our current knowledge and understanding of inorganic adjuvant systems. It is clear that both the particle size and shape of inorganic nanoparticles are important in controlling the immune response they stimulate, and thus we aim in this thesis to use high-throughput methods to control these and assess the effect on immunogenicity. Further, extensive efforts are made to develop computational models and identify structure/property relationships which could permit the immune response to an inorganic material to be predicted *a priori*. This would ultimately permit thousands of materials to be assessed *in silico* before lead materials were synthesised for onward study. The major aims of this thesis are as follows:

- To use continuous hydrothermal processes to synthesise an array of different AlO(OH), hydroxyapatite and zinc oxide samples, to fully characterise the resultant products, and to test these for adjuvant activity;
- To elucidate structure/property relationships linking the physicochemical properties of these nanoparticles to the immune response they stimulate, as a step towards engineering materials to provoke a particular desired response;

- To extend the previous work undertaken by Williams *et al.* [134] by synthesising a broader family of layered double hydroxide (LDH) materials, fully characterising these, exploring their adjuvanticity *in vitro* and developing structure/property relationships;
- To develop computational methods to model zeta potential *in silico*, particularly for LDH materials. This has not been done to date, and hence computational simulations will be implemented to seek a proxy for this experimental physicochemical property, so as to replace it in the immunological equation deduced by Williams and co-workers [134] and permit an *in silico* screen of candidate adjuvant materials;
- To explore in more depth the immunological effects of hydroxy double salt (HDS) materials, by synthesising, characterising, and assessing *in vitro* a variety of Zn(II)-containing hydroxy double salts;
- Attempts will also be made to elucidate relationships between the physicochemical properties of the HDSs and the immune response they provoke, and also to perform computational calculations and identify relationships between simulated parameters and the *in vitro* response.

1.6 References

1. French-Presse, A., *India and 10 Other Asian Countries Declared Polio Free*, in *The Guardian*. 2014.
2. WHO, *Guidelines for Screening and Treatment of Precancerous Lesions for Cervical Cancer Prevention*. Who Guidelines. 2013. 58.
3. NIAID, *Vaccine Benefits*, in *Benefits for You and Others*. 2014.
4. Rashid, H., Khandaker G., and Booy R., *Vaccination and Herd Immunity: What More Do We Know?* Current Opinion in Infectious Diseases, 2012. **25**(3): p. 243-249.
5. Davis, M.M. and Bjorkman P.J., *T-Cell Antigen Receptor Genes and T-Cell Recognition.* Nature, 1988. **334**: p. 395-402.
6. Petteri Arstila, T., et al., *A Direct Estimate of the Human Ab T Cell Receptor Diversity.* Science, 1999. **286**: p. 958-961.
7. Robins, H.S., et al., *Comprehensive Assessment of T-Cell Receptor Beta-Chain Diversity in Alphabeta T Cells.* Blood, 2009. **114**(19): p. 4099-107.
8. Qi, Q., et al., *Diversity and Clonal Selection in the Human T-Cell Repertoire.* Proc Natl Acad Sci U S A, 2014. **111**(36): p. 13139-44.
9. Schlissel, M.S., *Regulating Antigen-Receptor Gene Assembly.* Nat Rev Immunol, 2003. **3**(11): p. 890-9.
10. DeFranco, A.L., Locksley R.M., and Robertson M., *Immunity: The Immune Response in Infectious and Inflammatory Disease*. 2007, Sunderland, MA: New Science Press Ltd.

11. Radbruch, A., et al., *Competence and Competition: The Challenge of Becoming a Long-Lived Plasma Cell.* Nat Rev Immunol, 2006. **6**(10): p. 741-50.
12. Banchereau, J. and Steinman R.M., *Dendritic Cells and the Control of Immunity.* Nature, 1998. **392**: p. 245-252.
13. Walsh, K.P. and Mills K.H., *Dendritic Cells and Other Innate Determinants of T Helper Cell Polarisation.* Trends Immunol, 2013. **34**(11): p. 521-30.
14. Romagnani, S., *Th1/Th2 Cells.* Inflammatory Bowel Diseases, 1999. **5**(4): p. 285-94.
15. Martinez, F.O., et al., *Macrophage Activation and Polarization.* Front. Biosci., 2008. **13**: p. 453-461.
16. MacPherson, G. and Austyn J., *Exploring Immunology: Concepts and Evidence*. 2012: Wiley.
17. Ozao-Choy, J., Lee D.J., and Faries M.B., *Melanoma Vaccines: Mixed Past, Promising Future.* Surg. Clin. North Am., 2014. **94**(5): p. 1017-1030.
18. Mannie, M.D. and Curtis A.D., *Tolerogenic Vaccines for Multiple Sclerosis.* Human Vaccines & Immunotherapeutics, 2013. **9**(5): p. 1032-1038.
19. Clem, A.S., *Fundamentals of Vaccine Immunology.* J Glob Infect Dis, 2011. **3**(1): p. 73-8.
20. Dhillon, S. and Curran M.P., *Live Attenuated Measles, Mumps, Rubella, and Varicella Zoster Virus Vaccine (Priorix-Tetra).* Paediatr Drugs, 2008. **10**(5): p. 337-47.
21. Organisation, W.H., *Polio Vaccines: Who Position Paper, January 2014*. 2014. p. 73-92.
22. NIAID. *Types of Vaccines*. 2012 3rd April 2012; Available from: http://www.niaid.nih.gov/topics/vaccines/understanding/Pages/typesVaccines.aspx.
23. Plotkin, S.A., *Vaccines: Past, Present and Future.* Nature Medicine, 2005. **11**(4 Suppl): p. S5-11.
24. Aranda, F., et al., *Trial Watch: Peptide Vaccines in Cancer Therapy.* Oncoimmunol., 2013. **2**(12): p. e26621.
25. Saade, F. and Petrovsky N., *Technologies for Enhanced Efficacy of DNA Vaccines.* Expert Review of Vaccines, 2012. **11**(2): p. 189-209.
26. Moyle, P.M. and Toth I., *Modern Subunit Vaccines: Development, Components, and Research Opportunities.* ChemMedChem, 2013. **8**(3): p. 360-76.
27. Oyston, P. and Robinson K., *The Current Challenges for Vaccine Development.* Journal of Medical Microbiology, 2012. **61**(Pt 7): p. 889-94.
28. Pulendran, B., Li S., and Nakaya H.I., *Systems Vaccinology.* Immunity, 2010. **33**(4): p. 516-29.
29. Kirby, D.J., Kaur R., and Perrie Y., *Formulation and Characterisation of Plga Microspheres as Vaccine Adjuvants*, in *Immunomic Discovery of Adjuvants and Candidate Subunit Vaccines*, D.R. Flowers and Y. Perrie, Editors. 2013, Springer: New York. p. 263-.
30. Edelman, R., *Vaccine Adjuvants.* Reviews of Infectious Diseases, 1980. **2**(3): p. 370-383.
31. Beverly, *Immunology of Vaccination*, in *British Medical Bulletin, The British Council*. 2002. p. 15-28.
32. Montomoli, E., et al., *Current Adjuvants and New Perspectives in Vaccine Formulation.* Expert Review of Vaccines, 2011. **10**(7): p. 1053-1061.
33. FDA. *Common Ingredients in U.S. Licensed Vaccines*. [Web page] 2014 1st May 2014; Available from: http://www.fda.gov/BiologicsBloodVaccines/SafetyAvailability/VaccineSafety/ucm187810.htm.
34. Glenny, A.T. and Barr M., *The Precipitation of Diphtheria Toxoid by Potash Alum.* Journal of Pathology and Bacteriology, 1931. **34**(2): p. 131-138.
35. Glenny, A.T., et al., *The Antigenic Value of Toxoid Precipitated by Potassium Alum.* J. Pathol. Bacteriol., 1926. **29**: p. 38-45.
36. Goto, N., et al., *Local Tissue Irritating Effects and Adjuvant Activities of Calcium Phosphate and Aluminium Hydroxide with Different Physical Properties.* Vaccine, 1997. **15**(12-13): p. 1364-1371.

37. Gupta, R.K. and Siber G.R., *Adjuvants for Human Vaccines—Current Status, Problems and Future Prospects.* Vaccine, 1995. **13**(14): p. 1263-1276.
38. Relyveld, E.H., Hencoq E., and Raynaud M., *Etude De La Vaccination Antidiphterique De Sujets Alergiques Avec Une Anatoxine Pure Adsorbee Sur Phosphate De Calcium.* Bull. WHO, 1964. **30**: p. 321-325.
39. Allan, S., *Explaining Alum: Immunologists' Dirty Little Secret.* Nature Reviews Immunology, 2008. **8**(5).
40. Hem, S.L., et al., *Preformulation Studies-the Next Advance in Aluminum Adjuvant-Containing Vaccines.* Vaccine, 2010. **28**(31): p. 4868-4870.
41. Heineman, T.C., et al., *A Randomized, Controlled Study in Adults of the Immunogenicity of a Novel Hepatitis B Vaccine Containing Mf59 Adjuvant.* Vaccine, 1999. **17**(22): p. 2769-2778.
42. Exley, C., Siesjo P., and Eriksson H., *The Immunobiology of Aluminium Adjuvants: How Do They Really Work?* Trends in Immunology, 2010. **31**(3): p. 103-109.
43. Lee, M., et al., *Mg2+ Ions Reduce Microglial and Thp-1 Cell Neurotoxicity by Inhibiting Ca2+ Entry through Purinergic Channels.* Brain Research, 2011. **1369**: p. 21-35.
44. HogenEsch, H., *Mechanism of Immunopotentiation and Safety of Aluminum Adjuvants.* Frontiers in Immunology, 2013. **3**.
45. Hem, S.L., Johnston C.T., and HogenEsch H., *Imject((R)) Alum Is Not Aluminum Hydroxide Adjuvant or Aluminum Phosphate Adjuvant.* Vaccine, 2007. **25**(27): p. 4985-4986.
46. Parks, G.A., *Isoelectric Points of Solid Oxides Solid Hydroxides and Aqueous Hydroxo Complex Systems.* Chemical Reviews, 1965. **65**(2): p. 177-&.
47. Seeber, S.J., White J.L., and Hem S.L., *Predicting the Adsorption of Proteins by Aluminum-Containing Adjuvants.* Vaccine, 1991. **9**(3): p. 201-203.
48. Stryer, L., *Biochemistry*. 1981: W. H. Freeman.
49. Mazur, A. and Harrow B., *Textbook of Biochemistry*. 1971: Saunders.
50. Bleam, W.F., et al., *A P-31 Solid-State Nuclear-Magnetic-Resonance Study of Phosphate Adsorption at the Boehmite Aqueous-Solution Interface.* Langmuir, 1991. **7**(8): p. 1702-1712.
51. Liu, J.C., et al., *Adsorption of Phosphate by Aluminum Hydroxycarbonate.* Journal of Pharmaceutical Sciences, 1984. **73**(10): p. 1355-1358.
52. Lu, F., et al., *Control of Antigen-Binding to Aluminum Adjuvants and the Immune Response with a Novel Phosphonate Linker.* Vaccine, 2013. **31**(40): p. 4362-7.
53. Chang, M.-F., et al., *Degree of Antigen Adsorption in the Vaccine or Interstitial Fluid and Its Effect on the Antibody Response in Rabbits.* Vaccine, 2001. **19**(20): p. 2884-2889.
54. Iyer, S., HogenEsch H., and Hem S.L., *Relationship between the Degree of Antigen Adsorption to Aluminum Hydroxide Adjuvant in Interstitial Fluid and Antibody Production.* Vaccine, 2003. **21**(11-12): p. 1219-1223.
55. Seeber, S.J., White J.L., and Hem S.L., *Solubilization of Aluminum-Containing Adjuvants by Constituents of Interstitial Fluid.* J. Parenter. Sci. Technol., 1991. **45**: p. 156-9.
56. Hansen, B., et al., *Relationship between the Strength of Antigen Adsorption to an Aluminum-Containing Adjuvant and the Immune Response.* Vaccine, 2007. **25**(36): p. 6618-6624.
57. Romero Mendez, I.Z., et al., *Potentiation of the Immune Response to Non-Adsorbed Antigens by Aluminum-Containing Adjuvants.* Vaccine, 2007. **25**(5): p. 825-33.
58. Kanra, G., et al., *Effect of Aluminum Adjuvants on Safety and Immunogenicity of Haemophilus Influenzae Type B-Crm-197 Conjugate Vaccine.* Paediatrics Int., 2003. **45**: p. 314-318.
59. Berthold, I., et al., *Immunogenicity in Mice of Anthrax Recombinant Protective Antigen in the Presence of Aluminum Adjuvants.* Vaccine, 2005. **23**(16): p. 1993-1999.

60. Flebbe, L.M. and Braley-Mullen H., *Immunopotentiating Effects of the Adjuvants Sgp and Quil A: I. Antibody Responses to T-Dependent and T-Independent Antigens.* Cell Immunol., 1986. **99**: p. 119-127.
61. Gupta, R.K., et al., *Vaccine Design: The Subunit and Adjuvant Approach*. 1995, New York: Plenum.
62. Watkinson, A., et al., *Increasing the Potency of an Alhydrogel-Formulated Anthrax Vaccine by Minimizing Antigen-Adjuvant Interactions.* Clin. Vacc. Immunol., 2013. **20**(11): p. 1659-68.
63. Egan, P.M., et al., *Relationship between Tightness of Binding and Immunogenicity in an Aluminum-Containing Adjuvant-Adsorbed Hepatitis B Vaccine.* Vaccine, 2009. **27**(24): p. 3175-3180.
64. Peek, L.J., et al., *Effects of Stabilizers on the Destabilization of Proteins Upon Adsorption to Aluminum Salt Adjuvants.* Journal of Pharmaceutical Sciences, 2007. **96**(3): p. 547-557.
65. Estey, T., et al., *Evaluation of Chemical Degradation of a Trivalent Recombinant Protein Vaccine against Botulinum Neurotoxin by Lysc Peptide Mapping and Maldi-Tof Mass Spectrometry.* Journal of Pharmaceutical Sciences, 2009. **98**(9): p. 2994-3012.
66. Vessely, C., et al., *Stability of a Trivalent Recombinant Protein Vaccine Formulation against Botulinum Neurotoxin During Storage in Aqueous Solution.* Journal of Pharmaceutical Sciences, 2009. **98**(9): p. 2970-2993.
67. Clapp, T., et al., *Vaccines with Aluminum-Containing Adjuvants: Optimizing Vaccine Efficacy and Thermal Stability.* J. Pharm. Sci., 2011. **100**(2): p. 388-401.
68. Morefield, G.L., *A Rational, Systematic Approach for the Development of Vaccine Formulations.* AAPS Journal, 2011. **13**: p. 191-200.
69. Hem, S.L. and HogenEsch H., *Relationship between Physical and Chemical Properties of Aluminum-Containing Adjuvants and Immunopotentiation.* Expert Review of Vaccines, 2007. **6**(5): p. 685-698.
70. Jiang, D., et al., *Relationship of Adsorption Mechanism of Antigens by Aluminum-Containing Adjuvants to in Vitro Elution in Interstitial Fluid.* Vaccine, 2006. **24**(10): p. 1665-9.
71. Sokolovska, A., Hem S.L., and HogenEsch H., *Activation of Dendritic Cells and Induction of Cd4(+) T Cell Differentiation by Aluminum-Containing Adjuvants.* Vaccine, 2007. **25**(23): p. 4575-4585.
72. Gretz, J.E., et al., *Lymph-Borne Chemokines and Other Low Molecular Weight Molecules Reach High Endothelial Venules Via Specialized Conduits While a Functional Barrier Limits Access to the Lymphocyte Microenvironments in Lymph Node Cortex.* Journal of Experimental Medicine, 2000. **192**(10): p. 1425-1439.
73. Smith, D.M., Simon J.K., and Baker J.R., *Applications of Nanotechnology for Immunology (Vol 13, Pg 592, 2013).* Nature Reviews Immunology, 2013. **13**(9).
74. Lanzavecchia, A., *Mechanisms of Antigen Uptake for Presentation.* Current Opinion in Immunology, 1996. **8**(3): p. 348-54.
75. Petros, R.A. and DeSimone J.M., *Strategies in the Design of Nanoparticles for Therapeutic Applications.* Nature Reviews Drug Discovery, 2010. **9**(8): p. 615-627.
76. Burgdorf, S., Lukacs-Kornek V., and Kurts C., *The Mannose Receptor Mediates Uptake of Soluble but Not of Cell-Associated Antigen for Cross-Presentation.* Journal of Immunology, 2006. **176**(11): p. 6770-6.
77. Burgdorf, S., et al., *Distinct Pathways of Antigen Uptake and Intracellular Routing in Cd4 and Cd8 T Cell Activation.* Science, 2007. **316**(5824): p. 612-6.
78. Ghimire, T.R., et al., *Alum Increases Antigen Uptake, Reduces Antigen Degradation and Sustains Antigen Presentation by Dcs in Vitro.* Immunology Letters, 2012. **147**(1-2): p. 55-62.

79. Harrison, W., *Some Observations on the Use of Alum Precipitated Diphtheria Toxoid*.* American Journal of Public Health and the Nations Health, 1935. **25**(3): p. 298-300.
80. Iglesias, E., et al., *Influence of Aluminum-Based Adjuvant on the Immune Response to Multiantigenic Formulation.* Viral Immunology, 2006. **19**(4): p. 712-721.
81. Hem, S.L., *Elimination of Aluminum Adjuvants.* Vaccine, 2002. **20**: p. S40-S43.
82. Hutchison, S., et al., *Antigen Depot Is Not Required for Alum Adjuvanticity.* FASEB J, 2012. **26**(3): p. 1272-9.
83. Kool, M., et al., *Alum Adjuvant Boosts Adaptive Immunity by Inducing Uric Acid and Activating Inflammatory Dendritic Cells.* Journal of Experimental Medicine, 2008. **205**(4): p. 869-882.
84. Mosca, F., et al., *Molecular and Cellular Signatures of Human Vaccine Adjuvants.* Proceedings of the National Academy of Sciences of the United States of America, 2008. **105**(30): p. 10501-10506.
85. Wilcock, L.K., Francis J.N., and Durham S.R., *Aluminium Hydroxide Down-Regulates T Helper 2 Responses by Allergen-Stimulated Human Peripheral Blood Mononuclear Cells.* Clinical and Experimental Allergy, 2004. **34**(9): p. 1373-1378.
86. Rimaniol, A.C., Gras G., and Clayette P., *In Vitro Interactions between Macrophages and Aluminum-Containing Adjuvants.* Vaccine, 2007. **25**(37-38): p. 6784-6792.
87. Seubert, A., et al., *The Adjuvants Aluminum Hydroxide and Mf59 Induce Monocyte and Granulocyte Chemoattractants and Enhance Monocyte Differentiation toward Dendritic Cells.* Journal of Immunology, 2008. **180**(8): p. 5402-5412.
88. Marichal, T., et al., *DNA Released from Dying Host Cells Mediates Aluminum Adjuvant Activity.* Nature Medicine, 2011. **17**(8): p. 996-1002.
89. Rock, K.L., et al., *The Sterile Inflammatory Response.* Annual Review of Immunology, 2010. **28**: p. 321-42.
90. Ahrens, S., et al., *F-Actin Is an Evolutionarily Conserved Damage-Associated Molecular Pattern Recognized by Dngr-1, a Receptor for Dead Cells.* Immunity, 2012. **36**(4): p. 635-645.
91. Zhang, J.G., et al., *The Dendritic Cell Receptor Clec9a Binds Damaged Cells Via Exposed Actin Filaments.* Immunity, 2012. **36**(4): p. 646-657.
92. Flach, T.L., et al., *Alum Interaction with Dendritic Cell Membrane Lipids Is Essential for Its Adjuvanticity.* Nature Medicine, 2011. **17**(4): p. 479-U121.
93. Kool, M., et al., *Cutting Edge: Alum Adjuvant Stimulates Inflammatory Dendritic Cells through Activation of the Nalp3 Inflammasome.* The Journal of Immunology, 2008. **181**(6): p. 3755-3759.
94. Tschopp, J. and Schroder K., *Nlrp3 Inflammasome Activation: The Convergence of Multiple Signalling Pathways on Ros Production?* Nature Reviews Immunology, 2010. **10**(3): p. 210-215.
95. Agostini, L., et al., *Nalp3 Forms an Il-L Beta-Processing Inflammasome with Increased Activity in Muckle-Wells Autoinflammatory Disorder.* Immunity, 2004. **20**(3): p. 319-325.
96. Zhang, H.Y., et al., *Processing Pathway Dependence of Amorphous Silica Nanoparticle Toxicity: Colloidal Vs Pyrolytic.* Journal of the American Chemical Society, 2012. **134**(38): p. 15790-15804.
97. Chen, C.J., et al., *Myd88-Dependent Il-1 Receptor Signaling Is Essential for Gouty Inflammation Stimulated by Monosodium Urate Crystals.* Journal of Clinical Investigation, 2006. **116**(8): p. 2262-2271.
98. Li, H.F., Nookala S., and Re F., *Aluminum Hydroxide Adjuvants Activate Caspase-1 and Induce Il-1 Beta and Il-18 Release.* Journal of Immunology, 2007. **178**(8): p. 5271-5276.
99. Eisenbarth, S.C., et al., *Crucial Role for the Nalp3 Inflammasome in the Immunostimulatory Properties of Aluminium Adjuvants.* Nature, 2008. **453**(7198): p. 1122-U13.

100. Li, H.F., et al., *Cutting Edge: Inflammasome Activation by Alum and Alum's Adjuvant Effect Are Mediated by Nlrp3.* Journal of Immunology, 2008. **181**(1): p. 17-21.
101. Kool, M., et al., *Alum Adjuvant Stimulates Inflammatory Dendritic Cells through Activation of the Nalp3 Inflammasome.* Journal of Immunology, 2008. **181**(6): p. 3755-3759.
102. Hornung, V., et al., *Silica Crystals and Aluminum Salts Activate the Nalp3 Inflammasome through Phagosomal Destabilization.* Nature Immunology, 2008. **9**(8): p. 847-856.
103. De Gregorio, E., Tritto E., and Rappuoli R., *Alum Adjuvanticity: Unraveling a Century Old Mystery.* Eur J Immunol, 2008. **38**(8): p. 2068-71.
104. Mckee, A.S., et al., *Alum Induces Innate Immune Responses through Macrophage and Mast Cell Sensors, but These Sensors Are Not Required for Alum to Act as an Adjuvant for Specific Immunity.* Journal of Immunology, 2009. **183**(7): p. 4403-4414.
105. Exley, C., *When an Aluminium Adjuvant Is Not an Aluminium Adjuvant Used in Human Vaccination Programmes.* Vaccine, 2012. **30**(12): p. 2042-2042.
106. Cain, D.W., et al., *Disparate Adjuvant Properties among Three Formulations of "Alum".* Vaccine, 2013. **31**(4): p. 653-660.
107. Franchi, L. and Nunez G., *The Nlrp3 Inflammasome Is Critical for Aluminium Hydroxide-Mediated Il-1 Beta Secretion but Dispensable for Adjuvant Activity.* Eur J Immunol, 2008. **38**(8): p. 2085-2089.
108. Kool, M., Fierens K., and Lambrecht B.N., *Alum Adjuvant: Some of the Tricks of the Oldest Adjuvant.* J. Med. Microbiol., 2012. **61**(Pt 7): p. 927-34.
109. Awate, S., Babiuk L.A., and Mutwiri G., *Mechanisms of Action of Adjuvants.* Front Immunol, 2013. **4**: p. 114.
110. Tagliabue, A. and Rappuoli R., *Vaccine Adjuvants: The Dream Becomes Real.* Hum. Vaccines, 2008. **4**(5): p. 347-349.
111. Mata-Haro, V., et al., *The Vaccine Adjuvant Monophosphoryl Lipid a as a Trif-Biased Agonist of Tlr4.* Science, 2007. **316**(5831): p. 1628-1632.
112. Schwarz, T.F., *Clinical Update of the As04-Adjuvanted Human Papillomavirus-16/18 Cervical Cancer Vaccine, Cervarix.* Adv. Ther., 2009. **26**(11): p. 983-98.
113. Bourne, N., et al., *Herpes Simplex Virus (Hsv) Type 2 Glycoprotein D Subunit Vaccines and Protection against Genital Hsv-1 or Hsv-2 Disease in Guinea Pigs.* J. Infec. Dis., 2003. **187**(4): p. 542-549.
114. Garcon, N., Wettendorff M., and Van Mechelen M., *Role of As04 in Human Papillomavirus Vaccine: Mode of Action and Clinical Profile.* Expert Opin. Biol. Ther., 2011. **11**(5): p. 667-677.
115. Garcon, N. and Van Mechelen M., *Recent Clinical Experience with Vaccines Using Mpl- and Qs-21-Containing Adjuvant Systems.* Expert Rev. Vaccines, 2011. **10**(4): p. 471-486.
116. Sun, B.B., et al., *Engineering an Effective Immune Adjuvant by Designed Control of Shape and Crystallinity of Aluminum Oxyhydroxide Nanoparticles.* ACS Nano, 2013. **7**(12): p. 10834-10849.
117. Tsuchiya, S., et al., *Induction of Maturation in Cultured Human Monocytic Leukemia-Cells by a Phorbol Diester.* Cancer Research, 1982. **42**(4): p. 1530-1536.
118. Li, X.R., Aldayel A.M., and Cui Z.R., *Aluminum Hydroxide Nanoparticles Show a Stronger Vaccine Adjuvant Activity Than Traditional Aluminum Hydroxide Microparticles.* Journal of Controlled Release, 2014. **173**: p. 148-157.
119. Lundqvist, M., et al., *Nanoparticle Size and Surface Properties Determine the Protein Corona with Possible Implications for Biological Impacts.* Proceedings of the National Academy of Sciences of the United States of America, 2008. **105**(38): p. 14265-14270.
120. Banks, W.A. and Kastin A.J., *Aluminum-Induced Neurotoxicity - Alterations in Membrane-Function at the Blood-Brain-Barrier.* Neuroscience and Biobehavioral Reviews, 1989. **13**(1): p. 47-53.

121. Tomljenovic, L., *Aluminum and Alzheimer's Disease: After a Century of Controversy, Is There a Plausible Link?* Journal of Alzheimers Disease, 2011. **23**(4): p. 567-598.
122. Shaw, C.A. and Tomljenovic L., *Aluminum in the Central Nervous System (Cns): Toxicity in Humans and Animals, Vaccine Adjuvants, and Autoimmunity.* Immunol Res, 2013. **56**(2-3): p. 304-16.
123. Chafi, A.H., et al., *Absence of Aluminum in Alzheimers-Disease Brain-Tissue - Electron-Microprobe and Ion Microprobe Studies.* Neurosci Lett, 1991. **123**(1): p. 61-64.
124. Landsberg, J.P., Mcdonald B., and Watt F., *Absence of Aluminum in Neuritic Plaque Cores in Alzheimers-Disease.* Nature, 1992. **360**(6399): p. 65-68.
125. Gherardi, R., et al., *Macrophagic Myofasciitis Lesions Assess Long-Term Persistence of Vaccine-Derived Aluminium Hydroxide in Muscle.* Brain, 2001. **124**(9): p. 1821-1831.
126. Gherardi, R.K., et al., *Macrophagic Myofasciitis: An Emerging Entity.* Lancet, 1998. **352**(9125): p. 347-352.
127. Gherardi, R.K., et al., *Biopersistence and Brain Translocation of Aluminum Adjuvants of Vaccines.* Front Neurol, 2015. **6**: p. 4.
128. Gupta, R.K., et al., *Adjuvant Properties of Aluminum and Calcium Compounds*, in *Vaccine Design*. 1995, Springer. p. 229-248.
129. Gupta, R.K., et al., *Adjuvants - a Balance between Toxicity and Adjuvanticity.* Vaccine, 1993. **11**(3): p. 293-306.
130. WHO, *Who Vaccine Safety*. 1999, Weekly Epidemiological Record. p. 337-348.
131. Baylor, N.W. *Extrinsic Adjuvants in the Use of Allergen Immunotherapy Aluminium Hydroxide: Mechanism of Action and Safety Assessment*. in *13th International Paul-Ehrlich-Seminar*. 2011. Washington DC: FDA.
132. Li, A., et al., *The Use of Layered Double Hydroxides as DNA Vaccine Delivery Vector for Enhancement of Anti-Melanoma Immune Response.* Biomaterials, 2011. **32**(2): p. 469-477.
133. Li, A., et al., *Signalling Pathways Involved in the Activation of Dendritic Cells by Layered Double Hydroxide Nanoparticles.* Biomaterials, 2010. **31**(4): p. 748-756.
134. Williams, G.R., et al., *Immunity Induced by a Broad Class of Inorganic Crystalline Materials Is Directly Controlled by Their Chemistry.* Journal of Experimental Medicine, 2014. **211**(6): p. 1019-1025.
135. Austyn, J.M., O'hare D., and Williams G.R. *Adjuvants.* 2013. WO2013140136 A1, PCT/GB2013/050636. Application
136. Rives, V., *Layered Double Hydroxides: Present and Future*. 2001: Nova Science Publishers.
137. Evans, D.G. and Slade R.C.T., *Structural Aspects of Layered Double Hydroxides.* Layered Double Hydroxides, 2006. **119**: p. 1-87.
138. Amin, M., Lim L.W., and Takeuchi T., *Determination of Common Inorganic Anions and Cations by Non-Suppressed Ion Chromatography with Column Switching.* Journal of Chromatography A, 2008. **1182**(2): p. 169-175.
139. Weir, M.R., Moore J., and Kydd R.A., *Effects of Ph and Mg:Ga Ratio on the Synthesis of Gallium-Containing Layered Double Hydroxides and Their Polyoxometalate Anion Exchanged Products.* Chemistry of Materials, 1997. **9**(7): p. 1686-1690.
140. Cavani, F., Trifiro F., and Vaccari A., *Hydrotalcite-Type Anionic Clays: Preparation, Properties and Applications.* Catalysis Today, 1991. **11**(2): p. 173-301.
141. Mills, S.J., et al., *Nomenclature of the Hydrotalcite Supergroup: Natural Layered Double Hydroxides.* Mineralogical Magazine, 2012. **76**(5): p. 1289-1336.
142. Miyata, S., *Anion-Exchange Properties of Hydrotalcite-Like Compounds.* Clays and Clay Minerals, 1983. **31**(4): p. 305-311.
143. Miyata, S. and Okada A., *Synthesis of Hydrotalcite-Like Compounds and Their Physicochemical Properties - Systems Mg2+-Al3+-So42- and Mg2+-Al3+-Cro42-.* Clays and Clay Minerals, 1977. **25**(1): p. 14-18.

144. Feitknecht, W., *The Formation of Double Hydroxides between Bi- and Tri-Valent Metals.* Helvetica Chimica Acta, 1942. **25**: p. 555-569.
145. Reichle, W.T., *Synthesis of Anionic Clay-Minerals (Mixed Metal-Hydroxides, Hydrotalcite).* Solid State Ionics, 1986. **22**(1): p. 135-141.
146. de Roy, A., et al., *Anionic Clays: Trends in Pillaring Chemistry*, in *Expanded Clays and Other Microporous Solids*, M. Occelli and H. Robson, Editors. 1992, Springer US. p. 108-169.
147. He, J., et al., *Preparation of Layered Double Hydroxides.* Layered Double Hydroxides, 2006. **119**: p. 89-119.
148. Majoni, S. and Hossenlopp J.M., *Controlled Release Kinetics in Hydroxy Double Salts: Effect of Host Anion Structure.* Advances in Physical Chemistry, 2014. **2014**: p. 12.
149. Yan, S., et al., *Polarized Immune Responses Modulated by Layered Double Hydroxides Nanoparticle Conjugated with Cpg.* Biomaterials, 2014. **35**(35): p. 9508-16.
150. Wang, J., et al., *The Enhanced Immune Response of Hepatitis B Virus DNA Vaccine Using Sio2@Ldh Nanoparticles as an Adjuvant.* Biomaterials, 2014. **35**(1): p. Biomater.
151. Goto, N., et al., *Studies on the Toxicities of Aluminum Hydroxide and Calcium-Phosphate as Immunological Adjuvants for Vaccines.* Vaccine, 1993. **11**(9): p. 914-918.
152. Relyveld, E.H., *Preparation and Use of Calcium Phosphate Adsorbed Vaccines.* Dev Biol Stand, 1986. **65**: p. 131-6.
153. Aggerbeck, H. and Heron I., *Adjuvanticity of Aluminum Hydroxide and Calcium-Phosphate in Diphtheria-Tetanus Vaccines .1.* Vaccine, 1995. **13**(14): p. 1360-1365.
154. Aggerbeck, H., Fenger C., and Heron I., *Booster Vaccination against Diphtheria and Tetanus in Man - Comparison of Calcium-Phosphate and Aluminum Hydroxide as Adjuvants .2.* Vaccine, 1995. **13**(14): p. 1366-1374.
155. Goto, N., et al., *Local Tissue Irritating Effects and Adjuvant Activities of Calcium Phosphate and Aluminium Hydroxide with Different Physical Properties.* Vaccine, 1997. **15**(12): p. 1364-1371.
156. Gupta, R.K. and Siber G.R., *Adjuvants for Human Vaccines - Current Status, Problems and Future-Prospects.* Vaccine, 1995. **13**(14): p. 1263-1276.
157. Relyveld, E.H., Henocq E., and Raynaud M., *[Study of the Antidiphtheria Vaccination of Allergic Subjects with a Pure Anatoxin Absorbed on Calcium Phosphate].* Bull World Health Organ, 1964. **30**: p. 321-5.
158. Jiang, D.P., et al., *Structure and Adsorption Properties of Commercial Calcium Phosphate Adjuvant.* Vaccine, 2004. **23**(5): p. 693-698.
159. Pazar, B., et al., *Basic Calcium Phosphate Crystals Induce Monocyte/Macrophage Il-1 Beta Secretion through the Nlrp3 Inflammasome in Vitro.* Journal of Immunology, 2011. **186**(4): p. 2495-2502.
160. Wack, A., et al., *Combination Adjuvants for the Induction of Potent, Long-Lasting Antibody and T-Cell Responses to Influenza Vaccine in Mice.* Vaccine, 2008. **26**(4): p. 552-561.
161. He, Q., et al., *Calcium Phosphate Nanoparticles Induce Mucosal Immunity and Protection against Herpes Simplex Virus Type 2.* Clinical and Diagnostic Laboratory Immunology, 2002. **9**(5): p. 1021-1024.
162. He, Q., et al., *Calcium Phosphate Nanoparticle Adjuvant.* Clinical and Diagnostic Laboratory Immunology, 2000. **7**(6): p. 899-903.
163. Mountford, A.P., Fisher A., and Wilson R.A., *The Profile of Igg1 and Igg2a Antibody Responses in Mice Exposed to Schistosoma Mansoni.* Parasite Immunol, 1994. **16**(10): p. 521-7.
164. Leynadier, F., et al., *Immunotherapy with a Calcium Phosphate-Adsorbed Five-Grass-Pollen Extract in Seasonal Rhinoconjunctivitis: A Double-Blind, Placebo-Controlled Study.* Clinical and Experimental Allergy, 2001. **31**(7): p. 988-996.

165. Behera, T. and Swain P., *Antigen Adsorbed Calcium Phosphate Nanoparticles Stimulate Both Innate and Adaptive Immune Response in Fish, Labeo Rohita H.* Cellular Immunology, 2011. **271**(2): p. 350-359.
166. Volkova, M.A., et al., *Adjuvant Effects of Chitosan and Calcium Phosphate Particles in an Inactivated Newcastle Disease Vaccine.* Avian Diseases, 2014. **58**(1): p. 46-52.
167. Olmedo, H., et al., *Comparison of the Adjuvant Activity of Aluminum Hydroxide and Calcium Phosphate on the Antibody Response Towards Bothrops Asper Snake Venom.* Journal of Immunotoxicology, 2014. **11**(1): p. 44-49.
168. Joyappa, D.H., et al., *Calcium Phosphate Nanoparticle Prepared with Foot and Mouth Disease Virus P1-3cd Gene Construct Protects Mice and Guinea Pigs against the Challenge Virus.* Veterinary Microbiology, 2009. **139**(1-2): p. 58-66.
169. Zhou, W.B., et al., *Just-in-Time Vaccines: Biomineralized Calcium Phosphate Core-Immunogen Shell Nanoparticles Induce Long-Lasting Cd8(+) T Cell Responses in Mice.* Nanomedicine-Nanotechnology Biology and Medicine, 2014. **10**(3): p. 571-578.
170. Jones, S., et al., *Protein Coated Microcrystals Formulated with Model Antigens and Modified with Calcium Phosphate Exhibit Enhanced Phagocytosis and Immunogenicity.* Vaccine, 2014. **32**(33): p. 4234-42.
171. Wang, X., et al., *Zn- and Mg- Containing Tricalcium Phosphates-Based Adjuvants for Cancer Immunotherapy.* Sci Rep, 2013. **3**: p. 2203.
172. Kozlova, D., et al., *Calcium Phosphate Nanoparticles Show an Effective Activation of the Innate Immune Response in Vitro and in Vivo after Functionalization with Flagellin.* Virol Sin, 2014. **29**(1): p. 33-9.
173. Lee, D.D., Aiolova, M. *Calcium Phosphate Delivery Vehicle and Adjuvant.* 2003. Brookline, MA. U.P. Application,
174. Roy, R., et al., *Zinc Oxide Nanoparticles Provide an Adjuvant Effect to Ovalbumin Via a Th2 Response in Balb/C Mice.* Int Immunol, 2014. **26**(3): p. 159-72.
175. Matsumura, M., et al., *Adjuvant Effect of Zinc Oxide on Th2 but Not Th1 Immune Responses in Mice.* Immunopharmacology and Immunotoxicology, 2010. **32**(1): p. 56-62.
176. Winchurch, R.A., Togo J., and Adler W.H., *Supplemental Zinc (Zn-2+) Restores Antibody-Formation in Cultures of Aged Spleen-Cells .2. Effects on Mediator Production.* Eur J Immunol, 1987. **17**(1): p. 127-132.

Chapter 2 : Experimental Methods

2.1 Introduction

A variety of different adjuvant candidates were synthesised in this thesis and were characterised using a number of techniques, modelled *in silico* and tested *in vitro*. This chapter will give an overview of the main principles underlying each of the experimental and analytical methods employed.

2.2 Particle Engineering

2.2.1 Batch Hydrothermal Synthesis

Batch hydrothermal synthesis utilises near-critical water to generate a highly crystalline product within a pressure vessel placed in an autoclave (**Figure 2.1A**).

Various microparticle- and nanoparticle-scale boehmite [γ-AlO(OH)] morphologies can be synthesised *via* batch hydrothermal processes, including leaf-like [1], platelets [2, 3] and fibre-shaped particles [4]. The morphology can be controlled by varying the precursor concentration, the pH of the reaction mixture, residence time and reaction temperature [5]. For example, Liu and co-workers [1] synthesised leaf-like boehmite microparticles with a 0.6 M solution of aluminium chloride hexahydrate at 160 °C for 12 hours; however, on increasing the concentration to 0.8 M, 3D flower-like structures were obtained. The different morphologies obtained are depicted in **Figure 2.1** (**B, C**).

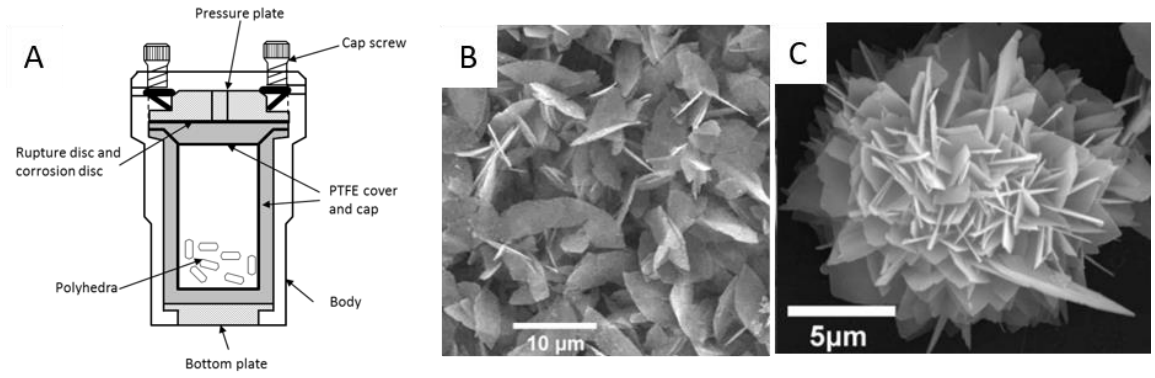

Figure 2.1: ***(A) A schematic representation of the Teflon-lined stainless steel pressure vessel used in batch hydrothermal synthesis; scanning electron micrographs of (B) leaf-like; and (C) flower-like boehmite superstructures, reproduced from ref [1].***

2.2.2 Continuous Plastic Flow Synthesis

Continuous plastic flow synthesis (CPFS) uses sub-100 °C deionised water flowing through polytetrafluoroethylene (PTFE) tubing, heated by a silicon oil bath, to aid the reaction between two precursors (see **Figure 2.2**). The residence time is determined by the length of the PTFE tubing coiled within the silicon oil bath. Close-to ambient temperature water as used in this method has a high dielectric constant (ε = 78 at 25 °C [6]); due to its capacity to generate hydrogen bonds, it acts as a weak solvent for non-polar, organic substances.

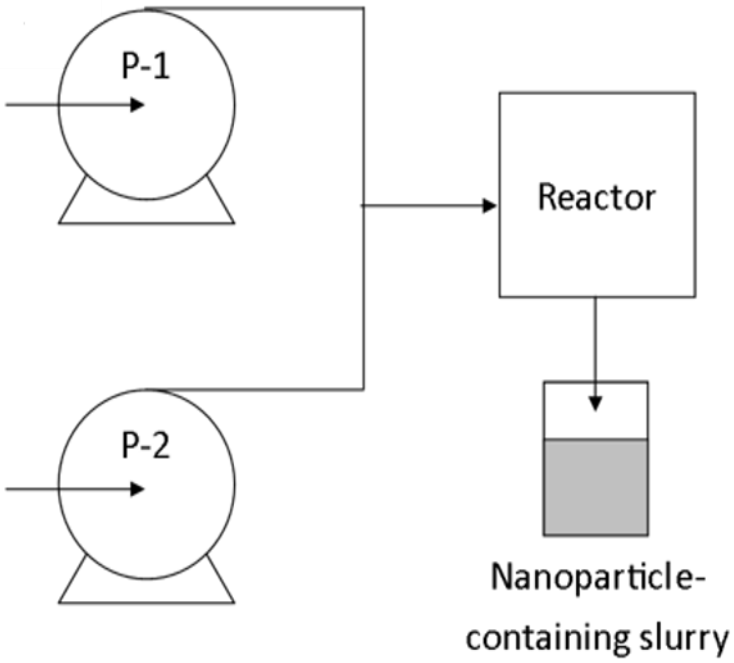

Figure 2.2: ***Schematic representation of the CPFS reactor. P1 and P2 denote HPLC pumps for two separate precursor feeds which mix at a T-junction to initiate reaction. The resultant mixture is heated in an oil bath (reactor) for a defined time period prior to collection of the precipitated product.***

The Clean Materials Technology Group at UCL has used the CPFS process to control both particle size and shape for different nanomaterials including cobalt oxide and silver nanoparticles [7]. Synthesising AlO(OH) in this manner is an attractive approach because the reactions can be performed at low temperatures and pressures, making them economically viable, and the process can readily be made Good Manufacturing Practice (GMP).

2.2.3 Continuous Hydrothermal Flow Synthesis

Continuous hydrothermal flow reactors (**Figure 2.3**) use super-critical water – obtained at temperatures above 400 °C – to generate highly crystalline products [8]. Spectroscopic and computer simulation studies by Cummings *et al.* [9] highlight supercritical water as having a third of the capacity for hydrogen-bond formation of ambient temperature water (as used in the CPFS system), so it exhibits a lower dielectric constant.

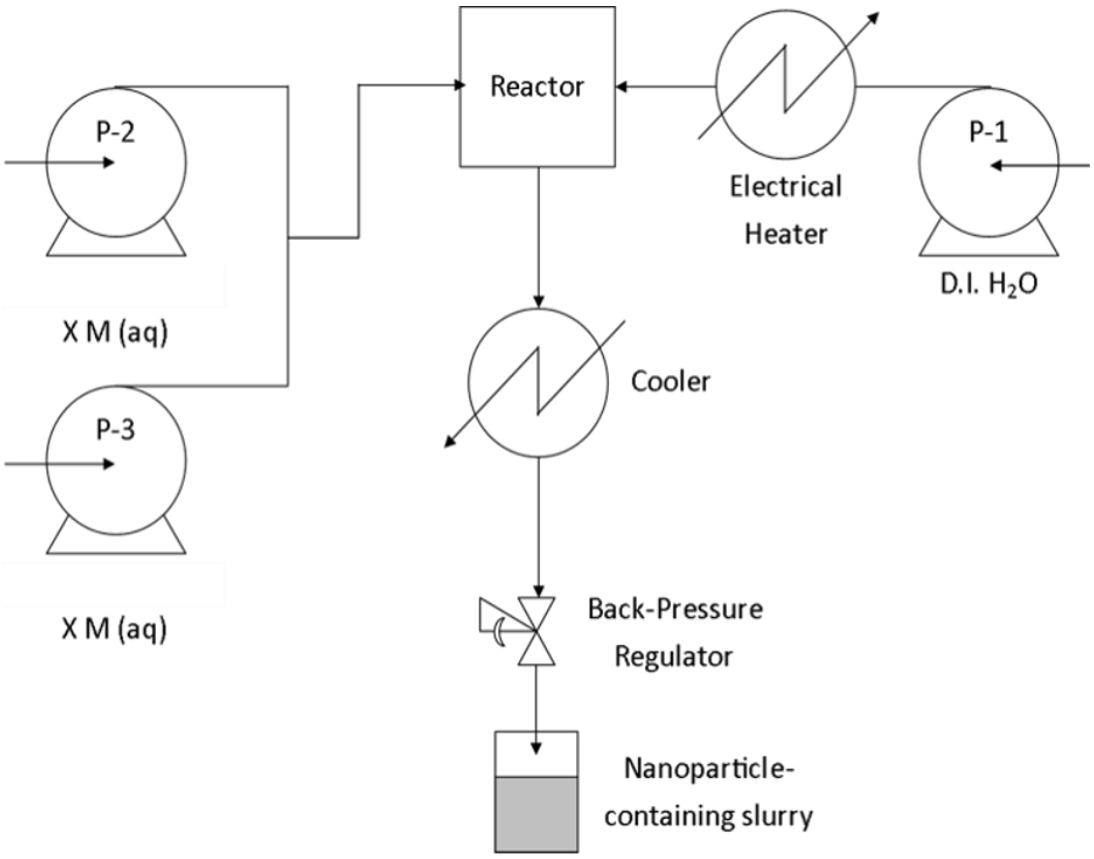

***Figure 2.3:* Schematic representation of the continuous hydrothermal flow synthesis (CHFS) reactor. P1, P2 and P3 denote high pressure diaphragm pumps with P1 providing the heated deionised water feed and P2 and P3 the precursor solution feeds.**

Initial continuous hydrothermal flow synthesis (CHFS) studies into boehmite synthesis by Hakuta [10] demonstrated that different particle sizes and morphologies may be obtained, with morphology being dependent on aluminium salt concentration. It proved possible to convert rhombic AlO(OH) platelets into a hexagonal platelet morphology when both the temperature and pressure parameters were controlled (400 °C and 30 MPa, respectively).

Further experimental work conducted by Hakuta [11] controlled the reaction time through varying the temperature of the pre-heated deionised water feed. A 20 second residence time and 350 °C reaction temperature produced pure phase hexagonal AlO(OH) particles of average diameter 70 nm. Increasing the residence time to 60 seconds also produces pure phase, hexagonal AlO(OH) particles, but with average diameter of 250 nm. Additional work indicated the role of higher pressures in generating larger particle sizes [11].

All three approaches described above will be used within this work. The advantages and disadvantages of these hydrothermal processes are listed in **Table 2.1**.

***Table 2.1:* Advantages and disadvantages of batch, continuous plastic flow synthesis (CPFS) and continuous hydrothermal flow synthesis (CHFS) processes.**

Advantages	Disadvantages
Batch Hydrothermal Synthesis	
Synthesise single- or mixed-metal oxides	High temperatures and pressures required, therefore have high energy costs
Highly crystalline product	Small yields
Can control oxidation state of product	Long reaction times
	Low reproducibility between batches
Continuous Plastic Flow Synthesis	
Low temperatures and atmospheric pressure, thus low energy costs and ease of translation to GMP	Poorly crystalline product at temperatures ≤90 °C
High yields	Scale-up
Short residence times (≈10 minutes)	
Pure phase and reproducible product	
Continuous Hydrothermal Flow Synthesis	
High yields	High temperatures (≥400 °C)
High reaction rates with short residence times (<10 seconds)	High pressures (≈240 bar)
High product reproducibility between experiments	Risk of metal contamination from pipework
Highly crystalline product	
Can control particle size and morphology (*via* temperature, pressure, pH, flow rates etc…)	
Easily scaled-up	

2.3 In silico *modelling*

There are a variety of different methods of simulating structures using computational chemistry: these include density functional theory [12], molecular dynamics [13] and classical codes [14]. The work in this thesis uses the latter *in silico* method.

2.3.1 Interatomic Potentials as a Description of Interatomic Forces

In 1918, Max Born and Alfred Landé devised an equation coupling a short-range repulsive term with a long-range Coulombic interaction, called the Born-Landé equation – **Equation 2.1** [15]. Determination of lattice energy is possible from the electrostatic potential of the ionic lattice and a repulsive-energy term:

Equation 2.1

$$U_{ij}^{Born-Landé} = \frac{b}{r_{ij}^{n}}$$

where b and n are both variables which denote equilibrium interionic separation when n equals 9. Building on this, in 1932, Born introduced a short-range potential entitled the Born-Mayer equation [16] – **Equation 2.2** – with A and p being variable parameters.

Equation 2.2

$$U_{ij}^{Born-Mayer} = Aexp^{-\frac{r_{ij}}{\rho}}$$

The Lennard-Jones potential (**Equation 2.3**, [17, 18]) is an extension of the Born-Landé equation with the introduction of an attractive component for van der Waals interaction modelling as well as use of r_{ij}^{-6} dependence as deduced by London [19-22];

Equation 2.3

$$U_{ij}^{Lennard-Jones} = \frac{b}{r_{ij}^{n}} - \frac{C}{r_{ij}^{6}}$$

with n equalling 12. Modification of the variable C controls the strength of the Lennard-Jones interaction. Removing the repulsive-component of the Lennard-Jones potential and replacing it with the Born-Mayer equation gives the Buckingham potential (**Equation 2.4**, [23]):

Equation 2.4

$$U_{ij}^{Buckingham} = Aexp^{-\frac{r_{ij}}{\rho}} - \frac{C}{r_{ij}^{6}}$$

A, p and C are all variable parameters; when C equals zero, the Born-Mayer equation is implemented for short-range interatomic potentials.

Short-range potentials require cut-off points because after exceeding a certain distance within the lattice, the interactions' contribution to energy becomes negligible and thus can be omitted. Numerical values of cut-offs can be determined through iterative, identical, calculations which have increasing values of short-range cut-offs; the cut-off is then plotted against lattice energy. A plateau in the curve indicates the cut-off value has been reached because the calculated interionic interaction no-longer contributes to the overall energy. Cut-off values reduce computation time, and therefore lead to faster results.

Two-body covalent bonds are described by short-range interatomic potentials (**Equation 2.5**):

Equation 2.5

$$U_{r_{ij}} = \frac{1}{2}k(r_{ij} - r_o)^2$$

A more accurate description is given by the Morse potential (**Equation 2.6**), proposed by Philip Morse in 1929 [24]; this is a type of two-body interaction. The Morse potential is conveniently used to model covalently bonded atoms in a system, due to the parameter values becoming the dissociation energy of a diatomic species (D_e), the equilibrium bond length (r_0) and a final term which is defined through coupling the dissociation energy, of a term, to the vibrational energy for the stretching mode of the structure (a) [25].

Equation 2.6

$$U_{ij}^{Morse} = D_e[(1 - e(-a(r - r_0)))^2 - 1]$$

Three-body interactions (**Equation 2.7**) model bond angles and, similar to two-body terms, the equation exists as a simple, harmonic spring, with θ being the angle between the interatomic vectors $i - j$ and$j - k$.

Equation 2.7

$$U_{\theta_{ijk}} = \frac{1}{2}k(\theta_{ijk} - \theta_o)^2$$

Furthermore, more sophisticated four-body potentials (**Equation 2.8**) can be implemented for dihedral or improper torsion angles. The latter is based on the generation of planes with the atoms 1-2-3 and 2-3-4 and the angle, ψ, exists between these two planes:

Equation 2.8

$$U_{\psi} = \frac{1}{2}k(\psi - \psi_o)^2$$

Coulombic interactions (**Equation 2.9**) contribute up to 90% of the total energy for ionic structures; they are represented by a relatively simplistic equation with q being the charge on the ions i and j. The distance between the two charges is denoted r.

Equation 2.9

$$U_{ij}^{Coulomb} = \frac{q_i q_j}{4\pi\epsilon_0 r_{ij}}$$

2.3.2 Ewald Summation Method

The Ewald summation provides a fast computational method for electrostatic quantities such as energies and forces [26], thus is often implemented over the slowly converging Coulombic equation. The concept is based on splitting the slowly convergent direct sum method into two distinct series for faster computation; thus the terms of the $1/r$ interaction are separated.

2.3.3 Force-Fields

2.3.3.1 Layered Double Hydroxides

Randall Cygan is the main author of the ClayFF force field [27], which was designed for simulation studies on hydrated crystalline compounds, as well as their interfaces with liquid phases [28]. This general force field treats the majority of the interatomic interactions as non-bonded potentials to accommodate modelling of both large- and highly-disordered systems [27]. Ionic-covalent parameters for metal-oxygen interactions with hydrated phases are included, alongside a simple point charge model for water [29]. All metal-oxygen interactions are described by standard 12-6 Lennard-Jones potentials combined with Coulombic charges, with all atoms carrying point charges.

Coulombic charges for oxygen and hydrogen atoms vary dependent on their bonding environment; *i.e.* their occurrence in either a hydroxyl moiety or in a water molecule. Furthermore, the force field incorporates harmonic terms to describe bond stretching and bond angle bending (three-body harmonic terms) in hydroxyl and water entities.

With reference to layered double hydroxides (LDHs), the ClayFF force field can be implemented for a variety of different intercalates, thus removing the requirement for a new model for each individual LDH material.

2.3.3.2 Hydroxy Double Salts

LDH-FF [30] is a force field that was developed through modifications to both the DREIDING and ClayFF [27] force-fields. The former force-field applies general force constants and geometry parameters instead of individual ones, as is the case for ClayFF, that are dependent on the atom combinations within bonds or angles [31]. These are efficient for their respective target structures, but they cannot model the ever-evolving class of layered materials because they only describe a limited number of metal cations. Therefore, the LDH-FF aimed to address this issue by adding in relevant interatomic potential parameters to allow *in silico* modelling of all the octahedrally co-ordinated metal cations within the hydroxide layer of the LDH. However, for this work, it was implemented for the simulation of hydroxy double salts (HDSs). HDSs contain both octahedral and tetrahedral M^{2+} cations in their layers, but the literature reports successful simulations of these materials using the LDH-FF [32].

2.3.4 Energy Minimisation

To determine the equilibrium of a crystal structure, energy minimisation calculations are used which involve iterative numerical procedures and the adjustment of ion-positions within the lattice until the force exerted upon it equates to zero (**Equation 2.10**);

Equation 2.10

$$\frac{\delta U_L}{\delta r} = 0$$

where the U_L term represents the lattice energy of a lattice which consists of N ions with co-ordinates r', defined through the original co-ordinates r.

Computer simulation studies can readily locate local energy minima because upon reaching the lowest point in an energy trough (denoted "Local Energy Minimum" in **Figure 2.4**), the calculation ceases at the predicted optimum conformation of the input structure [33]. Iterative calculations are required to obtain global energy minima for simulated structures. One such method is the Newton-Raphson approximation which utilises second derivatives to converge on the global energy minimum for the input structure (**Figure 2.4**). However, this numerical process increases the computation time for calculations [33].

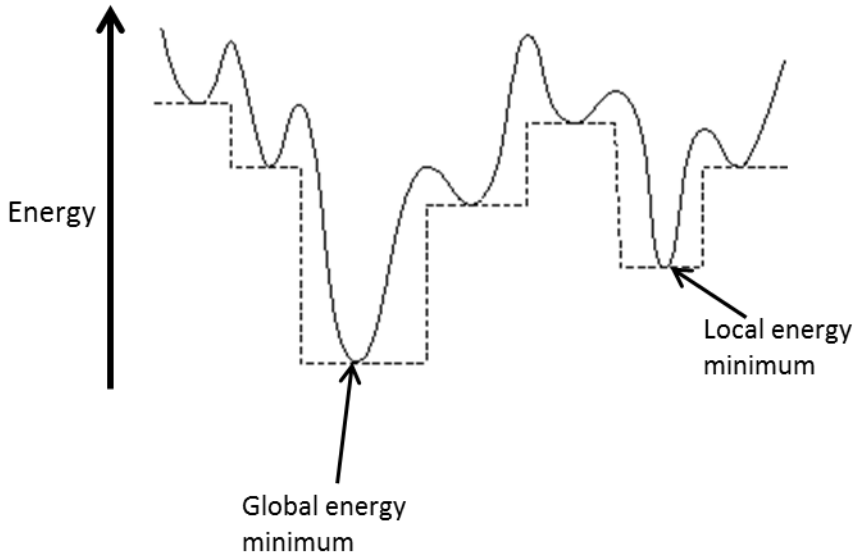

Figure 2.4: ***A graphical representation of local and global energy minima; adapted from http://doye.chem.ox.ac.uk/research/gopt.html.***

2.4 Characterisation

2.4.1 Powder X-ray Diffraction

Powder X-ray diffraction (P-XRD) is a characterisation technique based upon the fact that a beam of X-rays can be diffracted by planes of atoms in a crystal. These diffracted X-rays are recorded by a detector which logs the angles at which they arise, and this information helps determine the spacing between the various planes of atoms within a sample. The resultant diffraction pattern is a plot of the intensity of reflections against the angle, 2θ, whereby θ is both the incident and reflected angle arising between the X-ray beam and the sample.

Reflected X-rays have the potential to constructively interfere with one another when the Bragg condition is met (**Equation 2.11**). In this setting, "d" is the spacing between the planes, θ is the angle between the incident and reflected beams and the plane, and "n" is an integer for the order of the reflection. In any material, there are multiple different sets of planes of atoms that can cause diffraction, and each set of planes is defined by three Miller indices (denoted h, k and l), as is shown in **Equation 2.11**. Each set of indices corresponds to how the planes intersect the x, y and z axes of the material's unit cell. Each crystalline material has its own unique "fingerprint" diffraction pattern which can be analysed to provide information on the crystal structure.

Equation 2.11

$$n\lambda = 2d_{hkl}sin\theta$$

A diffraction pattern's resolution is dependent on the number of aligned planes that are contributing to a given reflection. Use of the Scherrer equation – given in **Equation 2.12** – provides a means of calculating the average dimensions of the crystallites in the sample. The information required for this calculation is the angular width of the diffraction peak at half its height (β; the full width-half maximum) and the diffraction angle θ (both of these values must be in radians). L denotes the crystallite size, and K is a constant.

Equation 2.12

$$L = \frac{K\lambda}{\beta cos\theta}$$

It is important to remember that the K-constant reflects the sample morphology, therefore data must be cautiously analysed if the morphology of the sample is not known or irregular. For simplicity, the value of K used within this work is 1. The crystallite size is not the only factor contributing to the width of reflections in the P-XRD pattern: strain in the particles is also important, and there will always be some inherent broadening from the instrument. Hence, the values calculated by the Scherrer equation are often not exact (unless rigorous calibration is performed). Nevertheless, they can be useful to compare series of samples.

2.4.2 Scanning Electron Microscopy

Scanning electron microscopy (SEM, **Figure 2.5**) allows for the direct visualisation of a solid material's morphology. A high degree of magnification is achieved because the wavelength of the electron beam is far less than that of visible light, allowing for a higher resolution image to be obtained.

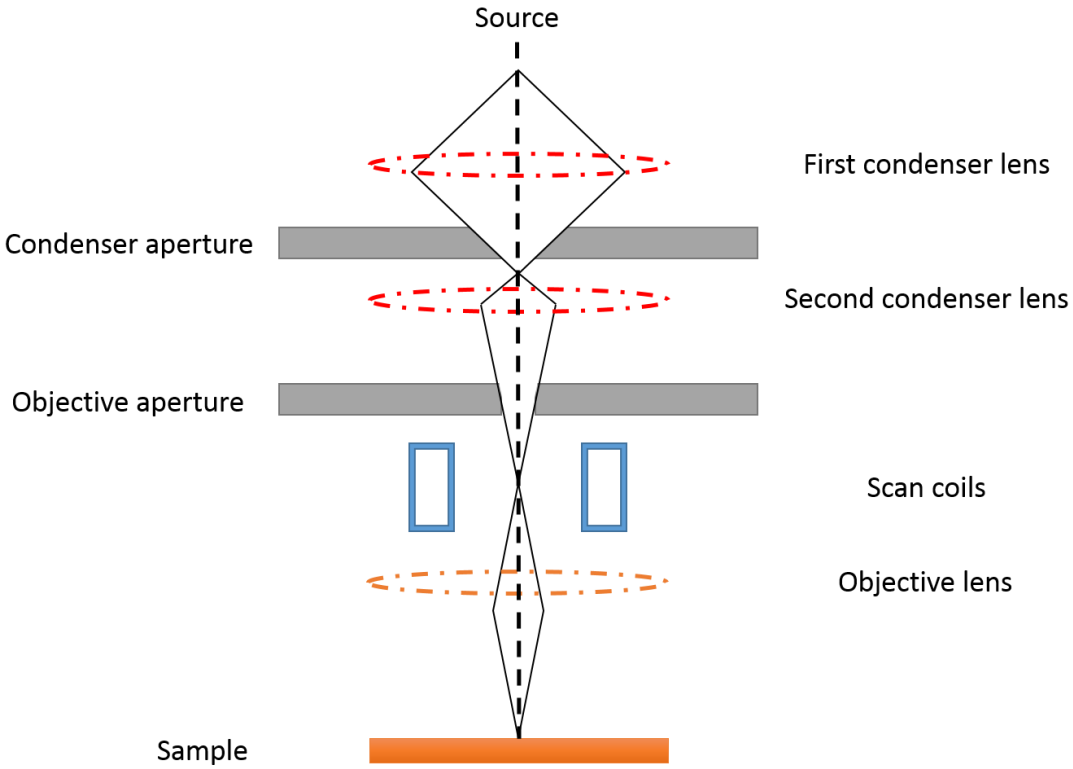

***Figure 2.5:* Schematic diagram of the SEM instrumentation.**

A sample is usually coated with a thin layer of a conducting metal prior to analysis; this conductive coating prevents charging of the sample with the electron beam in the high vacuum, high voltage, environment of the SEM chamber. The sample surface is bombarded with an accelerated electron beam to generate signals at the point of contact. X-rays, backscattered- and secondary-electrons are emitted as a result, with the latter signal type giving rise to a high resolution image which can be used for subsequent size and morphology analysis.

2.4.3 Fourier Transform Infra-Red Spectroscopy

The original means of infra-red (IR) spectroscopy was a dispersive method which separated individual frequencies of energy emitted from an IR source; modern methods adopt the Fourier transform (FT) technique because it is high-throughput and has high sensitivity.

In FTIR, the spectrometer splits the incident IR beam into two separate beams *via* a beamsplitter; ideally, this will transmit 50% of the original IR beam to a moving mirror and the remaining 50% will reach a stationary mirror – as depicted in **Figure 2.6**. The reflected beams recombine at the beamsplitter where either constructive or destructive interference occur. An interferogram arises from this interference, as the path difference between the two beams varies. This must be converted to a frequency spectrum for analytical interpretation; therefore, the FT calculation is performed, generating a spectral means of analysis.

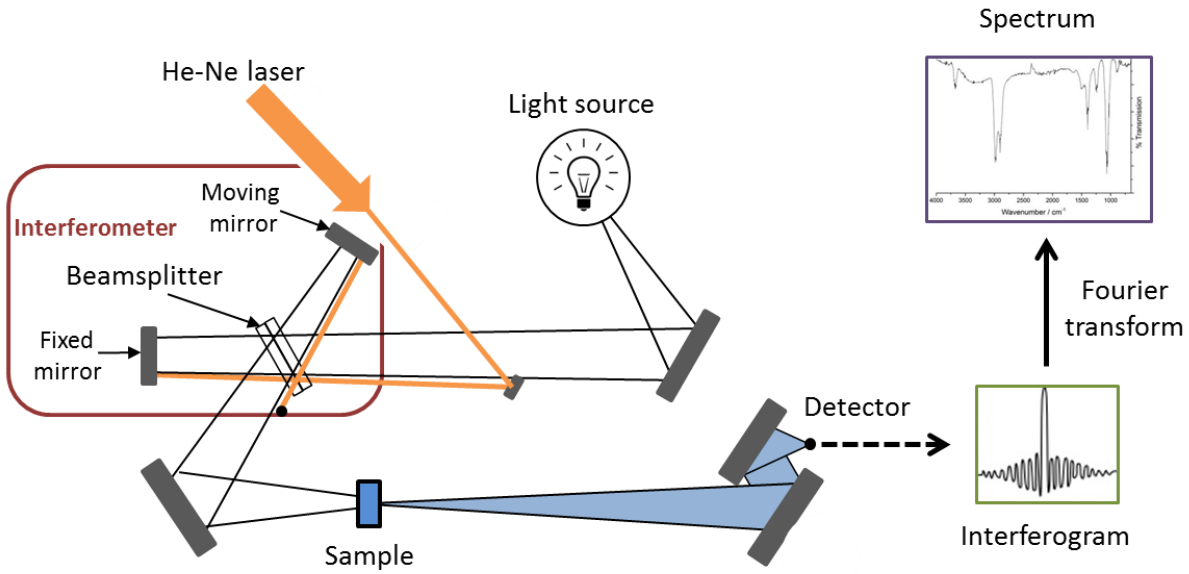

***Figure 2.6:* Schematic diagram of the key aspects of an FTIR spectrometer.**

Absorption in the infra-red (IR) spectrum causes vibrational and rotational changes to a molecule or extended material. A material will only absorb the IR radiation if the absorption alters its dipole moment, but in the systems reported in this work this condition is met. As a result, FTIR provides structural information about the samples prepared, for example indicating the presence of functional groups and bonding interactions.

2.4.4 Nuclear Magnetic Resonance

Nuclear magnetic resonance (NMR, **Figure 2.7**) exploits the spin properties of atomic nuclei to elucidate information on the structure of a sample. The application of a magnetic field causes the different spin states of nuclei, which are degenerate in the absence of a field, to have different energies. The nuclei will adopt the lowest-energy configuration, giving rise to a macroscopic magnetisation which is the basis of NMR spectroscopy.

Nuclear magnetic moments (NMMs) are deflected away from their lowest energy configuration by implementation of radiofrequency irradiation. The resultant deflected NMMs begin rotating (precessing) about the static magnetic field, with the frequency of this precession being dependent on several factors including the type of atom(s) present and the strength of the magnetic field. Samples are placed in a small wire coil, and the precessing magnetic field induces an alternating voltage in the coil to generate an NMR signal.

Spin-active atomic nuclei respond to a specific resonance frequency which can be interpreted to give information on its position in a chemical structure. The frequencies of precessing NMMs are translated to resonance lines in an NMR spectrum. Each position is representative of a nucleus and its location in the overall chemical structure.

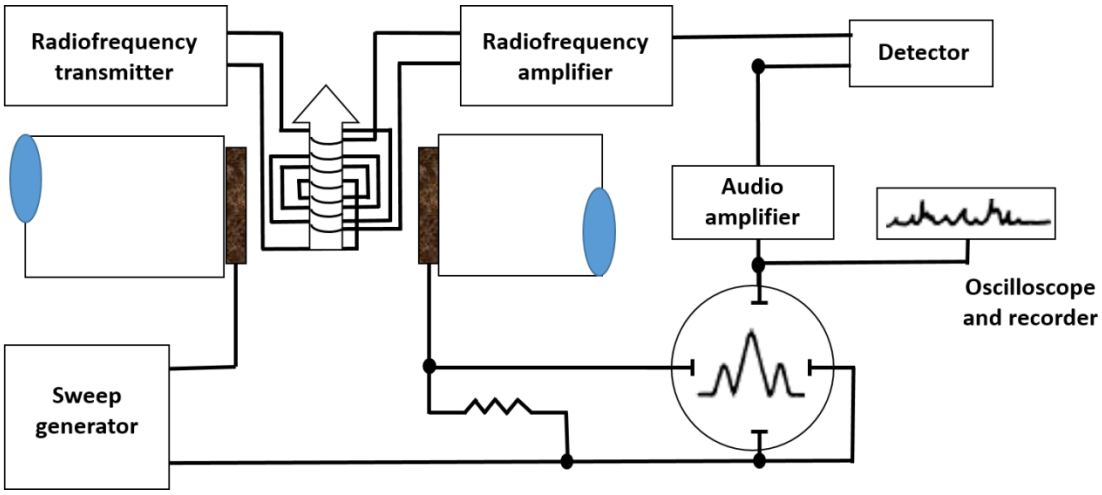

Figure 2.7: ***Schematic representation of a nuclear magnetic resonance spectrometer. The sweep generator aids the passage of radiofrequencies through the resonance frequencies of the sample-of-interest, whereby they are transmitted by the radiofrequency transmitter and amplified (radiofrequency amplifier) for subsequent detection (by the detector) and amplified again (audio amplifier) in order to be displayed as a spectrum on the recorder.***

2.4.5 Thermogravimetric Analysis

Thermogravimetric analysis (TGA) is a quantitative measure of the change in the mass of a sample as a function of temperature or time. The sample is usually subjected to a gradual increase in temperature, in a controlled atmosphere with an inert gas (usually nitrogen). The analyser comprises four key parts: the electrobalance and its controller, the furnace and temperature sensors, the computer and the data acquisition device. In this work, TGA has been used to explore the thermal degradation patterns of selected samples.

In order to determine decomposition it can be helpful to overlay the TGA curve with the derivative thermogravimetric curve, which depicts the rate of mass change with respect to time. The derivative trace provides information to help deduce the separate degradation events.

2.4.6 X-ray Photoelectron Spectroscopy

X-ray photoelectron spectroscopy (XPS) is a surface analytical technique. The average sampling depth is a few nanometres, and because of this samples must be prepared in a glove box to prevent surface contamination which can confound analysis.

The technique involves irradiating a sample with low energy X-rays in order to induce the photoelectric effect. The energy of the emitted photoelectrons is quantified by an electron spectrometer. Like SEM, the sample is analysed in a vacuum chamber, which aids the transmission of photoelectrons to the analyser and reduces the risk of re-contamination of the prepared sample.

XPS excites the core electrons from the atoms within a sample. Since the energies of these are largely unaffected by the local environment and bonding, we can use XPS to deduce the elemental composition of a sample, as well as obtain information about the co-ordination numbers of the atoms.

2.4.7 Surface Area Analysis

By adsorbing inert (usually nitrogen) gas onto the surface of a solid, it is possible to calculate the surface area of the adsorbent material. As a result of measuring the amount of gas that is adsorbed to the solid as a function of the pressure of gaseous nitrogen, an adsorption isotherm can be produced. Pressure is expressed as P/P_0, where P denotes the pressure of nitrogen and P_0 represents the saturated vapour pressure at the adsorption temperature, with an anticipated range of $0 \leq P/P_0 \geq 1.0$. When nitrogen is the adsorbate, adsorption isotherms are usually collected at 77 K when the saturated nitrogen vapour pressure is 1.0 atmosphere.

Adsorption of nitrogen onto the sample can be either *via* van der Waals or dative interactions and adsorption isotherms are categorised according to the porosity of the adsorbent. There are six isotherm categories under the IUPAC classification system (**Figure 2.8** - [34]).

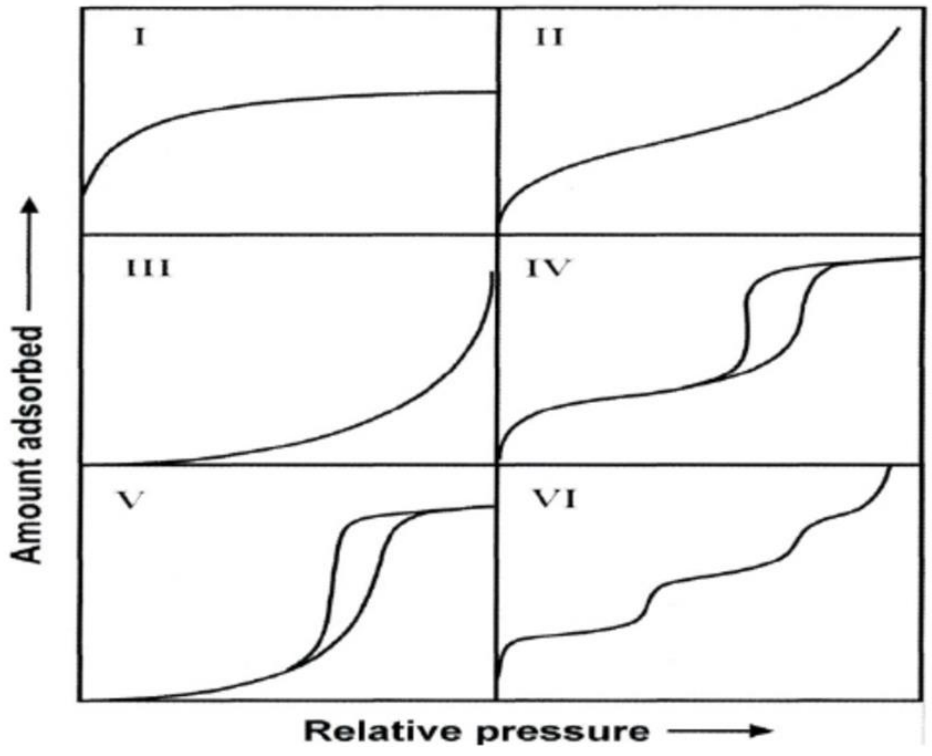

Figure 2.8: ***IUPAC classification of isotherms [34]. Type I arises from a monolayer forming on the sample's surface, II from non-porous materials with multiple adsorption layers, III indicates no adsorption layers, IV represents mesoporous samples, Type V is similar to Type III, having very few interactions arising between the adsorbent and adsorbate, and Type VI corresponds to materials with inconsistent pore sizes, resulting to the multiple steps in the adsorption curve.***

The Braunauer, Emmett and Teller (BET) model is an extension of the Langmuir model and is applied to samples with Type I adsorption isotherms, with the main assumption being that a monolayer of gas is formed on the absorbent. The BET model contains its own set of assumptions, which include: (i) the adsorbate may form multiple layers on the sample's surface, and (ii) interactions between the vapour and the surface correspond to adsorption/desorption. The BET equation is given in **Equation 2.13**:

Equation 2.13

$$\frac{P}{V(P_0 - P)} = \frac{1}{V_m c} + \frac{(c-1)}{V_m c} \cdot \frac{P}{P_0}$$

P is the equilibrium pressure of the adsorbate and P_0 is the saturated vapour pressure. V is the volume of nitrogen gas adsorbed at P/P_0, whilst V_m is the volume of nitrogen gas adsorbed to form the monolayer and the constant c is attributed to the net heat of adsorption. By plotting the two quantities in **Equation 2.14**, a linear relationship between P/P_0 values of 0.05 and 0.35 is obtained:

Equation 2.14

$$\frac{P}{V(P_0 - P)} \; vs. \frac{P}{P_0}$$

The intercept $\frac{1}{V_m c}$ and the slope $\frac{(c-1)}{V_m c}$ can be used to calculate the value of V_m and thus the sample's surface area. The surface area is normally calculated with the desorption isotherm (**Equation 2.15**) with N_A being Avogadro's constant (6.022 x 10^{23} mol^{-1}), A_M denoting the cross-sectional area of the adsorbate molecule (0.162 nm^2 for nitrogen gas) and M_V representing the gram molecular volume (22,414 mL):

Equation 2.15

$$S_A = \frac{N_A x A_M x V_m}{M_V}$$

2.4.8 Pore Volume Analysis

The Barrett, Joyner and Halenda (BJH) method is used to calculate pore size distribution of porous solid samples within this thesis; it is implemented for analysis of mesoporous solid samples (type IV isotherms). It should be noted that the assumptions made here differ from those of the BET equation used for surface area analysis, but since they are being used to calculate different properties this should not be problematic. The BJH method is based on the Kelvin equation (**Equation 2.16**):

Equation 2.16

$$ln\frac{P}{P_0} = \frac{-2\gamma V_m}{rRT}.cos\theta$$

Where P/P_0 gives the relative vapour pressure at which condensation occurs in the pores with a liquid nitrogen droplet of radius r, and a contact angle of the condensed liquid within the pore of θ. γ denotes the surface tension, V_m is the molar volume of the liquid, R is the universal gas constant, and T is the temperature in Kelvin.

The following assumptions are made for the BJH method:

1. All pores are of a uniform shape
2. All pores are in the mesoporous range of 2 – 50 nm

Pores in the surface of the adsorbent material can affect the shape of the adsorption/desorption isotherm because the equilibrium vapour pressure above a condensed liquid in a pore, where the surface of the liquid has a meniscus, is lower than that above a liquid with a flat surface.

The Kelvin equation relates the equilibrium vapour pressure of a liquid in a pore to both the radius of the pore, r, and the contact angle, θ. As the equilibrium vapour pressure above a curved surface is lower than that obtained for a flat surface, the vapour condenses in the pores at lower P/P_0 values than that of a flat surface. It also follows that narrow pores fill at lower pressures than wider ones. Using the pressure at which condensation occurs, it is possible to calculate the radius of the pores in the solid material – see **Equation 2.17**.

Equation 2.17

$$r = -\frac{2.(8.85.10^{-3}).(3.467.10^{-5})}{(8.314).(77.3).\ln(\frac{P}{P_0})}$$

The BJH method includes a correction term for the pore radius, accounting for a film of condensed vapour lining the pore wall, and thus the pore radius is larger than the radius calculated for the meniscus.

2.4.9 Zeta Potential

The zeta potential (ZP) is a physical property arising when particles are dispersed in liquid for the generation of a suspension. It can be used to determine a formulation's stability and is defined as the charge at the boundary between the inner and outer layers in the electrical double layer. In order to obtain a zeta potential measurement, an electric field must be applied to a dispersion of particles contained within a folded, zeta-capable cell (**Figure 2.9**), which allows the negatively-charged particles to move towards the cathode (**Figure 2.9**) with a velocity that is related to their zeta potential. The velocity is determined using a laser interferometric technique that calculates the electrophoretic mobility, and thus zeta potential, of the particles.

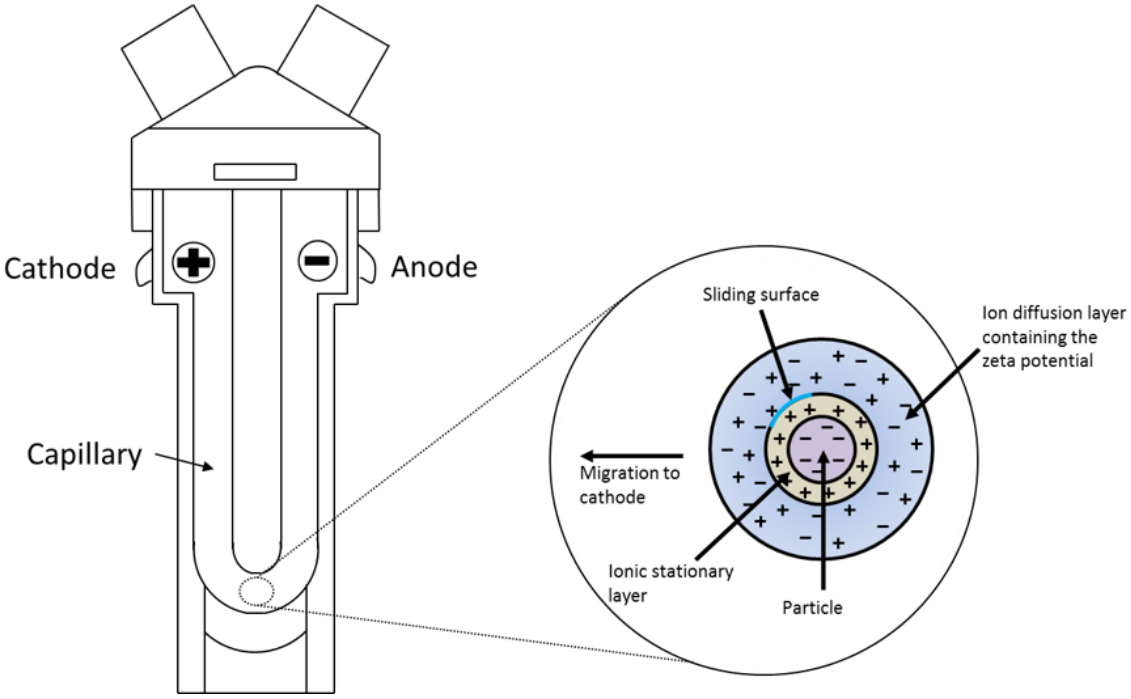

Figure 2.9: ***The folded, zeta-capable capillary cell used in zeta potential measurements. Application of an electrical current causes particles bearing a negative surface charge to migrate to the cathode (indicated by the left arrow).***

However, stability problems with the dispersion or solution can hinder the calculation of zeta potential values. It is possible for aggregates to form in these systems if the particles adhere to one another, and these may sediment due to the effects of gravity. A loosely bound aggregate is referred to as a "floc", and in such instances the particles can easily be separated by shaking. However, if the particles aggregate to generate a tightly-bound coagulant this cannot be broken apart and ultimately will result in caking, which occurs when densely packed sediments which cannot be re-dispersed are formed. After sedimentation, particles have limited or no velocity following the application of an electric field, therefore, their electrophoretic mobility cannot be calculated.

2.4.10 Dynamic Light Scattering

Dynamic light scattering (DLS) measures Brownian (random, non-directed) motion and relates this to the size of the particles in the sample. DLS shines a laser beam through the sample and uses the resultant fluctuations in intensity of scattered light to deduce the rate of movement and hence the size of the particles. A speckle pattern (see **Figure 2.10**) is obtained by the machine with each dot representing an active particle. The bright regions indicate constructive interference between scattered light of the same phase, whilst dark regions highlight destructive interference of out-of-phase scattered light.

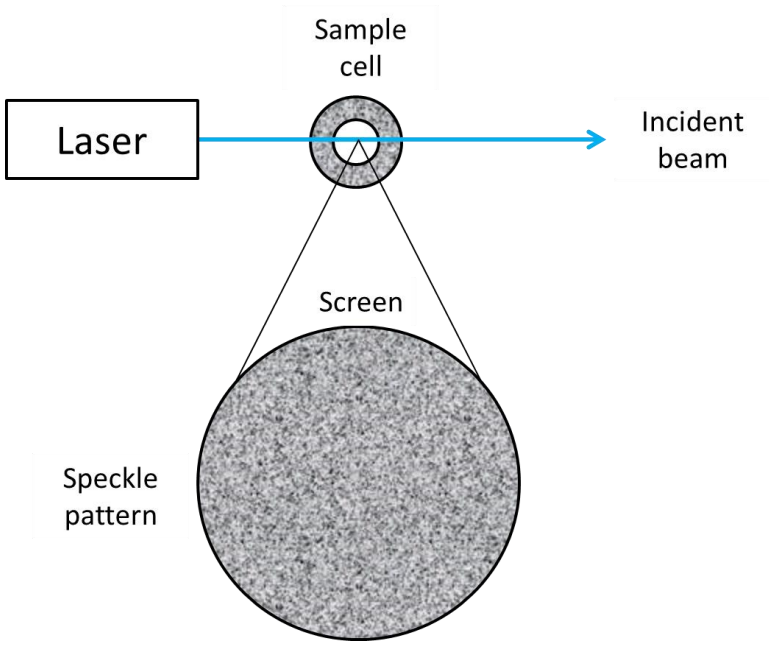

***Figure 2.10:* Schematic of the speckle pattern seen by DLS. Moving particles generate a speckle pattern which is not static and constantly evolves with changes in the suspension due to particle movement.**

Consistent with Brownian motion, large particles move more slowly and cause reduced intensity fluctuations. As a result, the speckle pattern does not change as frequently as is seen with smaller particles in suspension. These changes in the scattering pattern are used to determine particle size with the DLS technique.

2.5 Immunoassay Experiments

2.5.1 RAW264.7 Cell Line

The murine macrophage RAW264.7 cell line was used for immunoassay experiments. This is a semi-adherent cell line derived from adult, male BALB/c mice with Abelson leukaemia virus-induced tumours. This macrophage cell line was selected for immunological studies because macrophages are antigen-presenting cells, and thus important mediators of the immune response. Macrophages are fundamental in engulfing and processing pathogenic entities for presentation of the antigen to T-cells.

2.5.2 Cell Viability Assays

Cell viability assays used the Alamar Blue reagent which exploits the reducing environment of healthy cells' cytosol. Alamar Blue is sodium resazurin dissolved in complete-Dulbecco's Modified Eagle Medium (DMEM) to a concentration of 5mM. Sodium resazurin is a non-toxic compound that can permeate cell membranes. Once inside the cells' cytosol, the minimally fluorescent blue solution is reduced to a highly fluorescent purple sodium resorufin compound by healthy, living cells. The change in fluorescence can be quantified using a plate reader. It is possible for the resazurin to be reduced by the medium too, however; therefore, it is necessary to have appropriate controls to make sure that the changes observed can be attributed to the cell viability rather than any other factors.

2.5.3 Cytokine Production Assays

A "sandwich" Enzyme-Linked ImmunoSorbent Assay (ELISA) provides a quantitative means of determining the cytokine concentrations produced (in this work by RAW264.7 macrophages) in response to adjuvant exposure. After culture, the supernatant is isolated and frozen for future analysis.

The assay works by coating a clean absorbent plastic plate with a capture antibody specific for the cytokine of interest. The plate then has any non-specific binding sites blocked *via* a protein buffer solution. The defrosted cytokine-containing supernatants are added, and the cytokine molecule therein will be bound by the capture antibody. After an incubation period, the supernatant is aspirated and the plate washed prior to the addition of a specific primary antibody which binds to, and hence "sandwiches", the cytokine of interest.

Subsequently, an enzyme-linked secondary antibody is added and binds to the primary antibody. Finally, unbound enzyme-antibody conjugates are removed prior to the addition of a 2,2'-azino-bis(3-ethylbenzothiozoline-6-sulphonic acid) [ABTS] substrate solution. The substrate is converted by the enzyme to a fluorescent molecule which is quantified to determine the relative concentration of cytokine in the supernatant.

2.5.4 Confocal Microscopy

Confocal microscopy uses laser light sources, with the excitation line bandwidth being determined by the source. The laser beam illuminates the entire visual field, rapidly scanning across the sample in a raster fashion. The fluorescence recorded at each point is measured by the photomultiplier tube to generate a complete image (**Figure 2.11**). The key advantage of this microscopy technique is that you can excite different fluorophores, within different regions of a cell, at the same time to view them as a single image.

Confocal is a sophisticated fluorescence microscopy with a pinhole situated directly in front of the photomultiplier tube (this is used for the detection of weak signals) to remove all out-of-focus fluorescence, with the hole diameter controlling the vertical distance from which fluorescence is detected (capture). Therefore, optical slices can be produced which allow the three-dimensional structure of a cell to be visualised. A smaller pinhole diameter corresponds to thinner optical slices.

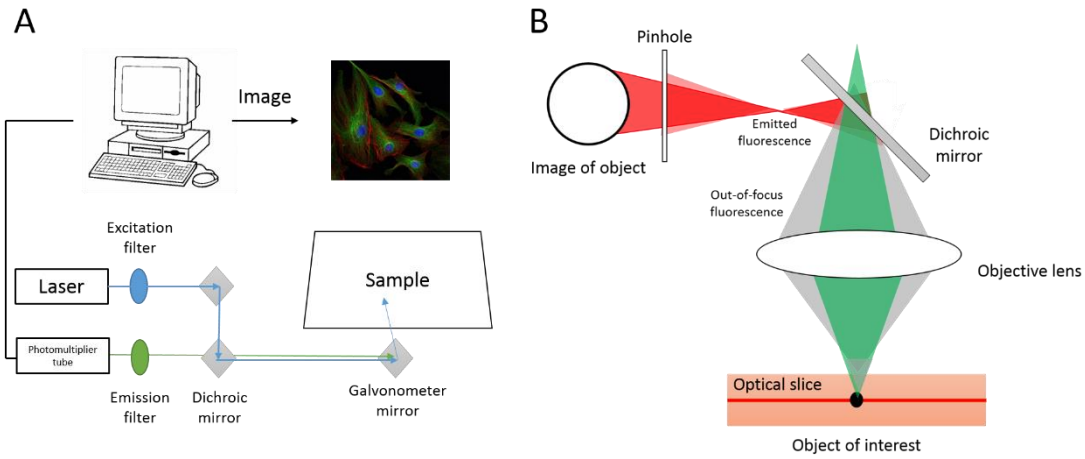

***Figure 2.11:* (A) schematic representation of a confocal microscope and (B) the function of the pinhole. The objective lens is located near to the sample and, thus, has a short focal length. The dichroic mirrors have different reflection and transmission properties at different wavelengths, while the galvanometer mirror is an electrochemical device which deflects light beams in response to electrical currents.**

Altering the focus of the microscope enables a 3-dimensional (3D) image of the object to be formed; each image is known as a "z-section" and can be stacked on top of one another to create a single 3D image.

2.6 References

1. Liu, Y., et al., *Hydrothermal Synthesis of Microscale Boehmite and Gamma Nanoleaves Alumina.* Materials Letters, 2008. **62**(8-9): p. 1297-1301.
2. Lepot, N., et al., *Synthesis of Platelet-Shaped Boehmite and Gamma-Alumina Nanoparticles Via an Aqueous Route.* Ceramics International, 2008. **34**(8): p. 1971-1974.
3. Yanagisawa, K., et al., *Hydrothermal Synthesis of Boehmite Plate Crystals.* Journal of the Ceramic Society of Japan, 2007. **115**(1348): p. 894-897.
4. Wang, X.P., et al., *Simple Synthesis Route of Mesoporous Alooh Nanofibers to Enhance Immune Responses.* Rsc Advances, 2013. **3**(22): p. 8164-8167.
5. Adschiri, T., Kanazawa K., and Arai K., *Rapid and Continuous Hydrothermal Synthesis of Boehmite Particles in Subcritical and Supercritical Water.* Journal of the American Ceramic Society, 1992. **75**(9): p. 2615-2618.
6. Uematsu, M. and Franck E.U., *Static Dielectric-Constant of Water and Steam.* Journal of Physical and Chemical Reference Data, 1980. **9**(4): p. 1291-1306.

7. Denis, C.J., et al., *Nucleation and Growth of Cobalt Oxide Nanoparticles in a Continuous Hydrothermal Reactor under Laminar and Turbulent Flow.* Crystal Growth & Design, 2015. **15**(9): p. 4256-4265.
8. Adschiri, T., Hakuta Y., and Arai K., *Hydrothermal Synthesis of Metal Oxide Fine Particles at Supercritical Conditions.* Industrial & Engineering Chemistry Research, 2000. **39**(12): p. 4901-4907.
9. Cummings, P.T., et al., *Simulation of Supercritical Water and of Supercritical Aqueous-Solutions.* Journal of Chemical Physics, 1991. **94**(8): p. 5606-5621.
10. Hakuta, Y., et al., *Chemical Equilibria and Particle Morphology of Boehmite (Alooh) in Sub and Supercritical Water.* Fluid Phase Equilibria, 1999. **158**: p. 733-742.
11. Hakuta, Y., et al., *Effects of Hydrothermal Synthetic Conditions on the Particle Size of Gamma-Alo(Oh) in Sub and Supercritical Water Using a Flow Reaction System.* Materials Chemistry and Physics, 2005. **93**(2-3): p. 466-472.
12. Parr, R.G., *Density Functional Theory of Atoms and Molecules*, in *Horizons of Quantum Chemistry: Proceedings of the Third International Congress of Quantum Chemistry Held at Kyoto, Japan, October 29 - November 3, 1979*, K. Fukui and B. Pullman, Editors. 1980, Springer Netherlands: Dordrecht. p. 5-15.
13. Haile, J., *Molecular Dynamics Simulation*. Vol. 18. 1992: Wiley, New York.
14. Gale, J.D., *Gulp: A Computer Program for the Symmetry-Adapted Simulation of Solids.* Journal of the Chemical Society-Faraday Transactions, 1997. **93**(4): p. 629-637.
15. Born, M. and Lande A., *The Absolute Calculation of the Crystal Properties with the Help of Bohr's Atomic Model.* Sitzungsberichte Der Koniglich Preussischen Akademie Der Wissenschaften, 1918: p. 1048-1068.
16. Born, M. and Mayer J.E., *For the Lattice Theory of Ionic Crystals.* Physica B-Condensed Matter, 1932. **75**(1-2): p. 1-18.
17. Jones, J.E., *On the Determination of Molecular Fields - Ii from the Equation of State of a Gas.* Proceedings of the Royal Society of London Series a-Containing Papers of a Mathematical and Physical Character, 1924. **106**(738): p. 463-477.
18. Lennard-Jones, J.E., *Cohesion.* Proceedings of the Physical Society, 1931. **43**: p. 461-482.
19. Eisenschitz, R. and London F., *About the Relationship of the Van Der Waals Forces to the Covalent Bonding Forces.* Zeitschrift für Physik, 1930. **60**(7-8): p. 491-527.
20. London, F., *On the Theory and Systematic of Molecular Forces.* Zeitschrift für Physik, 1930. **63**(3-4): p. 245-279.
21. London, F., *Some Characteristics and Uses of Molecular Force.* Zeitschrift Fur Physikalische Chemie-Abteilung B-Chemie Der Elementarprozesse Aufbau Der Materie, 1930. **11**(2/3): p. 222-251.
22. London, F., *The General Theory of Molecular Forces.* Transactions of the Faraday Society, 1937. **33**(0): p. 8b-26.
23. Buckingham, R.A., *The Classical Equation of State of Gaseous Helium, Neon and Argon.* Proceedings of the Royal Society of London Series a-Mathematical and Physical Sciences, 1938. **168**(A933): p. 264-283.
24. Morse, P.M., *Diatomic Molecules According to the Wave Mechanics. Ii. Vibrational Levels.* Physical Review, 1929. **34**(1): p. 57-64.
25. Gale, J. *General Utility Lattice Program (Gulp) Manual Version 3.0.*
26. Ewald, P.P., *The Calculation of Optical and Electrostatic Grid Potential.* Annalen Der Physik, 1921. **64**(3): p. 253-287.
27. Cygan, R.T., Liang J.J., and Kalinichev A.G., *Molecular Models of Hydroxide, Oxyhydroxide, and Clay Phases and the Development of a General Force Field.* Journal of Physical Chemistry B, 2004. **108**(4): p. 1255-1266.
28. Shahsavari, R., Pellenq R.J., and Ulm F.J., *Empirical Force Fields for Complex Hydrated Calcio-Silicate Layered Materials.* Physical Chemistry Chemical Physics, 2011. **13**(3): p. 1002-11.

29. Berendsen, H.J.C., Grigera J.R., and Straatsma T.P., *The Missing Term in Effective Pair Potentials.* Journal of Physical Chemistry, 1987. **91**(24): p. 6269-6271.
30. Zhang, S.T., et al., *Valence Force Field for Layered Double Hydroxide Materials Based on the Parameterization of Octahedrally Coordinated Metal Cations.* Journal of Physical Chemistry C, 2012. **116**(5): p. 3421-3431.
31. Mayo, S.L., Olafson B.D., and Goddard W.A., *Dreiding: A Generic Force Field for Molecular Simulations.* The Journal of Physical Chemistry, 1990. **94**(26): p. 8897-8909.
32. Kaassis, A.Y.A., et al., *Hydroxy Double Salts Loaded with Bioactive Ions: Synthesis, Intercalation Mechanisms, and Functional Performance.* Journal of Solid State Chemistry, 2016. **238**: p. 129-138.
33. Zvelebil, M.J. and Baum J.O., *Understanding Bioinformatics*. 2008: Garland Science.
34. Sing, K.S., *Reporting Physisorption Data for Gas/Solid Systems with Special Reference to the Determination of Surface Area and Porosity (Recommendations 1984).* Pure and applied chemistry, 1985. **57**(4): p. 603-619.

Chapter 3 : Particle Engineering of Aluminium Oxyhydroxide

3.1 Introduction

AlO(OH) is the most commonly used adjuvant in vaccine formulations [1]. It can be synthesised *via* different hydrothermal routes to control its crystal habit [2], as is discussed in more detail in **Section 1.2.1.5**.

The objective of the work reported in this chapter was to develop a library of AlO(OH) samples with different particle size and shape, to characterise these, and to perform a range of immunoassays. Different preparative methods were investigated, using nitrate, chloride and sulphate salts of aluminium in the presence of a precipitating agent – either sodium or potassium hydroxide. The ultimate goal was to relate the particle size and shape of the synthesised adjuvant materials to their immunogenicity *in vitro*, in the hope of being able to tune the immune response through chemistry.

3.2 Materials and Methods

3.2.1 Synthesis

3.2.1.1 Continuous Plastic Flow Reactor

A schematic representation of the continuous plastic flow synthesis (CPFS) apparatus is presented in **Figure 3.1**. Two high-performance liquid chromatography (HPLC) pumps supply two streams of liquid to a T-piece.

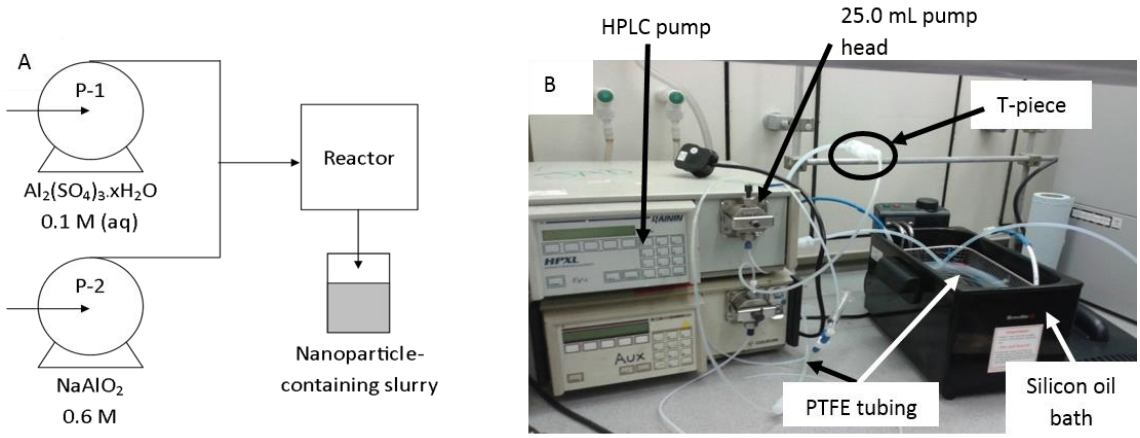

***Figure 3.1:* (A) Diagrammatic representation of the continuous plastic flow synthesis (CPFS) process, with the example of aluminium sulphate as the precursor. 'P-1' and 'P-2' are high pressure liquid chromatography (HPLC) pumps, and 'reactor' denotes a heated silicon oil bath; (B) photograph of the CPFS apparatus.**

One pump was designated for the aluminium salt precursor solution (P-1), and the second for the precipitating agent (P-2) precursor, *e.g.* aluminium sulphate and sodium aluminate, respectively (see **Figure 3.1**). Both precursors are pumped at a rate of 10 mL min^{-1} (at atmospheric pressure) through 1/16" inner diameter polytetrafluoroethylene (PTFE) tubing, before mixing at the T-piece junction. The mixture then flows through an 8 metre length of 1/8" diameter PTFE tubing, coiled inside a silicon oil bath, to give a residence time of 10 minutes. The flow rates were controlled digitally by the HPLC pump interface (Gilson model 305/25.0 mL pump head), while the temperature of the silicon oil bath was set by a thermostat. The pH of both precursors, the pH of the product slurry, and the temperature of the oil bath were monitored throughout the experiment.

The product slurry was continuously collected from the output-end of the coiled PTFE -tubing. A solid white product was then recovered by centrifugation (4500 rpm for 5 minutes) and washed with copious amounts of deionised water. Sequential rounds of washing and centrifugation were performed until the conductivity of the supernatant water was reduced to a value less than 50 S m^{-1}. The product was then freeze-dried at -40 °C under vacuum (between 70-80 mTorr) for approximately 24 hours (Virtis Genesis 35XL freeze drier) prior to characterisation and further analysis.

Precursor slurries of 0.6 M sodium aluminate (Sigma Aldrich, 0011138491) and 0.1 M aluminium sulphate hydrate (Alfa Aesar, 17927-65-0) were initially made up in deionised water. These solutions had pH values of 14 and 4, respectively. Other salts were also explored and details will be given in **Sections 3.4.3 and 3.4.4**.

3.2.1.2 Continuous Hydrothermal Flow Synthesis

A diagrammatic depiction of a three-pump lab scale continuous hydrothermal flow synthesis (CHFS) process is presented in **Figure 3.2A**. The majority of the core components were constructed from Swagelok™ 316 SS components. Control and monitoring of reaction conditions (*i.e.* pump flow rates, heater output and process temperature) was achieved real-time on a computer (CompactRio, National Instruments) using the LabView™ software (National Instruments). Three high-pressure diaphragm pumps (Milton Roy, Primeroyal K) can be used simultaneously (see **Figure 3.2B**) with the first pump, denoted P-1 in **Figure 3.2A**, pumping deionised water. This flows at a rate of up to 80 mL min^{-1} (at 240 bar) through two custom made 7 kW heaters (denoted "electrical heater" in **Figure 3.2A**), with specific design details described by Gruar *et al.* [3]. The remaining pumps (P-2/P-3) are identical to P-1, and are used to deliver precursors – usually water-soluble metal salts, acids and bases – with a combined flow rate of up to 300 mL min^{-1}.

During the CHFS process, supercritical water (red arrow in **Figure 3.2C**, [3]) enters the inner pipe at the base of the confined jet reactor whilst the precursors (blue and green arrows in **Figure 3.2C**) are fed in below the outlet of supercritical water, which then exits the inner pipe as a turbulent jet [3]. The resultant mixture flows upwards (3/8" outer diameter (OD), 0.103" wall thickness, length 0.5m) prior to passing through a cooling pipe section (denoted "cooler" in **Figure 3.2A**) [1/4" OD, 0.049" wall thickness, length 1.5 m], around which cooling water flows concurrently (flow rate of 10 L min^{-1}, inlet T = 15 °C). The cooled product exits the CHFS process *via* a manually actuated back-pressure regulator (denoted "BPR" in **Figure 3.2B**; BPR, Tescom) and was continuously collected at atmospheric pressure [4].

The product was recovered in the same manner as for CPFS, described in **Section 3.2.1.1**.

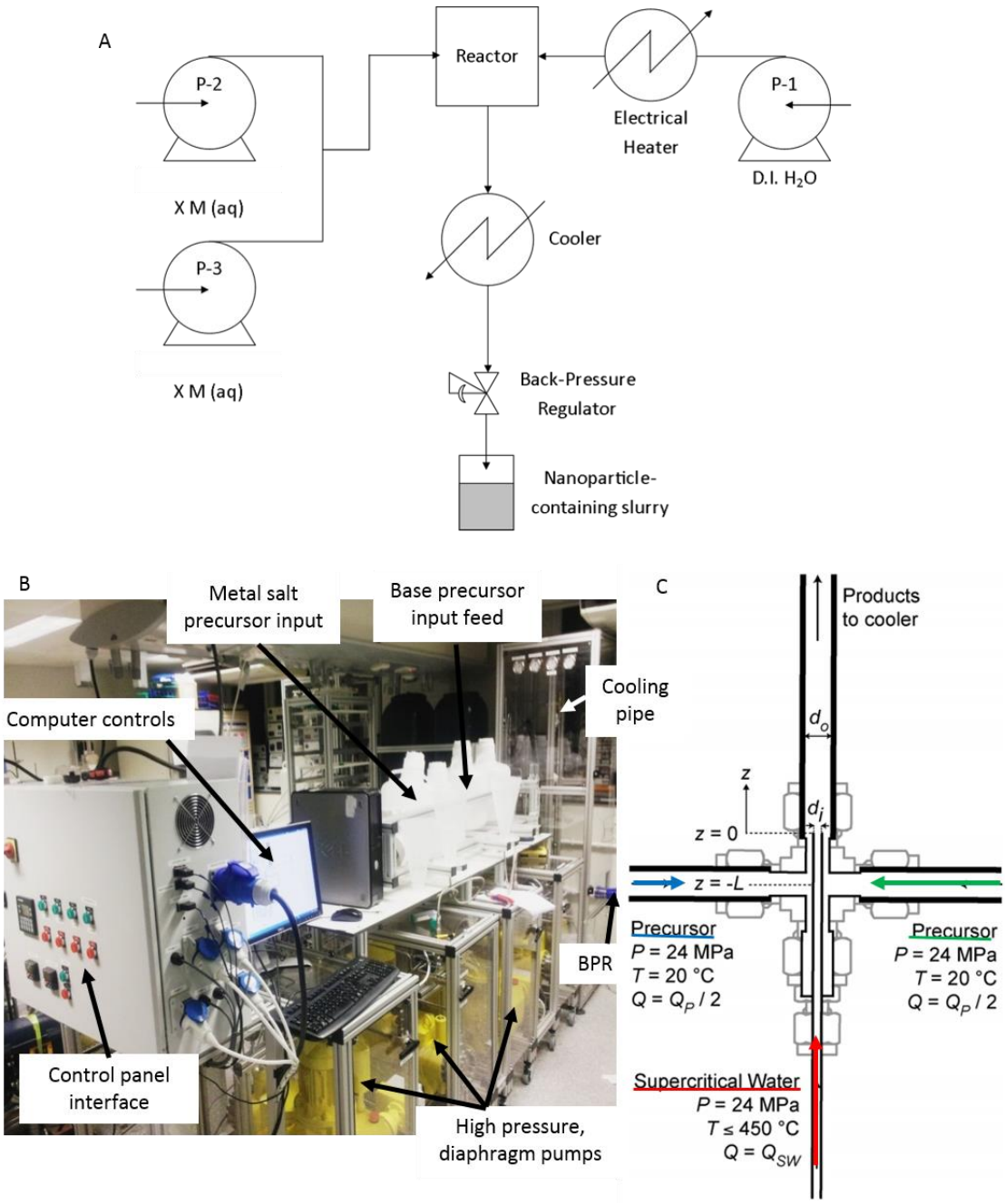

Figure 3.2: *(A) A diagrammatic representation of the CHFS reactor; P-1, P-2 and P-3 are pumps supplying deionised water (D.I. H_2O), aluminium nitrate nonahydrate [$Al(NO_3)_3 \cdot 9H_2O$] and potassium hydroxide (KOH), respectively. Adapted and reproduced from [5]; (B) a photograph of the 3-pump continuous hydrothermal reactor used for direct synthesis of aluminium oxyhydroxide nanoparticles; BPR = back-pressure regulator; and (C) the geometry of the confined jet reactor in CHFS; reprinted from ref [3], copyright © 2014, American Chemical Society.*

3.3 Characterisation

3.3.1 Powder X-Ray Diffraction

Powder X-ray diffraction (PXRD) patterns were collected using a Rigaku MiniFlex 600 diffractometer supplied with Cu-Kα radiation (λ = 1.5418 Å). Each sample was loaded onto an aluminium plate and scans were undertaken at a rate of 2.5° min^{-1} over a 2θ range of 3-70°. The X'Pert Data Viewer software package was used to visualise the data.

3.3.2 Scanning Electron Microscopy

Samples were prepared for scanning electron microscopy (SEM) by placing a small amount of each sample onto double-sided carbon tape fixed to an aluminium support, and then sputter coating with gold. A FEI Quanta 200 FEG ESEM was used for generating SEM images, which were collected by Mr David McCarthy or Mrs Kate Keen. Measurements of particle size and morphology were carried out using the freely available ImageJ software (http://imagej.nih.gov/ij/), on 300 individual particles.

3.3.3 Fourier Transform Infra-Red Spectroscopy

Fourier Transform Infra-Red (FTIR) spectroscopy was performed on a Perkin-Elmer Spectrum 100 instrument fitted with an attenuated total reflectance (ATR) accessory over the wavenumber range of 4000 to 650 cm^{-1}, with the resolution for each measurement being 1 cm^{-1}.

3.3.4 Solid State NMR Spectroscopy

^{27}Al-magic angle spinning (MAS) NMR was performed by Dr Abil Aliev (Department of Chemistry, UCL) using a Bruker Avance I spectrometer fitted with 4 mm double resonance MAS probes, where the X-channel is tuneable in the frequency range ^{15}N to ^{31}P and the decoupling channel is tuned to ^{1}H. The frequency used for ^{27}Al-MAS measurements was 78 MHz.

3.3.5 X-ray Photoelectron Spectroscopy

X-ray photoelectron spectroscopy was performed for the amorphous alum samples using a K-Alpha^{TM+} XPS System (ThermoFisher Scientific) supplied with a micro-focussed, monochromated Al K-α source. XPS spectra were obtained at the National EPSRC XPS Users' Service (NEXUS) at Newcastle University, an EPSRC Mid-Range Facility.

3.3.6 Zeta Potential Measurements

Zeta potential measurements were performed using a Nanozetasizer ZS (Malvern Instruments); 10 mg of each sample was dispersed in 1 mL of either phosphate-buffered saline (PBS) or ultrapure water with resistance of at least 18.2 mΩ (UP-water). The resultant suspension was transferred to a folded zeta-capable capillary cell (DTS 1070, Malvern Instruments) for measurements. Twelve measurements were recorded for each sample, with each suspension made up twice, and 6 measurements recorded on each. The data are reported as the mean ± the standard deviation.

3.3.7 *In vitro* and Immunoassay Experiments

Murine RAW264.7 cells (ATCC) were cultured in Dulbecco's Modified Eagle Medium (DMEM, Life Technologies) supplemented with 10% *v*/*v* foetal bovine serum (FBS, Life Technologies), 2 mM L-glutamine, 100 U mL^{-1} penicillin and 100 µg mL^{-1} streptomycin (Life Technologies) to produce complete-DMEM. Cells were maintained in culture flasks at 37 °C in a humidified atmosphere of 5% CO_2.

The maximum viable passage number is 18, because there are changes in transfection efficiency past 25 passages [6], and cells were passaged every 2 – 3 days. The cell concentration at the start of a new passage was 5x10^5 cells mL^{-1}.

3.3.7.1 Alamar Blue Assay

All assays were performed with RAW264.7 cells below passage number 15. Cytotoxicity assays were performed using the Alamar Blue® protocol, with cells cultured in 96 well flat-bottomed plates. 200 µL of a cell suspension at $5x10^5$ cells mL^{-1} was added to each well in the presence of 10 µL of lipopolysaccharide (LPS) solution or 10 µL of an adjuvant suspension (10 mg mL^{-1}) and incubated for 24 hours. The final concentrations were 100 ng mL^{-1} of LPS and 476 µg mL^{-1} of inorganic adjuvant. Commercially-used alum adjuvants (Alhydrogel and Adju-Phos, Brenntag Biotech) were used as controls at 10 mg mL^{-1} initial concentrations, giving rise to final concentrations of 476 µg mL^{-1} of each. Following a 24-hour exposure period, 40 µL of Alamar Blue® solution (5 mM sodium rezaurin in complete DMEM) was added to each well and the plates were further incubated at 37 °C. At various time points thereafter, measurements of optical densities at an excitation of 555 nm and emission of 585 nm were undertaken using a microplate reader (SpectraMax M2e, Molecular Devices). Independent experiments were performed in triplicate, with three plates per experiment and three tests per plate, giving rise to 27 replicates.

3.3.7.2 Enzyme-Linked Immuno-Sorbent Assay

RAW264.7 cells were stimulated with LPS, commercially available alums and synthesised AlO(OH) adjuvant samples, using the same protocol as in **Section 3.3.7.1**. Culture supernatants were collected after 24 hours following centrifugation of the 96-well plates; aspiration of 150 µL of the cell-free supernatant from each well was achieved through the use of a multi-channel pipette. These were transferred to a new plate and were stored at -20 °C until assayed for cytokines. Three independent experiments were performed, with three replicates in each.

Levels of tumour necrosis factor-alpha (TNF-α) and interleukin-6 (IL-6) in the cell-free supernatant were quantitatively determined using enzyme-linked immunosorbent assay (ELISA) kits according to the protocol suggested by the manufacturer (Insight Biotechnology). Colour development was monitored using a SpectraMax M2e microplate reader. End-point measurements of maximum optical density were obtained at 5-minute intervals for a period of 30 minutes with the plate reader set to 405 nm with wavelength correction set to 650 nm.

3.3.7.3 Fluorescence and Confocal Microscopy

All assays were performed with RAW264.7 cells below passage number 15.

Prior to assaying, the adjuvant samples were labelled with fluorescein isothiocyanate (FITC; Sigma Aldrich UK) by continuously mixing the material in a 5mM solution of FITC (5 mL) for at least 24 hours. Successive rounds of centrifugation and washing with PBS were undertaken until the supernatant of the sample was clear and colourless, in order to remove any unbound FITC from the adjuvant suspension.

A 24-well plate was used and 13 mm-diameter circular glass cover slips were added to each well. 50 µL of well-dispersed RAW264.7 cell suspension ($5x10^5$ cells mL^{-1}) was dropped onto the glass cover slip. FITC-labelled commercially-used alum adjuvants (Brenntag Biotech) were used as controls, alongside FITC-labelled adjuvant samples prepared in this work (10 mg mL^{-1} in PBS). A 10 µL volume of the labelled sample was dropped on top of the cell suspension, which was then incubated for 24 hours in a humidified atmosphere of 5% CO_2 at 37 °C.

After 24 hours, 10 µL of 0.1 µg mL^{-1} solution of 4', 6-diamidino-2-phenylindole (DAPI) stain (Sigma Aldrich, UK) was dropped onto the cell/sample droplet, which was then returned to the incubator for 30 minutes prior to capturing images using a fluorescent microscope (EVOS FL Cell Imaging System, Life Technologies Ltd) to determine the location of adjuvant sample in relation to the RAW264.7 cells. An x20 objective lens was used in this study. The FITC was excited at 470 nm and the emission fluorescence monitored at wavelengths of *ca.* 510 nm. The DAPI was excited at 360 nm and the emission fluorescence collected at *ca.* 450 nm. Overlays were obtained by stacking the two fluorophore images to determine any co-localisation.

Samples were prepared for analysis using a confocal microscope *via* application of 50 µL of a 4% v/v aqueous solution of formaldehyde (fixing agent) to the cell/adjuvant droplets, prepared as detailed above, at 4 °C. The plates were gently agitated for at least 30 minutes and the fixing solution was removed. The cells were then washed and 50 µL of complete-DMEM added. The cover slips were retrieved from the 24-well plate and mounted on a glass slide.

A Zeiss LSM 710 confocal microscope was used for these studies. It is equipped with a 30 mW 405 nm diode laser which is used for visualisation of the DAPI stain, a 25 mW argon ion laser (lines produced at 458, 488 [for the green FITC stain] and 514 nm), as well as a 25 mW 595 nm diode laser and a 5 mW 633 nm HeNe laser which are for red fluorophores. However, in this setting no red dyes were used, thus these lasers were used to determine any sample degradation.

3.4 Results and Discussion

3.4.1 Continuous Plastic Flow Synthesis – Sulphate System

3.4.1.1 Synthesis

Aluminium sulphate and sodium aluminate precursors were dissolved into deionised water to 0.1 and 0.6 M concentrations, respectively. The residence time was set to 10 minutes and reactions performed at 45, 65, 80 or 90 °C; see **Table 3.1**. Approximately one gram of product was obtained after 10 minutes of collection.

Table 3.1: ***Synthesis details for preparation of AlO(OH) particles via a continuous hydrothermal flow process, using aluminium sulphate as the aluminium source.***

Sample ID	$[Al_2(SO_4)_3 \cdot H_2O]$ / M	$[NaAlO_2]$ / M	Flow rate / mL min^{-1}	Reaction temperature / °C	Product pH
CPFS-Sulphate-45	0.1	0.6	20	45	6
CPFS-Sulphate-65	0.1	0.6	20	65	6
CPFS-Sulphate-80	0.1	0.6	20	80	14
CPFS-Sulphate-90	0.1	0.6	20	90	14

3.4.1.2 Characterisation

Powder XRD patterns of the products obtained are shown in **Figure 3.3**. The CPFS-Sulphate-45 and CPFS-Sulphate-65 samples were found to be completely amorphous, with no Bragg reflections visible in their P-XRD patterns. In contrast, all detectable reflections for the 80 and 90 °C products can be assigned by their positions to standard Bragg reflections of the boehmite polymorph of AlO(OH) [γ-AlO(OH)] [7]. No impurities were detected. The reflections observed are very broad, indicative of small crystallite sizes.

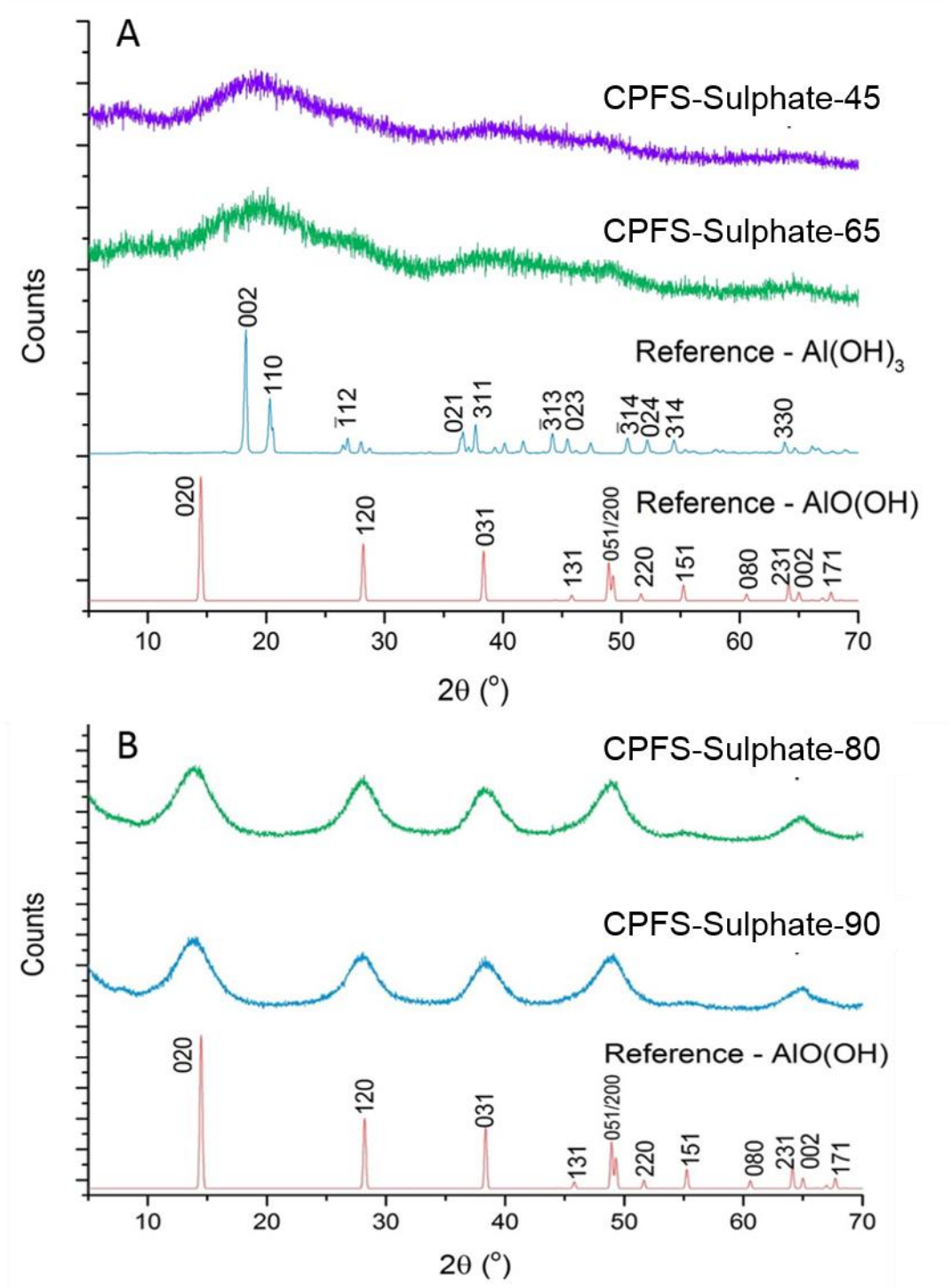

Figure 3.3: ***P-XRD patterns of AlO(OH) samples synthesised via the CPFS process. The reference pattern for γ-AlO(OH) is obtained from the ICSD (93734 [7]) as is that for the gibbsite polymorph of Al(OH)$_3$ (6162 [8]). The experimental patterns in (A) are of CPFS-Sulphate-45 and -65, whilst the crystalline materials in (B) are CPFS-Sulphate-80 and -90.***

In order to gain more information on the materials prepared, particularly the amorphous low-temperature systems, solid state NMR and XPS analyses were undertaken.

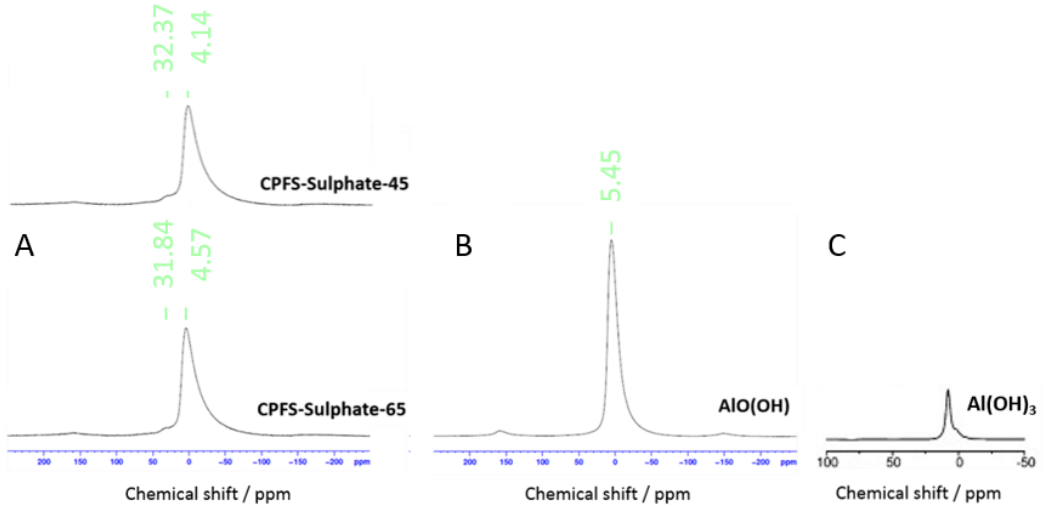

***Figure 3.4:* Solid state NMR spectra recorded to deduce the composition of the amorphous products from sub-60 °C synthesis, via comparison to a known γ-AlO(OH) standard. (A) the spectra obtained after CPFS synthesis at 45 and 65 °C; (B) the spectrum from γ-AlO(OH) synthesised at 90 °C and (C) a literature spectrum for the gibbsite polymorph of $Al(OH)_3$ [9].**

^{27}Al-MAS solid-state nuclear magnetic resonance (SS-NMR) spectra show that the CPFS-synthesised pure-phase AlO(OH) has a single peak arising at 5.45 ppm, whereas the CFPS-Sulphate-45 and CPFS-Sulphate-65 samples have two peaks (**Figure 3.4**). The main peak is observed at *ca.* 4.26 ppm indicative of octahedrally co-ordinated aluminium [10], with a second, smaller peak detected at *ca.* 33 ppm. These peak positions match closely with the literature data for γ-$Al(OH)_3$ at 7.5 and 36.5 ppm [11]. These findings indicate that below 70 °C the CPFS process is yielding amorphous gibbsite. The results of XPS analysis – **Table 3.2** – also tend to imply that these products comprise aluminium hydroxide [$Al(OH)_3$] [9, 12], although the O:Al ratio is less than 3:1 suggesting that some AlO(OH) or other Al-containing species may also be present.

The phase-pure CPFS-Sulfate-90 material has Al2*p* and O1*s* peaks at 74 and 532 eV, consistent with octahedral Al^{3+} and the presence of OH groups, respectively [10]. The amorphous samples analysed show an Al2*p* peak with a binding energy of 75 eV, which is consistent with the literature values for octahedrally co-ordinated aluminium [10].

Furthermore, CPFS-Sulphate-45 and CPFS-Sulphate-65 have O1*s* peaks at binding energies *ca.* 533 eV; this is indicative of amorphous content with OH groups present [10]. Overall therefore, while it is not possible to unambiguously determine the nature of the materials formed at 45 and 65 °C, it is clear that they do not comprise the desired AlO(OH) product, and the data suggest they are likely to be $Al(OH)_3$ phases.

***Table 3.2:* XPS analysis of the materials synthesised at 45, 65, and 90 °C, compared with expected data from reference [12], with atomic percentages listed for both aluminium and oxygen.**

Sample ID	Al 2p / %	O 1s / %	Ratio / O : Al	Expected ratio / O : Al [12]	Structure formed
CPFS-Sulphate-45	27.77	72.23	2.60	3	$Al(OH)_3$
CPFS-Sulphate-65	28.70	71.30	2.48	3	$Al(OH)_3$
CPFS-Sulphate-90	34.11	65.90	1.93	2	AlO(OH)

Increasing the temperature of the silicon oil bath thus appears to have caused a phase transition from $Al(OH)_3$ to AlO(OH), as well as an increase in the crystallinity of the product.

The particle size and morphology were analysed using SEM (**Figure 3.5**).

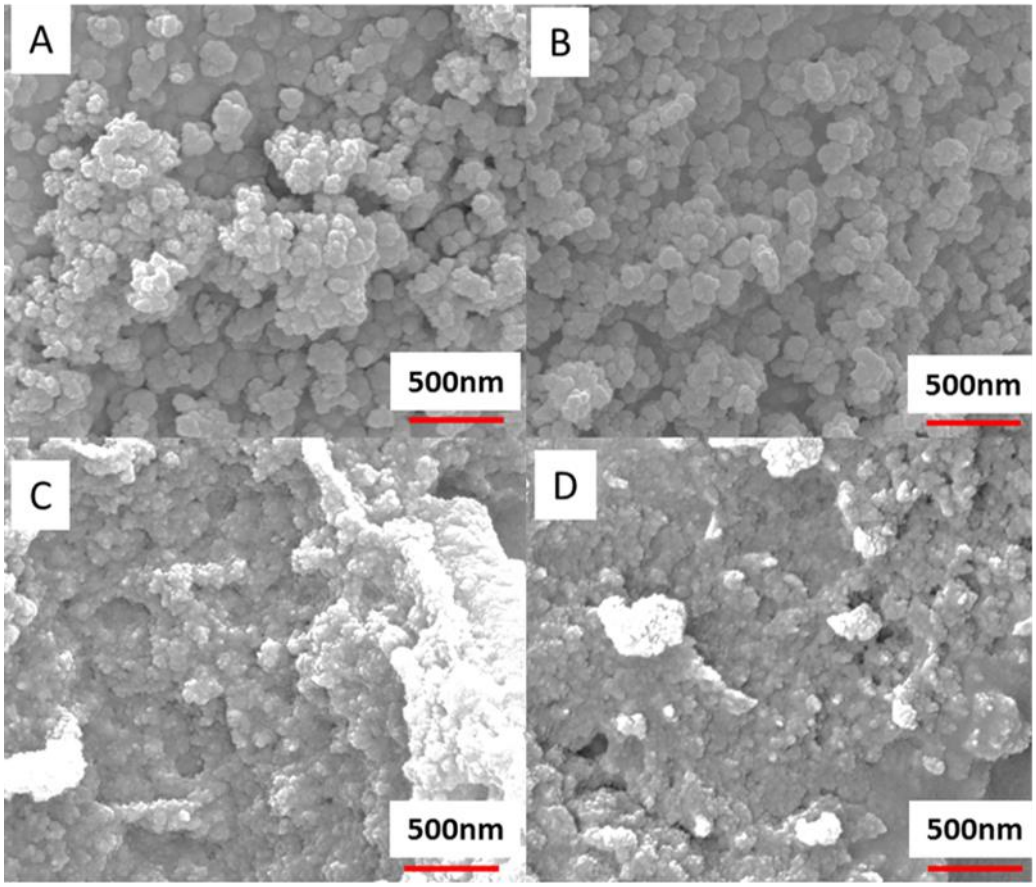

***Figure 3.5:* SEM images of the CPFS-Sulphate products synthesised at (A) 45, (B) 65, (C) 80 and (D) 90 °C.**

SEM images shows the product materials are composed of aggregates of nanoparticles exhibiting spherical morphology (**Figure 3.5A-D**). As a result, the Scherrer equation can be used to analyse the P-XRD patterns (with K = 1) and calculate average crystallite sizes – see **Table 3.3**.

Table 3.3: ***Details of mean crystallite and particle size and morphology of samples synthesised*** **via** ***the CPFS process using aluminium sulphate as the precursor. Mean crystallite size data was calculated using all visible reflections of the P-XRD pattern, mean ± standard deviation.***

Sample ID	Mean crystallite size by P-XRD / nm	Mean particle size by SEM / nm	Morphology
CPFS-Sulphate-45	Amorphous	75 ± 2	Spherical
CPFS-Sulphate-65	Amorphous	69 ± 13	Spherical
CPFS-Sulphate-80	5.1 ± 3.6	38 ± 9	Spherical
CPFS-Sulphate-90	6.7 ± 6.0	42 ± 11	Spherical

The Scherrer analysis of the X-ray diffraction data (**Table 3.3**) indicates a difference in crystallite size of roughly 1.6 nm between the 80 and 90 °C samples. Due to the amorphous nature of the 45 and 65 °C samples, crystallite size could not be determined by P-XRD. However, mean particle size data were additionally calculated from the SEM images by analysing 300 individual particles; the resultant data are also presented in **Table 3.3**. These reactions display a trend that increasing the reaction temperature not only results in a switch from producing gibbsite to boehmite, but also results in the collection of generally smaller particles. The latter is not documented in the literature [13, 14]. Considering the two pairs of samples (gibbsite and boehmite) separately, a higher temperature seems to give rise to slightly smaller particles, although they are the same within the standard deviations.

The values calculated from the Scherrer equation and SEM analysis both show the same trend. However, the Scherrer values are lower than the SEM values because the former are crystallite sizes for individual crystals within the powdered samples, whilst the SEM-derived particle sizes are calculated on the bulk – potentially aggregated – material.

FTIR spectra (**Figure 3.6**) of the phase-pure AlO(OH) materials depict a strong band at *ca*. 3250 cm^{-1} and a shoulder at *ca.* 3100 cm^{-1} which can be attributed to H-bonded v_s(Al)O-H and v_{as}(Al)O-H stretching vibrations of the hydroxyl moieties in the AlO(OH) nanoparticles, respectively [15, 16]. The band at 1050 cm^{-1} and the shoulder at 1125 cm^{-1} are assigned to the symmetric and asymmetric bending modes of (Al)-OH [17] whilst the band at 750 cm^{-1} is ascribed to the OH torsional mode [18]. The three peaks present in the range 1250 -1750 cm^{-1} are attributed to the Al-OH stretching and bending vibrations in the AlO(OH) lattice [19]. All the bands described are consistent with AlO(OH).

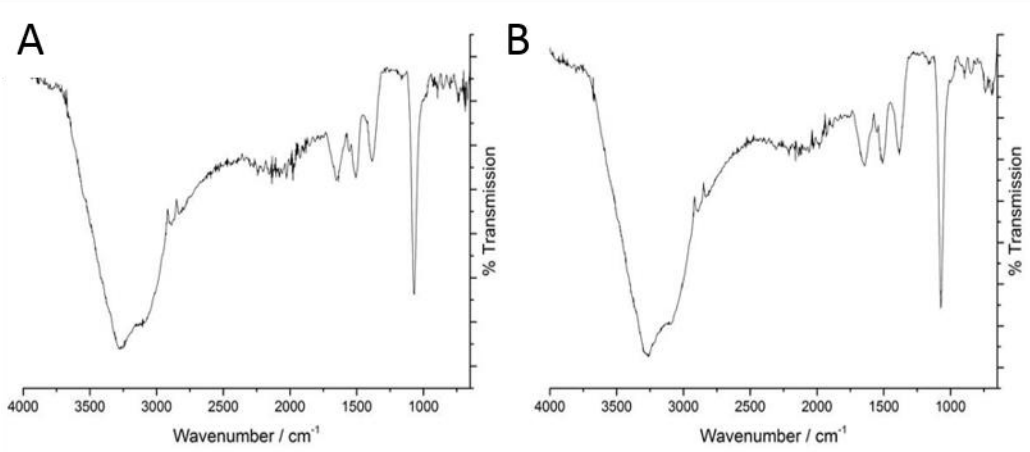

***Figure 3.6:* FTIR spectra of CPFS-Sulphate products synthesised at (A) 80 and (B) 90 °C.**

3.4.2 PEGylated Systems

Since the use of sub-100 °C temperatures to produce different crystal habits of boehmite was unsuccessful, producing spherical particles at all temperatures when the precursors were solely dissolved in deionised water, polyethylene glycol (PEG) solutions were explored as an alternative to deionised water. This enables the maximum temperature of the oil bath to exceed the 95 °C maximum temperature of deionised water; experiments can be performed up to 180 °C.

A PEGylated system was tested with aluminium sulphate as the aluminium source. Initially there were difficulties with poor precursor solubility in pure ethylene glycol. After resolving these issues by diluting in water, one synthesis was performed at 100 °C but the precursor solutions solidified in the PTFE tubing and caused a blockage. Therefore, the reactions were stopped because further testing with this solvent system would cause damage to the reactor. As a result, it was concluded that the use of PEG was not practicable here, and instead experiments moved on to explore other Al precursor salts.

3.4.3 Continuous Plastic Flow Synthesis – Chloride System

Experimental optimisation was undertaken using different ratios of Al-source to precipitating agent (NaOH). The precipitating agent was changed from $NaAlO_2$ to NaOH for these experiments because the additional aluminium content of $NaAlO_2$ was not required to facilitate the formation and precipitation of AlO(OH).

Experiments performed using a 1:4 Al-source to base ratio did not yield any solid product, which we believe is because any solid formed would have dissolved in the highly basic environment formed as a result of the reaction. Reducing the ratio to 1:3 saw the generation of amorphous products (**Figure 3.7**). The experimental parameters for the products obtained with aluminium chloride as the precursor are detailed in **Table 3.4**.

Table 3.4: ***Synthetic details for attempted preparation of AlO(OH) particles via a continuous hydrothermal flow process, using aluminium chloride as the aluminium source.***

Sample ID	[$AlCl_3 \cdot 6H_2O$] / M	[NaOH] / M	Flow rate / mL min^{-1}	Reaction temperature / °C	Product pH
CPFS-Chloride-70	0.2	0.6	20	70	5
CPFS-Chloride-80	0.2	0.6	20	80	5
CPFS-Chloride-90	0.2	0.6	20	90	5

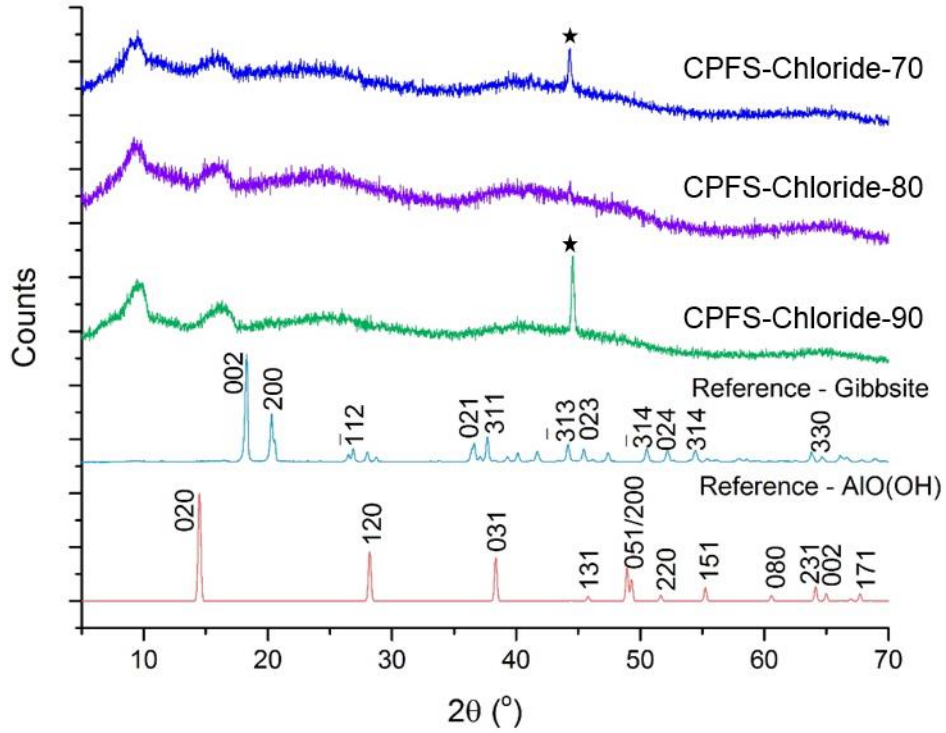

***Figure 3.7:* P-XRD patterns of samples synthesised via the CPFS process using aluminium chloride as the precursor; the reference pattern for γ-AlO(OH) is obtained from the ICSD (93734 [7]) as was that of γ-$Al(OH)_3$ (6162 [8]). The peaks marked with an asterisk (*) denote those attributed to the sample holder.**

As shown in **Figure 3.7**, amorphous P-XRD patterns were obtained for the three products, and therefore their identity cannot be confirmed by P-XRD alone. Solid state NMR and XPS analysis were undertaken in a bid to deduce the content and possible structures of these samples.

The O: Al ratios are indicative of the sample type, with data presented in **Table 3.5** [12]. The CPFS-Chloride samples analysed contain octahedrally co-ordinated aluminium within their structures, with Al2*p* peaks having a binding energy of *ca*. 75 eV, which is consistent with the literature values [10]. The O1*s* peaks are found at binding energies *ca*. 532 eV, meaning there are hydroxyl groups contained within the samples [10].

***Table 3.5:** XPS analysis of materials synthesised using aluminium chloride as the Al source. CPFS-Sulphate-90 is used as the aluminium oxyhydroxide reference standard, with expected ratios from the literature from [12], with atomic percentages listed for both aluminium and oxygen.*

Sample ID	Al 2p / %	O 1s / %	Ratio / O : Al	Expected ratio / O : Al [12]	Sample Type
CPFS-Chloride-70	32.76	67.25	2.05	2.00	AlO(OH)
CPFS-Chloride-80	32.65	67.35	2.06	2.00	AlO(OH)
CPFS-Chloride-90	33.33	66.67	2.00	2.00	AlO(OH)
CPFS-Sulphate-90	34.11	65.90	1.93	2.00	AlO(OH)

^{27}Al-MAS NMR spectra show pure-phase AlO(OH) of the boehmite polymorph (as described in **Section 3.4.1.2**) has a single peak arising at 5.45 ppm, whereas the chloride CPFS samples have two peaks (**Figure 3.8**). The main peak is observed *ca.* 4.3 ppm, with a second, smaller peak detected at *ca.* 32 ppm. The former peak provides evidence of octahedrally co-ordinated aluminium within the samples; however, given the XPS data indicate these materials are AlO(OH), the latter peak is anomalous and may arise due to an impurity or due to the presence of unsaturated aluminium at the surface of the NPs [20-23]. Coupling these data together suggests that these are all amorphous AlO(OH) products.

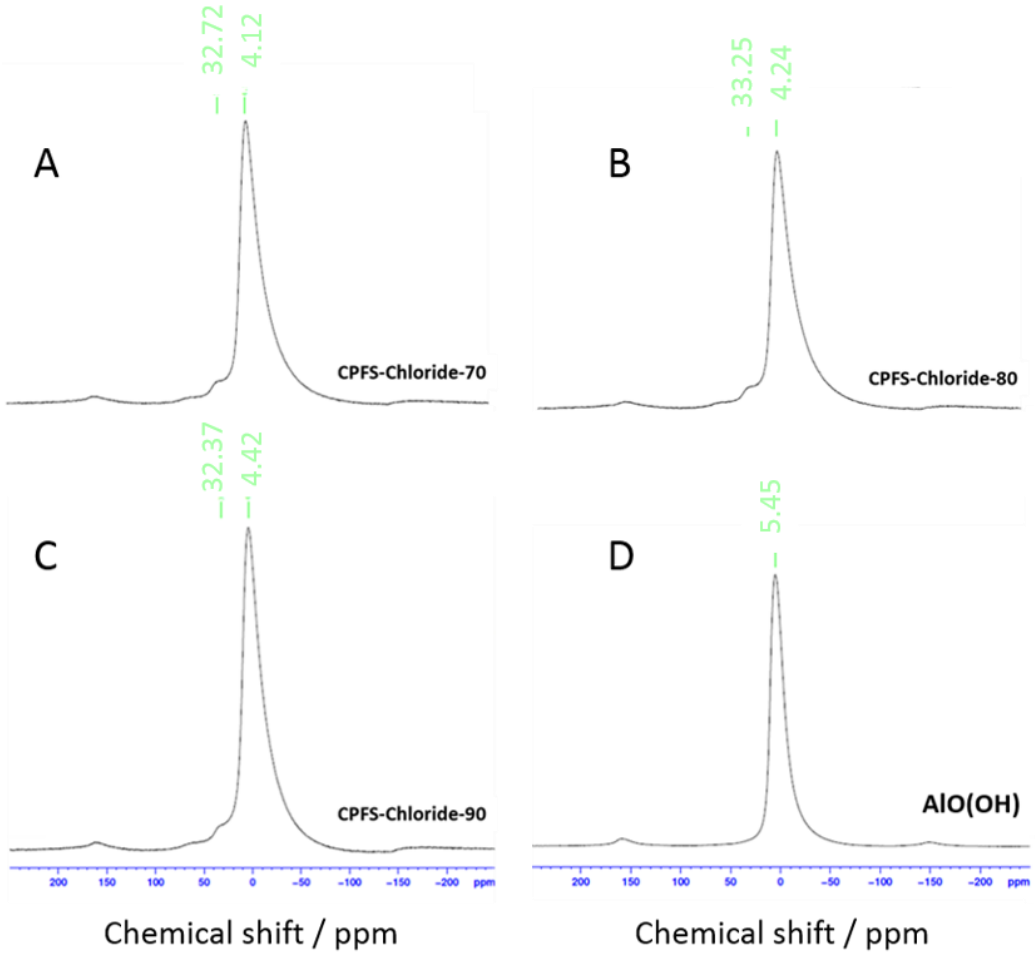

Figure 3.8: ***Solid state NMR data on the samples prepared from chloride precursors (A – C),*** **via** ***comparison to a known γ-AlO(OH) standard (D) synthesised at 90 °C using aluminium sulphate as the Al-source.***

The SEM images presented in **Figure 3.9** show aggregated particles in the samples. All three materials appear to have spherical morphology, with average particle size decreasing as the temperature of the reaction increased (**Table 3.6**). Therefore, there is evidence of some degree of particle engineering for the chloride system.

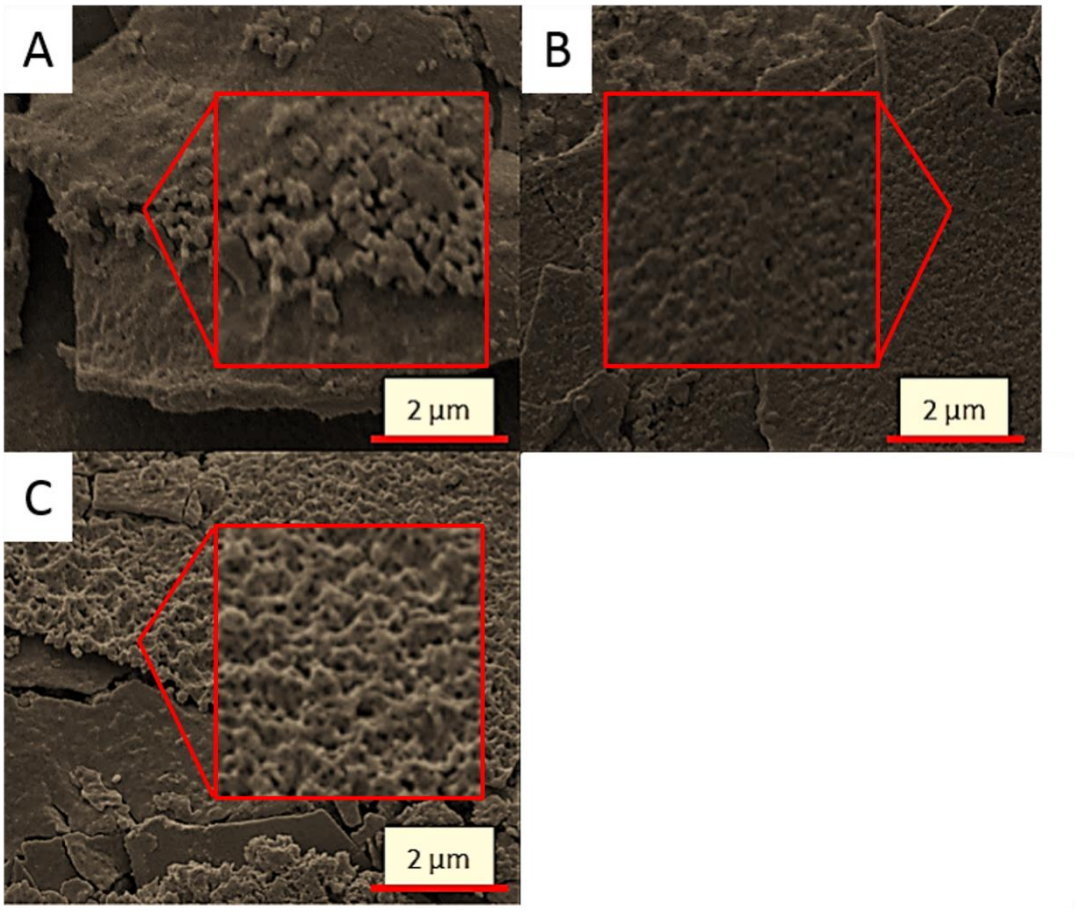

Figure 3.9: *SEM images of the CPFS-Chloride products synthesised at (A) 70, (B) 80 and (C) 90 °C. The larger shapes – evident in the background of the images – are those of the carbon stubs used in the mounting process.*

Table 3.6: *Details of mean particle size and morphology for the samples synthesised* **via** *the CPFS process using aluminium chloride as the precursor. The size and morphology were deduced using SEM analysis (Figure 3.9), mean ± standard deviation.*

Sample ID	Mean particle size *via* SEM / nm	Morphology
CPFS-Chloride-70	197.8 ± 49.7	Spherical, aggregate
CPFS-Chloride-80	91.0 ± 34.1	Spherical, aggregate
CPFS-Chloride-90	87.8 ± 20.4	Spherical, aggregate

3.4.4 Continuous Plastic Flow Synthesis – Nitrate System

A series of reactions were performed using Al nitrate as the Al-containing precursor (**Table 3.7**). Sodium aluminate was replaced with an alternative precipitating agent because the extra aluminium content was not required for AlO(OH) synthesis with aluminium nitrate as the Al-source. Poorly-crystalline gibbsite was obtained when the reactions were performed at 80 °C using aluminium nitrate and potassium hydroxide as the precursors (**Figure 3.10**), with some amorphous material also apparently present. However, increasing the temperature to 90 °C was sufficient to initiate a phase transition to produce the desired γ-AlO(OH). Broad peaks in the P-XRD pattern of CPFS-Nitrate-90 are indicative of the sample's small crystallite size (**Figure 3.10**).

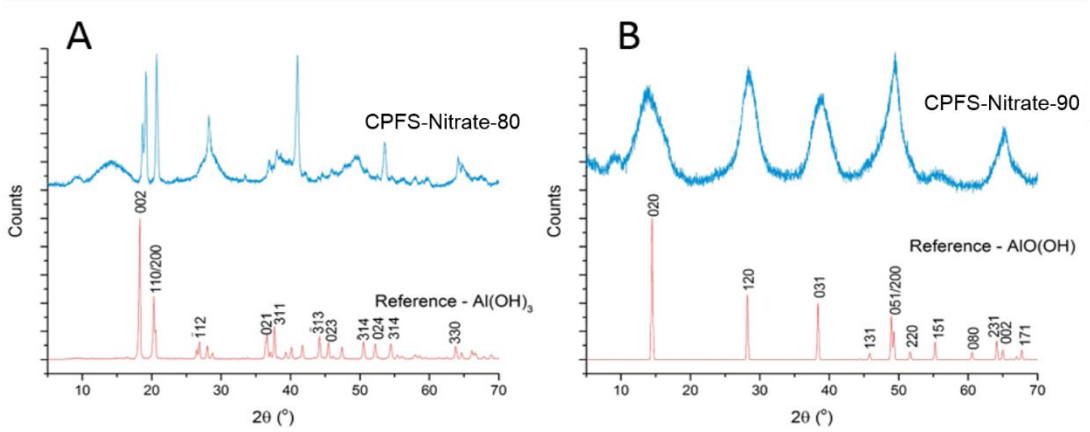

***Figure 3.10:* P-XRD patterns of samples synthesised via the CPFS process using aluminium nitrate as the precursor at (A) 80 and (B) 90 °C. The reference patterns for γ-AlO(OH) and γ-Al(OH)$_3$ were obtained from the ICSD - 93734 [7] and 6162 [8], respectively.**

The reaction conditions are detailed in **Table 3.7,** with a summary of the characterisation data listed in **Table 3.8**.

Table 3.7: ***Synthesis details for materials prepared via a continuous hydrothermal flow process, using aluminium nitrate as the aluminium source.***

Sample ID	$[Al(NO_3)_3 \cdot 9H_2O]$ / M	[KOH] / M	Flow rate / mL min^{-1}	Reaction temperature / °C	Supernatant pH
CPFS-Nitrate-80	0.2	0.8	20	80	11
CPFS-Nitrate-82	0.2	0.8	20	82	5
CPFS-Nitrate-84	0.2	0.8	20	84	11
CPFS-Nitrate-86	0.2	0.8	20	86	11
CPFS-Nitrate-88	0.2	0.8	20	88	12
CPFS-Nitrate-90	0.2	0.8	20	90	11

The initial two temperatures tested led to the formation of two phases, with 80 °C producing the gibbsite material and 90 °C giving rise to boehmite; see data in **Table 3.8**. Further investigations into the nitrate system were hence undertaken (**Table 3.7**), with temperature increments of 2 °C tested to deduce the point at which phase transition from gibbsite to boehmite occurs. The patterns in **Figure 3.11** provide evidence that this event happens when the reaction is performed at 86 °C, with the 84 °C product appearing to be a mixture of the two materials (see **Figure 3.11A**). No clear trend in particle or crystallite size can be elucidated across this temperature range, as is clear from the data in **Table 3.8**.

Table 3.8: ***Details of mean crystallite and particle size, morphology and product nature for samples synthesised via the CPFS process using aluminium nitrate as the precursor, mean ± standard deviation.***

Sample ID	Mean crystallite size by P-XRD / nm	Mean particle size *via* SEM / nm	Morphology	Product
CPFS-Nitrate-80	16.1 ± 10.12	147.0 ± 0.5	Rods	$Al(OH)_3$
CPFS-Nitrate-82	19.3 ± 18.55	87.1 ± 25.5	Spherical	$Al(OH)_3$
CPFS-Nitrate-84	19.9 ± 15.68	70.6 ± 21.5	Platelets	$Al(OH)_3$/AlO(OH)
CPFS-Nitrate-86	17.8 ± 23.2	82.0 ± 32.6	Spherical	AlO(OH)
CPFS-Nitrate-88	25.0 ± 24.4	82.8 ± 20.9	Rods	AlO(OH)
CPFS-Nitrate-90	3.9 ± 1.5	115.0 ± 25.5	Various	AlO(OH)

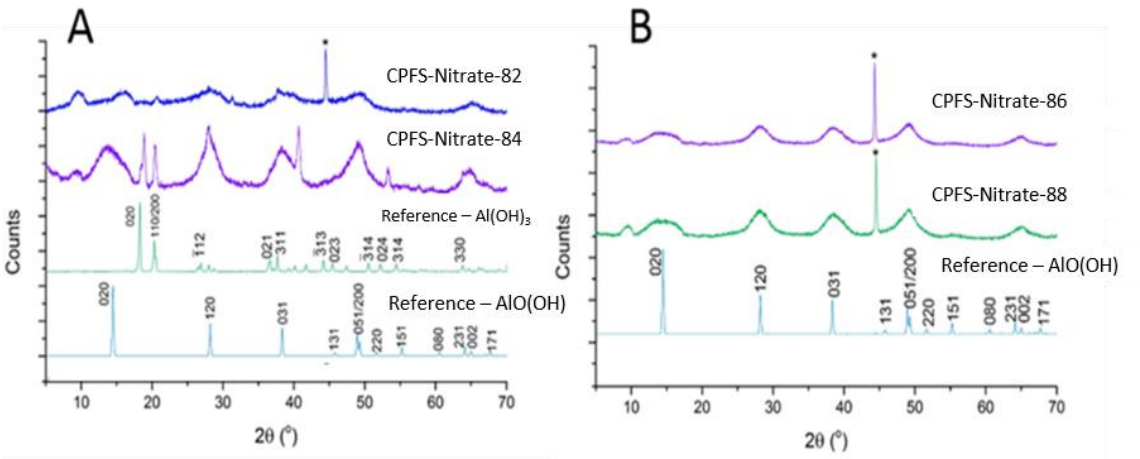

Figure 3.11: ***P-XRD patterns of alum samples synthesised via the CPFS process using aluminium nitrate as the precursor, with varying reaction temperatures, 82 and 84 °C (A) and 86 and 88 °C (B). The reference pattern for γ-AlO(OH) is obtained from the ICSD (93734 [7]) as was that of the gibbsite polymorph of Al(OH)₃ (6162 [8]). The peaks marked with an asterisk (*) denote those attributed to the plate holder.***

SEM images (**Figure 3.12**) provide visual evidence of the differences in particle morphology across the six materials. The magnified squares in **Figure 3.12** show enlargements of selected regions.

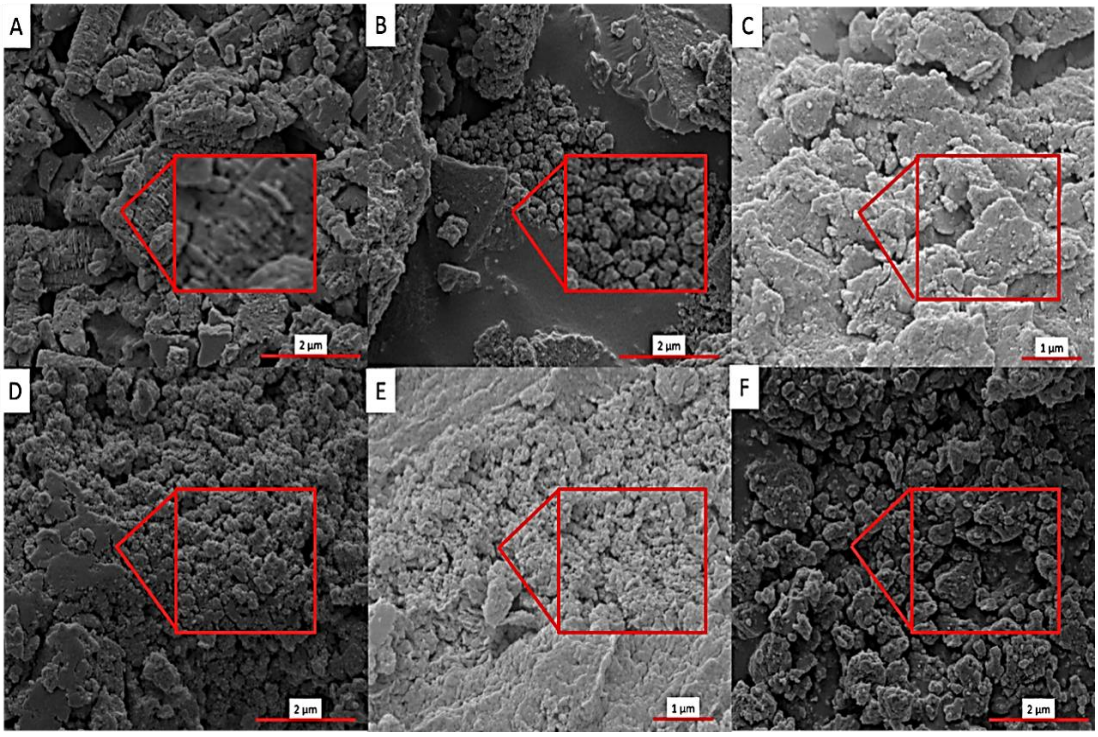

Figure 3.12: ***SEM images for CPFS-Nitrate samples prepared at (A) 80, (B) 82, (C) 84, (D) 86, (E) 88 and (F) 90 °C.***

As is evident from **Figure 3.12**, the particle size and shape were not consistent across the six samples prepared using Al nitrate, with different morphologies being obtained at different temperatures. These results thus suggest that particle habit and the Al hydroxide obtained can be engineered using this synthetic route.

3.4.5 CPFS Discussion

The effects of concentration and temperature on the morphology and particle size of nanoparticles produced by CPFS were studied. It is evident that concentration ratios of Al-source to precipitating agent are fundamental in generating solid products such that, if the ratio is incorrect, then any precipitate will dissolve in the excessively acidic or basic aqueous environment of the reaction. The three different synthetic routes investigated in this chapter show there is some evidence for control of both particle size and shape of the AlO(OH) products produced. Particle morphology was tuneable when using the nitrate synthetic route, whilst particle size seemed to be controlled when using a chloride Al-source.

The control obtained using the CPFS process appears to be limited, however; therefore, continuous hydrothermal flow reactor processes were investigated to assess whether greater control is achievable.

3.4.6 Continuous Hydrothermal Flow Synthesis

3.4.6.1 Synthesis

The CHFS process used an in-line mixed feed of water-soluble metal salt (aluminium nitrate nonahydrate) and base (potassium hydroxide) which instantly forms a solid precipitate upon mixing with a supercritical water flow (240 bar, 450 °C) [24]. A series of samples were prepared with varied precursor concentrations and flow rates, as detailed in **Table 3.9**.

***Table 3.9:** Experimental conditions for samples prepared using a continuous hydrothermal flow process with aluminium nitrate as the Al source and potassium hydroxide as the base. All reactions were performed at 450 °C with either a balanced or unbalanced flow rate. For instance, 80/80 denotes that each precursor (metal salt and base) were pumped at 80 mL min^{-1} each to give a combined flow rate of 160 mL min^{-1}.*

Sample ID	$[Al(NO_3)_3 \cdot 9H_2O]$ / M	[KOH] / M	Flow rate / mL min^{-1}	Mix-point temperature / °C	Product pH
CHFS-1	0.05	0.2	80/80	274	9
CHFS-2	0.05	0.2	80/50	314	9
CHFS-3	0.10	0.4	80/80	272	9
CHFS-4	0.10	0.4	80/50	314	9

3.4.6.2 Characterisation

Powder XRD patterns are shown in **Figure 3.13**. All observed reflections can be assigned by their positions to those of the reference pattern for the boehmite polymorph of AlO(OH) [7]. No peaks were observed belonging to impurities. Crystallite sizes were calculated using the Scherrer equation, as summarised in **Table 3.10**.

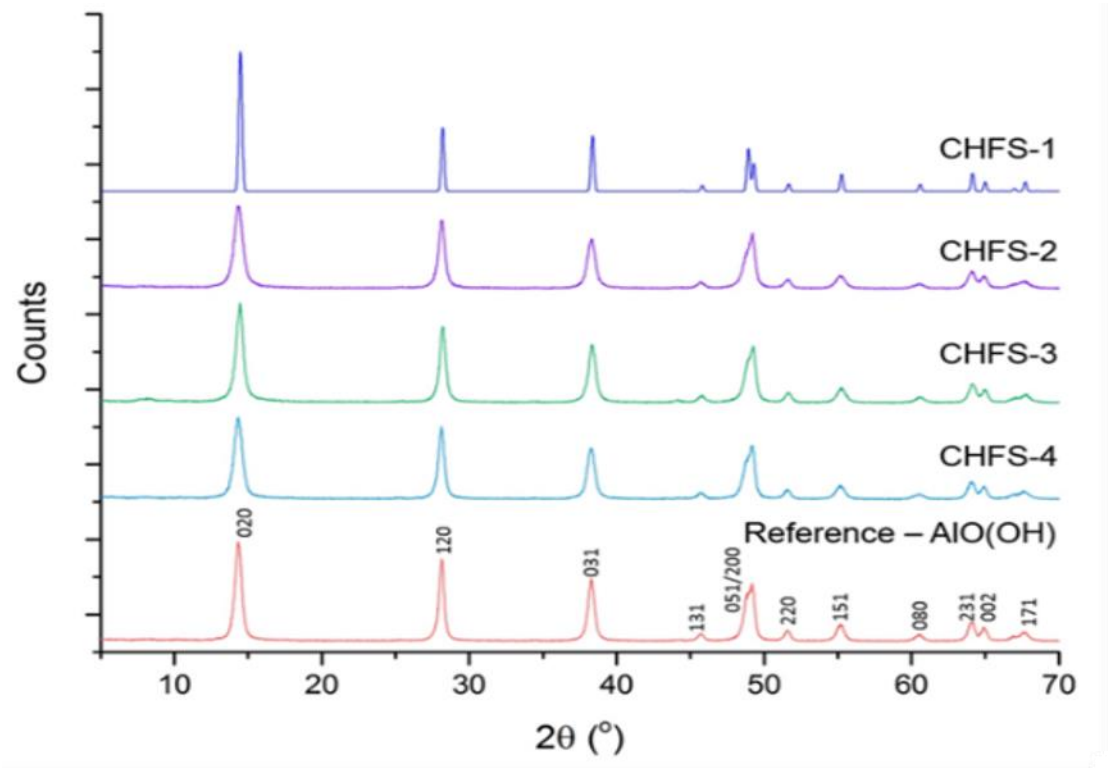

***Figure 3.13:** P-XRD patterns for samples synthesised by the CHFS process, including a reference pattern for the boehmite polymorph of AlO(OH) (ICSD: 93734 [6]).*

The CHFS samples display high crystallinity, as observed in the P-XRD patterns (**Figure 3.13**). They are found to have small crystallite sizes due to the limited time for growth following nucleation at the point of mixing in the confined jet mixer (**Figure 3.2C**). The rapid cooling procedures ensure that crystal growth is inhibited.

Table 3.10: ***Details of mean crystallite and particle size, morphology and product type of the samples synthesised via the CHFS process using aluminium nitrate as the precursor, mean ± standard deviation.***

Sample ID	Mean crystallite size by P-XRD / nm	Mean particle size *via* SEM / nm	Morphology	Product
CHFS-1	31.11 ± 16.20	69.04 ± 12.84	Spherical	AlO(OH)
CHFS-2	22.89 ± 8.20	66.39 ± 14.76	Hexagonal plates, rod-like particles	AlO(OH)
CHFS-3	28.30 ± 10.52	68.45 ± 16.42	Spherical	AlO(OH)
CHFS-4	35.58 ± 14.62	67.41 ± 14.21	Hexagonal plates, rod-like particles	AlO(OH)

SEM analysis (see **Figure 3.14A-D**) shows the reaction products are composed of nanoparticles of spherical morphology for CHFS-1 and -3. These samples were prepared with balanced flow rates of 80 mL min^{-1} for each precursor, giving rise to a mix-point temperature of 274 °C. In contrast, CHFS-2 and -4 were prepared with 80 and 50 mL min^{-1} flow rates for the Al-source and precipitating agent, respectively, creating a 314 °C mix-point temperature as there is a higher flow rate of the pre-heated precursor. A mixture of hexagonal platelets and rod-like particles with average particle size 66 - 67 nm were obtained for CHFS-2 and -4. These are smaller in size than those synthesised with lower mix-point temperatures.

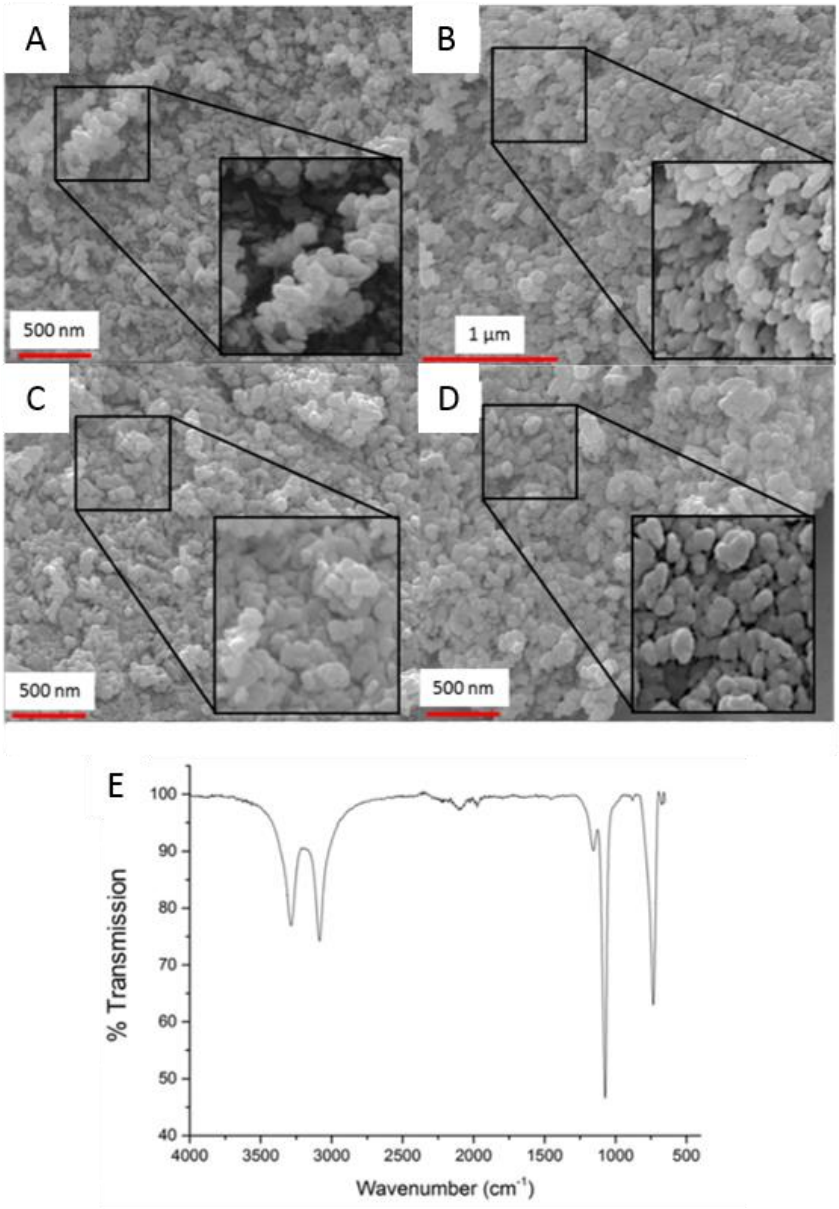

Figure 3.14: ***SEM images of the CHFS products: (A) CHFS-1, (B) CHFS-2, (C) CHFS-3 and (D) CHFS-4; and Fourier transform infra-red spectrum of (E) CHFS-2.***

The FTIR spectrum for the CHFS product (**Figure 3.14E**) is sharper than that obtained for CPFS products; this can be attributed to the better crystallised and more homogeneous nature of the reaction products here. There are two strong bands at 3100 and 3250 cm^{-1} which can be attributed to ν_{as}(Al)O-H and ν_{s}(Al)O-H stretching vibrations of the hydroxyl moieties in the AlO(OH) nanoparticles [15, 16]. The band at 1050 cm^{-1} and the shoulder at 1125 cm^{-1} are assigned to the symmetric and asymmetric bending modes of (Al)-OH respectively [17], whilst the band at 750 cm^{-1} is ascribed to the OH torsional mode [18]. All the bands described are consistent with AlO(OH).

3.4.6.3 CHFS Discussion

In the absence of base, no precipitate was collected; however, introduction of base in a 1:4 molar ratio (Al: KOH) resulted in the production of a white powder product. Pure phase AlO(OH) was obtained. The lack of solid product obtained with no base is in contrast to published work from Sue *et al.* [25], who obtained a biphasic product composed of AlO(OH) and Al_2O_3 with average crystallite sizes of 10.8 nm and 4.4 nm, respectively, when aluminium nitrate nonahydrate was used as the precursor in the absence of potassium hydroxide. It appears that the addition of base drives the reaction to a monophasic product. The only notable difference between the experiments reported here and the literature is the CHFS experimental set-up, because Sue and co-workers implement a quench at the end of the reaction. This could explain why they collected solid product in the absence of base (the quench may hold the pH at a value suitable for precipitation due to rapid cooling of the reaction product). In the reactions undertaken in this chapter, using $Al(NO_3)_3{\cdot}9H_2O$ and deionised water gave a product supernatant with a pH reading of 1 – in the absence of a quench – and so any solid product which may have formed is likely to have dissolved prior to collection due to the acidic environment.

The effects of concentration, temperature and flow rate on the morphology and particle size of aluminium oxyhydroxide were studied, with a summary of the data presented in **Table 3.10**. At low concentrations the impact of an unbalanced flow rate is evident (sample CHFS-2). Here the mix-point temperature increases to 314 °C due to reduced flow of the preheated water, producing highly crystalline AlO(OH). The samples collected were composed of hexagonal platelets and rod-like AlO(OH) particles with average crystallite size 51-60 nm. However, the CHFS-1 sample was synthesised with a balanced flow rate for a mix-point temperature of 274 °C, yielding highly crystalline AlO(OH) particles with spherical morphology and average crystallite size 61-70 nm. A similar trend is observed with higher precursor concentrations (samples CHFS-3 and CHFS-4). Therefore, altering the flow rates provides control over the particle shape through varying the mix-point temperature.

3.4.7 Synthetic Route Comparisons

All samples recovered from the CPFS synthetic routes were white in colour, suggesting there are no impurities. The PTFE tubing used within this reactor can be autoclaved which ensures sterility of the reaction products and potentially could conform to Good Manufacturing Practice (GMP) guidelines. However, the materials collected from the CHFS process had a slight blue discolouration to their appearance, indicating some form of contamination. It is thought that there is likely to be a degree of metal contamination due to the nature of the pipework installed in this reactor. *In vitro* cell viability assays (see **Section 3.5**) provide evidence that there is no cytotoxic effect caused by this contamination, but this is nevertheless a concern which must be addressed in future studies.

3.4.8 Zeta Potential Measurements

Previous studies have indicated that zeta potential (ZP) is important in determining immunogenicity [26]. Zeta potential values for the samples prepared are given in **Table 3.11**. Six CPFS samples do not have values listed in **Table 3.11** because the suspensions rapidly sediment within the zeta-capable cell, which resulted in unreliable and highly variable values being recorded. Longer sonication times were applied in an attempt to keep the samples dispersed in the solvent, but these efforts proved unsuccessful.

The zeta potential will vary with the dispersion medium: in the majority of cases, zeta potential measurements will become more negative when dispersed in phosphate-buffered saline (PBS) because of phosphate ion adsorption to the surface of the particles. In contrast, these anions are missing from the ultrapure water (UP-water) dispersant. As would be expected, CPFS-Sulphate-80 and CPFS-Nitrate-90 have less negative zeta potential measurements when dispersed in UP-water, indicating that these two suspensions are relatively unstable in this environment. Hence PBS may be a more optimum diluent, given the measurements are closer to a -30 mV reading which would likely lead to a stable colloidal dispersion [27]. All other samples' zeta potential values suggest relatively stable suspensions have formed with most values close to +30 or -30 mV [27].

Table 3.11: ***Zeta potential measurements for all the CPFS/CHFS samples, performed in both ultrapure water at resistivity of 18.2 mΩ and 0.01 M phosphate-buffered saline at pH 7.4. Lines marked "-" denote situations where the ZP could not be recorded owing to rapid sedimentation of the samples.***

	Zeta Potential / mV			
	Ultrapure water		Phosphate buffered saline	
Sample ID	0 minutes	10 minutes	0 minutes	10 minutes
CPFS-Sulphate-45	-	-	-	-
CPFS-Sulphate-65	-	-	-	-
CPFS-Sulphate-80	-7.53 ± 0.84	-8.03 ± 0.50	-21.63 ± 1.79	-23.52 ± 1.81
CPFS-Sulphate-90	-32.98 ± 0.28	-30.78 ± 0.78	-31.65 ± 1.18	-34.28 ± 1.19
CPFS-Chloride-70	36.3 ± 0.65	36.73 ± 0.50	-26.23 ± 1.79	-26.88 ± 1.21
CPFS-Chloride-80	37.23 ± 1.07	33.27 ± 0.63	-31.77 ± 2.39	-24.02 ± 1.31
CPFS-Chloride-90	35.67 ± 1.24	40.30 ± 0.91	-21.30 ± 0.83	-22.68 ± 1.21
CPFS-Nitrate-80	-35.15 ± 0.87	-33.70 ± 1.17	-27.30 ± 1.13	-27.73 ± 1.32
CPFS-Nitrate-82	-	-	-23.27 ± 0.94	-24.40 ± 1.48
CPFS-Nitrate-84	-	-	-	-
CPFS-Nitrate-86	-	-	-26.65 ± 1.96	-28.38 ± 1.57
CPFS-Nitrate-88	-	-	-	-
CPFS-Nitrate-90	-9.30 ± 0.41	-8.63 ± 0.62	-26.55 ± 1.68	-28.25 ± 1.30
CHFS-1	30.77 ± 1.42	22.88 ± 2.03	-17.13 ± 0.86	-19.57 ± 1.15
CHFS-2	26.15 ± 0.24	26.47 ± 0.23	-18.60 ± 1.43	-19.93 ± 1.23
CHFS-3	24.62 ± 0.97	25.48 ± 0.30	-14.27 ± 1.28	-15.82 ± 1.30
CHFS-4	26.08 ± 1.01	25.02 ± 0.99	-12.48 ± 1.25	-13.93 ± 1.23

Attempts were made to elucidate relationships between zeta potential measurements and the chemical nature of the nanoparticles, but none were obvious. For instance, it is evident from the data presented in **Table 3.12** and **Figure 3.15** that there are no discernible trends between the particle size of the NPs and their zeta potentials.

Table 3.12: ***The results of attempts to determine relationships between NPs' zeta potential measurements and their respective particle sizes – as determined by SEM analysis.***

Alum type	Experimental parameters		Equation	R^2 correlation
	x / nm	y / mV		
CPFS-Chloride	Particle size	ZP_UP water Initial	y = 2.2268x – 43.49	0.5156
		ZP_UP water 10 minutes	y = -0.4361x + 53.701	0.3967
		ZP_PBS Initial	y = -0.3078x + 29.531	0.4388
		ZP_PBS 10 minutes	y = 0.6052x + 52.511	0.2846
CPFS-Nitrate	Particle size	ZP_PBS Initial	y = -9.6079x – 141.42	0.3388
		ZP_PBS 10 minutes	y = -5.2712x – 35.495	0.1098
CHFS	Particle size	ZP_UP water Initial	y = 0.2246x + 61.767	0.2688
		ZP_UP water 10 minutes	y = -0.6403x + 83.793	0.7021
		ZP_PBS Initial	y = 0.0811x + 69.078	0.0374
		ZP_PBS 10 minutes	y = 0.0159x + 68.086	0.0016

There are no data for the CPFS-Sulphate samples in **Table 3.12** because there were not enough data points available. The same is true for the CPFS-Nitrate samples' and the zeta potential obtained using UP_Water as the dispersant; no data could be collected because rapid sedimentation occurred during the measurements.

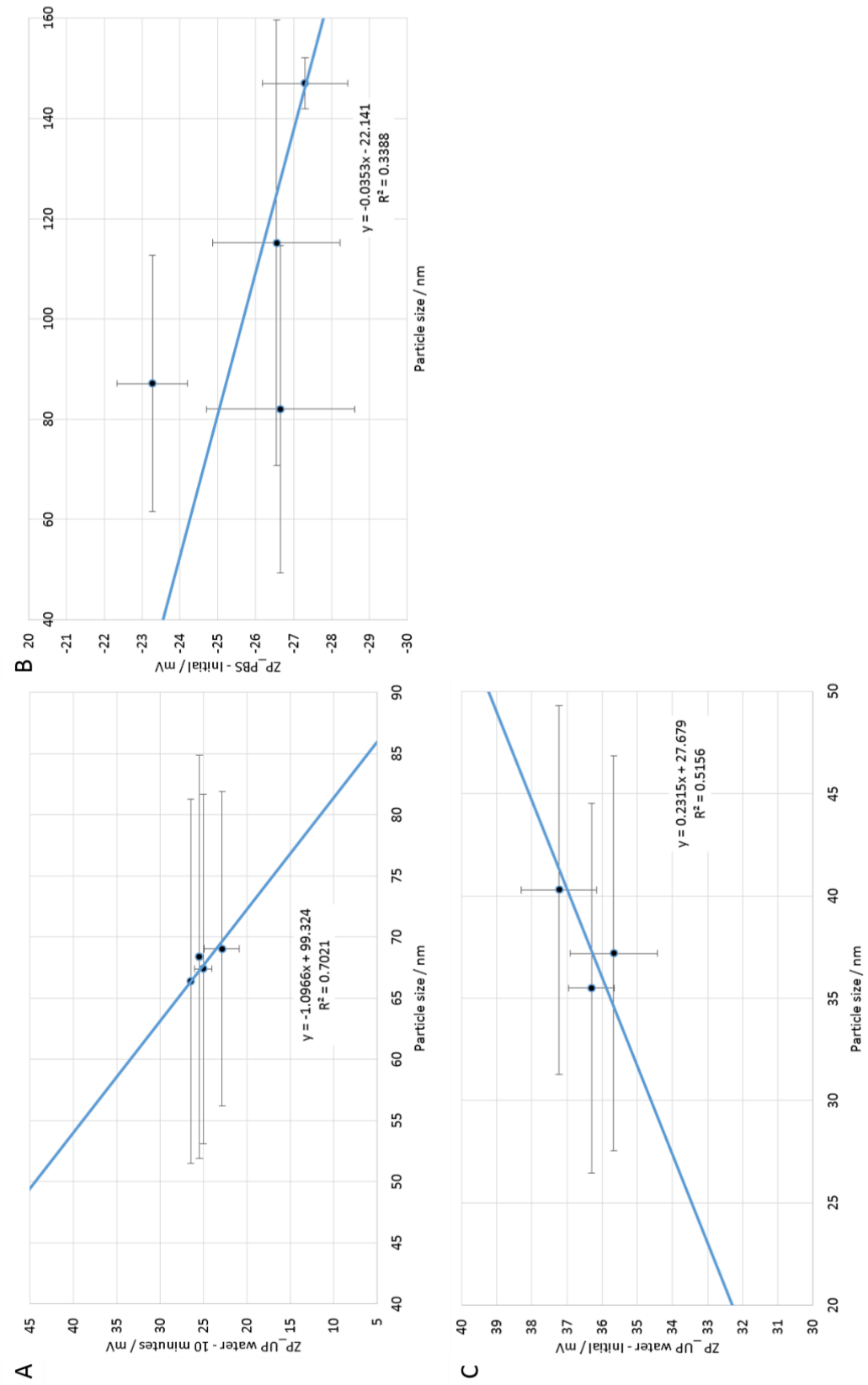

Figure 3.15: ***Plots of zeta potential vs particle size for (A) CPFS-Chloride, (B) CPFS-Nitrate and (C) CHFS samples using the experimental parameter which gave the strongest correlation for each synthesis route.***

3.5 *In vitro* Experiments

3.5.1 Cell Viability

Cellular cytotoxicity was quantified using the Alamar Blue assay after RAW264.7 cells had been incubated with the various samples prepared by both CHFS and CPFS processes; the resultant data can be found in **Figure 3.16**. Cell viability was greater than 90% in all cases. The adjuvant materials prepared in this work lead to viabilities indistinguishable from those of untreated cells or cells treated with the commercial Alhydrogel or Adju-Phos adjuvants.

3.5.2 Immunoassay experiments

Two cytokines were selected to gain insight into the immunomodulatory behaviour of the CPFS and CHFS samples. Tumour necrosis factor-alpha (TNF-α) is a pro-inflammatory cytokine predominantly secreted by macrophages. Its production initiates a cytokine cascade targeting the vascular endothelium [28] causing increased permeability, and leading to subsequent macrophage and neutrophil recruitment to the site of injection and induction an immune response. Interleukin-6 (IL-6) is another cytokine secreted by both T-cells and macrophages. It is often associated with a Th2 polarisation and is reported to be involved in the immune responses induced by aluminium-containing adjuvants [29].

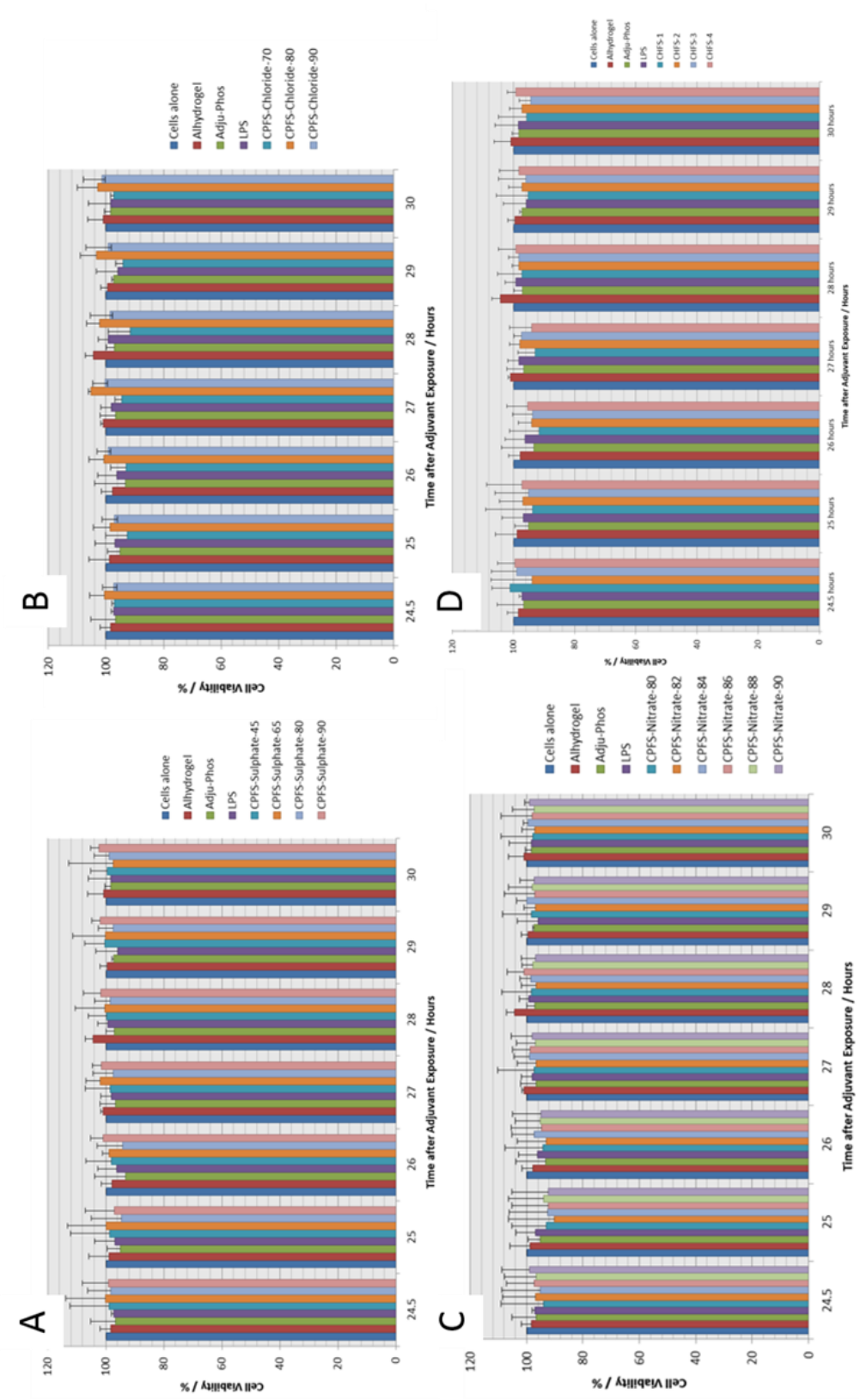

Figure 3.16: ***Cell viability results. RAW264.7 macrophages were exposed to AlO(OH) nanoparticles at 476 µg mL^{-1} for 24 hours. Cells exposed to commercial alums (Alhydrogel® and Adju-Phos®) were used for comparative purposes, alongside lipopolysaccharide (LPS). Cell viability was quantified by Alamar Blue assays with n=3 independent experiments and each individual experiment containing 9 replicates. Data are shown for (A) CPFS-Sulphate, (B) CPFS-Nitrate, (C) CPFS-Chloride and (D) CHFS materials.***

3.5.2.1 Sulphate precursor

The nanoparticles prepared using aluminium sulphate as the precursor in the CPFS reactor induce TNF-α production by murine macrophages (**Figure 3.17**). The four samples perform better than the commercially available alums; interestingly, as the synthesis temperature is increased, a reduction in TNF-α secretion appears to be observed. Comparing the four products, the size of the NPs and Al-content may provide a means of explaining this apparent trend. The two sub-70 °C $Al(OH)_3$ samples have approximate size of 70 nm; in contrast the two AlO(OH) samples (80 and 90 °C) have smaller nanoparticles of roughly 40 nm. Additionally, the Al-content is lower in the $Al(OH)_3$ samples than it is in the AlO(OH) samples [12]. Both the decrease in particle size and changes in the chemical composition of the NPs could lead to a lower TNF-α secretion pattern.

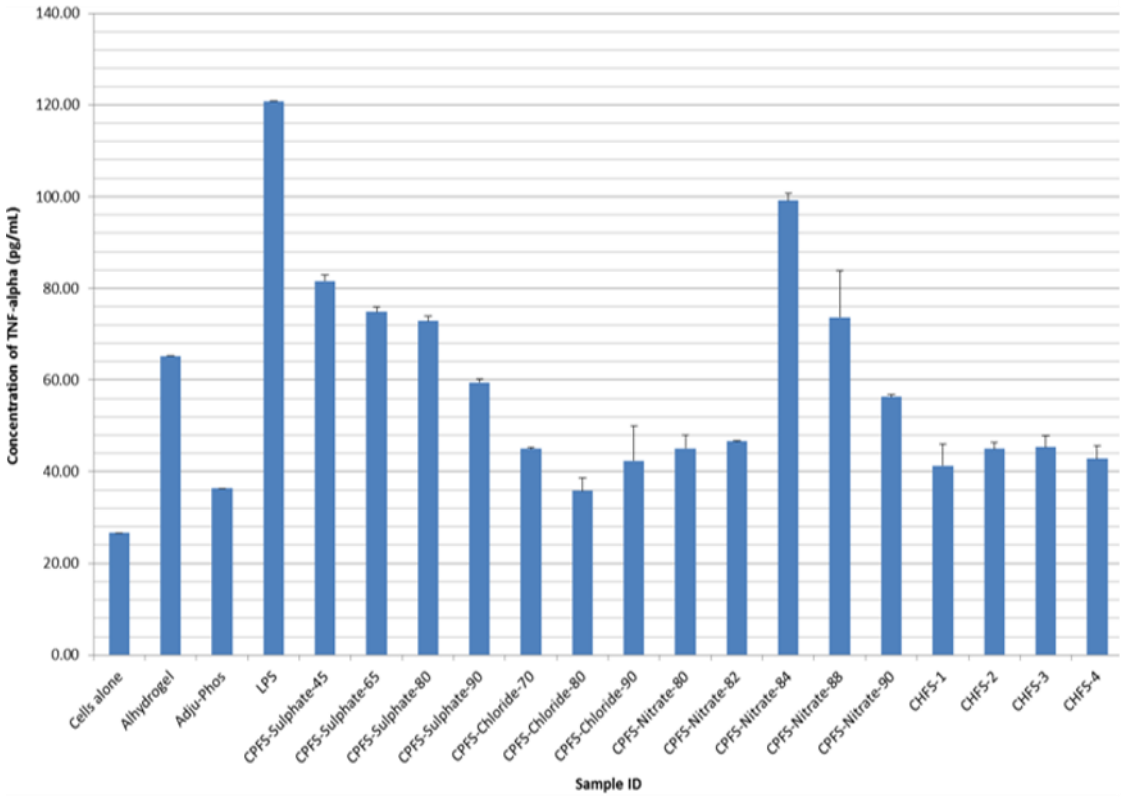

***Figure 3.17:** TNF-α production by RAW264.7 macrophages exposed to AlO(OH) nanoparticles at 476 µg mL^{-1} for 24 hours. Cells exposed to commercial alums (Alhydrogel® and Adju-Phos®) were used for comparative purposes with lipopolysaccharide (LPS) as a positive control. TNF-α cytokine secretion was quantified by ELISA assays (n=3) with each individual experiment containing 9 replicates.*

The inverse trend is recorded for the secretion of IL-6 (**Figure 3.18**), with production increasing with synthesis temperature. Experimental work by Sun and co-workers [2] on bone-marrow derived dendritic cells demonstrated that an increased length of boehmite rods induced much higher IL-6 production from these cells: nanorods of approximately 200 nm in length could induce the production of 2 – 3 times the concentration of IL-6 than rods of 150 nm lengths. In contrast, the spherical particles prepared in this work exhibited a maximum of 15 pg mL^{-1} difference in IL-6 production by RAW264.7 macrophages. This could be due to there being a size difference of *ca*. 30 nm across the four samples, whilst Sun *et al.* [2] had length differences of approximately 200 nm.

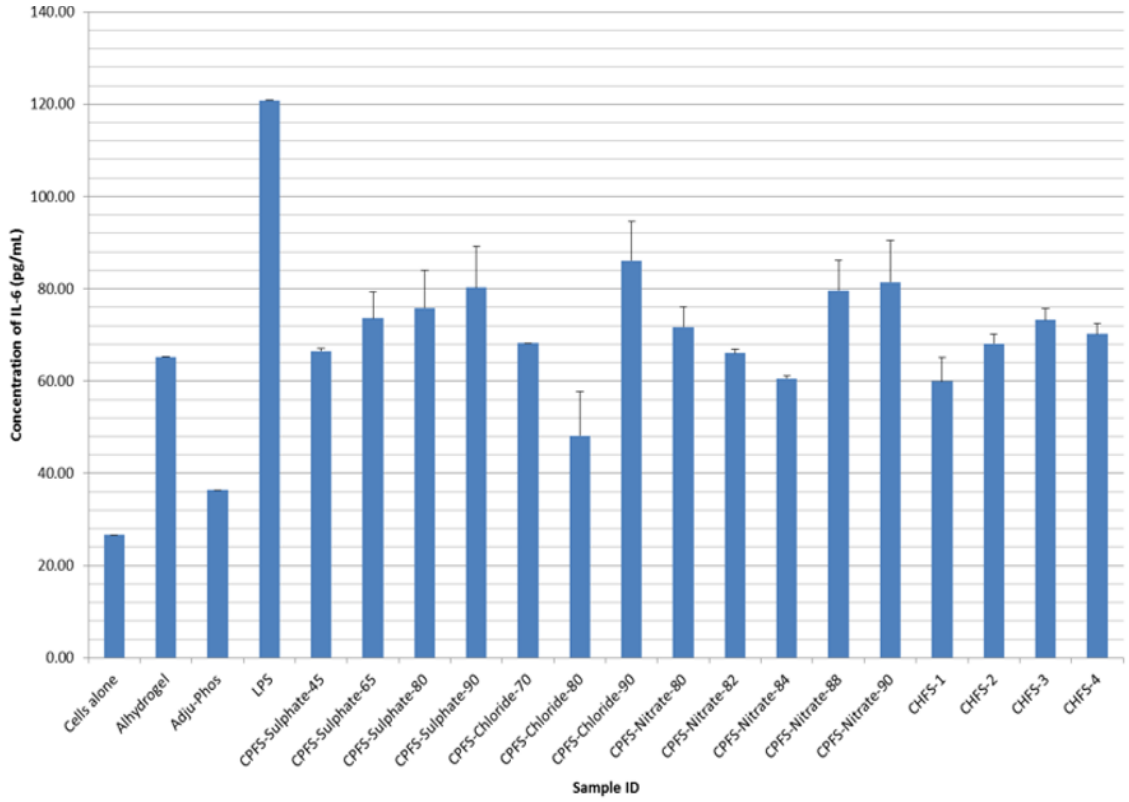

Figure 3.18: ***IL-6 production by RAW264.7 macrophages exposed to AlO(OH) nanoparticles at 476 µg mL^{-1} for 24 hours. Cells exposed to commercial alums (Alhydrogel® and Adju-Phos®) were used for comparative purposes with lipopolysaccharide (LPS) as a positive control. IL-6 cytokine secretion was quantified by ELISA assays. n=3, with each individual experiment containing 9 replicates.***

3.5.2.2 Chloride Precursor

All samples synthesised using the CPFS-Chloride protocol performed at least on par with of commercially available Adju-Phos in both assays. Samples prepared at the minimum and maximum reaction temperatures exhibit more IL-6 production than the mid-temperature materials. The greatest IL-6-output is recorded for the smallest particle sized NPs (*ca*. 88 nm at the maximum reaction temperature) with 86 pg mL^{-1} IL-6 production, which contradicts what is observed with the NPs synthesised using a nitrate Al-source (**Section 3.5.2.3**). No clear trends are evident in the TNF-α data, with all three samples leading to very similar levels of cytokine production.

3.5.2.3 Nitrate precursor

Considering the nitrate-precursor NPs, all performed at least on par with Adju-Phos in terms of both TNF-α and IL-6 production. The inflammatory cytokine profile for the $Al(OH)_3$ NPs prepared at 80 and 82 °C shows more IL-6 than TNF-α production – *ca*. 70 pg mL^{-1} IL-6 concentrations coupled with *ca*. 42 pg mL^{-1} TNF-α - thus suggesting a Th2-type immune response might be elicited following adjuvant application. The mixed-phase NPs generated at 84 °C could produce more TNF-α secretion (*ca.* 100 pg mL^{-1}) and less IL-6 which could indicate more of a bias to a Th1 response. These particles are smaller than those prepared at lower temperatures, and thus this work agrees with the literature in that smaller particles are more likely to induce Th1-type responses [30].

The pure-phase boehmite NPs produced at 88 and 90 °C appear to stimulate different *in vitro* immune responses. The decrease in crystallite size on going from 88 to 90 °C appears to have the effect of tailoring the cytokine profile towards IL-6, indicating that perhaps more of a Th2-type response might be initiated.

3.5.2.4 CHFS samples

All the alums synthesised by the CHFS process perform at least on par with Adju-Phos. As the particle morphology changes from spherical NPs to platelet/rod structures with CHFS-1 and 2, there is evidence of a marginal increase in the IL-6 output, with roughly constant TNF-α production.

The spherical NPs (CHFS-1 and 3) give an increase in IL-6 production when the crystallite size is reduced (CHFS-3 is smaller than 1); whereas the bi-phasic materials have similar IL-6 outputs. These findings might indicate that particle engineering-induced reduction of the crystallite size of the spherical AlO(OH) materials can lead tuning of the immune response.

3.5.3 Fluorescent Microscopy

Representative microscopy images are given in **Figure 3.19**. All the NPs were labelled with FITC and the RAW264.7 cells with the DAPI nuclear stain, giving rise to green and blue images under the fluorescent microscope, respectively. All the CHFS NPs prepared in this work appear as aggregates under the fluorescence microscope, with evidence of co-localisation of the aggregated spherical nanoparticles with the RAW264.7 cells. The images suggest that the NPs might elicit their immunogenic effect in a manner consistent with the suggestion of Flach and co-workers that lipid membrane disturbances result in immunogenicity [31].

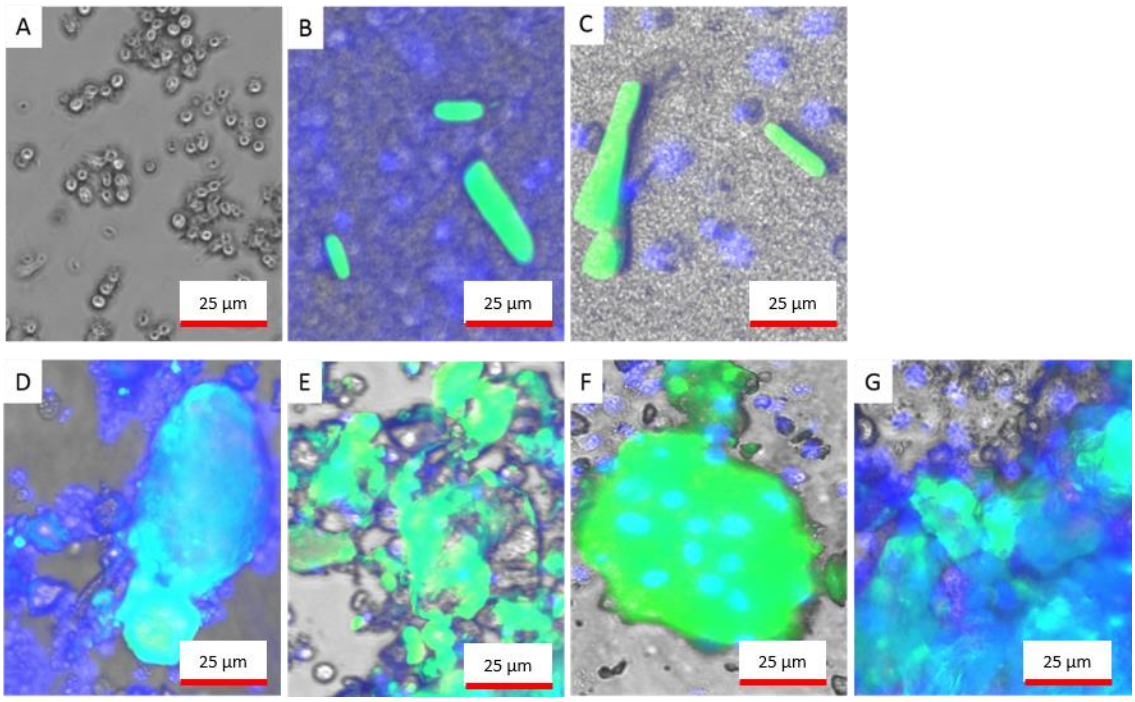

***Figure 3.19:* Fluorescent microscopy with FITC-labelled samples and DAPI nuclear staining; (A) cells alone, (B) Alhydrogel, (C) Adju-Phos, (D) CHFS-3, (E) CPFS-Sulphate-80, (F) CPFS-Nitrate-82; and (G) CPFS-Chloride-90.**

Confocal microscopy was also attempted, but the adherent nature of the RAW264.7 cells meant that they ruptured during transfer from a 24 well plate to a microscope slide for imaging and hence images could not be obtained.

3.6 Structure/Property Relationships

The complete data sets for each adjuvant prepared were assessed for relationships between the particles' physicochemical properties and the production of cytokines by RAW264.7 cells. The results are given in **Table 3.13**, with graphical depictions of some presented in **Figure 3.20**.

Caution must be taken in assessing the relationships deduced from these datasets, since the number of data points in each is relatively small. Often, there are no clear relationships between the properties of the particles and the immune response initiated (see **Table 3.13** and **Figure 3.20**), but in some cases there appear to be very distinct correlations present.

Table 3.13: ***Relationships between the physicochemical properties of the adjuvant particles prepared and cytokine production by RAW264.7 cells. It was not possible to deduce correlations for the CPFS-Sulphate materials due to having only a very limited number of data points, and due to rapid sedimentation of CPFS-Nitrate NPs in UP water no data are available here either. Particle size is recorded in nm and zeta potentials in mV.***

Alum type	Experimental parameter / x	Cytokine concentration / y	Equation	R^2 correlation
CPFS-Chloride	Particle size	TNF-α	y = -1.9305x + 113.75	0.9943
		IL-6	y = -5.1624x + 216.9	0.4375
	ZP_UP water	TNFα	y = -4.6152x 209.03	0.5909
		IL-6	y = -24.13x + 945.79	0.9939
	ZP_PBS	TNFα	y = 0.6452x + 58.087	0.5144
		IL-6	y = 3.6265x + 163.31	1.0000
CPFS-Nitrate	Particle size	TNF-α	y = -0.6876x + 140.27	0.6449
		IL-6	y = -0.0061x + 70.139	0.0005
	ZP_UP water	TNFα	---	---
		IL-6	---	---
	ZP_PBS	TNFα	y = 12.503x + 390.48	0.7824
		IL-6	y = -3.2366x – 14.484	0.5175
CHFS	Particle size	TNF-α	y = -0.338x + 66.521	0.0043
		IL-6	y = -3.7446x + 321.77	0.5793
	ZP_UP water	TNFα	y = -0.6312x + 60.583	0.7858
		IL-6	y = -1.753x + 115.01	0.6766
	ZP_PBS	TNFα	y = 0.5428x + 52.08	0.6201
		IL-6	y = 0.9792x + 83.141	0.2252

The CPFS-Chloride samples demonstrate strong relationships between experimental properties of the NPs and their elicited cytokine profiles (**Table 3.13**). The TNF-α production by RAW264.7 cells is strongly related to the particle size of the NPs (R^2 = 0.9943) – **Figure 3.20A**. Furthermore, the IL-6 output by the RAW cells is strongly related to zeta potential measured in both UP water and PBS (R^2 = 0.9939 and 1.0000, respectively) – **Figure 3.20B** and **C**, respectively.

The zeta potential measured for CPFS-Nitrate samples, using PBS as the dispersant, link well with the TNF-α secretion (R2 = 0.7858, **Figure 3.20D**). With reference to the CHFS samples, there is a relatively strong relationship evident for the production of TNF-α by RAW264.7 cells using the zeta potential measured when UP water was the dispersant (R^2 = 0.7858 – **Figure 3.20E**); when linking the same zeta potential measurements to the IL-6 production, an R^2 value of 0.6766 is obtained (**Figure 3.20F**). There are no other apparent trends between the two assayed cytokines and the three physicochemical properties selected for analysis.

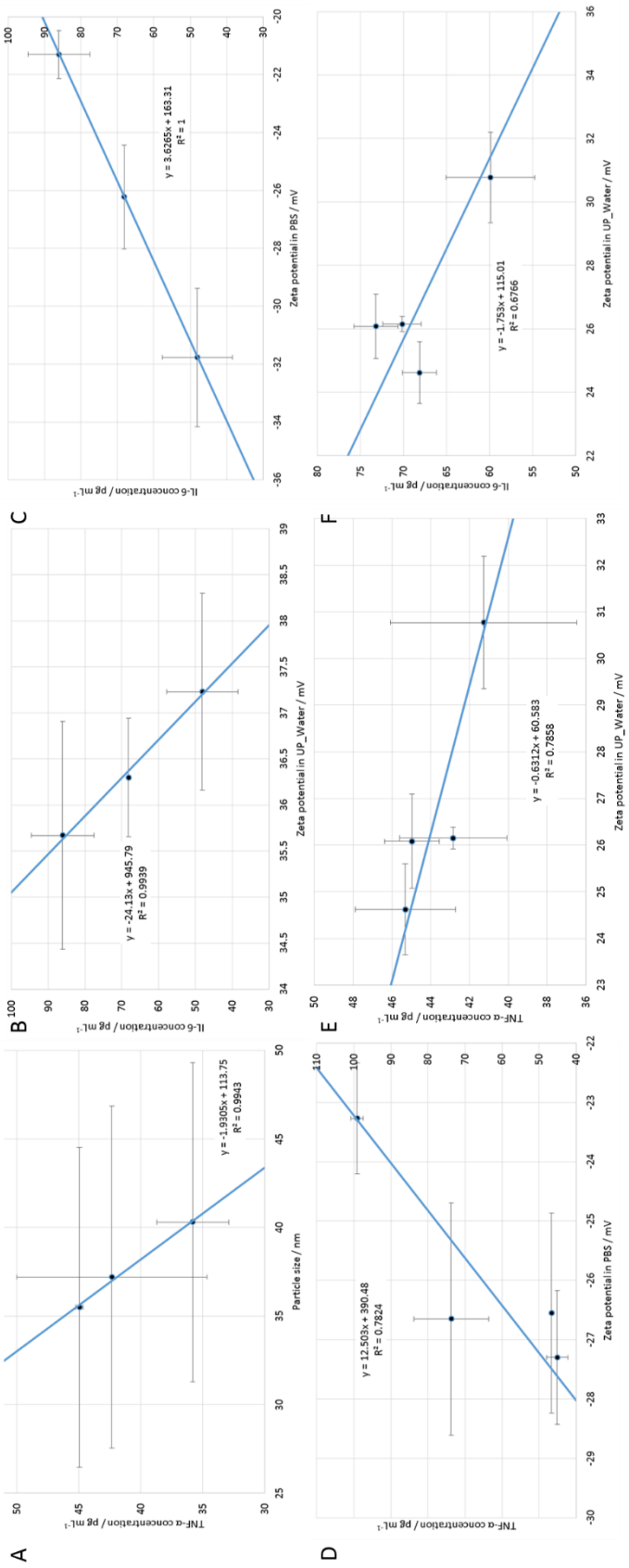

Figure 3.20: ***Graphical representation of six relationships described in Table 3.13 with (A-C) being connections deduced from experimental data of the CPFS-Chloride family of NPs, (D) CPFS-Nitrate family and (E-F) for the CHFS family.***

3.7 Conclusion

In conclusion, controlling the synthesis parameters of the CPFS process to tune the AlO(OH) particle size and morphology is non-facile; the use of low temperatures results in amorphous materials and while elevating the temperature does lead to a change in particle size, over the temperature range which can be accessed there are minimal changes. CPFS largely produces spherical nanoparticles with $Al(OH)_3$ or AlO(OH) composition. The nature of the precursors used and temperature impacts the phase formed, with gibbsite being synthesised at low temperatures and boehmite at higher ones. In addition, the crystallinity and morphology and the induced immune response are also affected.

Within the CHFS process, flow rates are a key parameter in controlling the particle shape and size of the boehmite prepared, as a result of an increase in temperature of the mix-point arising from an unbalanced flow rate. Particle morphology is dependent on the reaction temperature: low temperatures result in spherical particles – consistent with output of the CPFS process – whilst higher temperatures give rise to a mixture of both hexagonal platelets and rod-like nanoparticles.

There is little experimental evidence to suggest that changes in morphology of the CHFS NPs results in significantly different *in vitro* immune responses; all the samples tend to produce more IL-6 than TNF-α. That said, there is some degree of tunability in cytokine production, and all the materials prepared perform at least on a par with commercially available alum adjuvants. The samples prepared are generally not cytotoxic *in vitro*, with viabilities > 90%. This is favourable for onward application.

The CPFS samples are cheap to manufacture due to the low temperatures and pressures used within this system. However, the energy costs involved in the CHFS process could make this an unfavourable synthesis route. In addition, the process uses metal pipework which leads to metal corrosion by the supercritical water feed and contamination of the AlO(OH) samples.

Overall, it appears that using these processes to generate tuneable and bespoke adjuvants is likely to be challenging, and significant further development of the experimental procedures is required.

3.8 References

1. Maughan, C.N., S.G. Preston, and G.R. Williams, *Particulate inorganic adjuvants: recent developments and future outlook.* J Pharm Pharmacol, 2014.
2. Sun, B.B., et al., *Engineering an Effective Immune Adjuvant by Designed Control of Shape and Crystallinity of Aluminum Oxyhydroxide Nanoparticles.* ACS Nano, 2013. **7**(12): p. 10834-10849.
3. Gruar, R.I., C.J. Tighe, and J.A. Darr, *Scaling-up a Confined Jet Reactor for the Continuous Hydrothermal Manufacture of Nanomaterials.* Industrial & Engineering Chemistry Research, 2013. **52**(15): p. 5270-5281.
4. Marchand, P., *One Step Continuous Hydrothermal Flow Synthesis of Collodial Dispersions of Water Stable Titania Nanoparticles Inks* 2015.
5. Chaudhry, A.A., et al., *Synthesis and characterisation of magnesium substituted calcium phosphate bioceramic nanoparticles made via continuous hydrothermal flow synthesis.* Journal of Materials Chemistry, 2008. **18**(48): p. 5900-5908.
6. *Lipid maps thawing and passage procedure for RAW264.7*. 2004.
7. Bokhimi, X., et al., *Relationship between crystallite size and bond lengths in boehmite.* Journal of Solid State Chemistry, 2001. **159**(1): p. 32-40.
8. Saalfeld, H. and M. Wedde, *Refinement of Crystal-Structure of Gibbsite, Al(Oh)3.* Zeitschrift Fur Kristallographie, 1974. **139**(1-2): p. 129-135.
9. Liu, Z., et al., *Widening Synthesis Bottlenecks: Realization of Ultrafast and Continuous-Flow Synthesis of High-Silica Zeolite SSZ-13 for NOx Removal.* Angew Chem Int Ed Engl, 2015. **54**(19): p. 5683-7.
10. Malki, A., et al., *Calcination products of gibbsite studied by X-ray diffraction, XPS and solid-state NMR.* Journal of Solid State Chemistry, 2014. **215**: p. 8-15.
11. Isobe, T., et al., *Solid-state 1H and 27Al NMR studies of amorphous aluminum hydroxides.* J Colloid Interface Sci, 2003. **261**(2): p. 320-4.
12. Kloprogge, J.T., et al., *XPS study of the major minerals in bauxite: gibbsite, bayerite and (pseudo-)boehmite.* J Colloid Interface Sci, 2006. **296**(2): p. 572-6.
13. Adschiri, T., K. Kanazawa, and K. Arai, *Rapid and Continuous Hydrothermal Synthesis of Boehmite Particles in Subcritical and Supercritical Water.* Journal of the American Ceramic Society, 1992. **75**(9): p. 2615-2618.
14. Adschiri, T., K. Kanazawa, and K. Arai, *Rapid and Continuous Hydrothermal Crystallization of Metal-Oxide Particles in Supercritical Water.* Journal of the American Ceramic Society, 1992. **75**(4): p. 1019-1022.
15. Zhang, J., et al., *Self-assembly of flowerlike AlOOH boehmite 3D nanoarchitectures.* Journal of Physical Chemistry B, 2006. **110**(29): p. 14249-52.
16. Kiss, A.B., G. Keresztury, and L. Farkas, *Raman and Ir-Spectra and Structure of Boehmite (Gamma-Alooh) - Evidence for the Recently Discarded D-2h(17) Space Group.* Spectrochimica Acta Part a-Molecular and Biomolecular Spectroscopy, 1980. **36**(7): p. 653-658.
17. Feng, Y.L., et al., *One-step synthesis of hierarchical cantaloupe-like AlOOH superstructures via a hydrothermal route.* Crystal Growth & Design, 2008. **8**(4): p. 1426-1429.
18. Boumaza, A., et al., *Transition alumina phases induced by heat treatment of boehmite: An X-ray diffraction and infrared spectroscopy study.* Journal of Solid State Chemistry, 2009. **182**(5): p. 1171-1176.

19. Alemi, A., et al., *Boehmite (γ-AlOOH) nanoparticles: Hydrothermal synthesis, characterization, pH-controlled morphologies, optical properties, and DFT calculations.* physica status solidi (b), 2012. **249**(6): p. 1264-1270.
20. Kwak, J.H., et al., *Coordinatively unsaturated Al3+ centers as binding sites for active catalyst phases of platinum on gamma-Al2O3.* Science, 2009. **325**(5948): p. 1670-3.
21. Ahrem, L., et al., *Thermal Evolution of 4- and 5-fold Coordinated Al-Sites in Aluminum Hydroxide Fluorides with Low Fluorination Degree.* The Journal of Physical Chemistry C, 2016. **120**(17): p. 9236-9244.
22. Pecharromán, C., et al., *Thermal Evolution of Transitional Aluminas Followed by NMR and IR Spectroscopies.* The Journal of Physical Chemistry B, 1999. **103**(30): p. 6160-6170.
23. Chupas, P.J. and C.P. Grey, *Surface modification of fluorinated aluminas: Application of solid state NMR spectroscopy to the study of acidity and surface structure.* Journal of Catalysis, 2004. **224**(1): p. 69-79.
24. Chen, M., et al., *Modelling and simulation of continuous hydrothermal flow synthesis process for nano-materials manufacture.* Journal of Supercritical Fluids, 2011. **59**: p. 131-139.
25. Sue, K., et al., *Size-controlled synthesis of metal oxide nanoparticles with a flow-through supercritical water method.* Green Chemistry, 2006. **8**(7): p. 634-638.
26. Williams, G.R., et al., *Immunity induced by a broad class of inorganic crystalline materials is directly controlled by their chemistry.* Journal of Experimental Medicine, 2014. **211**(6): p. 1019-1025.
27. Instruments, M., *Zeta Potential Theory, in Zetasizer Nano Series User Manual - MAN0317 Issue 1.1*. 2004, Malvern Instruments Ltd: Enigma Business Park, Grovewood Road, Malvern, Worcestershire, WR14 1XZ, England. p. 15.2.
28. Dinarello, C.A., *Proinflammatory cytokines.* Chest, 2000. **118**(2): p. 503-8.
29. Serre, K., et al., *Molecular differences between the divergent responses of ovalbumin-specific CD4 T cells to alum-precipitated ovalbumin compared to ovalbumin expressed by Salmonella.* Molecular Immunology, 2008. **45**(13): p. 3558-3566.
30. Kumar, S., et al., *Shape and size-dependent immune response to antigen-carrying nanoparticles.* Journal of Controlled Release, 2015. **220**(Pt A): p. 141-8.
31. Flach, T.L., et al., *Alum interaction with dendritic cell membrane lipids is essential for its adjuvanticity.* Nature Medicine, 2011. **17**(4): p. 479-U121.

Chapter 4 : Particle Engineering of Hydroxyapatite Nanoparticles

4.1 Introduction

Calcium phosphate is a natural compound found within the human body [1], and has been widely used as an adjuvant in the diphtheria-pertussis-tetanus vaccination in France [2-4]. Characterisation of commercial calcium phosphate adjuvants determined their chemical composition to be $Ca_{10-x}(HPO_4)_x(PO_4)_{6-x}(OH)_{2-x}$, with "x" varying between 0 and 2 [5], and thus chemically these are calcium-deficient hydroxyapatite materials. The effect of the particle size and shape of hydroxyapatite have been investigated in the context of vaccinology, with crystalline needle-like particles found to evoke a stronger immune response than spherical particles [6]. Furthermore, smaller particles sizes were reported to be preferred for eliciting greater responses [6]. The previous patent report [6] is not completely clear in terms of exactly which measures were used to assess these improvements in immune response, however.

Previous work has identified that using the continuous plastic flow synthesis (CPFS) approach, it is possible to control the size and shape of hydroxyapatite particles [7]. The objective of the work reported in this chapter was to engineer hydroxyapatite particle size and morphology using the CPFS process, and then assess impact of these parameters on immunogenicity.

4.2 Materials and Methods

4.2.1 Continuous Plastic Flow Synthesis of Hydroxyapatite

The continuous plastic flow synthesis (CPFS) reactor set-up was similar to the system described in **Section 3.2.1.1**, but adapted to pre-heat both precursor feeds using additional oil baths, (see **Figure 4.1**). This CPFS system used a 9 m length of polytetrafluoroethylene tubing to give a 4.7 minute residence time when the combined flow rate equalled 25 mL min^{-1}. Individual flow rates of the two precursor feeds were 12.5 mL min^{-1}, with solutions of calcium nitrate (CaN; Sigma Aldrich UK) and diammonium hydrogen phosphate (DAP; Fisher Scientific) solutions used as the precursors.

Aqueous solutions of CaN and DAP were first prepared in deionised water. The pH of both precursor solutions was adjusted to 10 with addition of 2% *v*/*v* or 6% *v*/*v* ammonium hydroxide, resulting in final pH-adjusted solutions with concentrations of 0.6 M for CaN and 0.3 M for DAP. Ammonium hydroxide was used as a base source instead of potassium hydroxide to minimise carbonate formation in the solutions.

The product was rapidly cooled at the point of collection to cease the reaction. The white solid product was left to settle for approximately 30 minutes prior to recovery by centrifugation. The initial centrifugation cycle was performed at 4500 rpm for 5 minutes. Sequential rounds of washing and centrifugation were performed with methanol or water (50 mL per wash) as the solvent and 30 minute centrifugation times. Once the conductivity of the supernatant was reduced to a value less than 50 S m^{-1}, the product was dried in a vacuum oven at 40 °C for 24 h (Vacutherm, Heraeus Instruments).

For P-XRD characterisation, a small amount of the cleaned sample was subjected to a heat treatment (Carbolite CWF 1300 furnace) at a rate of 10 °C min^{-1} up to a temperature of 1000 °C, where it was held for 1 hour before cooling. This was undertaken to aid determination of the hydroxyapatite phase formed, since the fresh collected sample was amorphous. The bioactive, amorphous product was used for all other investigations.

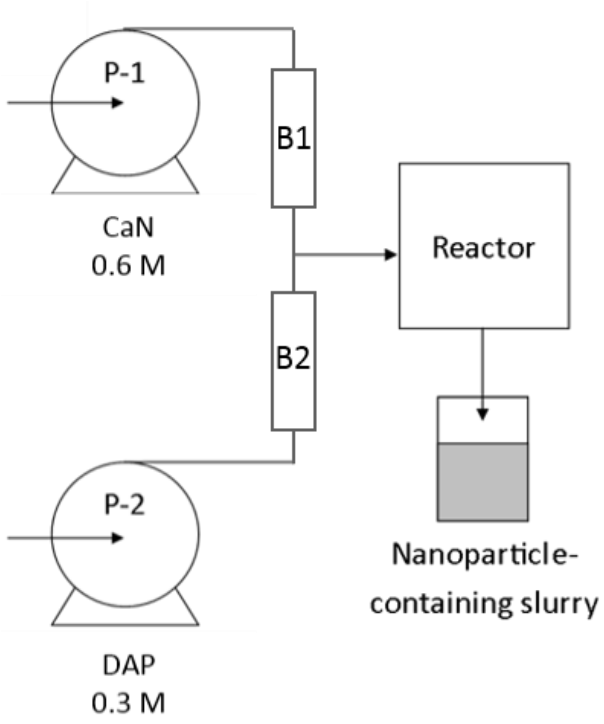

Figure 4.1: ***Tandem CPFS reactor design for the direct synthesis of hydroxyapatite nanoparticles with two HPLC pumps (P-1 and P-2) to pump the precursor solutions through PTFE-tubing immersed in preheated oil baths (B1 and B2, respectively) prior to mixing at the T-piece for reaction initiation.***

4.3 Materials Characterisation

4.3.1 Powder X-ray Diffraction

Powder X-ray diffraction (P-XRD) data were collected using a Rigaku MiniFlex 600 diffractometer supplied with Cu-Kα radiation (λ = 1.5418 Å). Each sample was loaded onto an aluminium plate and scans were undertaken at a rate of 2.5° min^{-1} over a 2θ range of 10-30°. Also, a STOE STADI-P diffractometer using a molybdenum source supplied with $K_{\alpha 1}$ radiation of wavelength 0.7107 Å. Each sample was loaded onto a transmission sample holder within zero-scattering polymer films and scans were undertaken at a rate of 1.25° min^{-1} over a 2θ range of 5-25°. The X'Pert Data Viewer software package was used to visualise and analyse the data.

4.3.2 Scanning Electron Microscopy

See **Section 3.3.2**.

4.3.3 Fourier Transform Infra-Red Spectroscopy

See **Section 3.3.3**.

4.3.4 Surface Area and Pore Volume Analysis

Surface area and pore volume measurements were made using a SA3100 instrument (Beckman Coulter) using nitrogen as the adsorptive gas. BET surface areas were calculated from the isotherm data using the in-built software. Prior to analysis, samples were degassed at 100 °C under vacuum for 10 minutes to remove any residual moisture and other volatiles.

4.3.5 Zeta Potential Measurements

See **Section 3.3.6**.

4.3.6 Immunoassay Experiments

See **Section 3.3.7**.

4.3.6.1 Alamar Blue Assay

See **Section 3.3.7.1**.

4.3.6.2 Enzyme-Linked Immuno-Sorbent Assay

See **Section 3.3.7.2**.

4.3.6.3 Fluorescence and Confocal Microscopy

See **Section 3.3.7.3**.

4.4 Results and Discussion

4.4.1 Continuous Plastic Flow Synthesis of Hydroxyapatite

Two different hydroxyapatite phases were obtained through altering the solvent used in the sequential centrifugation cleaning steps. Either deionised water or methanol were used to obtain pure phase- and calcium-deficient hydroxyapatite materials, respectively.

4.4.1.1 Particle Size Control

The temperature was altered in attempts to control the size and shape of the resultant hydroxyapatite nanoparticles. A summary of the reactions performed is presented in **Table 4.1**.

Table 4.1: ***Synthesis details for hydroxyapatite nanoparticles via a continuous hydrothermal flow process.***

Sample ID	[CaN] / M	[DAP] / M	Flow rate / mL min^{-1}	Reaction temperature / °C	Product pH	Clean-up Solvent
HA_70	0.6	0.3	25	70	9	Methanol
HA_80	0.6	0.3	25	80	9	Methanol
HA_90	0.6	0.3	25	90	9	Methanol
HA_90_Water	0.6	0.3	25	90	9	Deionised water

4.4.2 Materials Characterisation

The materials isolated from the CPFS reaction were found to be amorphous, as shown from the P-XRD patterns given in **Figure 4.2**, and thus from these data their chemical compositions and structures cannot be determined.

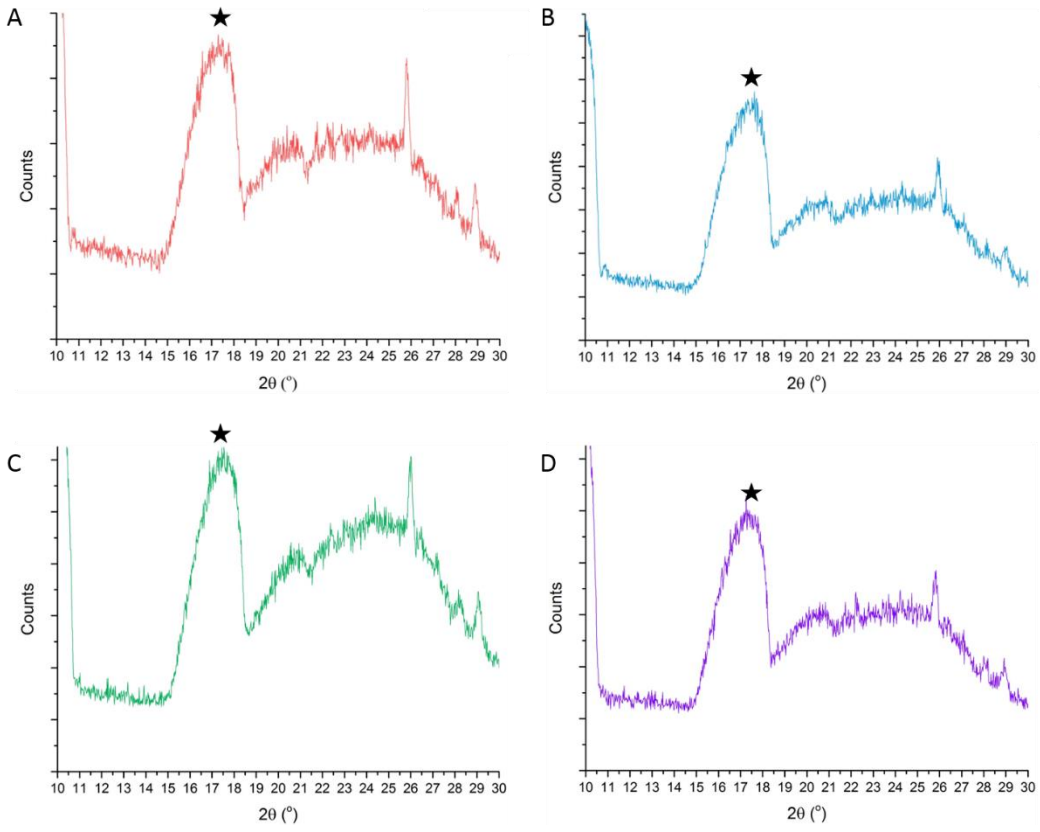

Figure 4.2: ***P-XRD patterns for the as-synthesised hydroxyapatite samples; with the asterisk (*) denoting peaks attributed to the aluminium plate that samples were mounted on. (A) HA_70, (B) HA_80, (C) HA_90, and (D) HA_90_Water.***

The literature reports that hydroxyapatite phases are stable up to 1200 °C [9-12], and thus small amounts of each CPFS sample were calcined at 1000 °C to obtain more insight on the materials formed. The resultant P-XRD patterns are shown in **Figure 4.3**. The calcination process will have facilitated crystallisation to allow more insight on the CPFS productions to be obtained, but should not have changed the chemical composition of the phases obtained at 70, 80 and 90 °C, as has been reported previously [7].

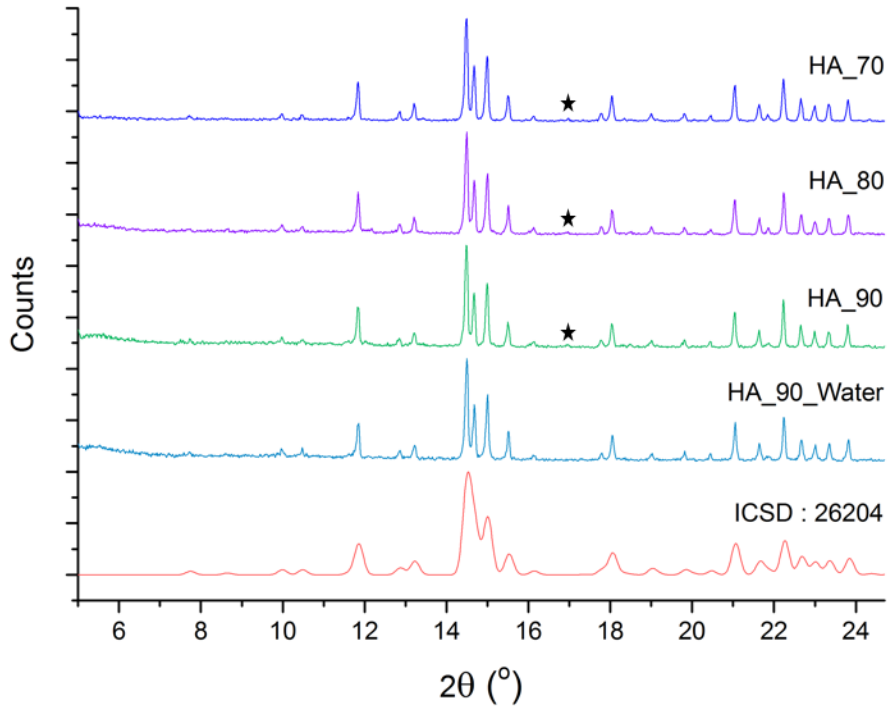

Figure 4.3: ***P-XRD patterns for hydroxyapatite samples with the reference pattern for hydroxyapatite (ICSD: 26204 [13]). Asterisks (*) noted on the pattern, denote a small reflection at*** ca. ***17° (2θ) which is attributed to the loss of calcium from the materials [14].***

All detectable reflections in **Figure 4.3** can be assigned by their positions to hydroxyapatite (HA) in accordance with published data (ICSD reference: 26204; [13]). No peaks were observed belonging to impurities. The reflections observed are sharp, indicative of high crystallinity post-calcination. The small reflections at *ca*. 17° (2θ) identify the three materials produced in methanol as calcium-deficient hydroxyapatites [14]. The presence of this reflection suggests a species with 10% calcium deficiency, and thus a composition of approximately $Ca_9(HPO_4)(PO_4)_5(OH)$ [14].

The HA_90_Water pattern does not contain this reflection (and is the same as the reference pattern). Therefore, when the cleaning solvent is changed from methanol to deionised water in this series of experiments, pure phase hydroxyapatite is obtained. These findings are summarised in **Table 4.2**.

Table 4.2: ***Details of the material generated for samples synthesised via the CPFS process.***

Sample ID	Product
HA_70	Ca-deficient HA
HA_80	Ca-deficient HA
HA_90	Ca-deficient HA
HA_90_Water	Pure phase HA

Calcium-deficient HA is most commonly used as a vaccine adjuvant [2-4], and thus it is encouraging that such a system can be produced in the CPFS approach, with an "x" value of 1 in the generic formula $Ca_{10-x}(HPO_4)_x(PO_4)_{6-x}(OH)_{2-x}$.

SEM analysis (**Figure 4.4** and **Table 4.3**) reveals that the particle size does not differ significantly between the four hydroxyapatite products. However, it is evident from **Figure 4.4** that the morphology changes depending on the reaction conditions and the washing treatment.

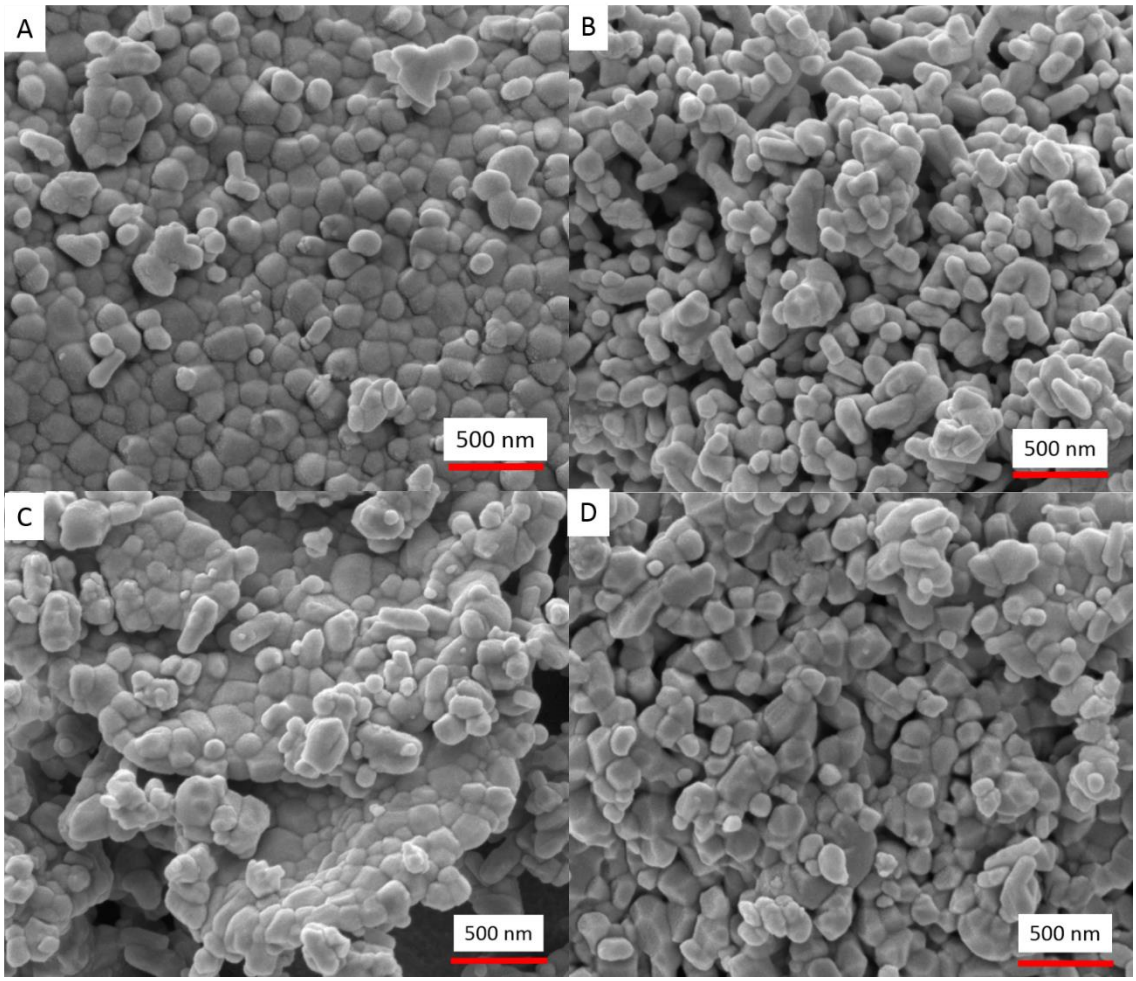

Figure 4.4: ***SEM images of the hydroxyapatite products (A) HA_70, (B) HA_80, (C) HA_90, and (D)*** **HA_90_Water.**

Table 4.3: ***Details of the mean particle size and morphology of the hydroxyapatite nanoparticles synthesised*** **via** ***the CPFS process, deduced with SEM image analysis, mean ± standard deviation.***

Sample ID	Mean particle size / nm	Morphology
HA_70	156 ± 34	Spherical
HA_80	159 ± 42	Spherical, rod-shaped
HA_90	158 ± 49	Spherical, rod-shaped
HA_90_Water	162 ± 35	Spherical, rod-shaped and platelets

Increasing the temperature used to prepare the calcium deficient samples HA_70 to HA_90 leads to a change of morphology from a solely spherical product at low temperature to samples consisting of both spherical and rod-shaped nanoparticles. The pure-phase hydroxyapatite has an additional platelet habit detected within the sample.

FTIR analysis was also performed, with the spectra presented in **Figure 4.5**. A shallow broad band is observed at *ca*. 3000 cm^{-1}; this is assigned to the absorption bands for hydroxyl groups present within the hydroxyapatite samples. Peaks at *ca*. 1090 and 1020 cm^{-1} can be attributed to the asymmetric stretching modes of P-O and that at *ca*. 960 cm^{-1} is assigned to the stretching modes of symmetric phosphate groups [15, 16]. All bands listed are consistent with those described for hydroxyapatite in the literature [15, 16].

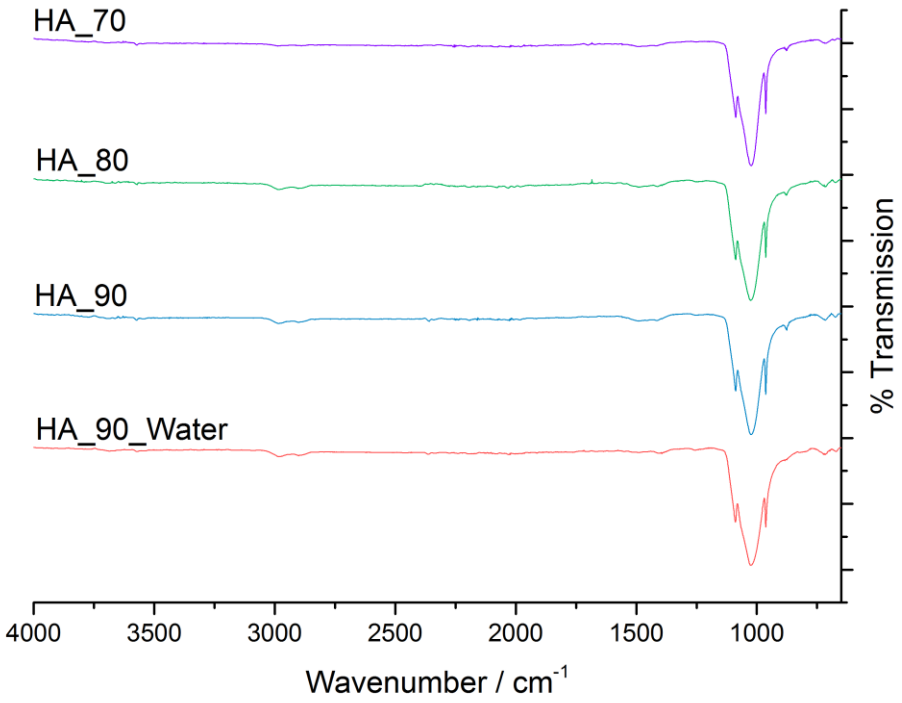

***Figure 4.5:* FTIR spectra of hydroxyapatite samples.**

4.4.3 Surface Area and Pore Volume

In all cases, the samples were dried at 100 °C under vacuum prior to analysis.

The isotherms, as presented in **Figure 4.6**, are evidently Type II. This classification of isotherm corresponds to the materials being non-porous, with multiple adsorption layers arising on the adsorbent's surface. This is supported by analysis of the pore volumes (**Table 4.4**); all samples have a pore volume less than 0.41 mL g^{-1}. The intermediate, plateau portion of the isotherm indicates the formation of a monolayer. A full adsorption/desorption program was run between 0 and 1 relative pressures to confirm the absence of any mesopores (mesoporous structures would exhibit a plateau in the isotherm at *ca*. 0.9 Ps/Po [17]).

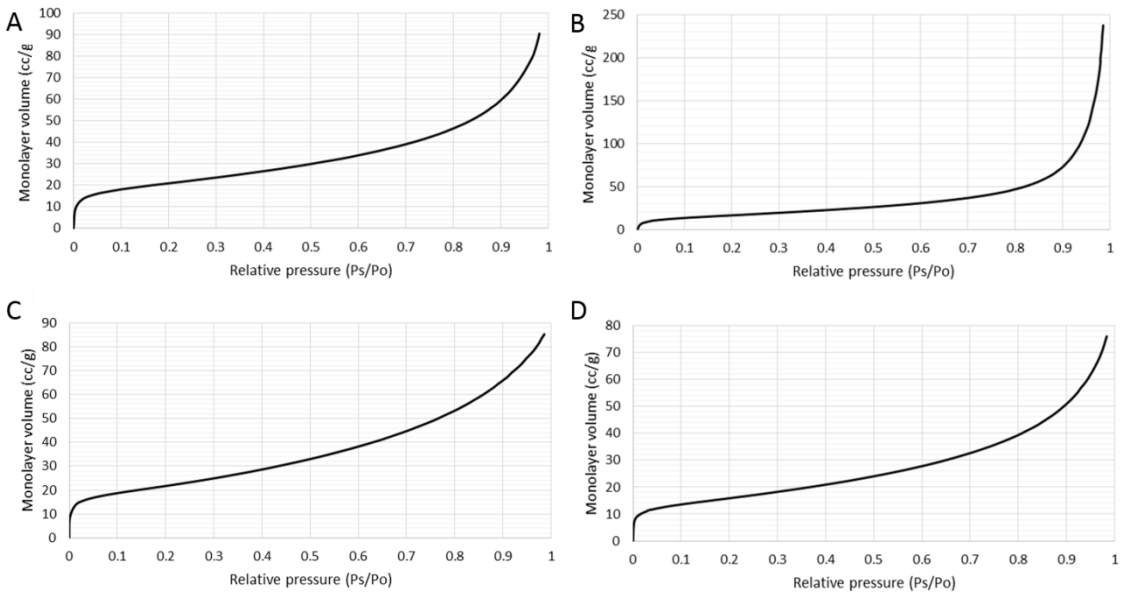

***Figure 4.6:** Adsorption isotherms of the hydroxyapatite materials showing (A) HA_70, (B) HA_80, (C) HA_90 and (D) HA_90_Water.*

***Table 4.4:** Surface area and pore volume data.*

Sample ID	Surface Area / $m^2 g^{-1}$	Pore volume / mL g^{-1}
HA_70	72.796	0.1551
HA_80	53.649	0.4094
HA_90	73.449	0.1341
HA_90_water	54.437	0.1244

The largest two hydroxyapatite NPs – as measured by SEM – exhibit the smallest surface areas, with 53.649 and 54.437 $m^2 g^{-1}$ for HA_80 and HA_90_Water, respectively. However, there is no clear trend: in terms of particle size, we see HA_70 < HA_80 ≈ HA_90 < HA_90_Water, but the surface area measurements follow the trend HA_90 < HA_70 > HA_90_Water < HA_80. This might be attributed to varied aggregation patterns in the different samples.

4.4.4 Zeta Potential Measurements

As mentioned in **Section 1.3.3**, the zeta potential has been shown to be an important physicochemical property in calculating the magnitude of the immune response to LDH adjuvants; therefore, this was also investigated for the hydroxyapatite class of materials. Data are presented in **Table 4.5** and **Table 4.6.** It is evident that changing the dispersion medium causes a change in the zeta potential: negative readings are recorded when PBS is used as the dispersant due to negative phosphate anions within the PBS solution being adsorbed to the surface of the NPs and altering the charge at the slipping plane. Positive readings are obtained when UP-water was used as the dispersant, and there is evidence of stable dispersions being formed with *ca*. +30 mV readings [18].

***Table 4.5:** Mean zeta potential measurements for the hydroxyapatite materials when dispersed in UP-water with resistance of 18.2 mΩ, presented as mean ± standard deviation.*

Sample ID	ZP initially / mV	ZP after 10 minutes / mV
HA_70	28.17 ± 1.11	28.87 ± 1.26
HA_80	32.40 ± 0.83	32.48 ± 1.34
HA_90	34.47 ± 0.66	37.15 ± 1.05
HA_90_water	24.25 ± 0.54	26.35 ± 0.89

***Table 4.6:** Mean zeta potential measurements for the hydroxyapatite materials, when dispersed in 0.01 M phosphate buffered saline (PBS) solution at pH 7.4; mean ± standard deviation.*

Sample ID	ZP initially / mV	ZP after 10 minutes / mV
HA_70	-8.9 ± 0.77	-1.6 ± 0.68
HA_80	-9.5 ± 0.93	-11.3 ± 0.51
HA_90	-9.8 ± 0.77	-12.6 ± 1.18
HA_90_water	-12.5 ± 0.88	-15.1 ± 2.25

Efforts were made to relate the zeta potential measurements to the particle size of the hydroxyapatite NPs, since such relationships were previous found to exist for AlO(OH) systems (see **Section 3.4.8**). None were evident for the UP water data set (**Table 4.7** and **Figure 4.7**).

***Table 4.7:* Relationships between zeta potential measurements and experimental properties of the hydroxyapatite materials.**

Experimental parameter / μm (x)	Zeta potential / mV (y)	Equation	R^2 correlation
Particle size	ZP in UP-water	y = -0.6757x + 137.04	0.1270
	ZP in UP-water (10 minutes)	y = -0.4855x + 108.25	0.0616
	ZP in PBS	y = -0.6004x + 85.096	0.8152
	ZP in PBS (10 minutes)	y = -2.2746x + 350.78	0.8505

However, there appears to be a structure/property relationship connecting the potentials measured in PBS with the particle size of the hydroxyapatite materials, suggesting that it may be possible to tune the zeta potential through varying the size of the particles. Visual representations of these relationships are presented in **Figure 4.7**. It should be noted, however, that the standard deviation in the size of the particles are large, which means that caution needs to be applied in drawing conclusions from these data.

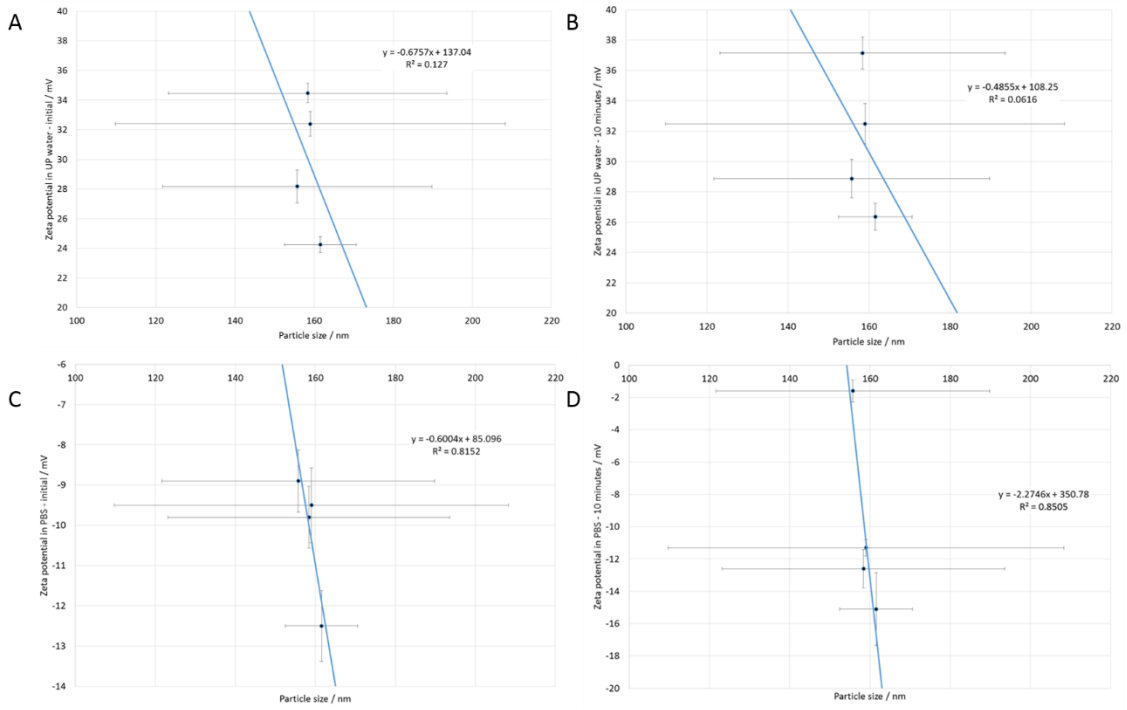

***Figure 4.7:* Graphical representation of the relationships described in Table 4.7; with panels A and B depicting connections between particle size (deduced by SEM analysis) with zeta potential measurements using UP-water and panels C and D with zeta potentials measured using PBS.**

4.4.5 *In Vitro* Experiments

4.4.5.1 Cell Viability

There is very little cytotoxicity recorded following exposure of the RAW264.7 macrophages to the hydroxyapatite nanoparticles (**Figure 4.8**), consistent with the biocompatible nature of this compound. These findings are in agreement with the literature [1]. In all cases, viability is observed to be above 90 %.

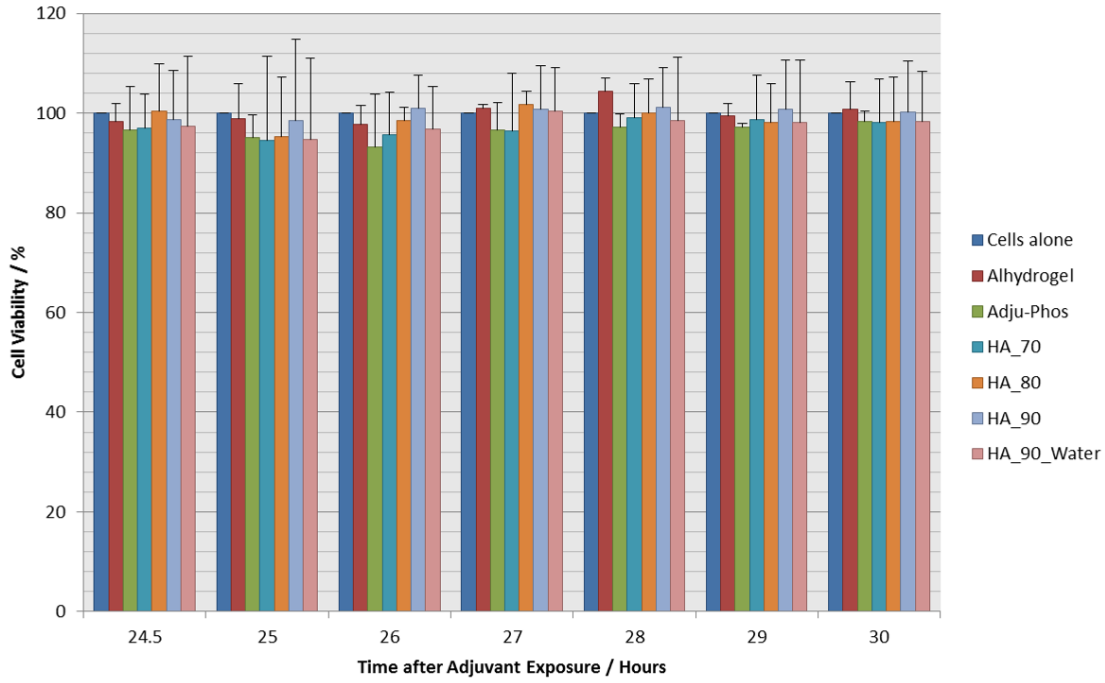

Figure 4.8: ***Cell viability results. RAW264.7 macrophages were exposed to hydroxyapatite particles at 476 µg mL^{-1} for 24 hours. Cells exposed to commercial alums (Alhydrogel and Adju-Phos) were used for comparative purposes and concentrations were the same as those used for hydroxyapatite. Cell viability was quantified by Alamar Blue assays with n=3; each independent experiment contained 9 replicates.***

4.4.5.2 Immunoassay Experiments

Cytokine secretions were quantified by means of an ELISA assay on the cell-free supernatants from the RAW264.7 cells. TNF-α secretion is constant with all the hydroxyapatite samples and there is no apparent impact of phase, size or morphology on this cytokine (**Figure 4.9**). The materials perform approximately on par with the commercial adjuvants, being somewhat more potent than Adju-Phos but less than Alhydrogel.

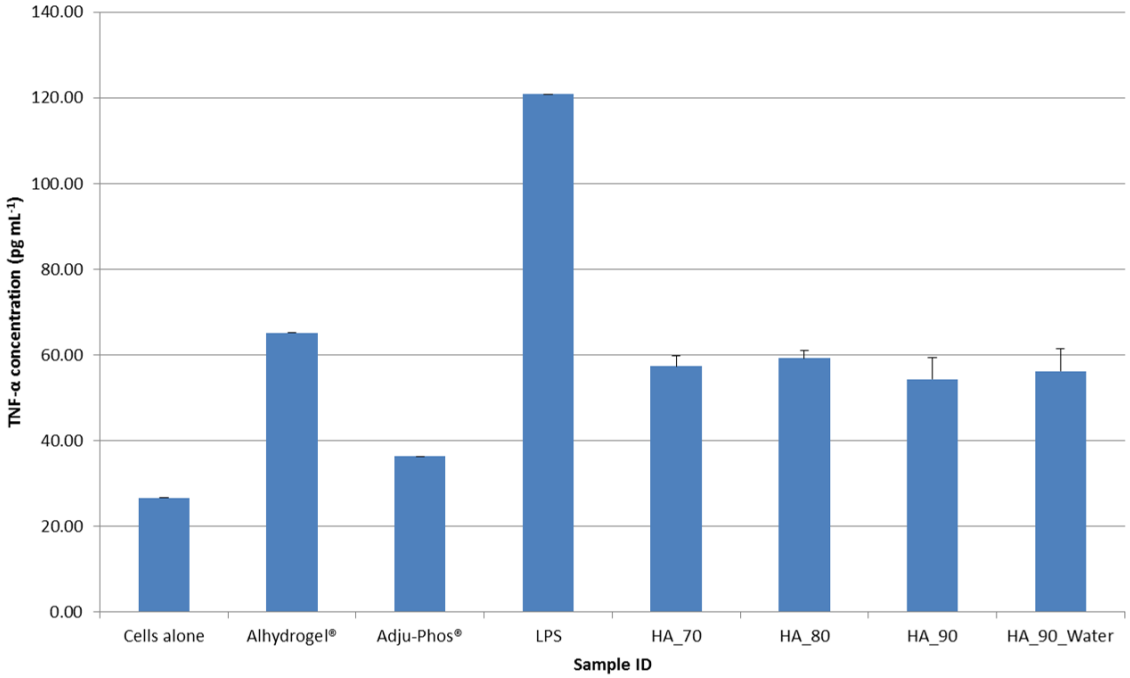

Figure 4.9: ***TNF-α production in response to hydroxyapatite adjuvants. RAW264.7 macrophages were exposed to hydroxyapatite materials at 476 µg mL^{-1} for 24 hours. Cell free supernatants were collected and TNF-α cytokine secretions were quantified*** **via** ***ELISA assays with n=3 and each independent experiment containing 9 replicates. Commercial alums (Alhydrogel and Adju-Phos) were used for comparative purposes and lipopolysaccharide (LPS) was used as a positive control.***

There is evidence of changes in the production of IL-6 by the RAW264.7 cells in response to application of the different hydroxyapatite NPs (**Figure 4.10**). A reduction in IL-6 concentration is seen with an increase in reaction temperature. This outcome may therefore be affected by the morphology of the NPs, which differs with the reaction temperature. The materials prepared at 70 and 80 °C show performance intermediate between the two commercial comparators, while those prepared at 90 °C (both Ca-deficient and non-deficient) are less potent than both.

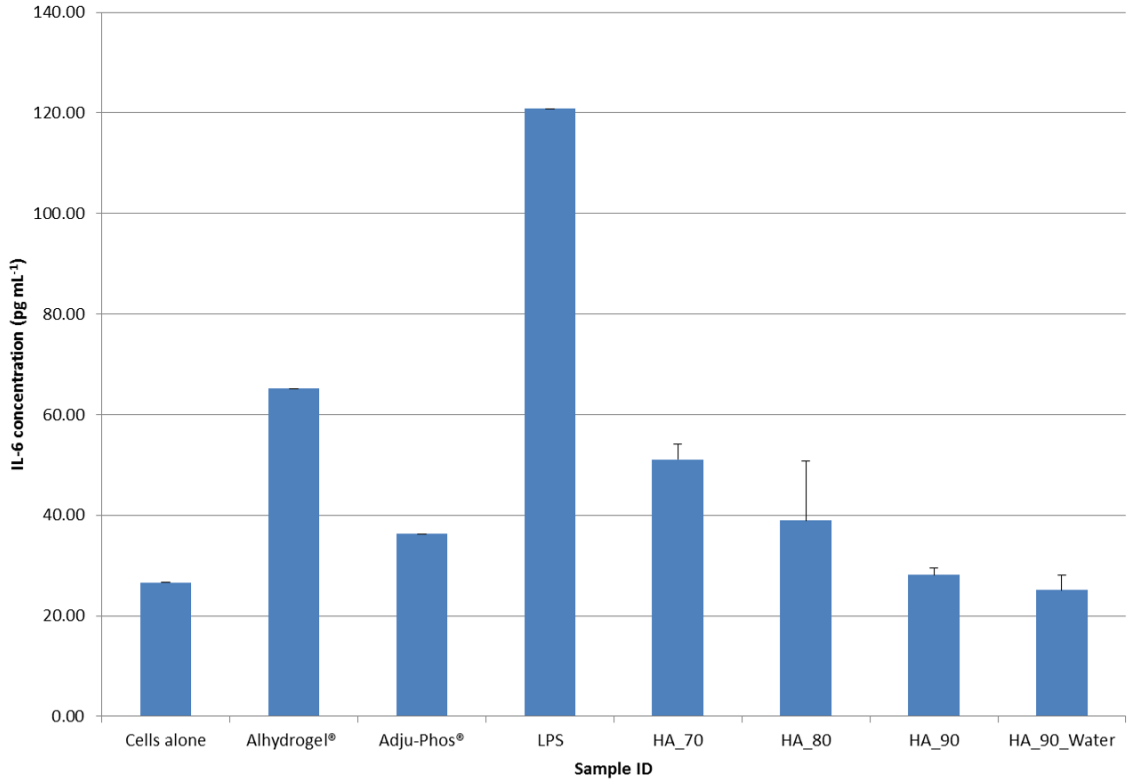

Figure 4.10: ***IL-6 production in response to hydroxyapatite adjuvants. RAW264.7 macrophages were exposed to hydroxyapatite materials at 476 µg mL^{-1} for 24 hours. Cell free supernatants were collected and IL-6 cytokine concentrations were quantified*** **via** ***ELISA assays with n=3 and each independent experiment containing 9 replicates. Commercial alums (Alhydrogel and Adju-Phos) were used for comparative purposes and lipopolysaccharide (LPS) was used as a positive control.***

4.4.5.3 Fluorescent microscopy

All hydroxyapatite materials were labelled with FITC and the RAW264.7 cells with the DAPI nuclear stain, giving rise to green and blue images under the fluorescent microscope, respectively. The four samples' interaction with the RAW cells was investigated with a fluorescent microscope, with images given in **Figure 4.11**.

All the hydroxyapatite materials are rod-like in appearance which suggests that aggregation of the NPs has occurred because their morphology differs from what is observed in the SEM images (**Figure 4.4**); the observed particle size is far greater too. Nevertheless, there is evidence of cellular attachment of the RAW cells to the surface of the samples. Flach and co-workers proposed the concept of lipid membrane disturbances as a possible mechanism of adjuvanticity for alum [19]; the fluorescent micrograph images in **Figure 4.11** are consistent with this theory.

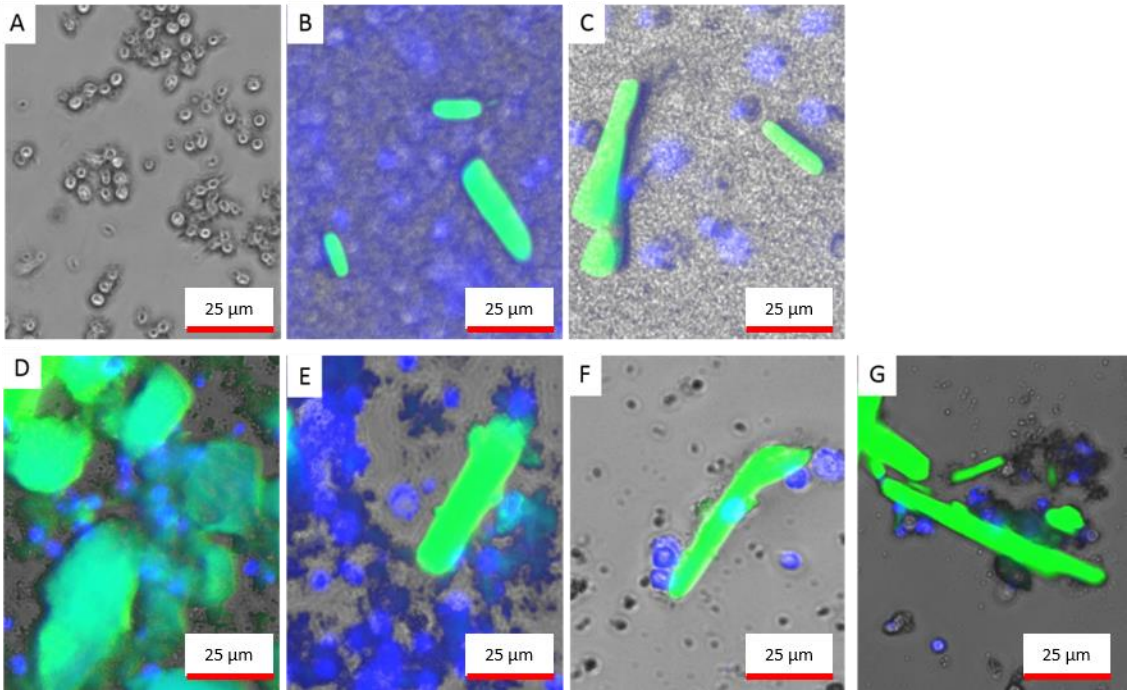

Figure 4.11: ***Fluorescent microscopy with FITC-labelled hydroxyapatite samples (green) with DAPI nuclear staining of RAW264.7 cells (blue); (A) cells alone, (B) Alhydrogel, (C) Adju-Phos, (D) HA_70, (E) HA_80, (F) HA_90; and (G) HA_90_Water.***

Confocal microscopy was undertaken but proved unsuccessful due to the semi-adherent nature of the murine macrophage cell line, meaning that the cells ruptured during the transfer stage from the plate to the microscope slide.

4.4.6 Structure/Property Relationships

Attempts were made to elucidate relationships between the immunological outputs of RAW264.7 macrophages following exposure to hydroxyapatite materials and the physicochemical properties of these samples (**Table 4.8**).

Table 4.8: ***Relationships between physicochemical properties and immunoassay data of the hydroxyapatite materials, with particle size being determined by SEM analysis (nm) and zeta potentials recorded in mV.***

Experimental parameter (x)	Cytokine concentration / pg mL^{-1} (y)	Equation	R^2 correlation
Particle size	TNF-α	y = -0.1073x + 73.801	0.0154
	IL-6	y = -4.226x + 705.86	0.7380
ZP in UP-water	TNF-α	y = -0.0432x + 58.07	0.0090
	IL-6	y = 0.1089x + 32.575	0.0018
ZP in UP-water (10 minutes)	TNF-α	y = -0.1503x + 61.475	0.1156
	IL-6	y = -0.3842x + 47.814	0.0234
ZP in PBS	TNF-α	y = 0.3741x + 60.588	0.0827
	IL-6	y = 5.7163x + 93.987	0.5981
ZP in PBS (10 minutes)	TNF-α	y = 0.1044x + 57.842	0.0886
	IL-6	y = 1.8957x + 55.064	0.9048

The correlation coefficients presented in **Table 4.8** indicate that there are very few relationships between these data, with the majority of the R^2 values not exceeding 0.12. TNF-α production by RAW264.7 cells has no strong relationships with either the particle size or zeta potential; however, the IL-6 concentration appears to be closely related to the zeta potential measurements recorded in PBS (10 minute-time point) with an R^2 value of 0.9048. There is also a slightly weaker trend observed for IL-6 concentrations with the particle size of the hydroxyapatite NPs obtained from SEM analysis, with an R^2 value of 0.7380 (**Table 4.8**). Visual representations of selected relationships are presented in **Figure 4.12**, with all other plots given in the **Appendix 2**.

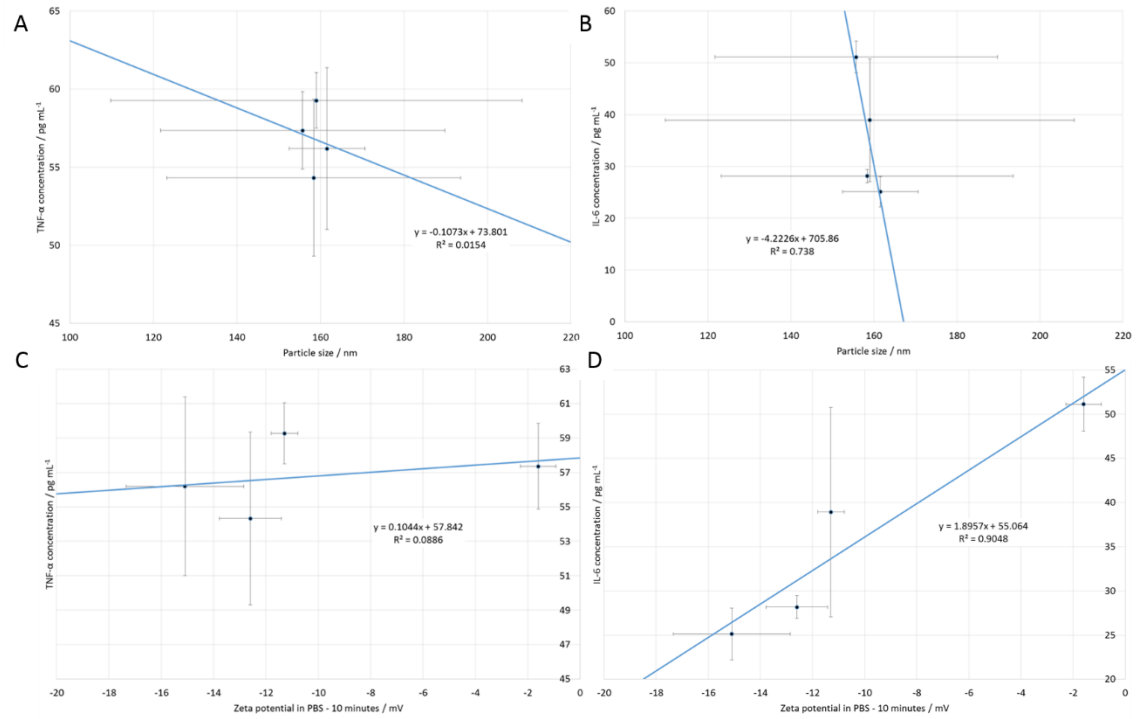

***Figure 4.12:* Graphical representation of relationships between the particle size data and (A) TNF-α and (B) IL-6 cytokine concentrations; together with the analogous relationships between the zeta potential measurements recorded in PBS (10 minute-time point) and (C) TNF-α and (D) IL-6.**

It appears that the PBS zeta potential seems to influence the production of IL-6 from RAW264.7 cells *in vitro*, but all other relationships are unclear given the errors in the data.

In the literature, it is reported that spherical particles of AlO(OH) stimulate weaker immune responses than rod-like particles (in terms of 400 and 1000 pg mL^{-1} production by macrophages, respectively) [20]. The HA_70 material consists solely of spherical nanoparticles and leads to the production of roughly equal amounts of IL-6 and TNF-α (**Figure 4.9** and **Figure 4.10**).

The addition of rod-like hydroxyapatite nanoparticles, obtained through increasing the reaction temperature, results in a decrease in IL-6 output with no change in TNF-α. This trend is different to that described in the literature by Sun *et al.*, who found that rod-like nanoparticles stimulate a greater IL-6 output, suggesting a Th2-type polarisation may be induced [20]. However, Sun explored AlO(OH), and in addition we have mixed populations of mixed particle habits here.

It appears that in the case of hydroxyapatite the introduction of rod-shaped particles leads to a reduction in immunogenicity. This effect is further accentuated in the HA_90_Water sample with a mixture of spherical, rod-like and platelet shaped nanoparticles (**Figure 4.9** and **Figure 4.10**). Thus, from these findings it appears that it is not universally true that rod shaped particles are more potent in their immunogenicity.

4.5 Conclusions

The adapted CPFS reactor provided an easy and reproducible means of synthesising hydroxyapatite. The NPs produced were found to be similar in size, regardless of the temperature used for reaction. However, SEM analysis provided evidence for a degree of particle engineering, in terms of the morphology: as the reaction temperature is increased, there is a change from a single morphology (spheres) to a biphasic mixture (spheres and rods). The solvent used for washing the product was shown to impact the hydroxyapatite phase collected. Deionised water gave rise to pure-phase hydroxyapatite, whilst use of methanol generated a calcium-deficient phase.

Assessment of the cytokine production induced following administration of the samples to RAW264.7 cells indicated that the TNF-α production is constant, regardless of the phase and particle shape. The IL-6 concentrations are found to vary however, indicating the potential to tune the immune response through hydroxyapatite particle engineering.

4.6 References

1. Goto, N., et al., *Studies on the Toxicities of Aluminum Hydroxide and Calcium-Phosphate as Immunological Adjuvants for Vaccines.* Vaccine, 1993. **11**(9): p. 914-918.
2. Goto, N., et al., *Local Tissue Irritating Effects and Adjuvant Activities of Calcium Phosphate and Aluminium Hydroxide with Different Physical Properties.* Vaccine, 1997. **15**(12): p. 1364-1371.
3. Gupta, R.K. and Siber G.R., *Adjuvants for Human Vaccines - Current Status, Problems and Future-Prospects.* Vaccine, 1995. **13**(14): p. 1263-1276.
4. Relyveld, E.H., Henocq E., and Raynaud M., *[Study of the Antidiphtheria Vaccination of Allergic Subjects with a Pure Anatoxin Absorbed on Calcium Phosphate].* Bull World Health Organ, 1964. **30**: p. 321-5.
5. Jiang, D.P., et al., *Structure and Adsorption Properties of Commercial Calcium Phosphate Adjuvant.* Vaccine, 2004. **23**(5): p. 693-698.

6. Lee, D.D. and Aiolova M. *Calcium Phosphate Delivery Vehicle and Adjuvant.* 2012. U.P. Application, US8333996 B2. WO2000015194 A1, US 09/153,133. Grant
7. Anwar, A., *Continuous Plastic Flow Synthesis and Characterization of Nanoscale Bioceramics*, 2014, UCL (University College London), PhD Thesis
8. *Lipid Maps Thawing and Passage Procedure for Raw264.7*. 2004 08/11/2004; 2:[Available from: http://www.lipidmaps.org/protocols/PP0000000100.pdf.
9. Mobasherpour, I., et al., *Synthesis of Nanocrystalline Hydroxyapatite by Using Precipitation Method.* Journal of Alloys and Compounds, 2007. **430**(1–2): p. 330-333.
10. Liu, C., et al., *Kinetics of Hydroxyapatite Precipitation at Ph 10 to 11.* Biomaterials, 2001. **22**(4): p. 301-6.
11. Koumoulidis, G.C., et al., *Preparation of Hydroxyapatite Via Microemulsion Route.* J Colloid Interface Sci, 2003. **259**(2): p. 254-60.
12. Chen, C.-W., et al., *Synthesis, Characterization, and Dispersion Properties of Hydroxyapatite Prepared by Mechanochemical-Hydrothermal Methods.* Journal of Materials Chemistry, 2004. **14**(15): p. 2425-2432.
13. Sudarsan.K and Young R.A., *Significant Precision in Crystal Structural Details - Holly Springs Hydroxyapatite.* Acta Crystallographica Section B-Structural Crystallography and Crystal Chemistry, 1969. **B 25**: p. 1534-&.
14. Guo, H., et al., *Biocompatibility and Osteogenicity of Degradable Ca-Deficient Hydroxyapatite Scaffolds from Calcium Phosphate Cement for Bone Tissue Engineering.* Acta Biomaterialia, 2009. **5**(1): p. 268-78.
15. Destainville, A., et al., *Synthesis, Characterization and Thermal Behavior of Apatitic Tricalcium Phosphate.* Materials Chemistry and Physics, 2003. **80**(1): p. 269-277.
16. Ślósarczyk, A., et al., *The Ftir Spectroscopy and Qxrd Studies of Calcium Phosphate Based Materials Produced from the Powder Precursors with Different Cap Ratios.* Ceramics International, 1997. **23**(4): p. 297-304.
17. Sing, K.S., *Reporting Physisorption Data for Gas/Solid Systems with Special Reference to the Determination of Surface Area and Porosity (Recommendations 1984).* Pure and Applied Chemistry, 1985. **57**(4): p. 603-619.
18. Malvern, *Zeta Potential Theory, in Zetasizer Nano Series User Manual - Man0317 Issue 1.1*. 2013, Malvern Instruments Ltd: Worcestershire, England. p. 15.2.
19. Flach, T.L., et al., *Alum Interaction with Dendritic Cell Membrane Lipids Is Essential for Its Adjuvanticity.* Nature Medicine, 2011. **17**(4): p. 479-U121.
20. Sun, B.B., et al., *Engineering an Effective Immune Adjuvant by Designed Control of Shape and Crystallinity of Aluminum Oxyhydroxide Nanoparticles.* ACS Nano, 2013. **7**(12): p. 10834-10849.

Chapter 5 : Particle Engineering of Zinc Oxide Nanoparticles

5.1 Introduction

Zinc oxide (ZnO) is a non-toxic entity commonly used as a dietary supplement [1]. There is a small body of literature in which ZnO nanoparticles have been explored as potential adjuvants. Work by Matsumura and colleagues involved inoculating BDA/1J mice with the model antigen ovalbumin (OVA) and 1 – 3 mg of ZnO, before the animals were sacrificed 21 days post-immunisation [2]. Exposure to ZnO significantly increased the production of both anti-OVA IgG1 and IgE antibodies, compared with the mouse subjects dosed with phosphate buffered saline (PBS) alone. The highest dose of ZnO (3 mg) saw an increase in OVA-specific splenocyte proliferation, coupled with elevated cytokine release profiles of IL-4, IL-5 and IL-17. However, no increases in either IgG2a or IFN-γ were observed. The authors concluded that ZnO provokes a Th2-type response which was found to be on par with that of the Imject alum used as a control. However, it is important to note that Imject alum is not identical to the alum adjuvant used in clinical vaccines [3]. Therefore, how ZnO compares with clinically-used alums adjuvants remains unknown. Matsumura hypothesised that some dissolution of the particles may have occurred, resulting in free zinc (II) cations being present; this has previously been reported to stimulate interleukin-4 (IL-4) production by T-cells [4].

A second study immunised BALB/c mice with OVA and ZnO nanoparticles (of < 50 nm in size) [1]. The conclusions drawn from the data were largely in agreement with those of Matsumura *et al*. [2], with anti-OVA IgG1 and IgE antibody titres being significantly increased following co-administration of ZnO and OVA. The splenocyte studies in this work revealed an increase in IL-2, IL-4, IL-6 and IL-17, whilst the production of both IL-10 and TNF-α declined. These data support ZnO adjuvant materials as being inducers of Th2-type responses.

There exists also some work where continuous hydrothermal syntheses of zinc oxide particles have been undertaken. Work by Ohara *et al.* describes a system whereby a solution of $Zn(NO_3)_2 \cdot 6H_2O$ mixes with supercritical water. A potassium hydroxide feed acts as a quench, and this system resulted in the generation of nanorods with average diameter of 150 nm and length 600 nm [5].

The key objective of the work described here was to synthesise ZnO particles of varying shape and size, then assess their immunological impact *in vitro*. By providing a better understanding of the parameters controlling the size of ZnO NPs, there are expected to be other benefits for the use of these materials in other applications such as sunscreen and paints.

5.2 Materials and Methods

5.2.1 Reactor Design for Continuous Hydrothermal Flow Synthesis of Nanoparticles

Three identical diaphragm pumps (Milton Roy, Primeroyal K, Pont Saint-Pierre, France) were used simultaneously, providing three pressurised feeds at 240 bar: 0.20 M zinc nitrate hexahydrate solution at a flow rate of 40 mL min^{-1} (P1; in **Figure 5.1.A**), 0.40 M potassium hydroxide solution at a flow rate of 40 mL min^{-1} (P2) and deionised water at a flow rate of 80 mL min^{-1} (P3).

The flow of zinc nitrate hexahydrate was heated to 450 °C using a bespoke 7 kW electrical heater, with specific design details described by Gruar *et al.* [6]. This hot stream was mixed with the flow of potassium hydroxide at room temperature in a confined jet mixer (**Figure 5.1B**) where the nanoparticles were formed. A deionised water quench was used and a second mixer was added between the confined jet mixer and the heat exchanger (depicted in the upper portion of **Figure 5.1B**).

In the second mixer, the hot nanoparticle slurry from the confined jet mixer entered the inner pipe and deionised water at room temperature flowed up through the outer annulus at 80 mL min^{-1}. This diluted the ZnO nanoparticle slurry, which as a result was rapidly cooled to *ca*. 100 °C prior to further cooling to room temperature in the counter-current heat exchanger.

In further syntheses, small amounts of aqueous Ti(II) were added to the Zn nitrate solution in order to obtain control of particle size, with mixed solutions made up at final concentrations of 0.02 and 0.06 M Ti(II) and 0.18 and 0.14 M Zn nitrate respectively. All samples were synthesised by Dr Alistair Holdsworth.[i]

The white, solid product was then recovered by centrifugation (4500 rpm for 5 minutes) and washed with copious amounts of deionised water. Sequential rounds of washing and centrifugation were performed until the conductivity of the supernatant water was reduced to a value less than 50 S m^{-1}. The washed product was freeze-dried in a Vitris Genesis 35XL Freeze Drier (SP Scientific) by first freezing to -40 °C followed by treatment at -60 °C for approximately 24 hours at 70-80 mTorr.

[i] The precise details of the Ti(II) salt used are confidential to Croda

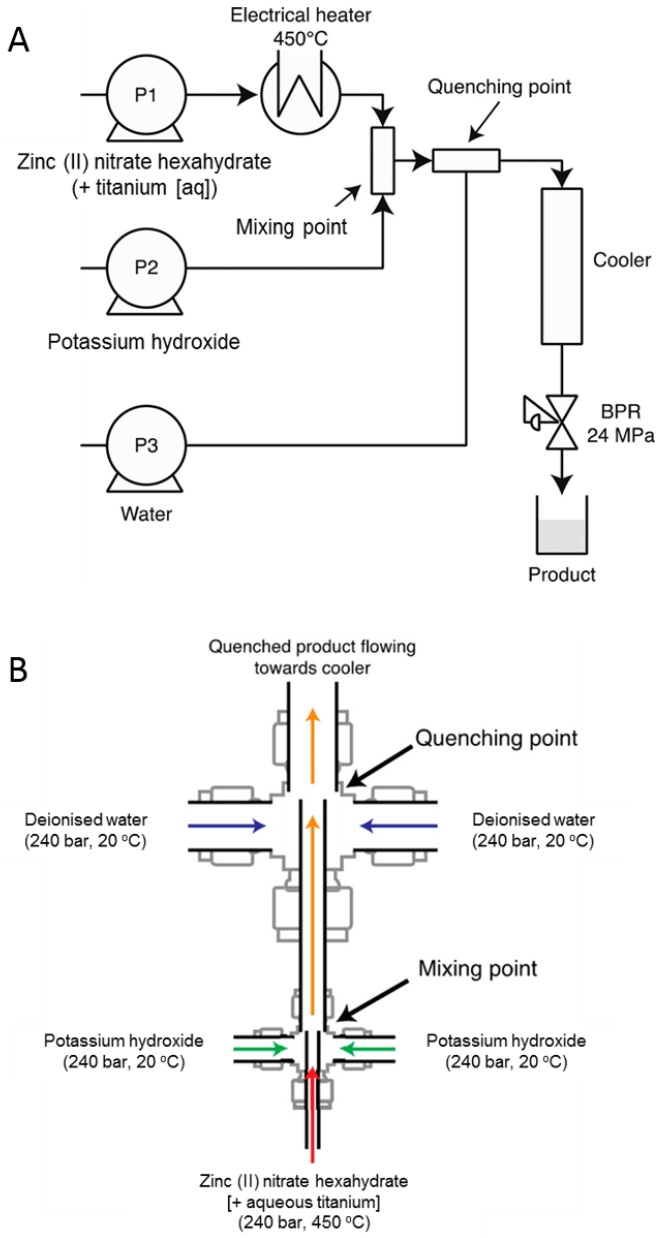

Figure 5.1: *(A) Simplified diagram of the CHFS process and (B) a diagram of the confined jet mixer for nanoparticle formation at mixing-point (lower part) with a downstream quench (upper part).*

5.3 Materials Characterisation

5.3.1 Powder X-ray Diffraction

See **Section 3.3.1**.

5.3.2 Scanning Electron Microscopy

See **Section 3.3.2**.

5.3.3 Fourier Transform Infra-Red Spectroscopy

See **Section 3.3.3**.

5.3.4 Surface Area and Pore Volume Analysis

See **Section 4.3.4**.

5.3.5 Zeta Potential Measurements

See **Section 3.3.6**.

5.3.6 Immunoassay Experiments

See **Section 3.3.7**.

5.3.6.1 Alamar Blue Assay

See **Section 3.3.7.1**.

5.3.6.2 Enzyme-Linked Immuno-Sorbent Assay

See **Section 3.3.7.2**.

5.3.6.3 Fluorescence and Confocal Microscopy

See **Section 3.3.7.3**.

5.4 Results and Discussion

5.4.1 Continuous Hydrothermal Flow Synthesis of Zinc Oxide

The reaction conditions for synthesis of the ZnO materials are presented in **Table 5.1**. Two of the three product slurries were acidic, whilst the product with the highest aqueous titanium content had a weakly alkaline pH.

Table 5.1: ***CHFS reaction conditions for the synthesis of different zinc oxide nanoparticles, P denotes pump, with P1 pumping deionised water, P2 pumping the zinc precursor Ti(II) salt solution (for Medium- and Small-ZnO reactions only) and P3 pumping the precipitating agent.***

	P1	P2			P3		Conditions		
Sample ID	Flow rate / mL min^{-1}	[$Zn(NO_3)_2{\cdot}xH_2O$] / M	[$Ti_{(aq)}$] / M	Flow rate / mL min^{-1}	[KOH] / M	Flow rate / mL min^{-1}	Reaction temperature / °C	Output temperature / °C	Output pH
Large ZnO	80	0.20	0.00	40	0.40	40	450	36	5.7
Medium ZnO	80	0.18	0.02	40	0.40	40	450	35	6.3
Small ZnO	80	0.14	0.06	40	0.40	40	450	36	8.7

5.4.2 Characterisation

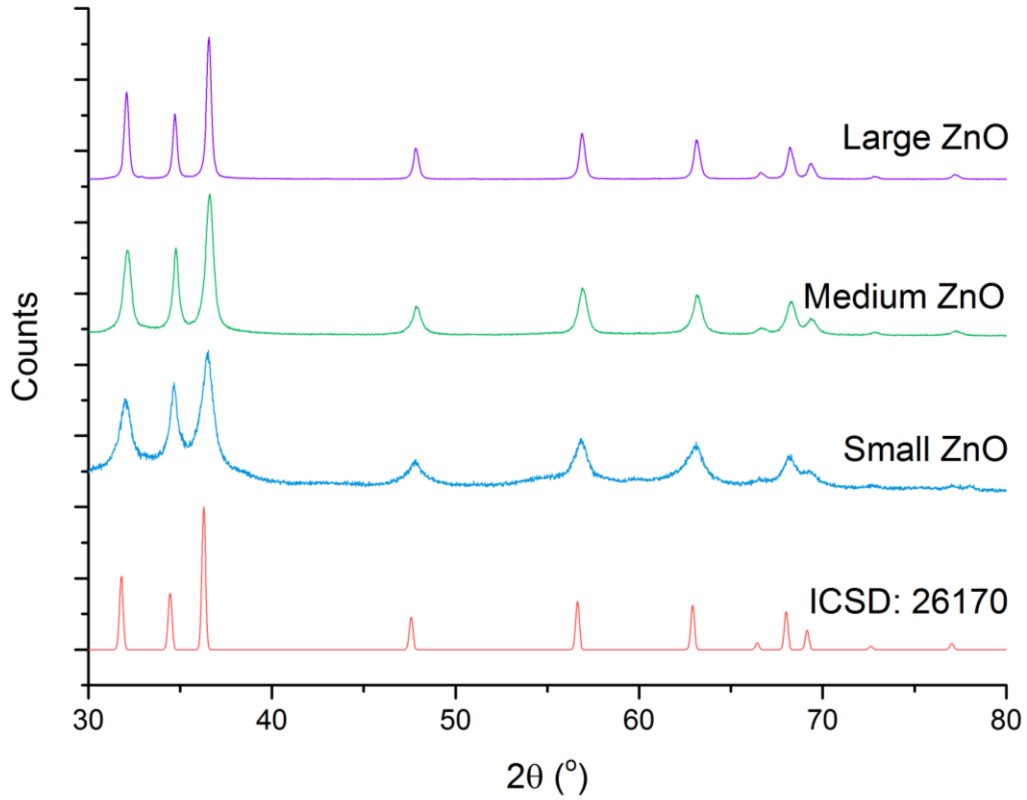

Figure 5.2: ***Panel displaying the P-XRD patterns obtained for the three zinc oxide samples to confirm their identity against the published wurtzite reference pattern (ICSD: 26170, [8]).***

P-XRD patterns of the samples are shown in **Figure 5.2**. All detectable reflections can be assigned by their positions in those present in the published pattern for the wurtzite polymorph of ZnO [8]. No peaks were observed belonging to impurities. All samples are highly crystalline and the reflections observed increase in broadness as increasing concentrations of Ti(II) are employed. This arises because the size of the crystallite decreases (**Table 5.2**).

Table 5.2: ***Crystallite size data calculated using the Scherrer equation with K = 1, given as mean ± standard deviation.***

Sample ID	Mean crystallite size / nm
Large ZnO	28.96 ± 4.02
Medium ZnO	18.98 ± 1.52
Small ZnO	11.70 ± 1.29

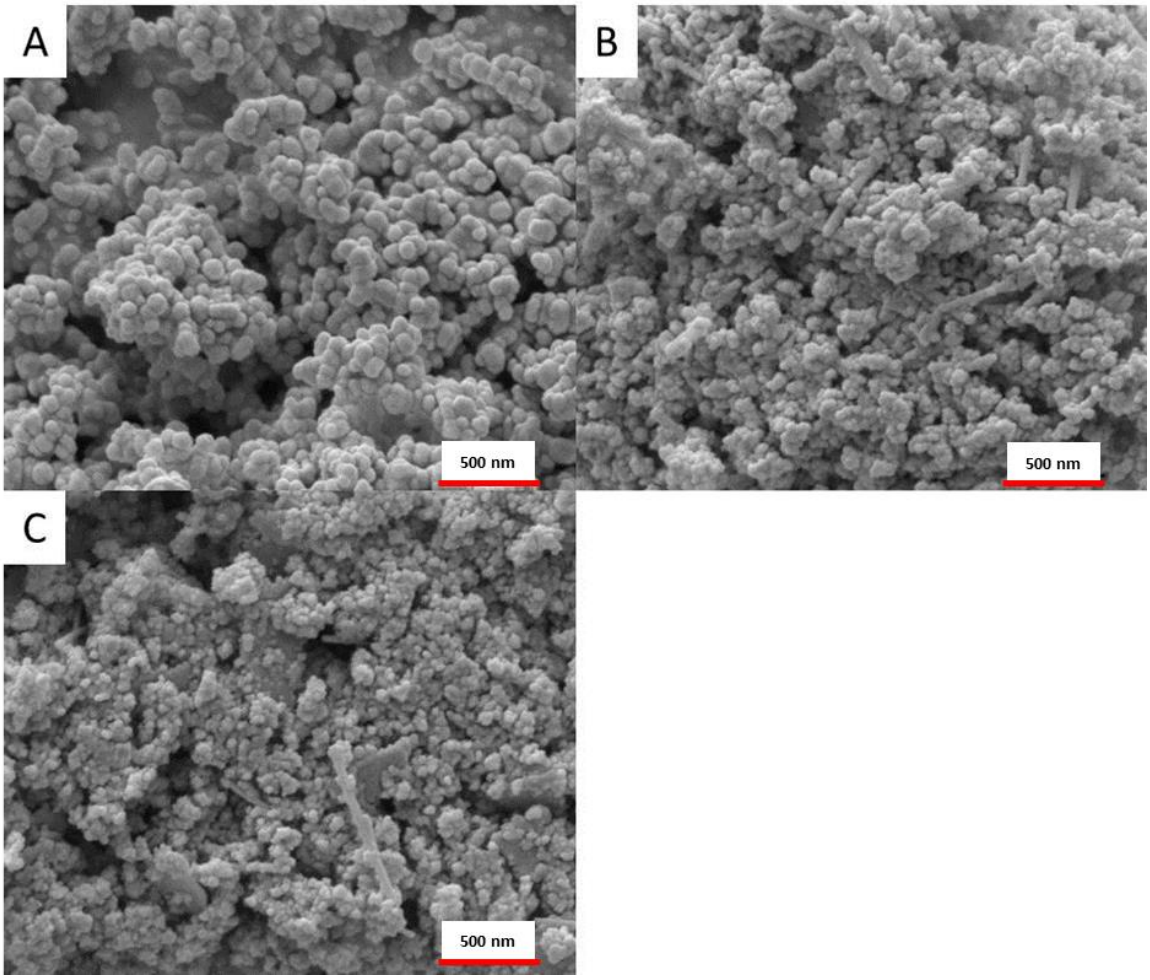

Figure 5.3: ***SEM images of the zinc oxide nanoparticles; (A) Large ZnO, (B) Medium ZnO and (C) Small ZnO.***

SEM images (**Figure 5.3**) revealed different shaped nanoparticles with varied sizes are produced with changes in the amount of Ti(II) added to the reaction. Samples with larger particles consisted solely of spherical nanoparticles, as shown in **Figure 5.3A**, whilst the samples with smaller particles were composed of mixed morphologies, as depicted in **Figure 5.3B, C**. Increasing the Ti concentration causes not only the production of smaller spherical nanoparticles, but also the formation of microparticles of different morphologies – platelets and rods – as summarised in **Table 5.3**.

***Table 5.3:** Mean particle size - categorised into morphology type - calculated from SEM analysis; mean ± standard deviation, both measured in nm. Measurements for rod-like particles are the length of the rod.*

	Particle size (in nm) for each ZnO Morphology		
Sample ID	●	□	⬣
Large ZnO	89.75 ± 24.85	-	-
Medium ZnO	46.18 ± 9.48	291.33 ± 86.21	-
Small ZnO	42.09 ± 9.04	359.05 ± 258.74	423.21 ± 104.33

FTIR analysis was performed on each of the samples (see **Figure 5.4**). While the P-XRD data clearly show the presence of phase-pure ZnO, the IR data are more complex. The broad peaks at *ca*. 3100-3500 cm^{-1} are attributed to the stretching modes of hydroxyl groups [9, 10], believed to arise from the presence of water, KOH or $Ti(OH)_2$ within the sample. The split peak *ca*. 2950 cm^{-1} is assigned to the bending modes of M-OH [9]. The sharp peaks at *ca*. 1740 and 1390 cm^{-1} are attributed to the carbon dioxide absorption in water molecules and M-OH modes, respectively. It should be noted that the transmission percentages are all very high (> 95 %), and thus we believe that we are simply observing small amounts of impurities in the samples here. Furthermore, the band spanning 980 – 650 cm^{-1} represents the vibrational modes of M-O bonds [9].

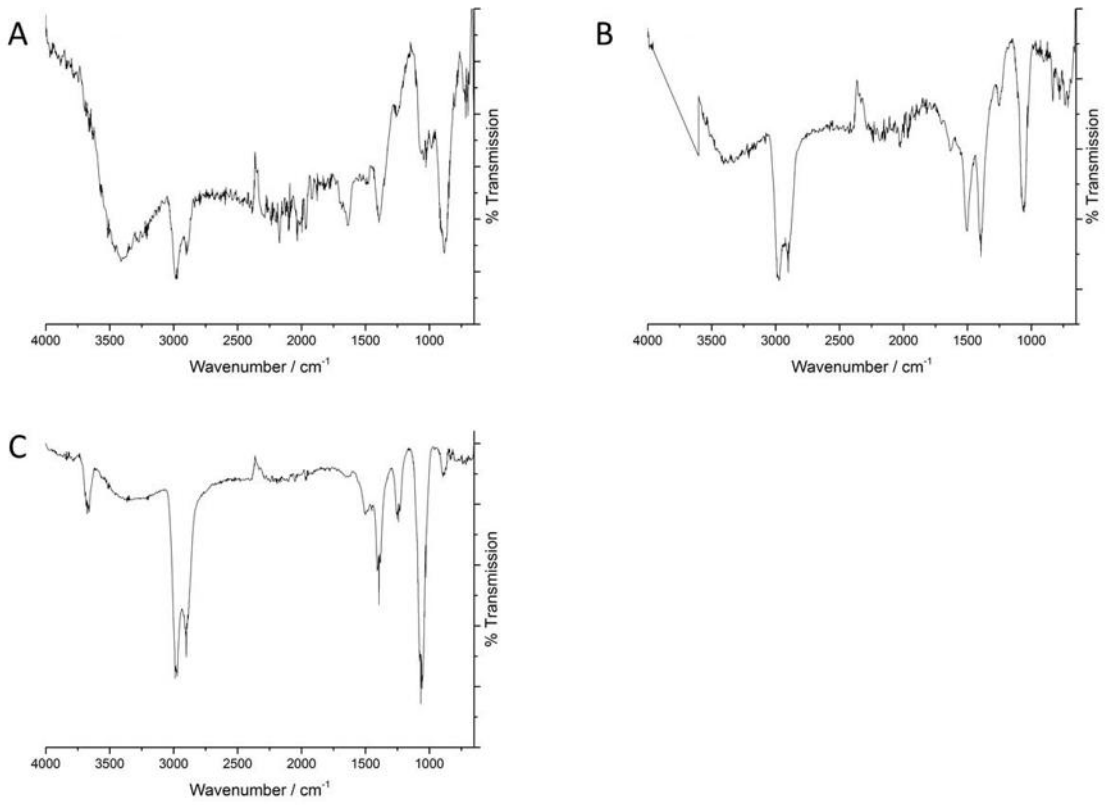

Figure 5.4: ***FTIR spectra obtained for (A) Large-ZnO, (B) Medium-ZnO and (C) Small-ZnO materials; with all percentage transmission values > 95%, so very little absorption by the ZnO NPs is occurring.***

5.4.3 Surface Area and Pore Volume

Surface area and pore volume analyses were completed for each of the three ZnO-NP samples, with the adsorption isotherms presented in **Figure 5.5**. In all cases, the samples were dried at 100 °C prior to analysis under vacuum.

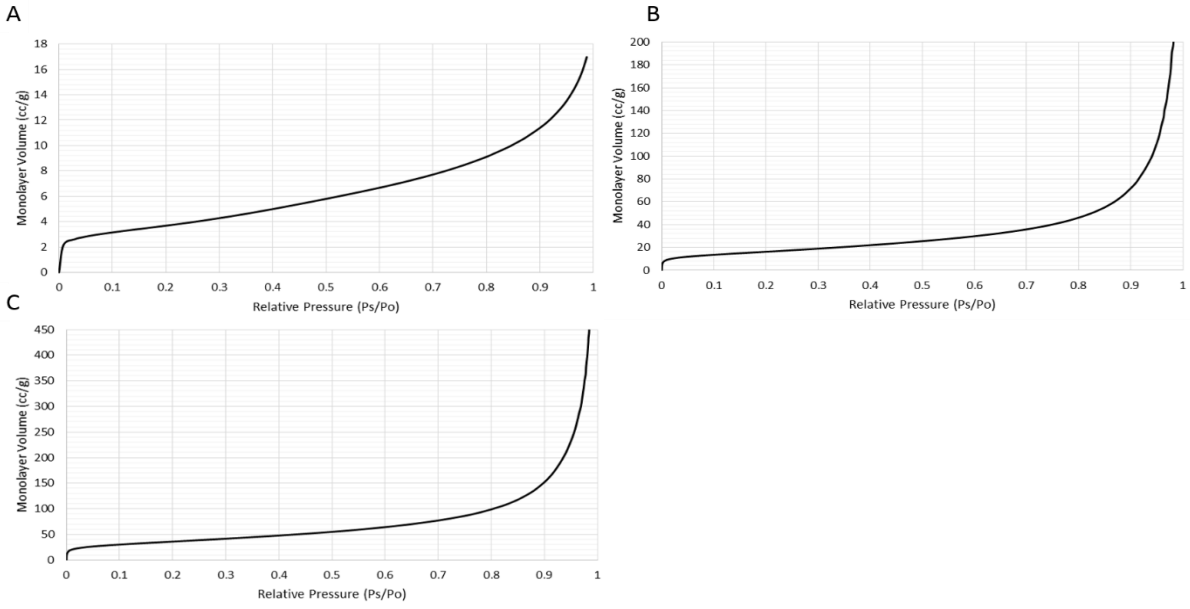

Figure 5.5: **Adsorption Isotherms of the three zinc oxide materials, (A) Large ZnO, (B) Medium ZnO, and (C) Small ZnO.**

Following the IUPAC isotherm classifications, these systems are all Type II, indicating that the samples are non-porous structures [11]. The plateau within the curves means that a monolayer was formed during this phase of the analysis. Surface area and pore volume data for the three ZnO materials are presented in **Table 5.4**.

Table 5.4: Surface area and pore volume data.

Sample ID	Surface Area / $m^2 g^{-1}$	Pore Volume / $mL g^{-1}$
Large ZnO	12.259	0.0269
Medium ZnO	51.363	0.3835
Small ZnO	115.08	0.9122

The data in **Table 5.4** demonstrate that a decrease in the size of the nanoparticles causes an increase in the surface area of the ZnO materials, as would be expected.

5.4.4 Zeta Potential Measurements

Zeta potential measurements were obtained using two different dispersants, ultrapure water (**Table 5.5**) and phosphate-buffered saline solution (PBS, **Table 5.6**).

Table 5.5: Zeta potential measurements for the three ZnO materials when dispersed in UP-water with conductivity of 18.2 mΩ; mean ± standard deviation.

Sample ID	Initial ZP / mV	ZP after 10 minutes / mV
Large ZnO	-3.27 ± 0.31	-2.97 ± 0.22
Medium ZnO	6.77 ± 0.37	6.13 ± 0.62
Small ZnO	-6.12 ± 2.53	-1.37 ± 0.31

Table 5.6: Mean zeta potential measurements for the three ZnO materials when dispersed in 0.01 M phosphate-buffered saline (PBS) solution at pH 7.4; mean ± standard deviation.

Sample ID	Initial ZP / mV	ZP after 10 minutes / mV
Large ZnO	-30.3 ± 1.95	-32.3 ± 1.14
Medium ZnO	-23.6 ± 1.47	-28.4 ± 2.19
Small ZnO	-28.8 ± 1.35	-27.6 ± 1.52

The zeta potential values in water are all close to zero. All zeta potential measurements recorded using PBS as the dispersant showed strongly negative values owing to the presence of phosphate anions which can adsorb to the surface of the ZnO materials.

Attempts were made to elucidate relationships between the sample size of the ZnO NPs and their zeta potential measurements; the results of these are detailed in **Table 5.7**.

Table 5.7: ***Relationships between zeta potential measurements and experimental properties of the ZnO materials.***

Experimental parameter / µm (x)	Zeta potential / mV (y)	Equation	R^2 correlation
Particle size	**ZP in UP-water**	y = -0.0595x + 2.6544	0.0538
	ZP in UP-water (10 minutes)	y = -0.1395x + 9.7857	0.6551
	ZP in PBS	y = -0.0817x – 22.717	0.3769
	ZP in PBS (10 minutes)	y = -0.0949x – 23.803	0.9932

For both dispersants, there appeared to be no apparent relationships between the data obtained from the initial zeta potential measurements and the particle size of the ZnO NPs, with R^2 values of 0.0538 and 0.3769 for UP-water and PBS, respectively (**Table 5.7**). For potentials measured at the 10 minute time point, there is a clear structure/property relationship linking the zeta potential in PBS with the particle size of the ZnO materials. Therefore, this suggests that the zeta potential may be tuned by varying the size of the ZnO NPs (R^2 value of 0.9932; **Table 5.7**). Visual representations of these are presented in **Figure 5.6**.

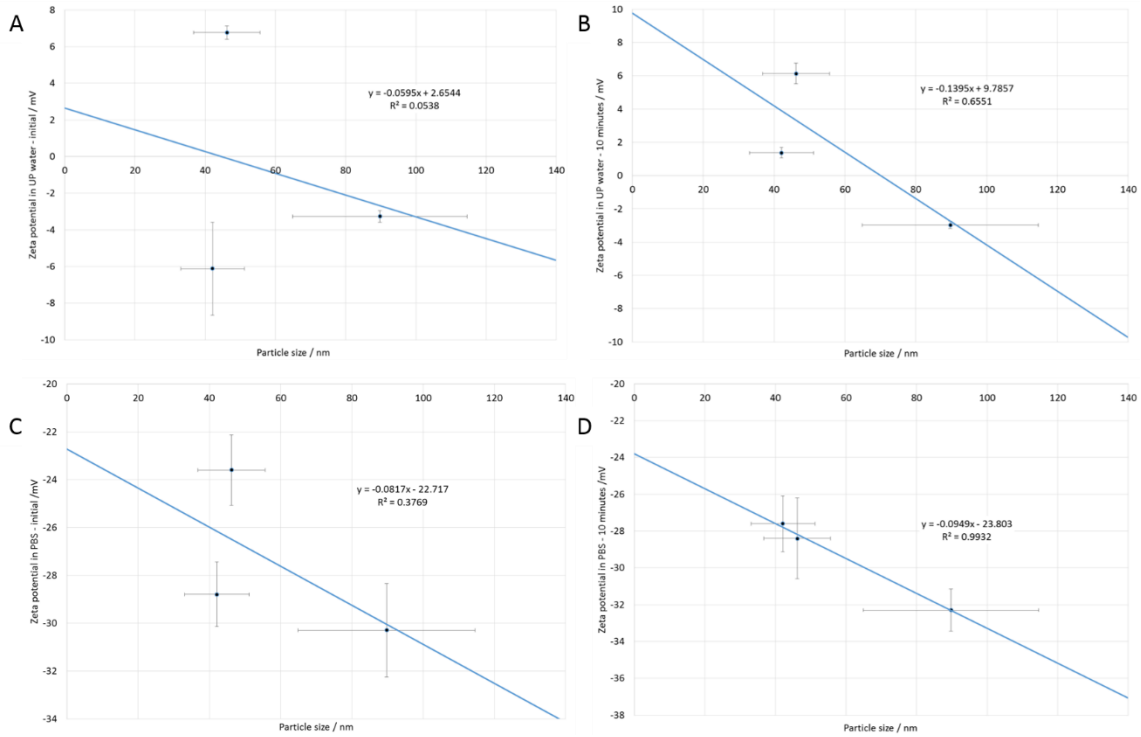

Figure 5.6: ***Graphical representation of the relationships described in Table 5.7, with panels A and B depicting connections between particle size (deduced by SEM analysis) with zeta potential measurements using UP-water and panels C and D those with zeta potentials measured in PBS.***

5.5 *In vitro* Experiments

5.5.1 Cell Viability

Cell viability data are given in **Figure 5.7**. In general, viability is high at all time points studied, at > 90 %. The viability at times below 27h is slightly lower than that after this time, which may be attributed to the doubling time of the RAW264.7 cells [12]. As a result, the cell count appears to diminish during the mitotic stages of cell division but the viability level is restored in the following hour. It appears that the adjuvant causes a temporary reduction in cell numbers, but these recover within an hour.

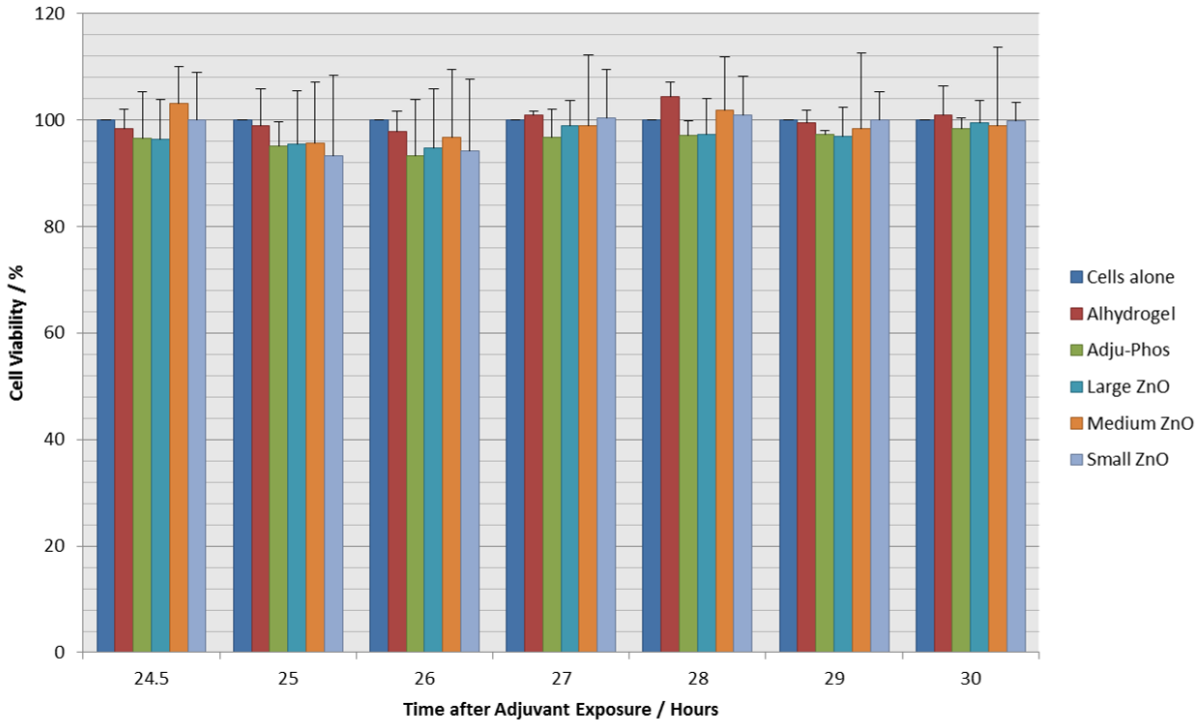

***Figure 5.7:* Cell viability results. RAW264.7 macrophages were exposed to ZnO nanoparticles at 476 µg mL^{-1} in PBS for 24 hours. Cells exposed to commercial alums (Alhydrogel® and Adju-Phos®) were used for comparative purposes. Cell viability was quantified by Alamar Blue assays with n = 3 and each individual experiment containing nine replicates.**

5.5.2 Immunoassay Experiments

Cytokine secretions were quantified by ELISA assays on the cell-free supernatants collected following a 24-hour exposure to the ZnO samples. TNF-α secretions are largely constant for all three ZnO materials, and there is no significant impact of the particle size or morphology on the production of this cytokine by RAW264.7 cells (**Figure 5.8**). That said, there appears to be a small decrease in TNF-α production as the particle size increases. The ZnO NPs give very similar results to the commercially used Alhydrogel adjuvant.

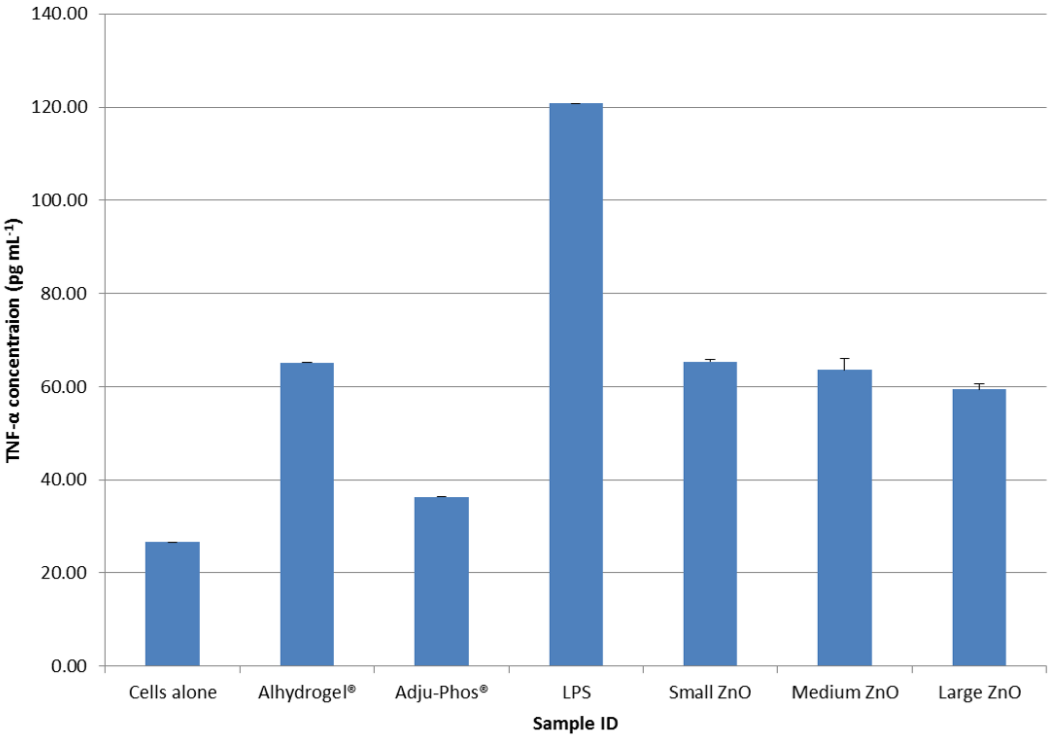

Figure 5.8: ***TNF-α production in response to ZnO adjuvants. RAW264.7 macrophages were exposed to ZnO nanoparticles or commercial adjuvants at 476 µg mL^{-1} for 24 hours, with lipopolysaccharide (LPS) used as a positive control. Cell-free supernatants were collected after this initial exposure period and the TNF-α cytokine secretions were quantified by ELISA assays with n = 3 and each individual experiments contained nine replicates.***

In contrast, there is evidence of distinct changes in the production of IL-6 induced by the RAW264.7 cells (**Figure 5.9**), with larger particles inducing much greater amounts of this cytokine. The concentration of IL-6 is similar to the concentration of TNF-α for both Small- and Medium-ZnO samples. However, for the Large-ZnO material, approximately 60 pg mL^{-1} of TNF-α is produced following exposure of RAW cells to this adjuvant candidate, whilst *ca.* 150 pg mL^{-1} IL-6 is secreted. The dominant cytokine for this material is IL-6, which suggests that the Large-ZnO might induce a Th2-type immune response, consistent with what has been reported in the literature for ZnO materials [1, 2]. This trend has also been postulated for AlO(OH) particles [13]. While the small and medium samples lead to the production of similar amounts of IL-6 to the commercial Alhydrogel, the large sample generates considerably more, and more even than the LPS positive control.

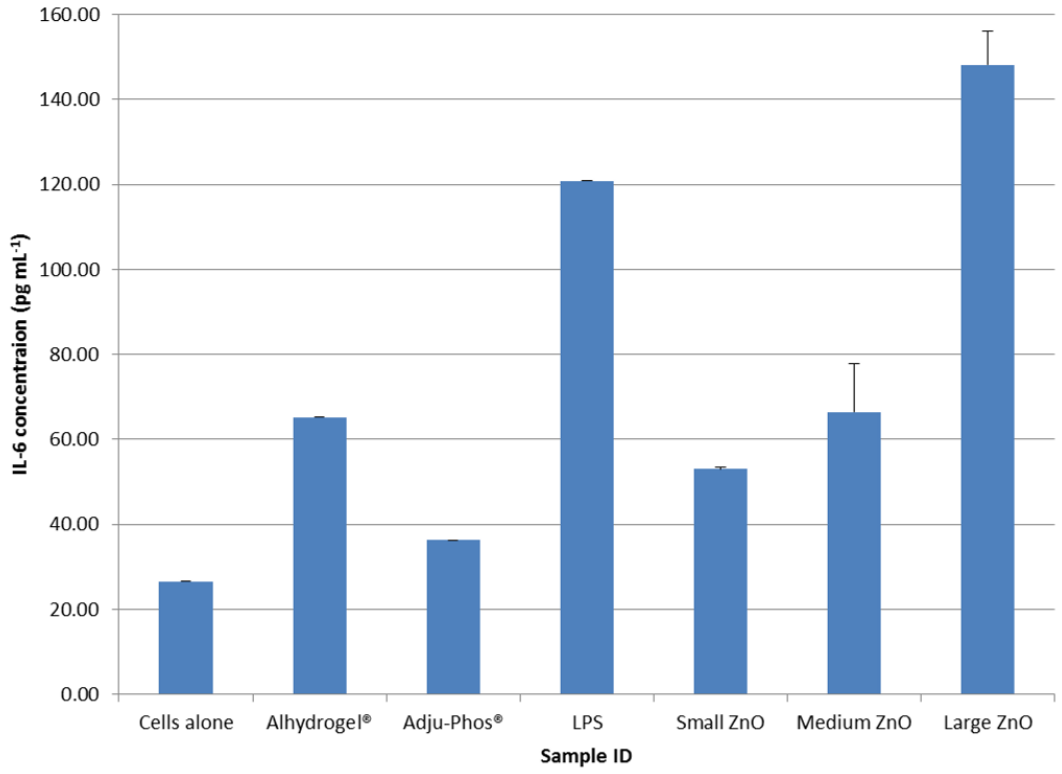

***Figure 5.9:* IL-6 production in response to ZnO adjuvants. RAW264.7 macrophages were exposed to ZnO nanoparticles or commercial adjuvants at 476 µg mL^{-1} for 24 hours, with lipopolysaccharide (LPS) being used as a positive control. Cell-free supernatants were collected after this initial exposure period and the IL-6 cytokine secretions were quantified by ELISA assays with n = 3 and each individual experiments contained nine replicates.**

5.5.3 Fluorescent Microscopy

All ZnO materials were labelled with FITC and the RAW264.7 cells with the DAPI nuclear stain giving rise to green and blue images under the fluorescent microscope, respectively. The three samples' interaction with the murine macrophages was investigated, with images presented in **Figure 5.10**. The ZnO materials appear to exhibit spherical and rod-like morphologies (**Figure 5.10**) with ZnO NPs appearing to have aggregated to form larger structures *in vitro*.

There is evidence of cellular attachment of the RAW264.7 macrophages to the surface of the ZnO materials (**Figure 5.10**). There are various proposed routes by which alum adjuvants function with one theory suggesting that disturbances of the cells' lipid membrane may evoke immunogenicity [14]; the interactions observed in **Figure 5.10** suggest the ZnO samples may also function *via* this mechanism.

Confocal microscopy was undertaken but proved unsuccessful due to the semi-adherent nature of the murine macrophage cell line meaning that the cells ruptured during the transfer stage from the transwell plate, to the microscope slide.

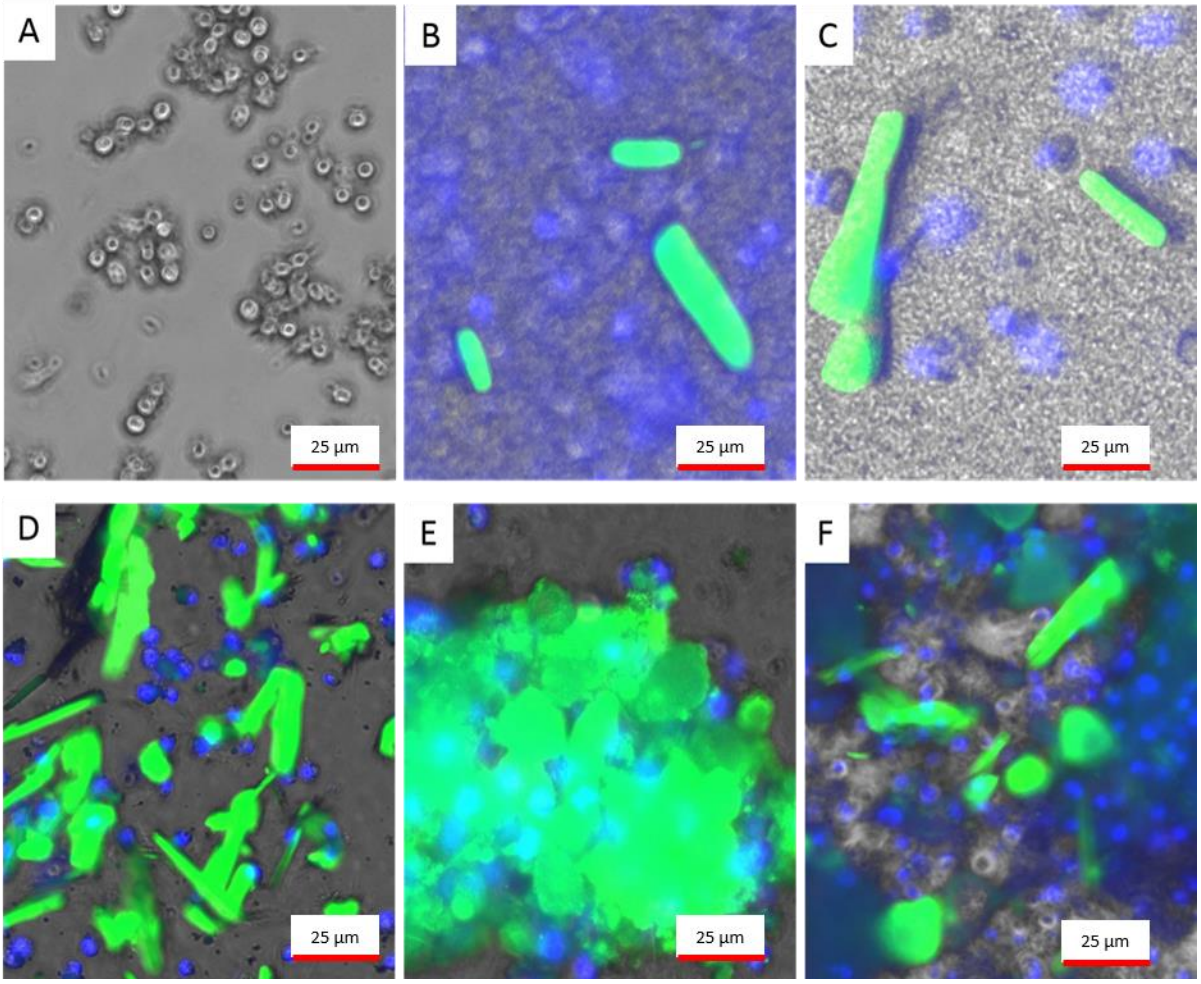

Figure 5.10: ***Fluorescent microscopy with FITC-labelled zinc oxide nanoparticles and DAPI nuclear staining of the RAW264.7 cells; (A) cells alone, (B) Alhydrogel, (C) Adju-Phos, (D) Large ZnO, (E) Medium ZnO; and (F) Small ZnO.***

5.6 Structure/Property Relationships

Analysis was performed to determine any potential links between the physicochemical properties of the ZnO NPs and their immunological effect on RAW264.7 cells. The results of these are presented in **Table 5.8**. There are strong structure/property relationships connecting the IL-6 output of RAW264.7 cells to either the zeta potential measured in PBS (at 10 minutes) or particle size of the ZnO materials. Similar relationships appear to exist for TNF-α, although the range over which the concentration varies is small. Therefore, it may be possible to tailor the elicited immune response through control of particle size and/or zeta potential (as discussed above in **Section 5.4.4**, these two parameters are themselves highly correlated). Visual representations of these relationships are presented in **Figure 5.11**.

***Table 5.8:* Relationships between experimental parameters and immunoassay data of the ZnO materials; with particle size (nm) being derived by SEM analysis and zeta potential measurements in mV.**

Experimental parameter (x)	Cytokine concentration / pg mL^{-1} (y)	Equation	R^2 correlation
Particle size	TNF-α	y = -0.1138x + 69.526	0.9524
	IL-6	y = 1.9471x – 26.319	0.9973
ZP in UP-water	TNF-α	y = 0.0064x + 62.78	0.0002
	IL-6	y = -1.3751x + 88.024	0.0327
ZP in UP-water (10 minutes)	TNF-α	y = 0.4477x + 62.098	0.4378
	IL-6	y = -8.7986x + 102.51	0.6046
ZP in PBS	TNF-α	y = 0.3729x + 73.081	0.1822
	IL-6	y = -8.3766x – 141.69	0.3270
ZP in PBS (10 minutes)	TNF-α	y = 1.2131x + 98.479	0.9811
	IL-6	y = -20.473x – 513.36	0.9991

In all other cases, no clear relationships can be elucidated (see plots located in **Appendix 3**).

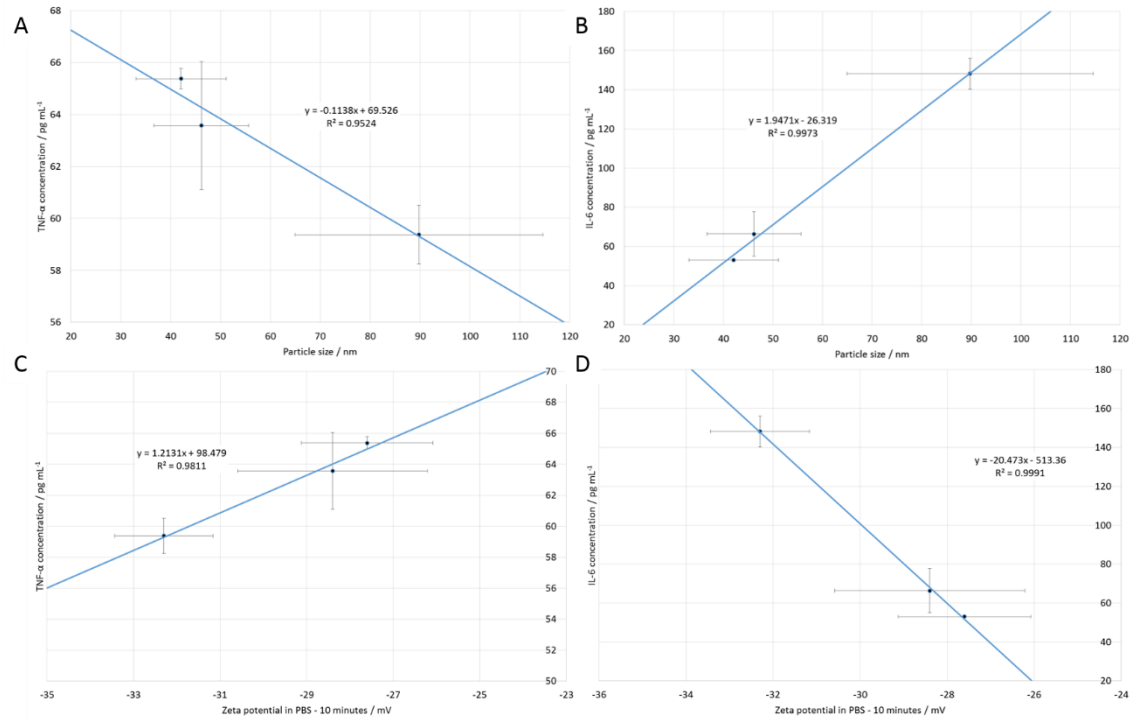

***Figure 5.11:* Graphical representation of the particle size data related to (A) TNF-α and (B) IL-6 cytokine concentrations; and the zeta potential measurements recorded in PBS (10 minute-time point) related with (C) TNF-α and (D) IL-6.**

From the literature, we anticipate Th2-type immune responses to be elicited *in vitro* following administration of ZnO particles [1, 2]. It appears that the samples generated in this work concur with these findings. However, the data presented here suggest that particle size of the ZnO materials can influence the immune response evoked, thus proposing a possible route to tune this towards a Th1-type response through decreasing the size of the nanoparticles (see **Figure 5.9**). In principle, this can be controlled *via* the precursor ratios used in reaction, with an increase in Ti(II) concentration likely to lead to smaller particles.

5.7 Conclusions

The synthesis of zinc oxide by a CHFS process has been studied using varying concentrations of zinc nitrate and aqueous Ti(II). An increase in the Ti(II) concentration is found to lead to a decrease in particle size and a wider range of particle morphologies seen within the sample.

High cell viabilities (> 90%) were observed following exposure to the different ZnO materials, indicating their biocompatibility. Assessment of the production of selected cytokines by ELISA confirmed the particles to be immunogenic. TNF-α production by RAW cells in response to ZnO application is approximately constant regardless of the size or morphology of the sample. However, IL-6 concentrations are profoundly impacted by these changes in the ZnO NPs, with larger particles generating more IL-6. This potentially provides a means of tuning the immune response for this type of adjuvant. Further, the amounts of both TNF-α and IL-6 produced are found to be correlated to the particle size and zeta potential of the NPs, indicating that ZnO NPs may comprise a broad family of immunoactive materials.

5.8 References

1. Roy, R., et al., *Zinc Oxide Nanoparticles Provide an Adjuvant Effect to Ovalbumin Via a Th2 Response in Balb/C Mice.* Int Immunol, 2014. **26**(3): p. 159-72.
2. Matsumura, M., et al., *Adjuvant Effect of Zinc Oxide on Th2 but Not Th1 Immune Responses in Mice.* Immunopharmacology and Immunotoxicology, 2010. **32**(1): p. 56-62.
3. Cain, D.W., et al., *Disparate Adjuvant Properties among Three Formulations of "Alum".* Vaccine, 2013. **31**(4): p. 653-660.
4. Winchurch, R.A., Togo J., and Adler W.H., *Supplemental Zinc (Zn-2+) Restores Antibody-Formation in Cultures of Aged Spleen-Cells .2. Effects on Mediator Production.* Eur J Immunol, 1987. **17**(1): p. 127-132.
5. Ohara, S., et al., *Continuous Production of Fine Zinc Oxide Nanorods by Hydrothermal Synthesis in Supercritical Water.* Journal of Materials Science, 2008. **43**(7): p. 2393-2396.
6. Gruar, R.I., Tighe C.J., and Darr J.A., *Scaling-up a Confined Jet Reactor for the Continuous Hydrothermal Manufacture of Nanomaterials.* Industrial & Engineering Chemistry Research, 2013. **52**(15): p. 5270-5281.
7. *Lipid Maps Thawing and Passage Procedure for Raw264.7*. 2004 08/11/2004; 2:[Available from: http://www.lipidmaps.org/protocols/PP0000000100.pdf.
8. Abrahams, S.C. and Bernstei.Jl, *Remeasurement of Structure of Hexagonal Zno.* Acta Crystallographica Section B-Structural Crystallography and Crystal Chemistry, 1969. **B 25**: p. 1233-&.
9. Gao, Y., et al., *Tio 2 Nanoparticles Prepared Using an Aqueous Peroxotitanate Solution.* Ceramics International, 2004. **30**(7): p. 1365-1368.
10. Sun, T., et al., *Preparation and Antibacterial Properties of Titanium-Doped Zno from Different Zinc Salts.* Nanoscale Res Lett, 2014. **9**(1): p. 98.
11. Sing, K.S., *Reporting Physisorption Data for Gas/Solid Systems with Special Reference to the Determination of Surface Area and Porosity (Recommendations 1984).* Pure and applied chemistry, 1985. **57**(4): p. 603-619.
12. Desimone, J., et al., *Geometrically Engineered Particles and Methods for Modulating Macrophage or Immune Responses*. 2013, Google Patents.
13. Sun, B.B., et al., *Engineering an Effective Immune Adjuvant by Designed Control of Shape and Crystallinity of Aluminum Oxyhydroxide Nanoparticles.* ACS Nano, 2013. **7**(12): p. 10834-10849.

14. Flach, T.L., et al., *Alum Interaction with Dendritic Cell Membrane Lipids Is Essential for Its Adjuvanticity.* Nature Medicine, 2011. **17**(4): p. 479-U121.

Chapter 6 : The Immunological Properties of Layered Double Hydroxides

6.1 Introduction

The immune response elicited following inoculation with layered double hydroxides (LDHs) has been found to be controlled by three physicochemical properties of the dosed LDH including the zeta potential, as discussed in **Section 1.3.3**. While two of these parameters (*c*-parameter and metal ion radius) can easily be computed or determined from literature sources, at present it is not possible to calculate the zeta potential *a priori*.

The liquid layer surrounding a particle is subdivided into the Stern inner layer (where ions are strongly bound) and the diffuse outer layer (where ions are less strongly associated). Any movement of the particle leads to movement of the ions inhabiting the notional boundary between the two layers. The charge at this surface ("slipping plane") is termed the zeta potential. We hypothesised that it should be possible to develop computational models of the LDH structure and use the properties of these to devise a simple proxy for the zeta potential.

The objective of the work reported here thus was to develop an *in silico* means of predicting the zeta potential of layer double hydroxide materials, with the aim of replacing this property in the equation developed in previous working linking immunogenicity to physicochemical properties (**Figure 6.1** [1]). This would allow us to forego the need to synthesise compounds prior to predicting their immune response, enabling a high-throughput *in silico* screening process to identify suitable LDH candidates for subsequent synthesis and *in vitro* / *in vivo* experimentation. This should ultimately permit thousands of compounds to be screened before a few lead compounds are down-selected. To expand the limits of the model, di-halide LDH materials were also synthesised for *in vitro* exploration.

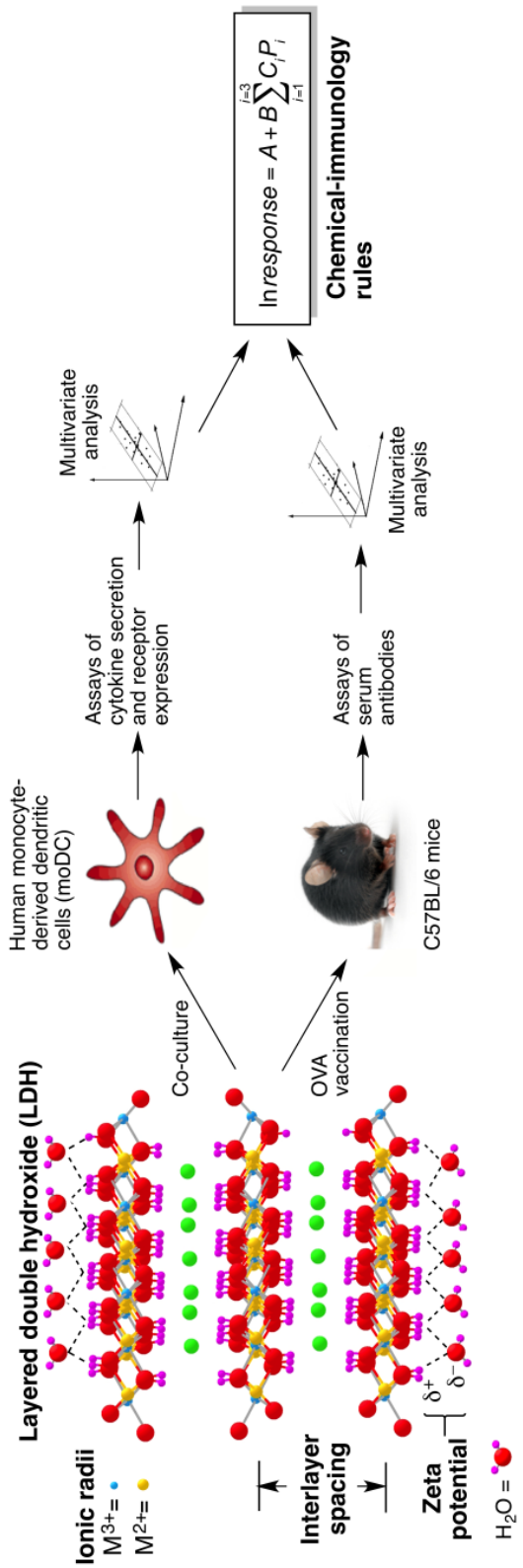

Figure 6.1: ***The systems vaccinology approach adopted by Williams et al. A series of layered double hydroxide materials was prepared, and the response of human dendritic cells in co-culture or of mice upon ovalbumin (OVA) vaccination quantified. The physicochemical properties of the LDHs were then considered to be causative of the immune response, and structure/property relationships elucidated. Reproduced from ref [1]. Copyright Rockefeller University Press 2014.***

6.2 Materials and Methods

6.2.1 $[LiAl_2(OH)_6]X{\cdot}yH_2O$ Synthesis Protocol

To control particle size of the synthesised LDHs, gibbsite [γ-$Al(OH)_3$, a kind gift from Professor Dermot O'Hare, Oxford University] was sieved to three different fractions: < 45, 53 – 63 and 71 – 90 µm using Endecotts test sieves and a Retsch sieve shaker. Li salts were sourced from Sigma Aldrich, UK.

0.5 g of the sieved gibbsite was added to 10 mL of a 10 M LiX salt solution (where X = Cl^-, Br^-, I^- or NO_3^-), placed in a sealed glass tube, and stirred vigorously at 110 °C overnight. Samples were left to cool completely then the product was retrieved using vacuum filtration, washed thoroughly with copious amounts of deionised water, and dried under vacuum with a small volume of acetone to aid the drying process.

6.2.2 Mixed Halide Synthesis Protocol

The smallest fraction of sieved gibbsite (< 45µm) was used to make a mixed halide intercalated material. 0.5 g of gibbsite was added to mixed LiCl / LiBr solutions with different Cl:Br ratios. The synthesis process was conducted as described in **Section 6.2.1**.

6.2.3 Characterisation

6.2.3.1 Powder X-Ray Diffraction

See **Section 3.3.1**.

6.2.3.2 Scanning Electron Microscopy

See **Section 3.3.2**.

6.2.3.3 Fourier Transform Infra-Red Spectroscopy

See **Section 3.3.3**.

6.2.3.4 X-ray Photoelectron Spectroscopy

See **Section 3.3.5**.

6.2.3.5 Zeta Potential Measurements

See **Section 3.3.6**.

6.2.3.6 Dynamic Light Scattering

Dynamic Light Scattering (DLS) was performed using a Nanozetasizer ZS (Malvern Instruments). 10 mg of LDH was dispersed in 1 mL of ethanol and placed in a semi-micro cuvette of 1.6 mL capacity and 10 mm light path (Fisher-Brand FB55147) for determination of particle size and size distribution.

6.2.3.7 *In silico* Simulations

Static lattice energy minimisations were performed using GULP (General Utility Lattice Program) Version 4.0 [2] with the scientific visual software GDIS (Graphical Display Interface for Structures [3]) to visualise the structures and generate structural depictions of the optimised layered double hydroxide structures.

6.2.4 Immunoassay Experiments

See **Section 3.3.7**.

6.2.4.1 Alamar Blue Assay

See **Section 3.3.7.1**.

6.2.4.2 Enzyme-Linked Immuno-Sorbent Assay

See **Section 3.3.7.2**.

6.2.4.3 Fluorescence and Confocal Microscopy

See **Section 3.3.7.3**.

6.3 Results and Discussion

6.3.1 Computer Simulation Set-Up

The ClayFF force field was implemented to simulate the structures of a hydroxide and two clay phases (portlandite, kaolinite and pyrophyllite, respectively) according to work by Cygan *et al*. [5] (see data in **Table 6.1**). These simulations were performed as calibrants to ensure that the force field was set up correctly and producing reliable data, and hence was suitable for subsequent LDH simulations. Comparison of our simulated data to Cygan's data suggests our layer cut-offs lead to an improved fit to the experimental data.

***Table 6.1:** A comparison of parameters calculated in this work and by Cygan* **et al** *[5] with experimental data for model systems.*

	Kaolinite $Al_2Si_2O_5(OH)_4$			Portlandite $Ca(OH)_2$			Pyrophyllite $AlSi_2O_5(OH)$		
	Simulated	Cygan [5]	Observed [6]	Simulated	Cygan [5]	Observed [7]	Simulated	Cygan [5]	Observed [8]
a / Å	5.173	5.190	5.154	3.567	3.693	3.589	5.098	5.192	5.160
b / Å	8.913	8.956	8.942	3.567	3.694	3.589	9.013	9.021	8.966
c / Å	7.235	7.361	7.391	4.908	4.796	4.911	9.382	9.459	9.347
α / °	91.85	90.77	91.92	90.0	82.04	90.0	95.32	91.38	91.18
β / °	105.23	104.17	105.05	90.0	97.99	90.0	100.29	98.97	100.46
γ / °	89.82	90.40	89.8	120.0	121.59	120.0	89.64	89.81	89.64

6.3.2 *In silico* Generation of $[LiAl_2(OH)_6]X{\cdot}yH_2O$ Structures

The gibbsite [γ-$Al(OH)_3$] structure is monoclinic and exhibits pseudo-hexagonal symmetry with unit cell parameters a ≈ 8.68 Å, b ≈ 5.08 Å and c ≈ 9.74 Å [9]. In $Al(OH)_3$, the trivalent aluminium cations occupy 2/3 of the octahedral holes in close-packed sheets of hydroxyl anions [10]. Following salt imbibition, the lithium cations occupy the remaining 1/3 of the octahedral holes to generate positively charged metal layers of formula $[LiAl_2(OH)_6]^+$. The unit cell expands in the direction perpendicular to the $Al(OH)_3$ place to accommodate the incoming guest anion and water molecules which now reside in the interlayer space – see **Figure 6.2**.

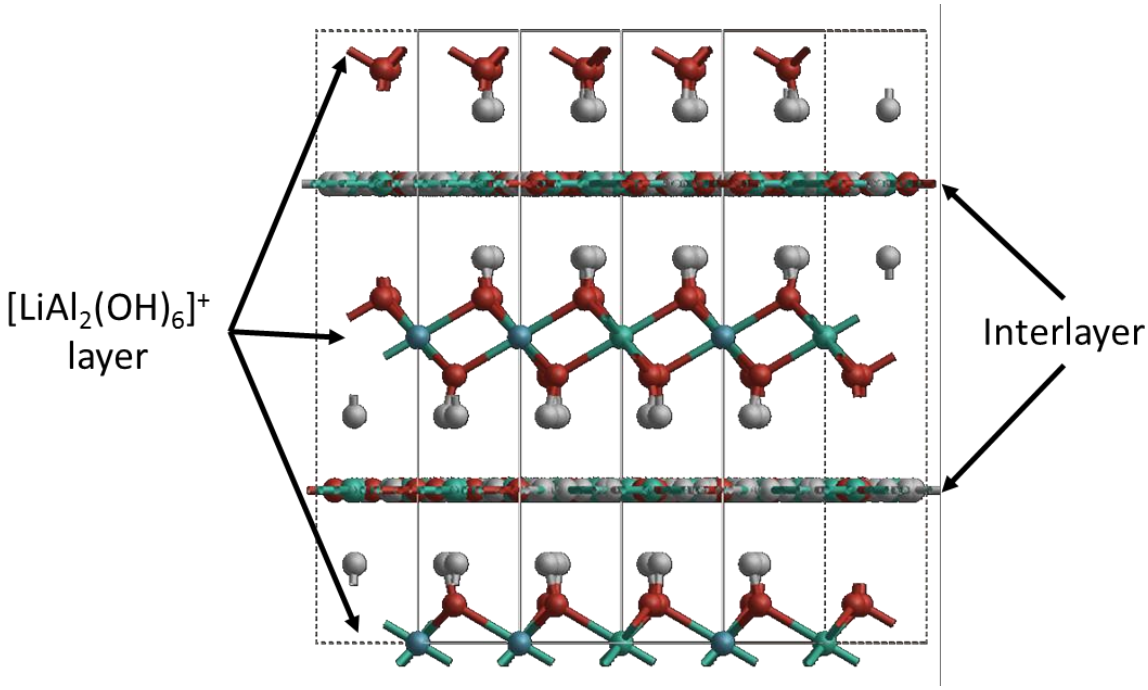

***Figure 6.2:** GDIS-generated image of $[LiAl_2(OH)_6]Cl{\cdot}yH_2O$ with $[LiAl_2(OH)_6]^+$ layers and interlayer regions labelled. Molecular water and chloride anions occupy the interlayer space.*

The original ClayFF forcefield permits the modelling of chloride systems, but does not include parameters to model bromide, iodide, nitrate and carbonate ions. Thus, additional interatomic potentials were added to the GULP input file to overcome this limitation (personal communication with Professor Julian Gale, Curtin University [11]; adapted from Fogg *et al*, [12]). The optimised system was achieved with the interatomic potentials listed in **Table 6.2** to **Table 6.5**.

***Table 6.2:* LDH framework potential parameters - Coulombic charges for bromide, iodide, nitrate and carbonate guest anions.**

Species	Coulombic charge / e
Br	-1.0000
I	-1.0000
N	0.4124
$O_{Nitrate}$	-0.4708
C	0.4280
$O_{Carbonate}$	-0.4760

***Table 6.3:* LDH framework potential parameters - interatomic potentials for bromide and iodide guest anions [12].**

Lennard-Jones: $\frac{A}{r^m} - \frac{B}{r^n}$

Interaction	A / kcal Å^9	B / kcal Å^6
Br – $O_{Hydroxyl}$	144784.0	2020.8
Br – $H_{Hydroxyl}$	10457.0	285.9
Br	0.0645	5.04
I	0.0979	5.40

***Table 6.4:** LDH framework potential parameters - interatomic potentials for nitrate guest anions [12].*

Harmonic: $\frac{1}{2}k_2(r-r_0)^2+\frac{1}{2}k_3(r-r_0)^2+\frac{1}{2}k_4(r-r_0)^4$				
Interaction	k_2 / eV Å^{-2}	k_3 / eV Å^{-3}	k_4 / eV Å^{-4}	r_0 / Å
N - O$_{Nitrate}$	50.6370	-408.2327	2779.8844	1.2645
Three-body Harmonic: $\frac{1}{2}k_2(\theta-\theta_0)^2+\frac{1}{6}k_3(\theta-\theta_0)^3+\frac{1}{12}k_4(\theta-\theta_0)^4$				
Interaction	k_2 / eV rad^{-2}	k_3 / eV rad^{-3}	k_4 / eV rad^{-4}	θ_0 / °
O$_{Nitrate}$ - N - O$_{Nitrate}$	10.2547	23.9655	74.9604	120.0
Torsion: $k(1+\cos(nphase(\phi-\phi_0)))$				
Interaction		k / eV	nphase	ϕ_0 / °
O$_{Nitrate}$ – N – O$_{Nitrate}$ - O$_{Nitrate}$		0.623163	+1	0.0
Lennard-Jones: $\frac{A}{r^m}-\frac{B}{r^n}$				
Interaction	A / kcal Å^9	B / kcal Å^6		
H - O$_{Nitrate}$	768.4	40.72		
H – N	888.1	61.30		
O$_{Layer}$ - O$_{Nitrate}$	16442.0	384.8		
O$_{Layer}$ - N	243936.0	84.2		

***Table 6.5:** LDH framework potential parameters - interatomic potentials for carbonate guest anions. Lennard-Jones interactions from Fogg [12], all other potentials from Archer [13].*

Harmonic: $\frac{1}{2}k_2(r-r_0)^2$				
Interaction	k_2 / eV Å^{-2}	r_0 / Å		
C - O$_{Carbonate}$	46.8331	0.00		
Three-body Harmonic: $\frac{1}{2}k_2(\theta-\theta_0)^2$				
Interaction	k_2 / eV rad^{-2}	θ_0 / °		
O$_{Carbonate}$ - C - O$_{Carbonate}$	1.7887	120.0		
Lennard-Jones: $\frac{A}{r^m}-\frac{B}{r^n}$				
Interaction	A / kcal Å^9	B / kcal Å^6		
H - O$_{Carbonate}$	670.8	43.30		
H – C	950.9	52.07		
O$_{Layer}$ - O$_{Carbonate}$	16585.0	450.5		
O$_{Layer}$ - C	20834.0	499.8		
Torsion: $k(1+\cos(nphase(\phi-\phi_0)))$				
Interaction		k / eV	nphase	ϕ_0 / °
O$_{Carbonate}$ – N – O$_{Carbonate}$ - O$_{Carbonate}$		0.151	+1	0.0
Morse: $D_e[1-\exp(-a(r-r_0)))^2-1]$				
Interaction		De / eV	A / Å^{-1}	r_0 / Å
O$_{Carbonate}$ - C		5.00	2.5155	1.20246

During the preliminary optimisation stages, the αβγ-angles fluctuated by 1-2% from the starting angles. However, following full optimisation, all the LDH materials result in α = β = γ = 90°.

Dehydrated $[LiAl_2(OH)_6]X$ systems (Li/Al-LDH) were modelled where X = Cl^-, Br^-, I^-, CO_3^{2-} and NO_3^- ; selected data are presented in **Table 6.6** and compared to others' published data. As noted in Cygan's paper, the Coulombic charge of lithium within LDH structures differs from the published value in the ClayFF input file. A charge of +1 eV was implemented for the monovalent lithium cation in the Li/Al-LDH species due to the stoichiometry of these LDH structures [5], whereas a +0.525 eV charge is implemented for structures such as Li_2O [14] which was used in the derivation of this partial charge.

***Table 6.6:** A comparison of simulated parameters for energy optimised, anhydrous Li/Al-LDH systems in this work and by Fogg [12] with experimental data for model systems.*

	$[LiAl_2(OH)_6]Cl$			$[LiAl_2(OH)_6]Br$			$[LiAl_2(OH)_6]NO_3$		
	Simulated	Fogg [12]	Observed [14]	Simulated	Fogg [12]	Observed [14]	Simulated	Fogg [12]	Observed [14]
a / Å	5.125	5.064	5.100	5.217	5.071	5.099	5.213	5.070	5.109
c / Å	14.563	14.736	14.299	14.875	15.474	14.946	12.708	14.154	14.374

The LDH materials were minimised using GULP with the space group of $P6_3/m$, and the optimised lattice parameters were found to be similar to the structural refinement values in the literature [12]. The values for the Cl and Br-containing systems are very close to those of Fogg's earlier simulation and the experimental values. There is a distinct difference in the *c*-parameter for the nitrate system, with Fogg's calculation yielding results much closer to the experimental value. $[LiAl_2(OH)_6]NO_3$ (Li/Al-Nitrate) is a disordered structure with its guest anions having partial occupancies, which reduces the symmetry within the system. The experimental value of the interlayer spacing is 14.374 Å [15], but the simulated result in this work is 12.708 Å (see **Table 6.6**). The Li/Al-Nitrate system described by Fogg is also dehydrated, and hence a possible reason for the differences in the *c*-parameters calculated may arise due to differences in the ClayFF force field parameters used (Fogg's model uses his own optimised set of parameter descriptions [12]). However, since overall our values are close to observed experimental data, and the model makes good chemical sense, our *in silico* model is appropriate for simulation of LDH structures.

$[LiAl_2(OH)_6]Br$ (Li/Al-Bromide) and $[LiAl_2(OH)_6]I$ (Li/Al-Iodide) are both isostructural halide intercalates of $[LiAl_2(OH)_6]Cl$ (Li/Al-Chloride), and the unit cells for all three were energy minimised in GULP using full symmetry. The results of simulations for Li/Al-Chloride, Li/Al-Bromide, and Li/Al-Iodide are given in **Figure 6.3**, with data from all the simulations summarised in **Table 6.7.**

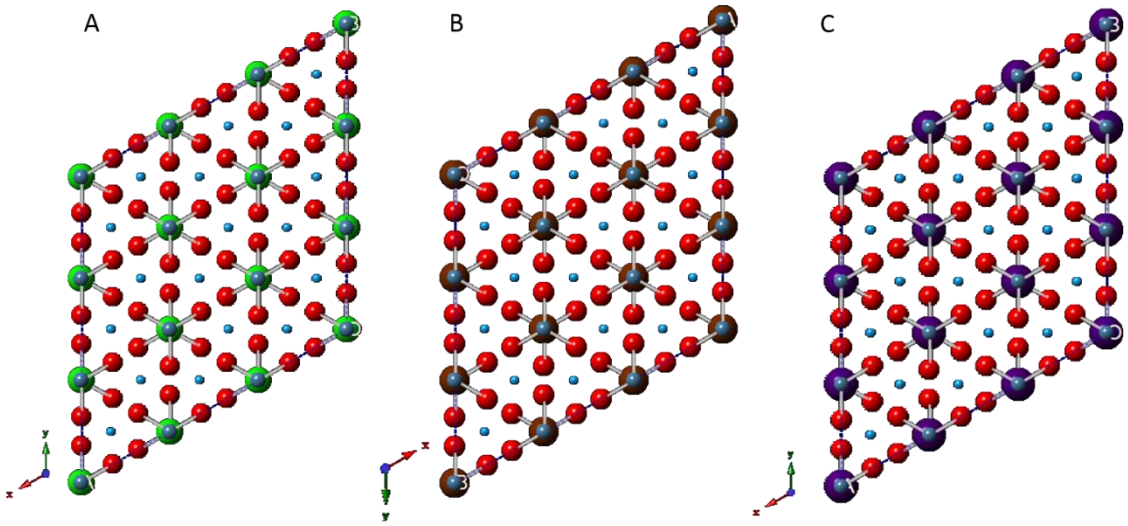

***Figure 6.3:* Supercell structures of fully optimised Li/Al-LDH materials where the intercalated guest anion is (A) chloride (green), (B) bromide (brown) and (C) iodide (purple); with oxygen (red) and hydrogen (blue).**

The supercells presented in **Figure 6.3** are composed of brucite-like sheets of $[LiAl_2(OH)_6]^+$, with octahedrally co-ordinated trivalent aluminium ions, alternating with interlayer regions of (A) chloride, (B) bromide and (C) iodide guest anions. The interlayer spacing parameter increases as group 17 of the periodic table is descended (see **Table 6.7**), which can be attributed to the increasing size of the anionic radius of the guest in the interlayer region. This observation arises concurrently with a decline in the energy of the systems, due to reduced electrostatic interactions.

The nitrate and carbonate systems demonstrate a collapse in the *c*-axis which is likely to be a result of dehydrating the structure, as well as ordering the anion arrangement within the interlayer space (**Table 6.7**).

***Table 6.7:* Simulated parameters for energy optimised, anhydrous Li/Al-LDH systems.**

	Li/Al-Chloride	Li/Al-Bromide	Li/Al-Iodide	Li/Al-Nitrate	Li/Al-Carbonate
a / Å	5.215	5.217	5.222	5.213	5.144
c /Å	14.563	14.875	15.461	12.708	10.614
Volume / Å^3	343.055	350.623	364.114	299.073	243.183
Energy /eV	-98.699	-98.361	-97.809	-100.681	-87.255

The size of the guest anion appears to impact the volume of the optimised structure and the interlayer spacing values. Small monovalent anion species have volumes greater than those with more complex intercalated guest anions (**Table 6.7**; Li/Al-Chloride compared to Li/Al-Carbonate). This is because the simulated carbonate and nitrate systems demonstrate a collapse in the *c*-axis in the dehydrated state, presumably as a result stronger intramolecular forces arising between the positive layers and the anionic species in these models resulting in a tighter unit cell conformation.

Given the accuracy of the energy minimisation used for the Li/Al-LDHs, compared to the published work, it can be concluded that the ClayFF force field poses a suitable model for LDH systems. Model construction can thus be extended for further studies with other LDH materials, such as $[Ca_2Al(OH)_6]X$ and $[Mg_2Al(OH)_6]X$ species (Ca/Al- and Mg/Al-LDHs, respectively).

6.3.2.1 Ca/Al- and Mg/Al-LDH Systems

Dehydrated Ca/Al-LDHs appear to consist of $[Ca_2Al(OH)_6]^+$ sheets with octahedrally co-ordinated calcium (II) cations, alternating with the interlayer guest anion, within the modelled structures. These materials have a net positive charge on their metal layers. In reality, the Ca/Al-LDHs have a seven co-ordinate Ca^{2+} cation which binds to six hydroxyl moieties in the $[Ca_2Al(OH)_6]^+$ layer and an interlayer water molecule [16]. It may be that the change in hydration state in these simulated structures causes this apparent change in coordination.

Furthermore, dehydrated Mg/Al-LDHs consist of $[Mg_2Al(OH)_6]^+$ metal layers with octahedrally co-ordinated magnesium (II) cations, alternating with the interlayer guest anion, within the modelled structures. These materials have a net positive charge on their metal layers.

The *in silico* data obtained for the Chloride and Nitrate species of both Ca/Al- and Mg/Al-LDHs are described in **Table 6.8**, these will be used for zeta potential proxy deductions in **Section 6.8.3**.

***Table 6.8:* Simulated parameters for energy optimised anhydrous Ca/Al- and Mg/Al-LDH systems.**

	Ca/Al-Chloride	Ca/Al-Nitrate	Mg/Al-Chloride	Mg/Al-Nitrate
a / Å	5.935	5.935	5.459	5.442
c /Å	17.031	17.031	16.879	14.706
Volume / Å^3	519.582	519.582	435.591	377.177
Energy /eV	-72.352	-72.352	-76.753	-77.620

In conclusion, successful modelling of the Li/Al-, Ca/Al- and Mg/Al-LDH structures was achieved using the dehydrated forms of the materials through implementation of the ClayFF force field with the addition of optimised parameters for bromide, iodide, nitrate and carbonate anions. The simulated data exhibit a close fit to the experimental values, and thus the calculated data can be potentially used in place of experimental data for the means of determining a proxy for the zeta potential. This will be discussed in **Sections 6.5.3** and **6.8**.

6.4 New LDH Materials Characterisation

Powder X-ray diffraction patterns of Li/Al-LDH materials prepared with the < 45 µm sieved-gibbsite fraction are shown in **Figure 6.4**. Identical patterns were obtained for the equivalent materials synthesised with the other two fractions of gibbsite. All detectable reflections can be assigned by their positions to standard diffraction peaks of published materials. No impurities were detected. The reflections observed are very sharp, indicative of the samples' high crystallinity.

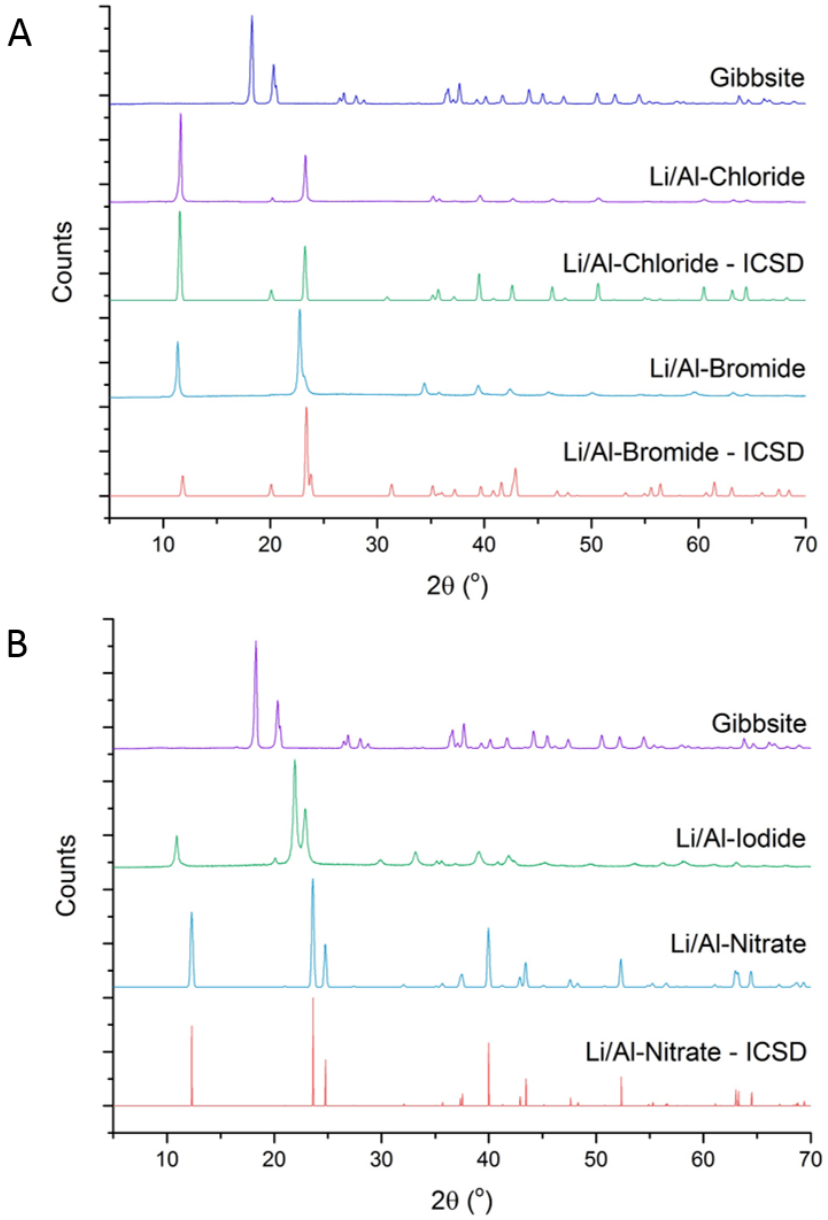

Figure 6.4: ***P-XRD patterns of Li/Al-LDH samples, synthesised with <45 µm gibbsite. (A) Li/Al-Chloride and –Bromide patterns alongside their reference patterns [15] and (B) Li/Al-Iodide and –Nitrate [15]; no reference patterns are available for the Li/Al-Iodide material in panel (B).***

Scanning electron microscopy (SEM) analysis shows that the reaction products are composed of particles with hexagonal platelet morphology (**Figure 6.5**). The images also highlight the sheet-stacking nature of these materials.

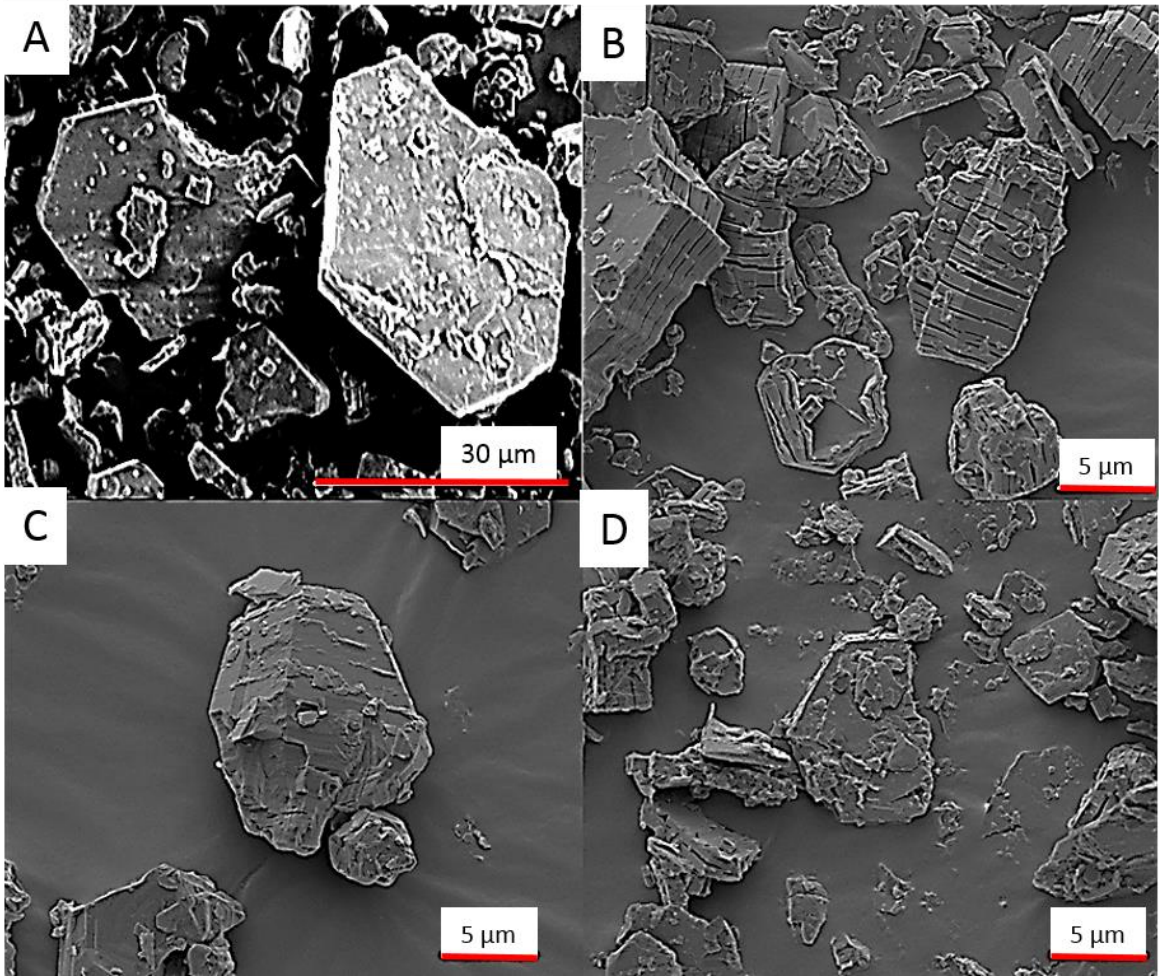

Figure 6.5: ***SEM images of Li/Al-LDH materials, synthesised with < 45 µm sieved gibbsite, where the intercalated guest anion is (A) chloride, (B) bromide, (C) iodide and (D) nitrate.***

The infrared spectra of the Li/Al-LDH materials are shown in **Figure 6.6**, and the major peak assignments for all samples are given in **Table 6.9**. The main band to note in the halide-intercalated structures can be attributed to the hydroxyl groups at *ca.* 940 cm^{-1} (**Figure 6.6A-C**), whilst the nitrate samples (**Figure 6.6D**) also exhibit sharp peaks *ca.* 1385 cm^{-1} which are assigned to V_3 absorption bands of nitrate [17]. There is a peak present *ca*. 1350 cm^{-1} for the Li/Al-iodide materials (**Figure 6.6C**) which may be attributed to carbonate contamination of the sample.

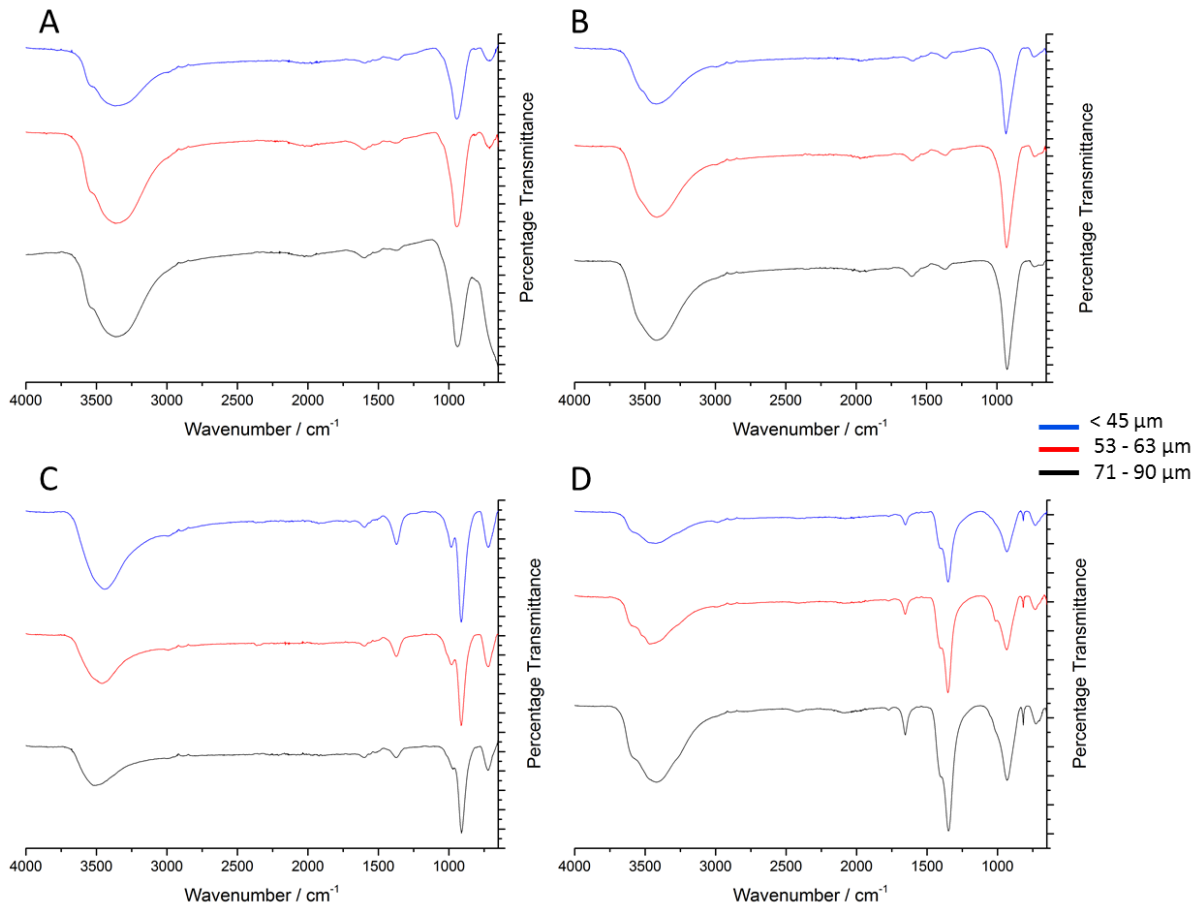

***Figure 6.6:** Fourier transform infrared spectra for Li/Al-LDHs where the guest anion is (A) chloride, (B) bromide, (C) iodide and (D) nitrate.*

***Table 6.9:** FTIR peak assignments for Li/Al-LDH materials – adapted from [18].*

Wavenumber / cm^{-1}	Assignment
3450	H-bonding stretching vibrations of hydroxyl group in $[LiAl_2(OH)_6]^+$ metal layer
1640	Water bending vibrations
1350	Carbonate incorporation
1030	Hydroxyl bending vibration in $[LiAl_2(OH)_6]^+$ metal layer
940	Hydroxyl moieties in the halide intercalated species
725	Al – O

All the different materials produced give identical FTIR spectra with each ion, irrespective of the size of the gibbsite used during synthesis. Considering all the data as a whole, it appears that all the materials were successfully synthesised and the data obtained are consistent with the literature.

6.5 Particle Size and Zeta Potential Measurements

Experiments were performed to determine if changing the particle size of the precursor gibbsite influences the zeta potential and size of the LDH materials.

6.5.1 Particle Size

A summary of all the particle size data collected is given in **Table 6.10**. The smallest gibbsite fraction appears to lead to smaller particles as the halide interlayer anion increases in size. The crystallite size determined by the Scherrer equation (P-XRD in **Table 6.10**) gives a smaller size than the particle size calculated by SEM or DLS, as would be expected.

***Table 6.10:** Collated crystallite and particle size data for the Li/Al-LDH materials; for SEM analysis, at least 20 particles were measured using the ImageJ software for the mean particle size.*

		P-XRD		DLS		SEM	
LDH Material	Gibbsite Fraction Size / µm	Mean size / nm	Standard Deviation / nm	Mean size / µm	Standard deviation / µm	Mean size / µm	Standard deviation / µm
Li/Al-Chloride	< 45	48.25	22.77	1.69	0.35	10.22	3.08
	53 – 63	37.26	16.60	1.63	0.24	8.99	4.24
	71 – 90	44.12	15.09	1.09	0.64	22.89	13.77
Li/Al-Bromide	< 45	45.37	19.01	1.54	0.24	8.58	4.44
	53 – 63	46.29	20.31	1.86	0.32	5.89	2.09
	71 – 90	32.19	12.78	0.72	0.26	17.68	8.95
Li/Al-Iodide	< 45	36.60	14.20	1.46	0.15	4.41	2.05
	53 – 63	33.19	15.90	1.46	0.18	4.50	2.26
	71 – 90	39.73	16.80	1.14	0.31	44.92	---
Li/Al-Nitrate	< 45	51.10	18.49	1.85	0.36	9.10	4.98
	53 – 63	44.45	14.44	0.91	0.35	5.76	3.78
	71 – 90	41.84	15.37	1.05	0.44	22.75	7.24

There do not appear to be any trends in the size for these materials across the different analysis types (**Table 6.10**). The SEM images provide us with visual depictions of the Li/Al-LDH samples, thereby giving arguably the most accurate method of calculating the mean particle size for these materials; therefore, the SEM dataset will be used in further work.

6.5.2 Zeta Potential Measurements

With ultrapure water as the diluent, positive zeta potential measurements were recorded – with the majority of the data being around +30 mV, which is associated with a stable suspension [19] (see data in **Table 6.11**). In contrast, when the LDH materials were dispersed in PBS, negative zeta potential measurements were obtained in the range 0 to -27 mV (**Table 6.12**). The latter outcome is likely to have occurred due to the presence of negatively charged phosphate anions within the PBS solution; these are attracted to the positive LDH layers and surround them, resulting in a negative zeta potential [20].

***Table 6.11:** Collated zeta potential data for all LDH materials measured with ultrapure water as the diluent.*

		0 minutes		+10 minutes	
LDH Material	Gibbsite Fraction Size / µm	Mean zeta potential / mV	Standard Deviation / mV	Mean zeta potential / mV	Standard Deviation / mV
Li/Al-Chloride	< 45	58.2	0.96	56.6	0.89
	53 – 63	26.4	2.46	18.6	0.78
	71 – 90	42.6	5.32	33.3	0.38
Li/Al-Bromide	< 45	51.6	1.17	45.9	1.12
	53 – 63	42.0	3.42	32.8	1.17
	71 – 90	20.6	2.00	15.9	0.50
Li/Al-Iodide	< 45	30.6	2.23	27.1	0.94
	53 – 63	37.9	2.82	34.7	2.36
	71 – 90	33.3	2.27	26.8	0.72
Li/Al-Nitrate	< 45	19.0	0.64	10.5	0.52
	53 – 63	32.9	1.72	22.4	0.93
	71 – 90	12.5	3.45	8.2	0.90

There are no apparent trends with the PBS-based dataset (**Table 6.12**), however, with ultrapure water there is a decrease in the measured zeta potential as the interlayer anion changes from Cl to Br to I, for samples made from the smallest gibbsite fraction. This relationship is not consistent across the LDHs made from the other two gibbsite fractions (data in **Table 6.11** and **Table 6.12**), which may be due to aggregation of the samples and subsequent sedimentation at the base of the zeta cell. Therefore, only the 45 µm fraction will be investigated further.

***Table 6.12:** Collated zeta potential data for all LDH materials measured in 0.01 M phosphate buffered saline (PBS) solution as the diluent, at pH 7.4.*

		0 minutes		+10 minutes	
LDH Material	Gibbsite Fraction Size / µm	Mean zeta potential / mV	Standard Deviation / mV	Mean zeta potential / mV	Standard Deviation / mV
Li/Al-Chloride	< 45	-10.85	1.71	-11.98	0.90
	53 – 63	-9.08	1.52	-10.37	1.13
	71 – 90	-15.37	0.56	-15.57	0.62
Li/Al-Bromide	< 45	-10.8	0.49	-8.82	0.74
	53 – 63	-13.22	0.88	-9.95	0.27
	71 – 90	-25.65	0.98	-26.72	2.19
Li/Al-Iodide	< 45	-13.85	0.83	-14.22	1.75
	53 – 63	-13.27	0.80	-11.75	0.84
	71 – 90	-15.82	0.85	-17.00	0.82
Li/Al-Nitrate	< 45	-13.32	0.83	-9.58	0.52
	53 – 63	8.00	2.40	5.12	0.71
	71 – 90	-17.13	0.48	-15.30	1.39

6.5.3 Zeta Potential Correlations

Attempts were made to elucidate any relationships between the mean particle sizes of LDHs generated from the 45 µm gibbsite fraction (as measured by SEM) and the zeta potential measurements of these Li/Al-LDH materials – the results are given in **Table 6.13**. Graphical representations are presented in **Figure 6.7**.

***Table 6.13:** Relationships between zeta potential measurements and experimental properties of the Li/Al-LDH materials.*

Experimental parameter / µm (x)	Zeta potential / mV (y)	Equation	R^2 correlation
Particle size	**ZP in UP-water**	y = 0.2076x – 1.9795	0.9979
	ZP in UP-water (10 minutes)	y = 0.1998x – 0.8937	0.9921
	ZP in PBS	y = 1.6425x + 27.173	0.9173
	ZP in PBS (10 minutes)	y = 0.6872x + 15.759	0.3874

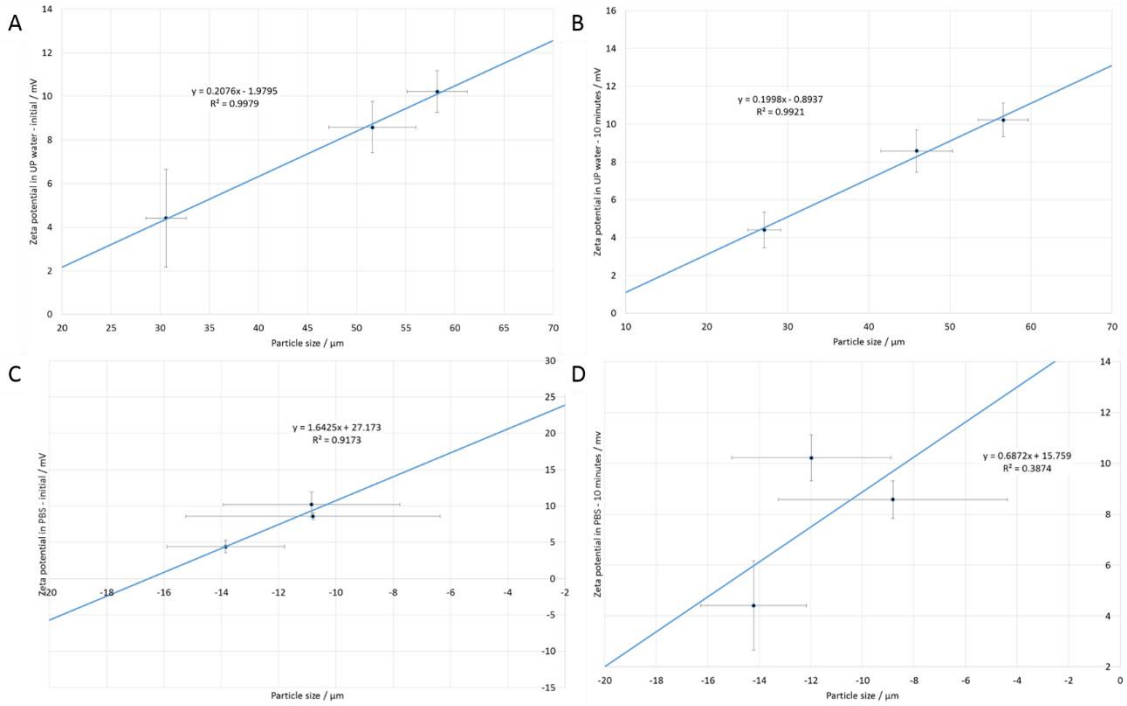

***Figure 6.7:* Graphical representations of the relationships described in Table 6.13; with panels A and B depicting correlations between particle size (deduced by SEM analysis) and zeta potential measurements using UP-water and panels C and D with zeta potentials measured in PBS.**

From the data in **Figure 6.7**, it appears that there are clear structure/property relationships connecting the zeta potential in water with the particle size; these suggest that it should be possible to tune the zeta potential through variation of particle size. In contrast, there are no clear relationships in the case of the potentials measured in PBS. This is presumably due to the presence of the phosphate anions complicating the system.

Furthermore, it is possible to draw correlations between the zeta potential measurements and the energy, volume or *a*-parameter values derived *in silico* (**Table 6.14** and **Figure 6.8**, with *a*-parameter plots located in **Appendix 4**).

***Table 6.14:* Relationships between zeta potential measurements and in silico-deduced properties of the Li/Al-LDH materials.**

In silico parameter (x)	Zeta potential / mV (y)	Equation	R^2 correlation
***a*-parameter / Å**	ZP in UP-water	y = -3992.3x + 20879	0.9975
Volume / Å³		y = -1.3394x + 519.07	0.9828
Energy / eV		y = -31.697x – 3068.7	0.9763
***a*-parameter / Å**	ZP in UP-water (10 minutes)	y = -4126.9x + 21577	0.9927
Volume / Å³		y = -1.400x + 536.83	1.0000
Energy / eV		y = -33.235x – 3223.5	0.9996
***a*-parameter / Å**	ZP in PBS	y = -463.46x + 2406.5	0.9153
Volume / Å³		y = -0.1522x + 41.847	0.8645
Energy / eV		y = -3.5809x – 363.8	0.8484
***a*-parameter / Å**	ZP in PBS (10 minutes)	y = -466.15x + 2420.7	0.3838
Volume / Å³		y = -0.1408x + 37.96	0.3063
Energy / eV		y = -3.2256x – 328.71	0.2853

There appear to be very distinct relationships between the zeta potential values observed experimentally in water and the modelled parameters (**Figure 6.8**). In contrast, the zeta potential measurements recorded using PBS as the dispersant display no such clear relationships (although there are reasonable correlations when considering the time zero values), consistent with the findings which were observed above with particle size.

The relationships described in **Table 6.14** indicate that a more negative calculated lattice energy corresponds to a more positive zeta potential measurement in UP water. Further, a smaller unit cell volume results in more positive zeta potentials in the same dispersant. This is sensible in terms of the chemistry of the systems. Considering the Li/Al-LDH particles, the exterior will display $[LiAl_2(OH)_6]^+$ sheets. Each formula unit carries one unit of charge, and the charge density at the surface will be closely related to the *a*-parameter, since the latter determines the area in which each charge unit is present. Comparing the zeta potentials to the calculated *a*-parameter, a smaller value for *a* gives rise to a greater positive charge density at the surface, with a strong negative correlation. Since the LDH-Chloride material has the highest positive charge density at the surface, it also has the most positive zeta potential in water.

A smaller *a*-parameter leads to a smaller cell volume, compounded by the smaller anions in the chloride case reading to a reduced *c*-paramater, and thus we also observe a clear relationship between cell volume and zeta potential. The smaller *a*- and *c*-parameters result in stronger ionic interactions between the anions and cations present, and thus a more negative lattice enthalpy; a correlation between this and zeta potential is hence also seen.

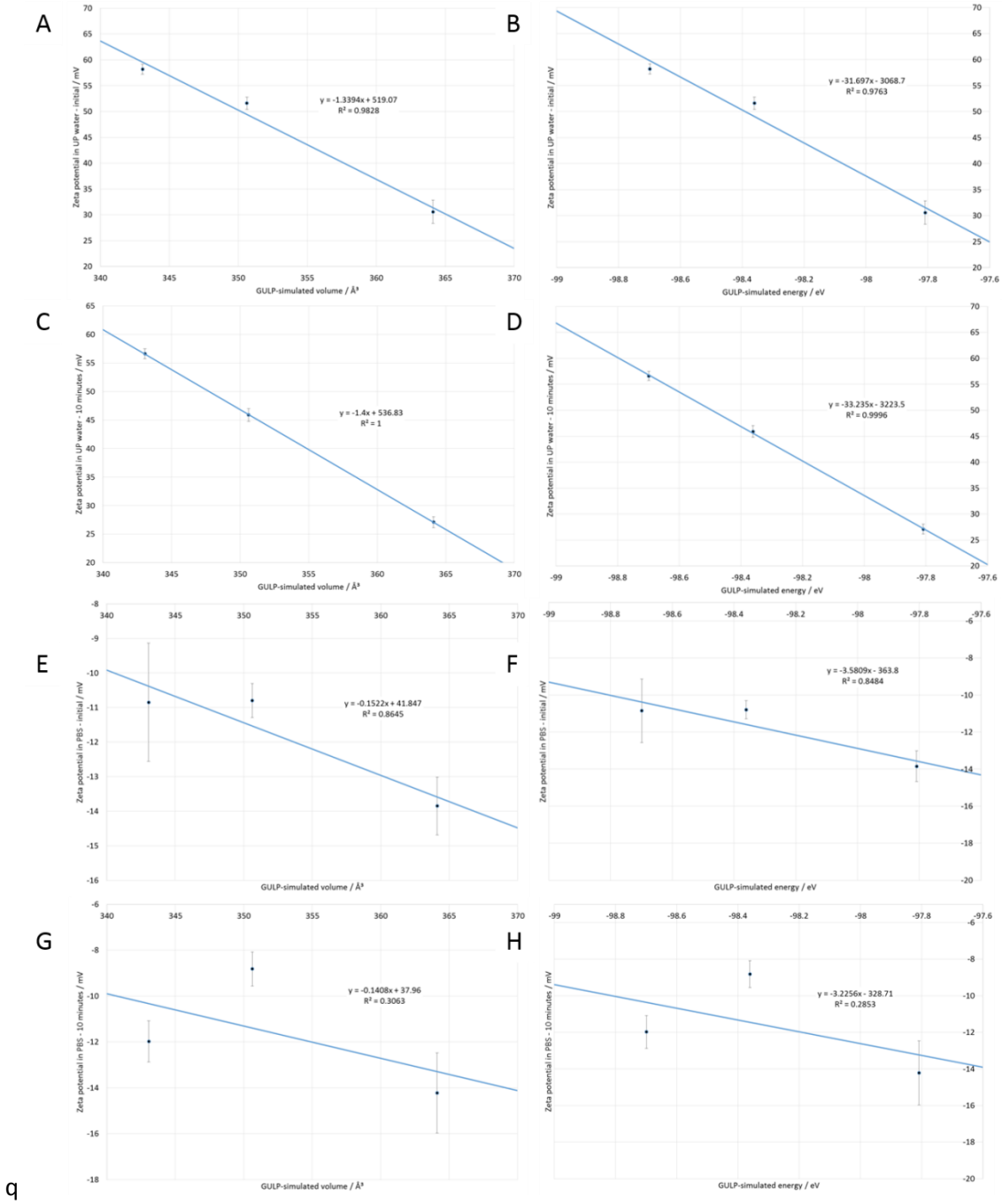

q

Figure 6.8: ***Graphical representation of the relationships described in Table 6.14; with calculated data for unit cell (UC) volume and lattice energy being correlated against zeta potential measurements in either UP water or PBS. (A) UP water (initial) with UC volume, (B) UP water (initial) with lattice energy, (C) UP water (10 minutes) with UC volume, (D) UP water (10 minutes) with lattice energy, (E) PBS (initial) with UC volume, (F) PBS (initial) with lattice energy, (G) PBS (10 minutes) with UC volume, and (H) PBS (10 minutes) with lattice energy.***

6.6 Mixed Halide LDH Materials

6.6.1 Mixed Halide Synthesis

In a bid to probe in more detail correlations between zeta potential and parameters from *in silico* work, a series of mixed halide Li/Al-LDH materials were synthesised, fully characterised, modelled *in silico*, and tested *in vitro* with RAW264.7 macrophages.

Initial efforts to synthesise chloride/bromide di-halide Li/Al-LDHs combined varied volumes of 10 M LiBr and LiCl salt solutions, while the reaction temperature was maintained at 110 °C and the mixture stirred for at least six hours. The resultant P-XRD patterns are very similar to that of Li/Al Chloride, with maybe slightly enlarged interlayer spacings. Selected patterns are presented in **Figure 6.9A**; all are largely identical for the first series of samples (LDH_1 – LDH_5). The patterns display 004 reflections of greater intensity than the 002 peaks, which is symptomatic of bromide incorporation (see **Figure 6.9A**). Reaction details and mean crystallite size analysis are presented in **Table 6.15.**

Table 6.15: ***Optimisation of the synthetic process for generation of mixed-halide Li/Al-LDH materials, including the crystallite size deduced from P-XRD patterns (mean ± standard deviation). The concentration of the LiBr solution was constant at 10 M. Both d-spacing values for the 002 reflection in LDH_6 are provided.***

Sample ID	[LiCl] / M	Volume LiCl / mL	Volume LiBr / mL	XRD Crystallite size / nm	*d*-spacing /Å
LDH_1	10	2.5	7.5	28.90 ± 3.82	7.71
LDH_2	10	4	6	27.66 ± 6.54	7.55
LDH_3	10	5	5	25.95 ± 3.25	7.30
LDH_4	10	6	4	22.12 ± 2.43	7.39
LDH_5	10	7.5	2.5	15.60 ± 4.12	7.42
LDH_6	10	5	5	30.49 ± 11.93	7.67 7.39
LDH_7	5	5	5	41.66 ± 11.01	7.63
LDH_8	2	5	5	34.54 ± 10.31	7.57
LDH_9	1	5	5	23.90 ± 8.09	7.11

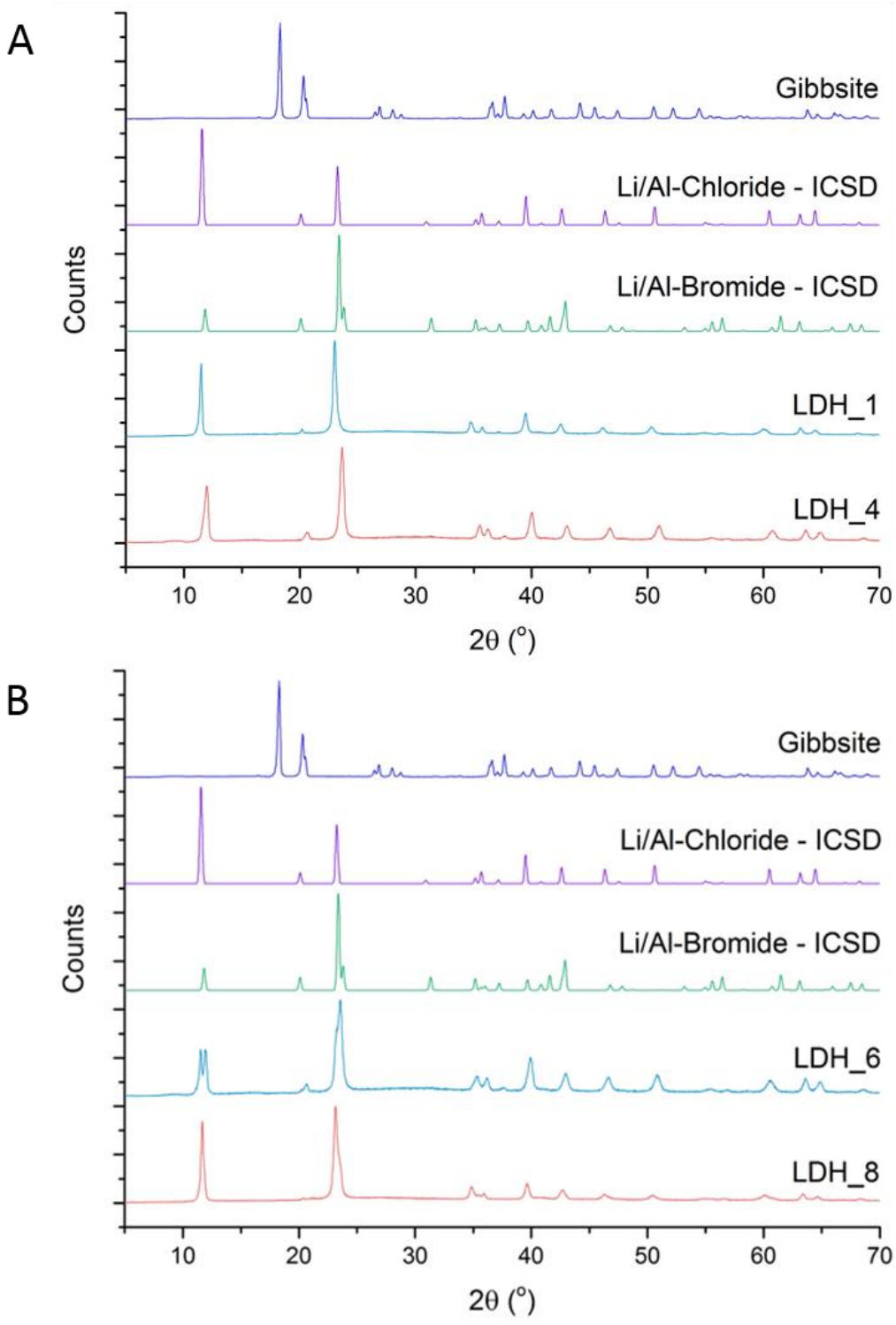

Figure 6.9: ***P-XRD patterns of Li/Al-LDH samples, synthesised with <45 µm gibbsite. (A) LDH_1 and LDH_4 and (B) LDH_6 and LDH_8, with reference patterns for Li/Al-Chloride and –Bromide in each panel [15].***

Representative P-XRD patterns are provided in **Figure 6.9B** for the di-halide materials synthesised through altering the concentration of the LiCl solution (LDH_6 to LDH_9). These again show evidence of bromide incorporation given the greater intensity of the 004 reflection *cf.* the 002. It is evident from the P-XRD patterns that there are two 002 reflections for the LDH_6 sample, with both *d*-spacing values given in **Table 6.15**. This might indicate a degree of phase separation, or possibly different hydration states. In order to quantify the balance of anions present, XPS analysis was undertaken; the compositions calculated from the resultant data are given in **Table 6.16**.

Table 6.16: ***Structural composition of the di-halide Li/Al-LDH materials, determined via XPS spectra.***

Sample ID	Structural composition
LDH_1	$[LiAl_2(OH)_6]\ Br_{0.49}Cl_{0.51}{\cdot}yH_2O$
LDH_2	$[LiAl_2(OH)_6]\ Br_{0.25}Cl_{0.75}{\cdot}yH_2O$
LDH_3	$[LiAl_2(OH)_6]\ Br_{0.14}Cl_{0.86}{\cdot}yH_2O$
LDH_4	$[LiAl_2(OH)_6]\ Br_{0.09}Cl_{0.91}{\cdot}yH_2O$
LDH_5	$[LiAl_2(OH)_6]\ Br_{0.04}Cl_{0.96}{\cdot}yH_2O$
LDH_6	$[LiAl_2(OH)_6]\ Br_{0.12}Cl_{0.88}{\cdot}yH_2O$
LDH_7	$[LiAl_2(OH)_6]\ Br_{0.38}Cl_{0.62}{\cdot}yH_2O$
LDH_8	$[LiAl_2(OH)_6]\ Br_{0.38}Cl_{0.62}{\cdot}yH_2O$
LDH_9	$[LiAl_2(OH)_6]\ Br_{0.71}Cl_{0.29}{\cdot}yH_2O$

The chemical composition of the synthesised materials highlights the need to use a large excess of LiBr over LiCl to obtain high Br contents in the LDH produced (*e.g.* see LDH_6 to LDH_9 in **Table 6.16**). Because of their smaller size and greater charge density, chloride ions will preferentially intercalate over bromide ions, and therefore reducing the amount of chloride in the reaction mixture should increase the chance of successful intercalation of bromide.

The data obtained *via* XPS indicate successful intercalation of both anions, with varying amounts of each in the interlayer (data in **Table 6.16**). The second series of materials, LDH_6 to LDH_9 have between 12 – 71% of the interlayer anions as bromide, giving a wide range of compositions. These will be carried forward for further testing using the relative compositions deduced by XPS analysis to model the structures *in silico*.

6.6.2 Further Mixed Halide Li/Al-LDH Materials Characterisation

Prior to *in silico* work, the characterisation of the LDHs produced was completed using SEM and FTIR analysis on the selected materials. The SEM images clearly demonstrate the LDHs to comprise hexagonal platelets with layered structures (**Figure 6.10**), and the FTIR spectra are all identical and contain the standard features expected with LDHs (**Figure 6.11**) with the same peak assignments as are previously listed in **Table 6.9**.

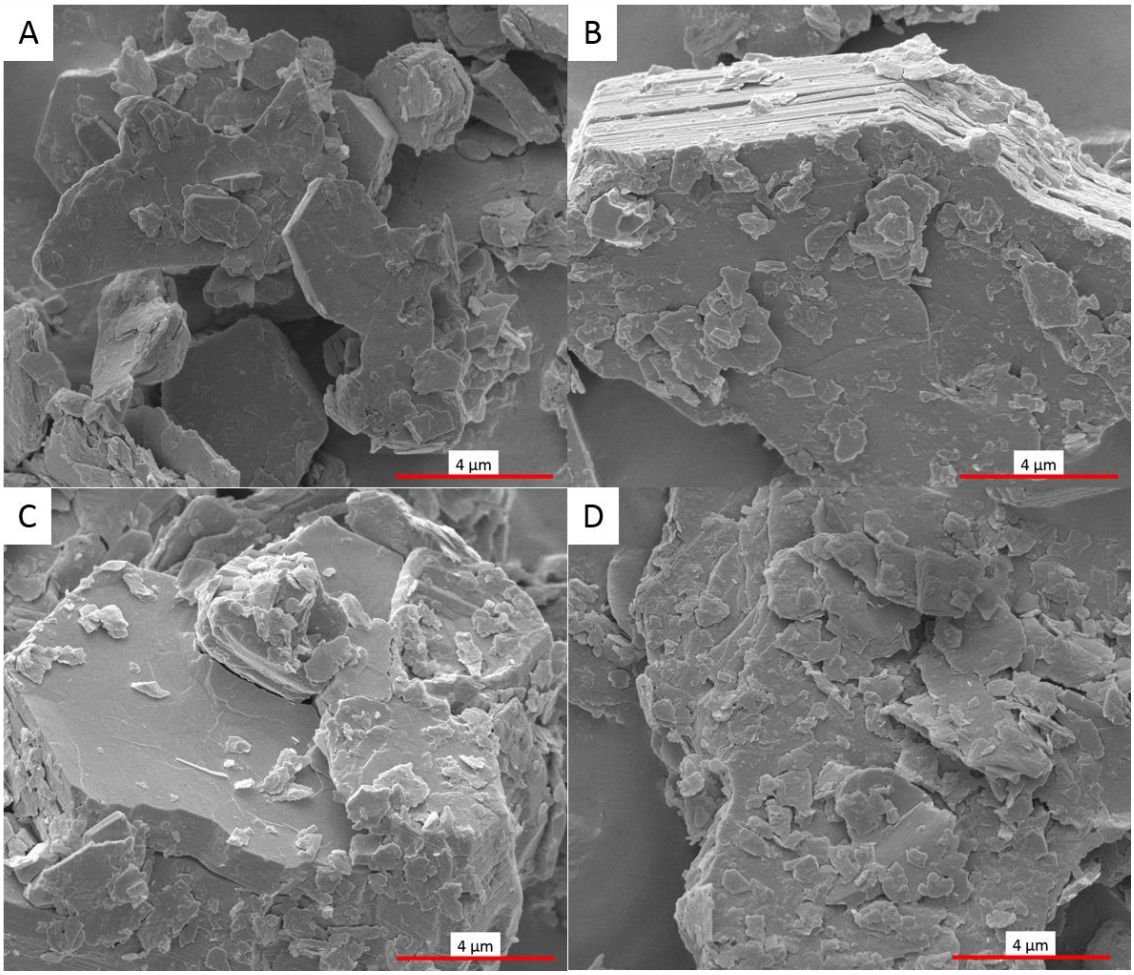

***Figure 6.10:* SEM images for the four mixed halide intercalates LDH_6 to LDH_9. (A) Li/Al-$Br_{0.12}Cl_{0.88}$, (B) Li/Al-$Br_{0.38}Cl_{0.62}$, (C) Li/Al-$Br_{0.62}Cl_{0.38}$ and (D) Li/Al-$Br_{0.71}Cl_{0.29}$.**

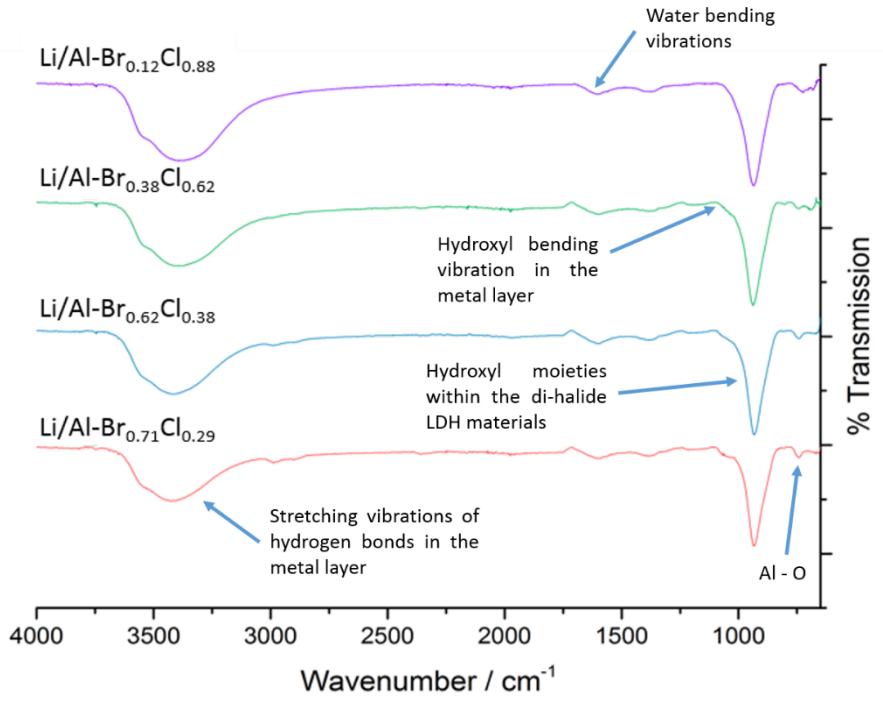

Figure 6.11: ***FTIR spectra comparing the four mixed-halide Li/Al-LDH materials LDH_6 to LDH_9.***

6.6.3 Zeta Potential Measurements

Measurements were recorded when the materials were dispersed in phosphate-buffered saline (**Table 6.17**) and ultrapure water (**Table 6.18**).

Table 6.17: ***Zeta potential measurements for the four mixed halide Li/Al-LDH materials of interest, performed in 0.01 M phosphate-buffered saline (PBS) solution of pH 7.4.***

		0 minutes	10 minutes
Sample ID	Sample ID	Zeta potential / mV	Zeta potential / mV
LDH_6	$Li/Al\text{-}Br_{0.12}Cl_{0.88}$	-25.85 ± 1.11	-23.27 ± 1.32
LDH_7	$Li/Al\text{-}Br_{0.38}Cl_{0.62}$	-18.77 ± 0.66	-13.12 ± 0.75
LDH_8	$Li/Al\text{-}Br_{0.62}Cl_{0.38}$	-16.02 ± 1.34	-19.57 ± 1.33
LDH_9	$Li/Al\text{-}Br_{0.71}Cl_{0.29}$	-14.55 ± 1.17	-17.25 ± 0.93

The zeta potentials obtained when using PBS as the dispersant are all negative, and the suspensions seem relatively stable over the 10 minute timescale.

***Table 6.18:** Zeta potential measurements for the four mixed halide Li/Al-LDH materials of interest, performed in UP-water with resistance of 18.2 mΩ.*

		0 minutes	10 minutes
Sample ID	Sample ID	Zeta potential / mV	Zeta potential / mV
LDH_6	Li/Al-$Br_{0.12}Cl_{0.88}$	12.26 ± 2.05	15.55 ± 1.30
LDH_7	Li/Al-$Br_{0.38}Cl_{0.62}$	37.48 ± 2.77	33.55 ± 1.34
LDH_8	Li/Al-$Br_{0.62}Cl_{0.38}$	32.62 ± 1.28	24.83 ± 1.02
LDH_9	Li/Al-$Br_{0.71}Cl_{0.29}$	35.07 ± 1.33	36.62 ± 1.47

There appears to be a trend in terms of how the potential varies with the Br content, such that when measured in PBS a higher bromide content leads to a more negative the zeta potential (0 minutes, **Table 6.17**). The zeta potential measurements for dispersions using ultrapure water (**Table 6.18**) are less positive than those recorded for the previously described pure Cl/Br intercalates (**Table 6.11**). Again, the suspensions appear relatively stable over the 10 minute timescale.

6.6.4 *In silico* modelling

The relative contents of chloride and bromide anions from the XPS data (**Table 6.16**) were translated into fractional occupancies. Calculated data generated using GULP are summarised in **Table 6.19**.

***Table 6.19:** Calculated unit cell parameters for energy optimised di-halide Li/Al-LDH systems. The difference in electronegativity is calculated by subtracting the electronegativity of the metal cation from the guest anionic species with the anionic component being a weighted mean of the two halide ions' electronegativity values using their percentages deduced by XPS analysis.*

LDH Material	a / Å	c / Å	Energy / eV	Volume / $Å^3$	Difference in electronegativity
$[LiAl_2(OH)_6]Cl$	5.215429	14.56306	-98.69947	343.0547	2.180
$[LiAl_2(OH)_6]Br_{1/8}Cl_{7/8}$	5.215692	14.61327	-98.64790	344.2721	2.155
$[LiAl_2(OH)_6]Br_{3/8}Cl_{5/8}$	5.216167	14.70099	-98.55412	346.4017	2.105
$[LiAl_2(OH)_6]Br_{5/8}Cl_{3/8}$	5.216583	14.77664	-98.47066	348.2401	2.055
$[LiAl_2(OH)_6]Br_{5/7}Cl_{2/7}$	5.216718	14.80145	-98.44299	348.8426	2.037
$[LiAl_2(OH)_6]Br$	5.217113	14.87473	-98.36110	350.6229	1.980

The data presented in **Table 6.19** compare well with the simulated data for the mono-halide materials, because they lie within the limits of the pure Cl/Br intercalates. A reduction in the chloride-content of the LDH leads to an increase in the *a*- and *c*- parameters, which is consistent with an increase in the anionic radius in the unit cell. The simulated value for energy becomes less negative on increasing the bromide content, because weaker interactions between the interlayer anions and the hydroxide layers arise as the size of the guest anion increases the distance between them and the charge density of the anion reduces.

6.7 *In Vitro* Experiments

6.7.1 Cell Viability

The viability of cells exposed to LDHs was determined by the Alamar Blue *in vitro* assay; the data obtained are given in **Figure 6.12** and **Figure 6.13**. In general, the cell viability is very close to the untreated cells control. However, there is evidence of a high degree of cell cytotoxicity for the mono-halide Li/Al-LDH materials (**Figure 6.12**) *ca*. 27 – 28 hours post-adjuvant exposure. This can be attributed to the doubling time of the RAW264.7 cell line [21]. As a result, the cell count appears to diminish during the mitotic stages of cell division but the viability level is restored in the following hour. Therefore, the adjuvant causes a temporary reduction in cell numbers, but these recover within an hour.

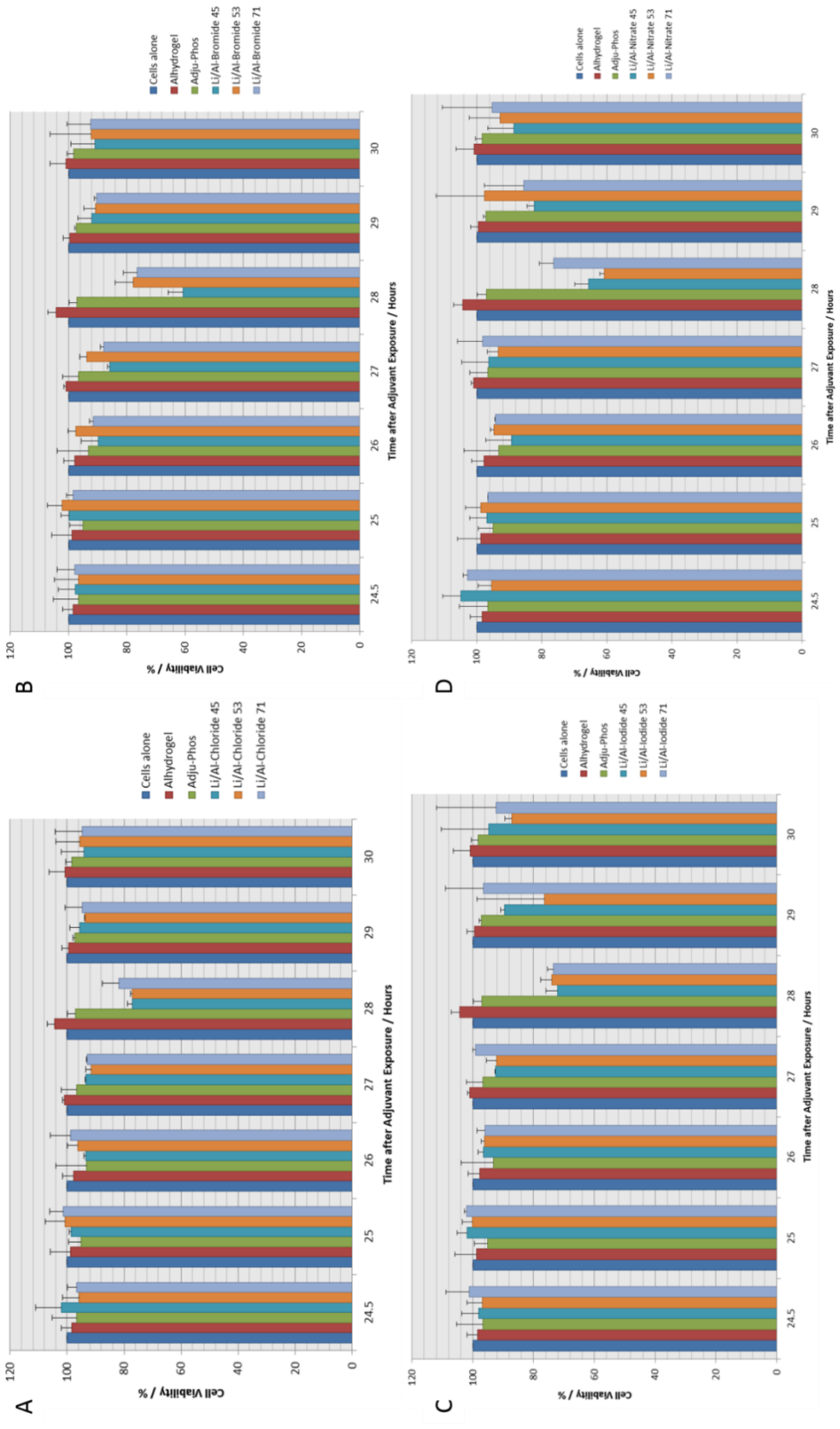

Figure 6.12: ***Cell viability results. RAW264.7 macrophages were exposed to Li/Al-LDH materials at 476 µg mL^{-1} for 24 hours, with <45, 53-63 and 71-90 µm fractions of gibbsite used for LDH synthesis. Cells exposed to commercial alums (Alhydrogel® and Adju-Phos®) were used for comparative purposes at the same concentrations as the Li/Al-LDH materials. Cell viability was quantified by Alamar Blue, with n = 3; each independent experiment contained nine replicates. (A) LDH_Chloride, (B) LDH_Bromide, (C) LDH_Iodide and (D) LDH_Nitrate.***

There is similarly little evidence of cell cytotoxicity for the mixed-halide Li/Al-LDH materials (**Figure 6.13**) with RAW264.7 cell exceeding 90% viability across all the samples.

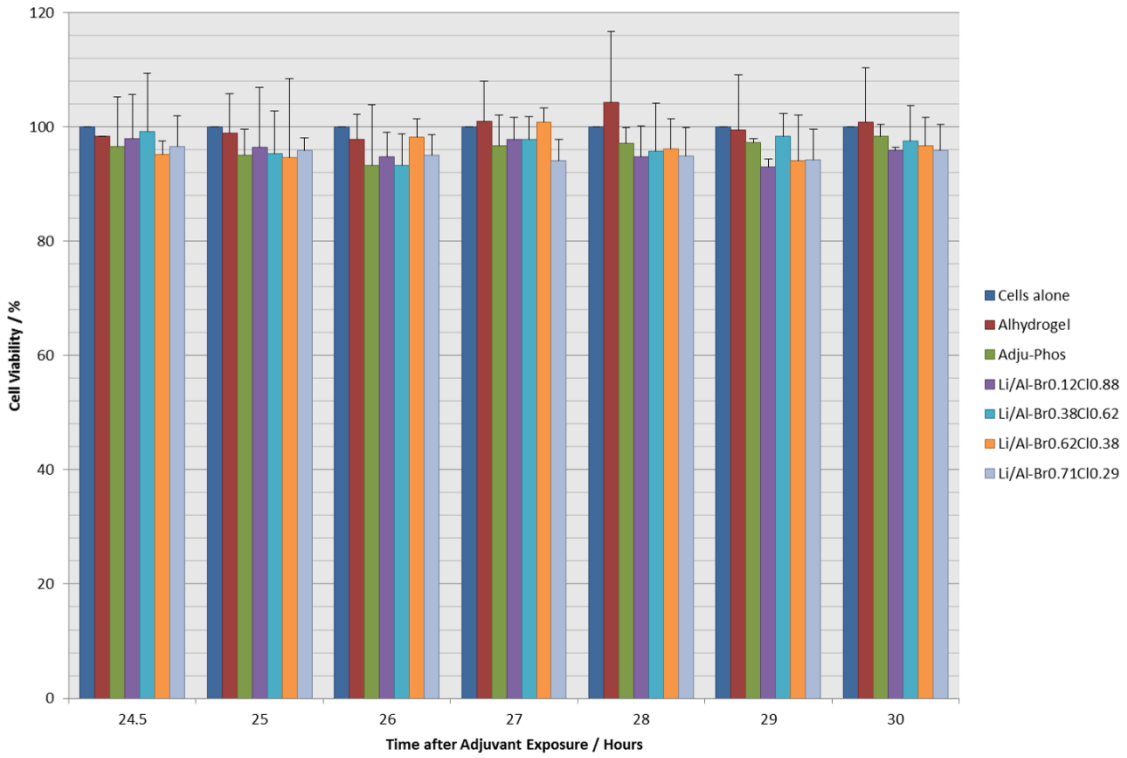

Figure 6.13: ***Cell viability results. RAW264.7 macrophages were exposed to mixed halide Li/Al-LDH materials at 476 µg mL^{-1} for 24 hours. Cells exposed to commercial alums (Alhydrogel® and Adju-Phos®) were used for comparative purposes at the same concentrations as the Li/Al-LDH materials. Cell viability was quantified by Alamar Blue with n = 3; each independent experiment contained nine replicates.***

6.7.2 Immunoassay Experiments

The immunological response of RAW264.7 cells exposed to LDHs was determined by ELISA assays; the data for TNF-α and IL-6 cytokine production are given in **Figure 6.14** and **Figure 6.15**. The tumour necrosis factor-alpha (TNF-α) cytokine release profile from RAW cells exposed to mono-halide Li/Al-LDHs is constant and does not change with the intercalated guest anion (**Figure 6.14**). However, increasing the size of the anion's radius induces an increase in interleukin-6 (IL-6) production (**Figure 6.15**), and therefore there is some evidence of a tuneable immune response.

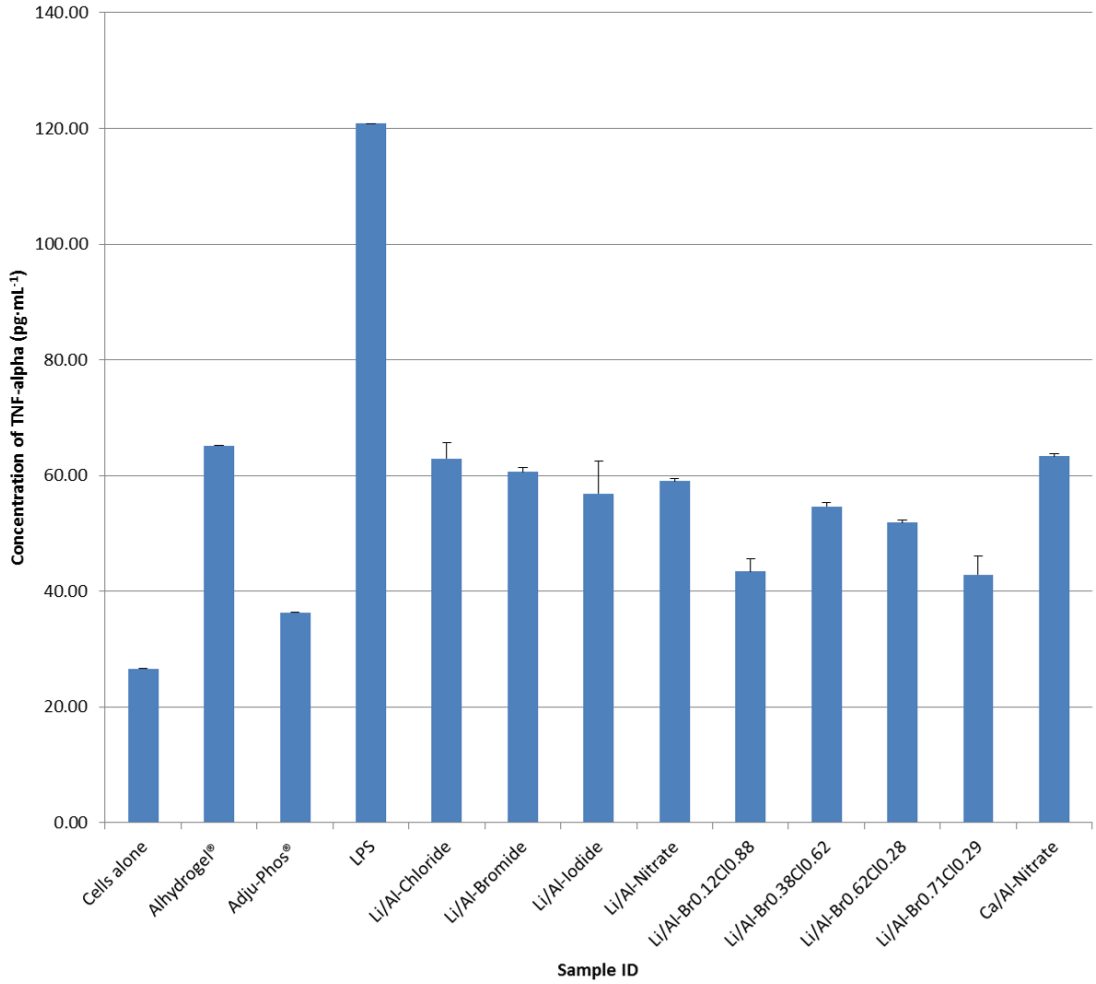

Figure 6.14: ***TNF-α production in response to LDH adjuvants. RAW264.7 macrophages were exposed to LDH materials at 476 μg mL^{-1} for 24 hours. Cell free supernatants were collected and TNF-α cytokine secretions were quantified*** **via** ***ELISA assays with n = 3 and each independent experiment containing nine replicates. Commercial alums (Alhydrogel and Adju-Phos) were used for comparative purposes at the same concentrations as the Li/Al-LDH materials and lipopolysaccharide (LPS) was used as a positive control.***

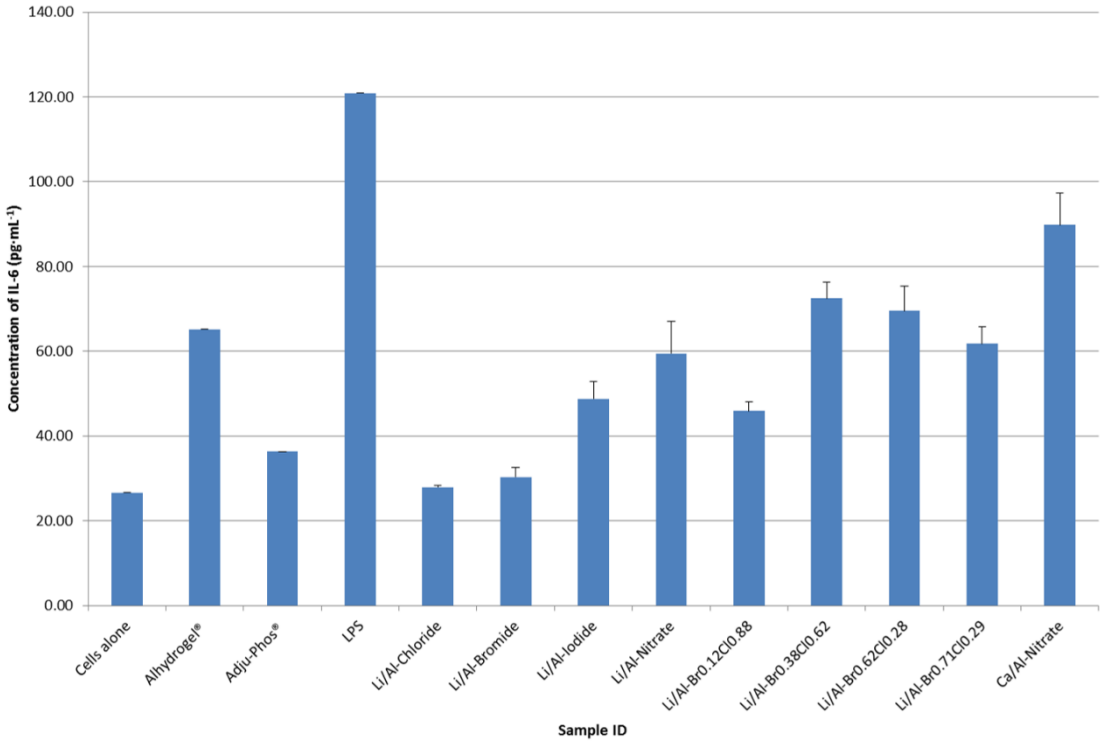

Figure 6.15: ***IL-6 production in response to LDH adjuvants. RAW264.7 macrophages were exposed to LDH materials at 476 µg mL^{-1} for 24 hours. Cell free supernatants were collected and IL-6 cytokine secretions were quantified via ELISA assays with n = 3 and each independent experiment containing nine replicates. Commercial alums (Alhydrogel and Adju-Phos) were used for comparative purposes at the same concentrations as the Li/Al-LDH materials and lipopolysaccharide (LPS) was used as a positive control.***

The cytokine profiles for the di-halide Li/Al-LDH materials are not consistent with the trend observed with the mono-halide species (**Figure 6.14** and **Figure 6.15**). For both TNF-α and IL-6, Li/Al-$Br_{0.38}Cl_{0.62}$ and Li/Al-$Br_{0.62}Cl_{0.38}$ cause the production of greater amounts of the cytokines than do Li/Al-$Br_{0.12}Cl_{0.88}$ and Li/Al-$Br_{0.71}Cl_{0.29}$. Therefore, the relative composition of the two anions in the interlayer region influences the immune response in a different manner. The Li/Al-$Br_{0.12}Cl_{0.88}$ and Li/Al-$Br_{0.71}Cl_{0.29}$ samples have the highest chloride and bromide content, respectively, and exhibit similar secretion patterns for both cytokines assayed. The two intermediate samples (Li/Al-$Br_{0.38}Cl_{0.62}$ and Li/Al-$Br_{0.62}Cl_{0.38}$) also have similar cytokine secretion patterns. Therefore, the dominant anion does not appear to impact the immune response elicited, and it may be that it is the relative composition of the two that modulates the cytokine output.

Overall, the *in vitro* data provides evidence that the LDH samples are likely to be safe to dose as adjuvants, and the data obtained indicate that it may be possible to tune the immune response by varying the composition of the materials.

Correlations between immune responses and zeta potentials will be explored in **Section 6.8**.

6.7.3 Fluorescent Microscopy

All LDH materials were labelled with FITC and the RAW264.7 cells with the DAPI nuclear stain. The Li/Al-Chloride/Bromide/Iodide/Nitrate materials' interaction with the RAW cells was visualised with fluorescent microscopy, with representative images given in **Figure 6.16**. The mixed halide species were also assessed. All the LDH particles are rod-like in appearance under the fluorescent microscope, which suggests that aggregation may have occurred since they exhibit platelet morphology by SEM analysis (**Figure 6.5**). There is some evidence of cellular attachment to the surface of the LDH particles. This is consistent with the suggestion of Flach *et al*. that lipid membrane disturbances contribute to the immunogenic effect of alum adjuvants [22].

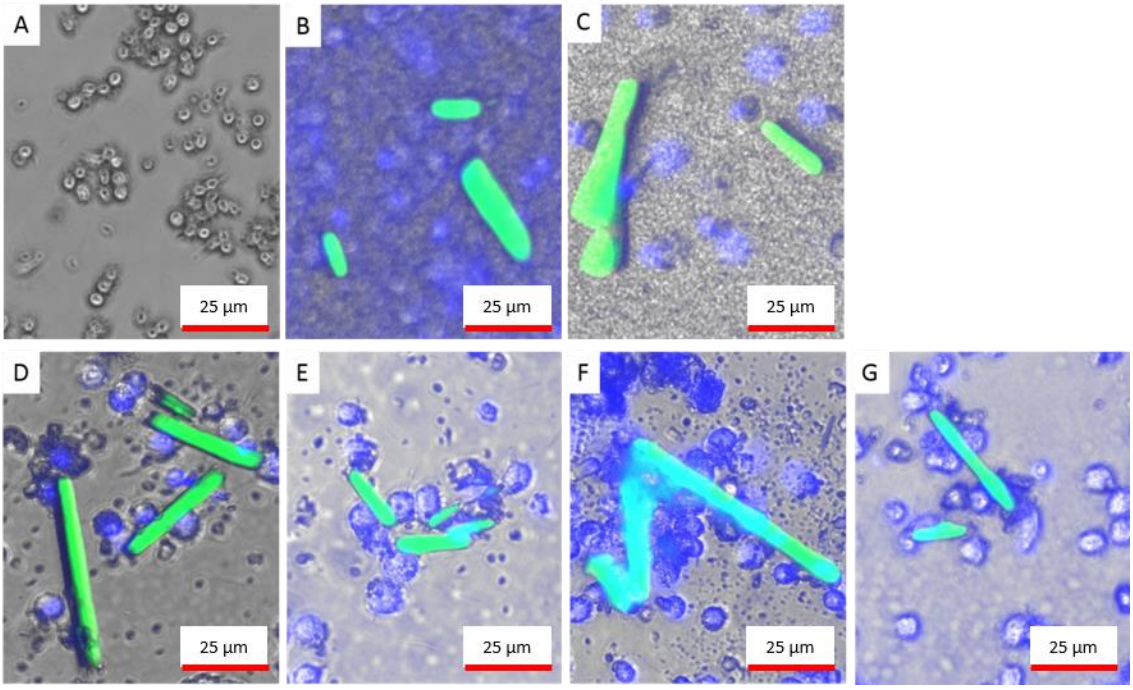

***Figure 6.16:* Fluorescent microscopy with FITC-labelled LDH materials (green) with DAPI nuclear staining of the RAW264.7 cell (blue); (A) cells alone, (B) Alhydrogel, (C) Adju-Phos, (D) LDH-Chloride, (E) LDH-Bromide, (F) LDH-Iodide; and (G) LDH-Nitrate.**

Confocal microscopy was attempted, but the adherent nature of the RAW264.7 cells meant that they ruptured during transfer from a 24 well plate to a microscope slide for imaging, and thus no images could be obtained.

6.8 Immune Response Predictions

6.8.1 Experimental Parameters

Correlations were determined between various experimental parameters and the immunological output of RAW264.7 cells in attempts to deduce a means of predicting the immune response induced by these materials. The results summarised in **Table 6.20** compare the cytokine concentrations with particle size and zeta potential measurements.

Table 6.20: ***Relationships between experimental parameters and immunoassay data for the single halide-intercalated Li/Al-LDH materials; with particle size (µm) being derived by SEM analysis and zeta potential measurements being recorded in mV.***

Experimental parameter (x)	Cytokine concentration / pg mL^{-1} (y)	Equation	R^2 correlation
Particle size	TNF-α	y = 1.0191x + 52.25	0.9858
	IL-6	y = -3.7541x + 64.72	0.9697
ZP in UP-water	TNF-α	y = 0.2104x + 50.288	0.9728
	IL-6	y = -0.7858x + 72.45	0.9835
ZP in UP-water (10 minutes)	TNF-α	y = 0.2058x + 51.245	0.9991
	IL-6	y = -0.7381x + 67.563	0.9318
ZP in PBS	TNF-α	y = 1.6136x + 79.228	0.8405
	IL-6	y = -6.4935x – 41.164	0.9865
ZP in PBS (10 minutes)	TNF-α	y = 0.5948x + 67.077	0.2755
	IL-6	y = -3.1536x – 1.1369	0.5613

It is evident that the immunological output of both TNF-α and IL-6 from RAW264.7 cells can be reliably predicted using physicochemical properties of the mono-halide LDH samples (see **Figure 6.17A and B** and **Table 6.20**). Both TNF-α and IL-6 production appear to be strongly correlated with the particle size data and zeta potential measurements obtained using UP-water (initial and 10 minutes) and PBS (initial measurements only). In contrast, there are no clear relationships observed when comparing the immunological output of RAW264.7 cells to the zeta potential measurements recorded with PBS as the dispersant at 10 minutes after forming the dispersion (R^2 = 0.2755 and 0.5613 for TNF-α and IL-6, respectively). The experimental parameter which gives the best correlations to both cytokines is the zeta potential measured initially with UP-water, with R^2 values of 0.9728 and 0.9835 for TNF-α and IL-6 secretions, respectively (**Figure 6.17A and B**).

Therefore, it is clear that the particle size and zeta potential of the mono-halide Li/Al-LDH materials can influence the secretion of TNF-α and IL-6 cytokines by RAW264.7 cells which may mean tuning the immune response is possible by varying the size of the LDHs. Good correlations with both are to be expected because it was found earlier (**Section 6.5.3**) that particle size and zeta potential are highly correlated. Similar relationships are also observed for the zeta potentials measured in UP-water, providing another potential means of tailoring the immune response *in vitro*.

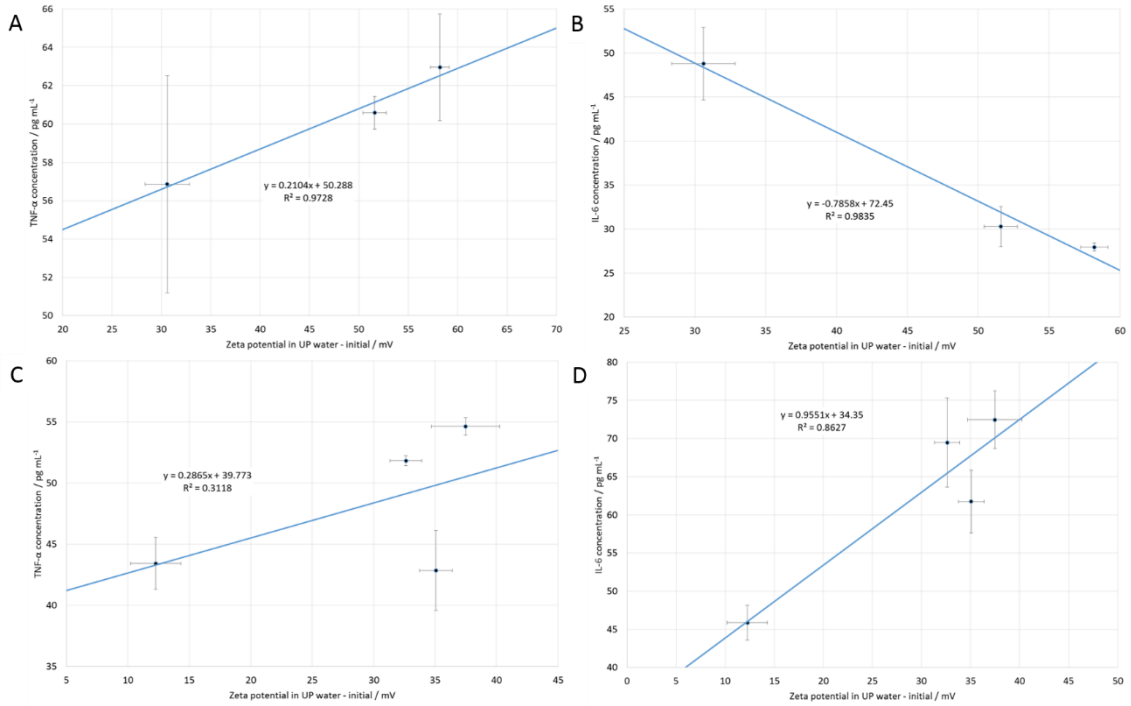

Figure 6.17: ***Graphical representation showing the relationships between the zeta potential measurements recorded in UP water immediately after dispersion formation and the mono-halide Li/Al-LDH materials' production of (A) TNF-α and (B) IL-6, and also those obtained with the di-halide species in terms of (C) TNF-α and (D) IL-6.***

For the di-halide Li/Al-LDH materials, there are no clear relationships between the physicochemical properties of the compounds and the immune response provoked (**Figure 6.17C and D** and **Table 6.21**).

Table 6.21: ***Relationships between experimental parameters and immunoassay data for the mixed halide-intercalated Li/Al-LDH materials. Particle size is measured in µm and zeta potentials are recorded in mV.***

Experimental parameter (x)	Cytokine concentration / pg mL^{-1} (y)	Equation	R^2 correlation
Particle size	TNF-α	y = 0.7339x + 24.225	0.8454
	IL-6	y = 0.8762x + 33.782	0.3001
ZP in UP-water	TNF-α	y = 0.2865x + 39.773	0.3118
	IL-6	y = 0.9551x + 34.35	0.8627
ZP in UP-water (10 minutes)	TNF-α	y = 0.139x + 44.343	0.0493
	IL-6	y = 0.8659x + 38.458	0.4761
ZP in PBS	TNF-α	y = 0.2807x + 53.462	0.0563
	IL-6	y = 1.7704x + 95.667	0.5572
ZP in PBS (10 minutes)	TNF-α	y = 0.8624x + 63.968	0.3815
	IL-6	y = 2.2962x + 104.41	0.6736

Attempts were also made to use the combined dataset from both the mono- and mixed-halide LDHs in order to obtain more insight: the findings are summarised in **Table 6.22**. Representative plots may be found in **Figure 6.18**, with all other plots located in **Appendix 4.**

***Table 6.22:* Relationships between experimental parameters and immunoassay data of the combined chloride/bromide mono- and di-halide intercalated Li/Al-LDH materials. Particle sizes are measured in µm and zeta potentials in mV.**

Experimental parameter (x)	Cytokine concentration / pg mL^{-1} (y)	Equation	R^2 correlation
Particle size	TNF-α	y = -0.3349x + 61.052	0.2808
	IL-6	y = 1.3231x + 18.355	0.8167
ZP in UP-water	TNF-α	y = 0.4528x + 35.565	0.7476
	IL-6	y = -0.5856x + 73.474	0.2330
ZP in UP-water (10 minutes)	TNF-α	y = 0.4465x + 36.857	0.6017
	IL-6	y = -0.7722x + 78.718	0.3353
ZP in PBS	TNF-α	y = 1.0332x + 69.389	0.4823
	IL-6	y = -1.3727x + 29.143	0.1586
ZP in PBS (10 minutes)	TNF-α	y = 1.3065x + 73.184	0.6858
	IL-6	y = -1.56+ 26.855	0.1822

It is evident that the correlations in **Table 6.22** are mainly representative of the trends observed for the di-halide species. The only truly convincing correlation is obtained for IL-6 production and the particle size of the Li/Al-LDH materials (**Figure 6.18**).

Overall, the correlations for the combined datasets are weaker than those obtained for the mono-halide species. However, in favourable instances it is possible to predict the immunological output of RAW264.7 macrophages following exposure to Li/Al-LDH materials *via* other experimental data obtained for these samples, when the two different classes of Li/Al-LDH material are considered separately.

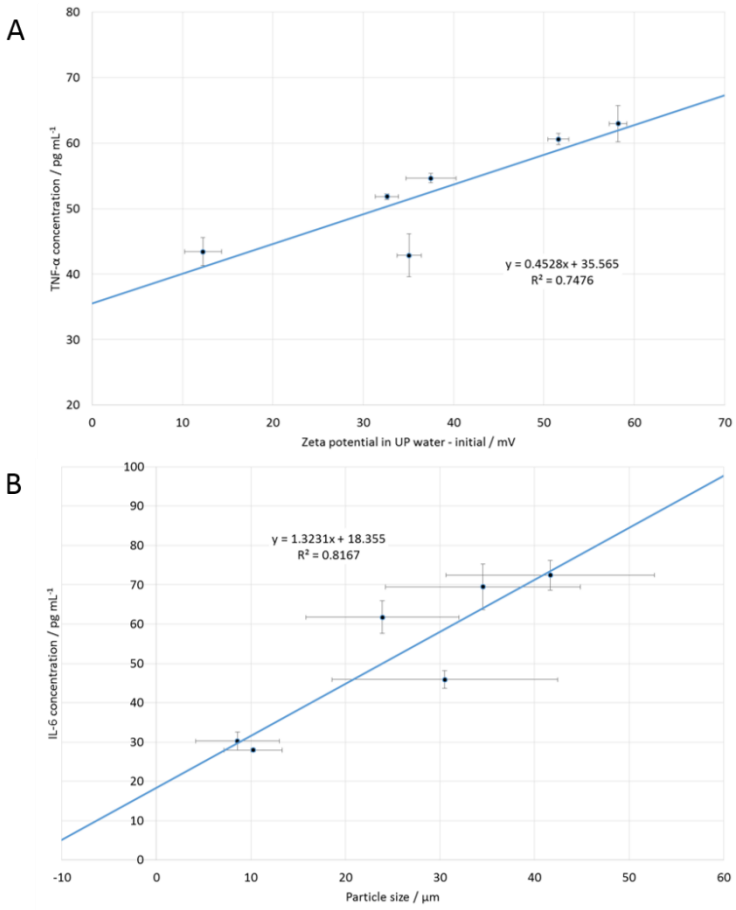

***Figure 6.18:* Graphical representation of (A) the effect of zeta potential in UP water immediately after dispersion formation with the combined mono- and di-halide Li/Al-LDH materials' inducing the simulation of TNF-α and (B) the effect of particle size on the production of IL-6 by RAW cells.**

6.8.2 Correlating Immune Response to Calculated Unit Cell Parameters

The principle of attempting to predict the immune response was expanded to use the *in silico* data obtained through structural optimisation of the Li/Al-LDH materials and also the difference in electronegativity, calculated by subtracting the electronegativity of the metal cation from the guest anionic species [23]. All calculated data for the mono-halide Li/Al-LDH samples appear to be strongly predictive of the concentration of cytokines produced by RAW cells exposed to them (minimum R^2 = 0.9090). The findings are summarised in **Table 6.23**, and exemplar plots are presented in **Figure 4.19**, with all other plots located in **Appendix 4**.

Table 6.23: ***Relationships between calculated and immunoassay data for the mono-halide Li/Al-LDH materials. The electronegativity difference is obtained by subtracting the electronegativity of the metal cation from that of the guest anionic species.***

In silico parameter (x)	Cytokine concentration / pg mL^{-1} (y)	Equation	R^2 correlation
a / Å	TNF-α	y = 846.98x + 4479.7	0.9867
	IL-6	y = 3116.7x – 16227	0.9684
Interlayer spacing / Å	TNF-α	y = -6.7356x + 160.94	0.9978
	IL-6	y = 24.287x – 327.82	0.9402
Difference in Electronegativity	TNF-α	y = 12.215x + 36.355	0.9999
	IL-6	y = -43.263x – 612.42	0.9090
Energy / eV	TNF-α	y = -6.8425x – 612.42	0.9999
	IL-6	y = 24.404x + 2434.3	0.9218
Volume / $Å^3$	TNF-α	y = -0.288x + 161.69	0.9988
	IL-6	y = 1.0344x – 329.06	0.9337

As previously described in **Section 6.5.3**, the zeta potential measurements of the mono-halide materials are closely related with calculated energy of the modelled structures, and therefore it seems that these energy values are a plausible proxy for the zeta potential. TNF-α and IL-6 cytokine production by the RAW264.7 cells is strongly correlated (R^2 = 0.9999 and 0.9218, respectively) with this energy value (see **Figure 6.19**).

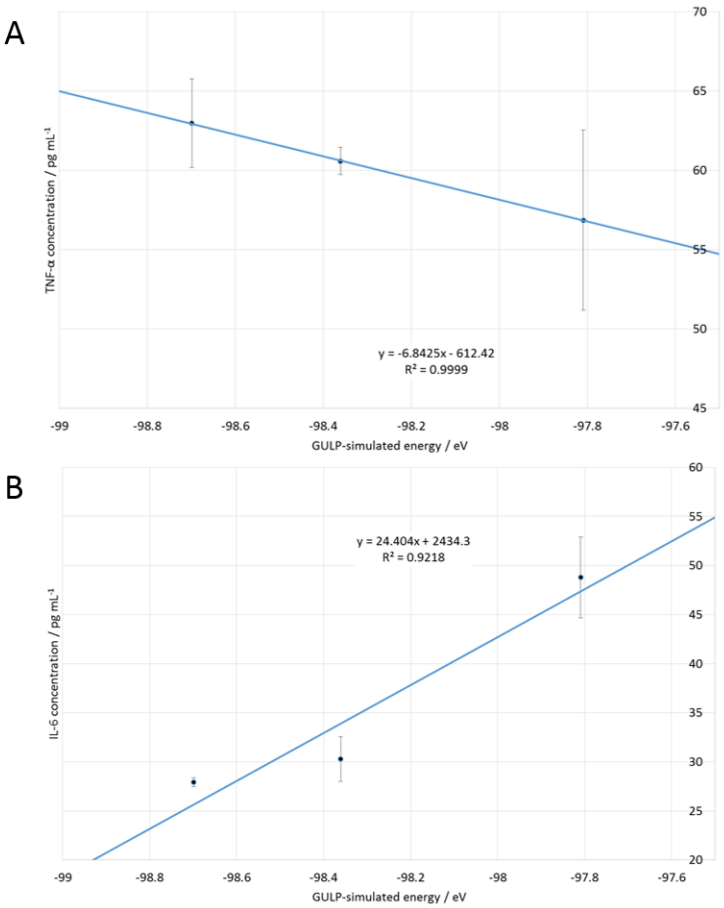

***Figure 6.19:* Graphical representation of the calculated lattice energy values with (A) TNF-α and (B) IL-6 concentrations secreted by RAW264.7 cells.**

It is not possible to reliably predict the cytokine production by RAW264.7 cells in response to di-halide Li/Al-LDHs; the highest R^2 is 0.4205 (**Table 6.24**). When combining the mono- and di-halide species' datasets together, the correlations were even weaker than those detailed in **Table 6.24** for the di-halide Li/Al-LDH materials.

***Table 6.24:* Relationships between calculated and immunoassay data of the di-halide Li/Al-LDH materials.**

In silico parameter (x)	Cytokine concentration / pg mL^{-1} (y)	Equation	R^2 correlation
a / Å	TNF-α	y = 1305.3x – 6760.5	0.0103
	IL-6	y = 16258x – 84743	0.3995
Interlayer spacing / Å	TNF-α	y = 7.298x – 59.265	0.0109
	IL-6	y = 89.037x – 1248.5	0.4205
Electronegativity	TNF-α	y = -6.7916x + 62.366	0.0037
	IL-6	y = -134.13x + 342.46	0.3588
Energy / eV	TNF-α	y = 6.1685x + 655.96	0.0092
	IL-6	y = 80.872x + 8030.6	0.3938
Volume / Å^3	TNF-α	y = 0.300x – 55.897	0.0108
	IL-6	y = 3.6649x – 1209.1	0.4023

Overall, it is evident that the pure halide Li/Al-LDH materials exhibit strong relationships between their simulated parameters and their *in vitro* cytokine production, but this is not observed for the di-halide systems and when the datasets are combined. This may arise due to the complexity of the Cl/Br materials, which means that correlating to only one parameter is insufficient in determining a strong relationship. Another reason for the complexity may be explained in part by the use of fractional occupancies to predict the location of both halide anions in the interlayer region, thus the weighted average resembles a Li/Al-Chloride material. Quantum calculations would enable all configurations of the di-halide LDHs to be considered; however, the issues within the model used here would be magnified with *ab initio* calculations at a great computational cost.

6.8.3 Immunological Equation

As previously described in **Section 1.3.3**, Williams and co-workers [1] deduced an immunological equation (**Equation 6.1**) to predict the magnitude of the *in vitro* immune response elicited following exposure to LDH materials. The A, B, and C_i parameters in **Equation 6.1** are coefficients for a given immunological response, and the P_i component is the value for each of three physiochemical properties.

Equation 6.1

$$\ln(response) = A + B\sum_{i=1}^{i=3} C_i P_i$$

The three physicochemical properties involved in the published work are the mono- or divalent cationic radius, the interlayer spacing and the zeta potential [1]. The former two properties can easily be obtained through the literature [24], whilst the latter has previously always been deduced through experimental measurements. Here we endeavoured to replace this with parameters generated from the *in silico* models described in **Section 6.3**.

The RStudio statistics package was utilised [25], with parameters obtained from *in silico* modelling being used in place of the experimental physicochemical properties of the LDHs. The aim was to try to correlate the response of human dendritic cells to these parameters by using the previously reported datasets [1]. All the physicochemical properties of the LDHs, both measured and simulated, were standardised to have mean of 0 and unit variance before being entered into the model. Every combination of three properties was assessed for its ability to reliably predict the immune response *a priori*, with three different arrangements proving to be good alternatives for the existing trio. These were (i) the *a*-parameter, interlayer spacing and GULP-simulated energy, (ii) the interlayer spacing, GULP-simulated energy and volume, and (iii) the *a*-parameter, GULP-simulated energy and volume. The GULP-simulated value for energy can replace the zeta potential component of the original set of physicochemical properties [1]; details of the A, B and C_i constants generated when doing so are listed in **Table 6.25**. It is important to note that the C_i values are correlation coefficients, which are multiplied by the standardised value for each corresponding physicochemical property for the C_iP_i component of **Equation 6.1**.

Table 6.25: ***Coefficient responses of human dendritic cells (DC) to LDHs* in vitro *can be expressed by Equation 6.1. Values for the constants A and B, and the coefficients C_i are shown for each respective DC response measured. For TNF-α and IL-6 the formula calculates ln (response / ng mL^{-1}), for other cytokines and chemokines it gives log (response / pg mL^{-1}), and for the cell surface markers (Section 1.2.1.3.2) ln (response / MFI). For any give response, the relative magnitudes of C_i for the three standardised (to have mean 0 and unit variance) properties are proportional to the influence that the respective properties have in controlling that response. The top table depicts data from Williams and co-workers [1] and the bottom table data using GULP-simulated energy as a proxy for the zeta potential.***

Response	A	B	C_i			Correlation
			Ionic radius (M^+ or M^{2+})	Interlayer spacing	Zeta potential	
IL-6	-3.244	1.899	0.883	0.053	-1.050	0.884
IL-8	7.735	-0.554	-1.032	0.162	1.041	0.556
IL-12p70	1.747	1.223	1.033	0.060	-1.122	0.843
TNF-α	-1.062	2.262	1.008	0.036	-1.122	0.909
IL-1β	2.790	2.941	0.911	0.087	-1.054	0.927
CD274	7.194	0.725	0.791	-0.095	-0.968	0.848
CD40	7.287	0.405	0.501	-0.011	-0.766	0.888
CD86	6.691	0.768	0.979	0.065	-1.099	0.921
Response	A	B	C_i			**Correlation**
			Ionic radius (M^+ or M^{2+})	Interlayer spacing	Energy	
IL-6	-3.359	1.752	-0.032	-0.172	-0.171	0.830
IL-8	7.706	-0.789	-0.091	0.149	0.218	0.576
IL-12p70	1.678	1.142	0.046	-0.115	-0.244	0.799
TNF-α	-1.746	2.151	0.056	-0.202	-0.209	0.893
IL-1β	2.645	2.914	-0.024	-0.037	-0.287	0.921
CD274	7.190	0.818	-0.045	-0.218	0.104	0.791
CD40	7.278	0.386	-0.181	-0.136	-0.118	0.858
CD86	6.656	0.752	0.0339	-0.165	-0.238	0.856

The calculated lattice energy within the system allows for direct replacement of the zeta potential whilst maintaining the reliability of the equation's predictions (**Table 6.25**), with the correlations being similar to those obtained in the literature. For example, for TNF-α, the literature correlation is 0.909 and that obtained using the zeta potential-proxy is 0.893. In one instance, the proxy model performs better than the published work, with an IL-6 correlation of 0.576, compared to the literature value of 0.556.

Williams *et al.* also were able to predict the *in vitro* response by dendritic cells to two untested LDHs, $[LiAl_2(OH)_6]NO_3{\cdot}yH_2O$ and $[Mg_2Al(OH)_6]Cl{\cdot}yH_2O$ [1]. This can also be achieved when replacing the zeta potential value with the simulated energy (**Figure 6.20**).

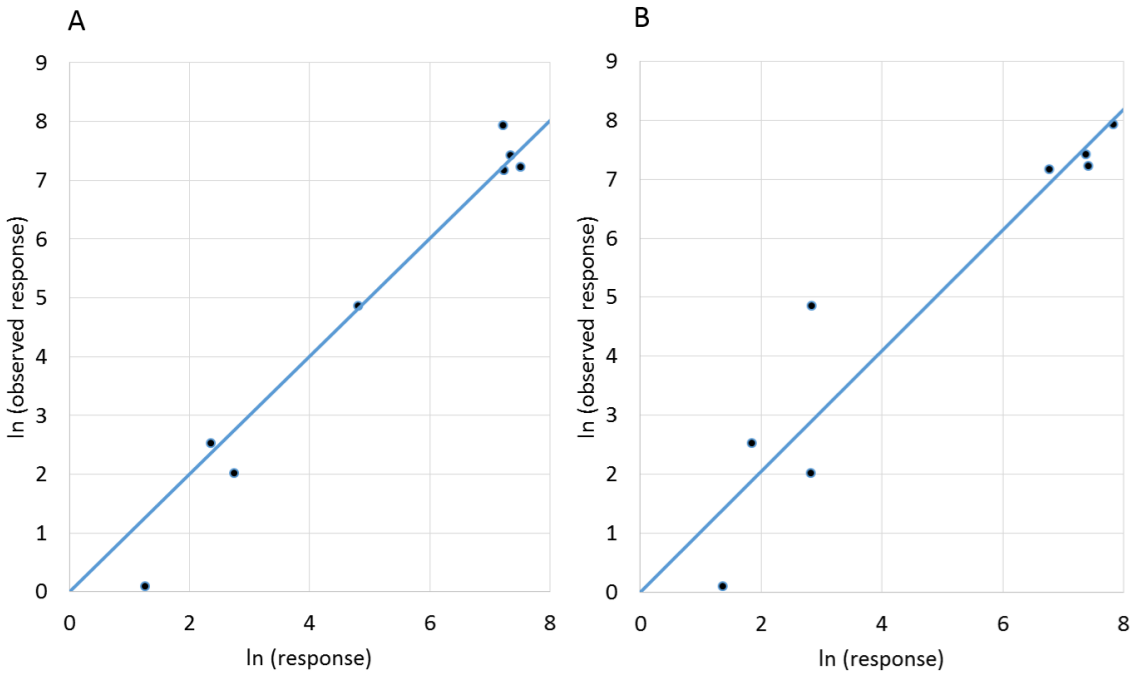

***Figure 6.20:** Multiple dendritic cell (DC) responses induced by newly synthesised LDHs can be predicted with a high degree of accuracy. DC response to $LiAl_2$-NO_3 were predicted with Equation 6.1 following calibration of the model using (A) experimental parameters from Williams and co-workers [1] and (B) replacing the zeta potential with the energy calculated in GULP. The observed responses are shown along a straight line of gradient 1, and the predicted ln responses as squares on the same plot.*

From the plots given in **Figure 6.20** it is clear that the use of a simulated parameter provides a reliable substitution for the experimental zeta potential measurements with the Li/Al-Nitrate LDH, this is also true for the Mg/Al-Chloride species with plots given in **Figure 6.21**.

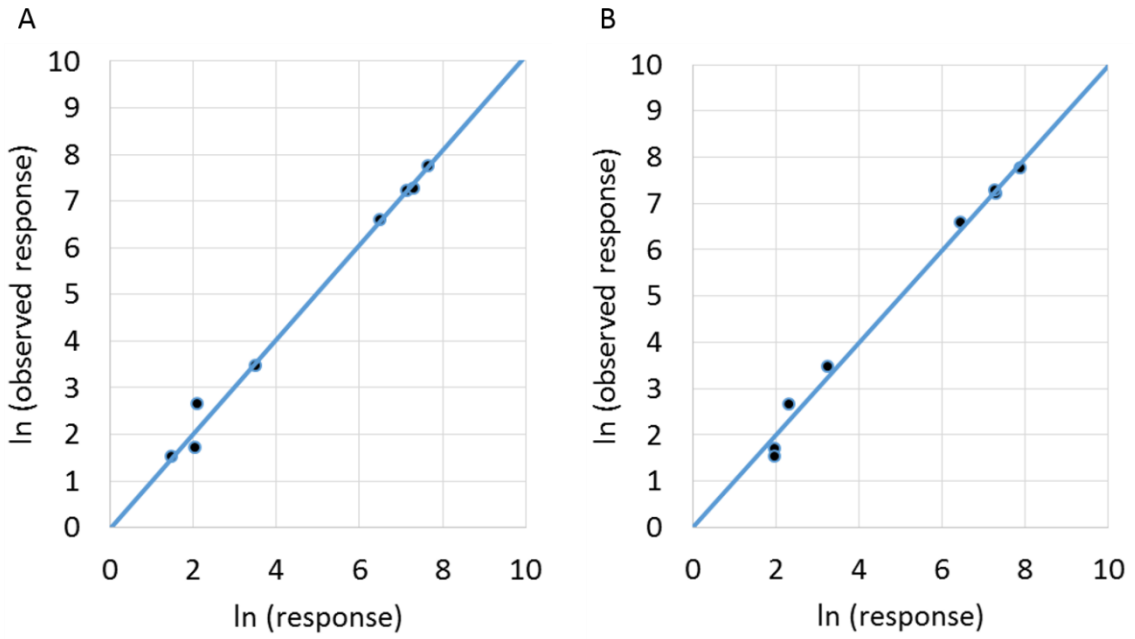

Figure 6.21: ***Multiple dendritic cell (DC) responses induced by newly synthesised LDHs can be predicted with a high degree of accuracy. DC response to Mg_2Al-Cl were predicted with Equation 6.1 following calibration of the model using (A) experimental parameters from Williams and co-workers [1] and (B) replacing the zeta potential with the energy calculated in GULP. The observed responses are shown along a straight line of gradient 1, and the predicted ln responses as squares on the same plot.***

It is perhaps at first sight surprising that a more negative lattice energy should lead to an improved immune response (**Figure 6.19** and **Table 6.23**). More negative lattice energies are associated with increased stability and reduced solubility of a system, and so if the LDHs were functioning through dissolution to free ions into solution, we would expect to see the reverse effect. The findings reported here provide a strong indication that dissolution is not a particularly significant factor in considering the immune response. LDH materials exhibit poor solubility at physiological pH and thus are unlikely to dissolute [26]. It is our hypothesis that the reason such a correlation with lattice energy is seen is because of the inter-relationship between the lattice energy and zeta potential; there is literature to suggest that alum adjuvants act through interactions with the cell membrane [22], and the zeta potential will affect the strength of these and thus can provide a basis for varying the adjuvanticity. Further experiments will be needed to confirm this, but it appears a viable explanation given the data presented here, and also in the literature [27].

Furthermore, three other combinations [(i) the *a*-parameter, interlayer spacing and GULP-simulated energy, (ii) the interlayer spacing, GULP-simulated energy and volume, and (iii) the *a*-parameter, GULP-simulated energy and volume] proved to be successful alternatives when predicting the *in vitro* immune response. Two of these conserved one of the original physicochemical properties used in the equation (interlayer spacing), with the remainder of the parameters being other simulated properties (**Table 6.26**). As discussed in **Section 6.5.3**, the calculated values for lattice energy, volume and *a*-parameter are highly correlated to the zeta potential (measured in UP water), and thus all can act as proxies for this value in the immunological equation. As for the energy, we believe that it is the fact that the volume and *a*-parameter can act as proxy values for the zeta potential, and the effect this has on interactions with the cell membrane, which permits them to be used to predict the immune response.

Table 6.26: ***Coefficient responses of human DC to LDHs in vitro can be expressed by Equation 6.1. Values for the constants A and B, and the coefficients C_i are shown for each respective DC response measured. The a-parameter, energy and interlayer spacing values used are simulated values obtained via GULP calculations.***

Response	A	B	C_i			Correlation
			a-parameter	Interlayer spacing	Energy	
IL-6	-3.376	1.771	0.145	-0.306	-0.228	0.827
IL-8	7.685	0.943	0.621	-0.319	-0.658	0.612
IL-12p70	1.675	1.190	0.344	-0.249	-0.491	0.813
TNF-α	-1.760	2.188	0.235	-0.244	-0.391	0.896
IL-1β	2.637	2.921	-0.727	-0.817	1.117	0.922
CD274	7.173	0.885	-0.774	-1.326	1.630	0.795
CD40	7.280	0.364	0.071	0.370	-0.733	0.818
CD86	6.652	0.798	-0.833	-1.149	1.523	0.860
Response	A	B	C_i			**Correlation**
			Interlayer spacing	Energy	Volume	
IL-6	-3.387	-1.797	0.579	0.217	-0.385	0.829
IL-8	7.686	-0.885	0.949	0.448	-0.974	0.601
IL-12p70	1.658	-1.277	0.835	0.434	-0.841	0.839
TNF-α	-1.773	-2.217	0.581	0.338	-0.493	0.898
IL-1β	2.642	-2.914	0.099	0.287	-0.003	0.922
CD274	7.178	-0.820	0.441	0.210	-0.243	0.768
CD40	7.280	-0.367	-0.372	-0.082	0.723	0.822
CD86	6.656	-0.750	0.235	0.268	-0.103	0.856
Response	A	B	C_i			**Correlation**
			a-parameter	Energy	Volume	
IL-6	-3.363	1.724	0.349	-0.285	-0.429	0.822
IL-8	7.688	0.957	0.880	-0.724	-0.482	0.613
IL-12p70	1.686	1.142	0.468	-0.534	-0.310	0.800
TNF-α	-1.748	2.154	0.399	-0.439	-0.340	0.893
IL-1β	2.658	2.908	-0.004	-0.261	-0.104	0.922
CD274	7.193	0.785	0.091	-0.159	-0.297	0.771
CD40	7.279	0.370	-0.344	0.196	-0.152	0.820
CD86	6.666	0.741	-0.024	-0.198	-0.147	0.855

Comparing the published data in **Table 6.25** to that presented in **Table 6.26** for the three sets of alternative physicochemical properties, it is evident that the majority of the correlations for the various chemokines, cytokines and cell surface markers are similar to those obtained in the published work, thereby suggesting a purely *in silico* means of predicting the immunological response *in vitro*. For example, the literature correlation value for the cytokine TNF-α, is 0.909; the correlations obtained using the alternative combinations range from 0.893 to 0.898

The predicted responses for the cytokine, chemokine and membrane molecules of human dendritic cells, following application of Li/Al-Nitrate, are plotted in **Figure 6.22** against the observed responses (both natural logarithms) using the three alternative combinations detailed in **Table 6.26**. This visual representation highlights how similar predictions are obtained using each set of properties, thereby emphasising that they are suitable alternatives to the published- and proxy-models. Therefore, it appears that we can predict the immune response in human dendritic cells using purely simulated properties, which means that in the future *in silico* adjuvant design may be possible.

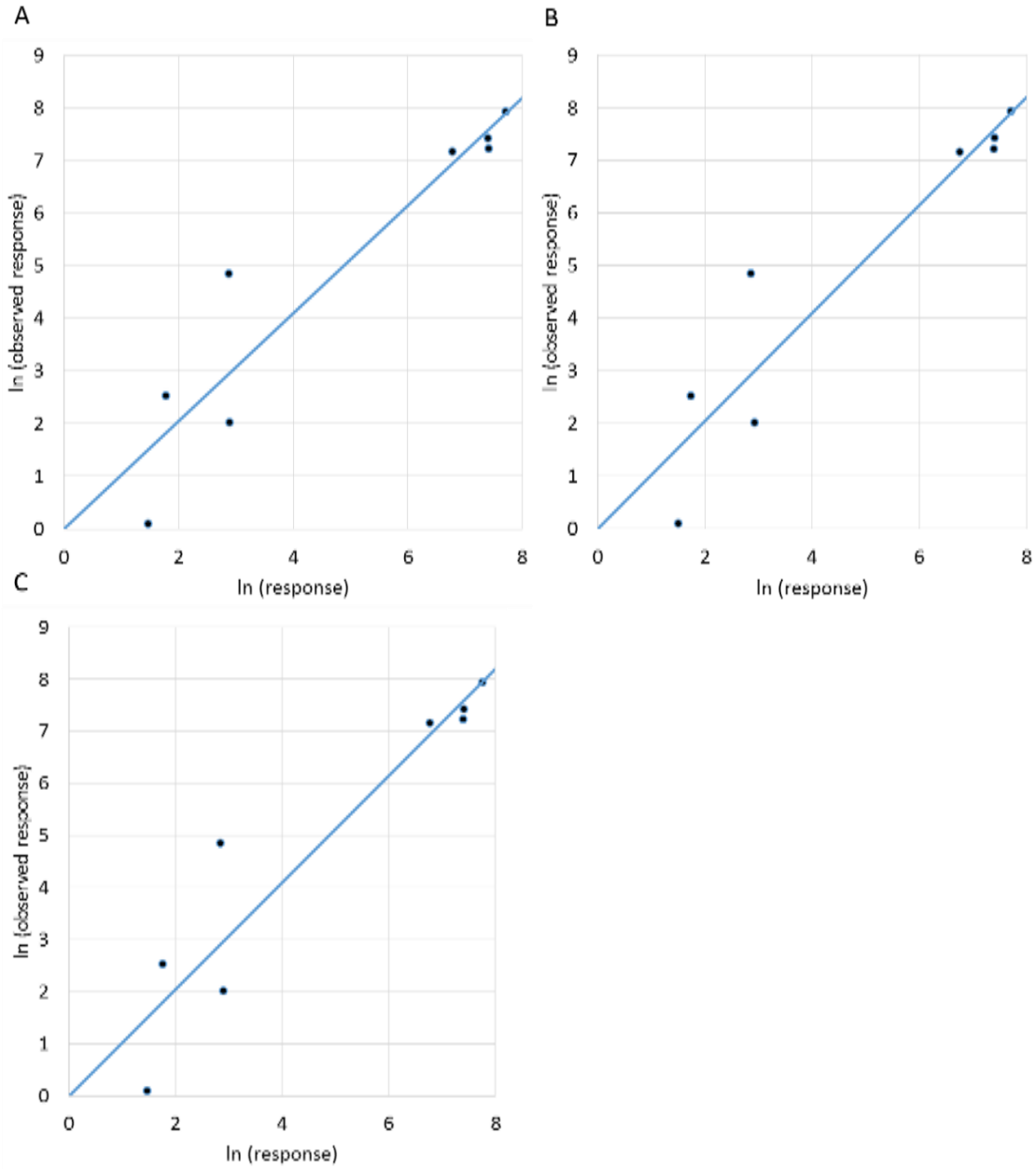

Figure 6.22: ***Multiple dendritic cell (DC) responses induced by newly synthesised LDHs can be predicted with a high degree of accuracy. DC response to $LiAl_2$-NO_3 were predicted with Equation 6.1 following calibration of the model using data from Williams and co-workers [1]. The observed responses are shown along a straight line of gradient 1, and the predicted ln responses as squares on the same plot. The plots present the alternative combinations with (A) a-parameter, interlayer spacing and energy, (B) a-parameter, energy and volume, and (C) interlayer spacing, energy and volume.***

6.9 Conclusions

Anhydrous LDH structures could be successfully modelled with the GULP simulation code [2] and implementation of the ClayFF force field [5]. Following synthesis and characterisation of a range of LDH materials, comparisons were performed between experimentally measured zeta potentials and simulated structural parameters, with the GULP-simulated value for energy proving a good proxy for this in favourable cases.

The mono-halide Li/Al-LDH materials' physicochemical properties appeared to be strongly causative of the immunological output of RAW264.7 cells; however, the same outcome was not observed for the di-halide systems, with few convincing relationships evident. A possible reason for this may be due to the increased complexity of the di-halide LDHs, such that relating properties to only one other parameter is insufficient in deducing strong connections in the data.

A key goal of this work was to be able to replace the zeta potential in the equation previously derived to predict the immune response from the physicochemical properties of LDHs. It was found that the energy of the structure as simulated *in silico* is able to fulfil this goal. Further, three alternative combinations of properties have been found to reliably predict the magnitude of the immunological response *in vitro*. All three include the energy value obtained from GULP with the other parameter in the trio being (a) *a*-parameter and interlayer spacing, (b) interlayer spacing and volume, and (c) *a*-parameter and volume. Therefore, these *in silico* properties of the LDH materials appear to be highly useful in predicting a material's immunogenical effect *in vitro*.

These findings offer the potential to screen many LDH structures *in silico* and predict their immunological effect with no laboratory work requirement, ultimately allowing an *in silico* – down-selection of lead candidates for further exploration and significantly reducing the cost and animal requirements of vaccine development.

6.10 References

1. Williams, G.R., et al., *Immunity induced by a broad class of inorganic crystalline materials is directly controlled by their chemistry.* Journal of Experimental Medicine, 2014. **211**(6): p. 1019-1025.
2. Gale, J.D., *GULP: A computer program for the symmetry-adapted simulation of solids.* Journal of the Chemical Society-Faraday Transactions, 1997. **93**(4): p. 629-637.
3. Fleming, S. *Graphical Display Interface for Structures (G D I S).* http://gdis.sourceforge.net/
4. *Lipid maps thawing and passage procedure for RAW264.7*. 2004 08/11/2004; 2:[Available from: http://www.lipidmaps.org/protocols/PP0000000100.pdf.
5. Cygan, R.T., Liang J.J., and Kalinichev A.G., *Molecular models of hydroxide, oxyhydroxide, and clay phases and the development of a general force field.* Journal of Physical Chemistry B, 2004. **108**(4): p. 1255-1266.
6. Bish, D.L., *Rietveld Refinement of the Kaolinite Structure at 1.5-K.* Clays and Clay Minerals, 1993. **41**(6): p. 738-744.
7. Desgranges, L., et al., *Hydrogen Thermal Motion in Calcium Hydroxide - Ca(O H)2.* Acta Crystallographica Section B-Structural Science, 1993. **49**: p. 812-817.
8. Lee, J.H. and Guggenheim S., *Single-Crystal X-Ray Refinement of Pyrophyllite-1tc.* American Mineralogist, 1981. **66**(3-4): p. 350-357.
9. Saalfeld, H. and Wedde M., *Refinement of Crystal-Structure of Gibbsite, Al(O H)3.* Zeitschrift Fur Kristallographie, 1974. **139**(1-2): p. 129-135.
10. Thiel, J.P., Chiang C.K., and Poeppelmeier K.R., *Structure of Lithium Aluminum Hydroxide Dihydrate (Li Al2 (O H)7.2 H2 O).* Chemistry of Materials, 1993. **5**(3): p. 297-304.
11. Gale, J.D.,*Query about ClayFF for GULP*, C.N. Maughan, Editor. 2014. p. 1
12. Fogg, A.M., et al., *Predicting guest orientations in layered double hydroxide intercalates.* Chemistry of Materials, 1999. **11**(5): p. 1194-1200.
13. Archer, T.D., et al., *An interatomic potential model for carbonates allowing for polarization effects.* Physics and Chemistry of Minerals, 2003. **30**(7): p. 416-424.
14. Zintl, E., Harder, A., Dauth, B., *Gitterstruktur der oxydem sulfide, selenide und telluride des lithiums, natriums und kaliums.* Zeitschrift fur Elektrochemie und angewandte physikalische chemie, 1934. **40**(8): p. 6.
15. Besserguenev, A.V., et al., *Synthesis and Structure of the Gibbsite Intercalation Compounds [Li Al2(O H)(6)] X {X=Cl, Br, N O3} and [Li Al2(O H)(6)] Cl. H2 O using Synchrotron X-Ray and Neutron Powder Diffraction.* Chemistry of Materials, 1997. **9**(1): p. 241-247.
16. Duan, X. and Evans D.G., *Layered Double Hydroxides*. 2006: Springer.
17. Hernandezmoreno, M.J., et al., *Ir Characteristics of Hydrotalcite-Like Compounds.* Physics and Chemistry of Minerals, 1985. **12**(1): p. 34-38.
18. Chisem, I.C. and Jones W., *Ion-Exchange Properties of Lithium Aluminum Layered Double Hydroxides.* Journal of Materials Chemistry, 1994. **4**(11): p. 1737-1744.
19. Instruments, M., *Zeta Potential Theory*, in *Zetasizer Nano Series User Manual - MAN0317 Issue 1.1*. 2004, Malvern Instrument Ltd.: Malvern Instruments Ltd., Enigma Business Park, Grovewood Road, Malvern, Worcestershire, WR14 1XZ, England. p. 15.2.
20. Lundqvist, M., et al., *Nanoparticle size and surface properties determine the protein corona with possible implications for biological impacts.* Proceedings of the National Academy of Sciences of the United States of America, 2008. **105**(38): p. 14265-14270.
21. Desimone, J., et al. *Geometrically engineered particles and methods for modulating macrophage or immune responses.* 2013. US20150037428. WO2013082111 A2, PCT/US2012/066790. Application
22. Flach, T.L., et al., *Alum interaction with dendritic cell membrane lipids is essential for its adjuvanticity.* Nature Medicine, 2011. **17**(4): p. 479-U121.

23. Pauling, L., *The nature of the chemical bond IV The energy of single bonds and the relative electronegativity of atoms.* Journal of the American Chemical Society, 1932. **54**: p. 3570-3582.
24. Shannon, R.D., *Revised Effective Ionic-Radii and Systematic Studies of Interatomic Distances in Halides and Chalcogenides.* Acta Crystallographica Section A, 1976. **32**(Sep1): p. 751-767.
25. R_Core_Team. *R: A Language and Environment for Statistical Computing.* 2016: Austria, Vienna, https://www.R-project.org
26. Barahuie, F., et al., *Development of drug delivery systems based on layered hydroxides for nanomedicine.* International Journal of Molecular Sciences, 2014. **15**(5): p. 7750-86.
27. Altankov, G., Richau K., and Groth T., *The role of surface zeta potential and substratum chemistry for regulation of dermal fibroblasts interaction.* Materialwissenschaft und Werkstofftechnik, 2003. **34**(12): p. 1120-1128.

Chapter 7 : Hydroxy Double Salts as Vaccine Adjuvants

7.1 Hydroxy Double Salts

7.1.1 Introduction

Hydroxy double salts (HDS) are a class of lamellar material with structural similarities to layered double hydroxides (LDHs). HDS materials contain two divalent metal cations in their hydroxide layer and have a general formula of $[(M^{2+}_{a}N^{2+}_{b})(OH)_{y}]^{(2a+2b-y)+}A^{n-}_{(2a+2b-y)/n}\cdot zH_2O$. Here, M^{2+} and N^{2+} denote two different divalent metal cation species and A^{n-} represents a charge-balancing, interlamellar anion – the nature of this anionic species and the water controls the interlayer separation [1].

With zinc (II)-based hydroxy double salts, the structure contains brucite-like sheets of $[Zn_3(OH)_8]^{2-}$ composition, in which 25% of the octahedral positions are vacant. Two Zn (II) cations adopt tetrahedral positions above and below these vacancies in the layer [2]. The tetrahedral Zn (II) anions are coordinated by a water molecule and three hydroxyl groups of the brucite-like sheets. The guest anion species (*e.g.* Cl^-, NO_3^-) reside between the resultant positively-charged $[Zn_5(OH)_8]^{2+}$ layers, compensating the positive charge [3, 4] – see **Figure 7.1**. This sub-class of HDS materials are defined as Type IIb structures according to Louer's classification [5-7].

HDSs differ from LDHs in that they generally have a smaller tolerance for difference in the ionic radii of the metal cations of the sheet structure. The radii of M^{2+} and N^{2+} tend to differ by no more than 0.05 Å whilst larger radii differences are accommodated in LDHs (*e.g.* Ca^{2+} and Al^{3+} differ by 0.48 Å) [3]. However, evidence from Brindley and Brown suggest that HDSs can tolerate a 0.22 Å difference, as demonstrated by the existence of a mixed Cd^{2+}/Cu^{2+} HDS material [9]. A number of HDSs have anion-exchange capacities, as described by Stahlin and Oswald [10].

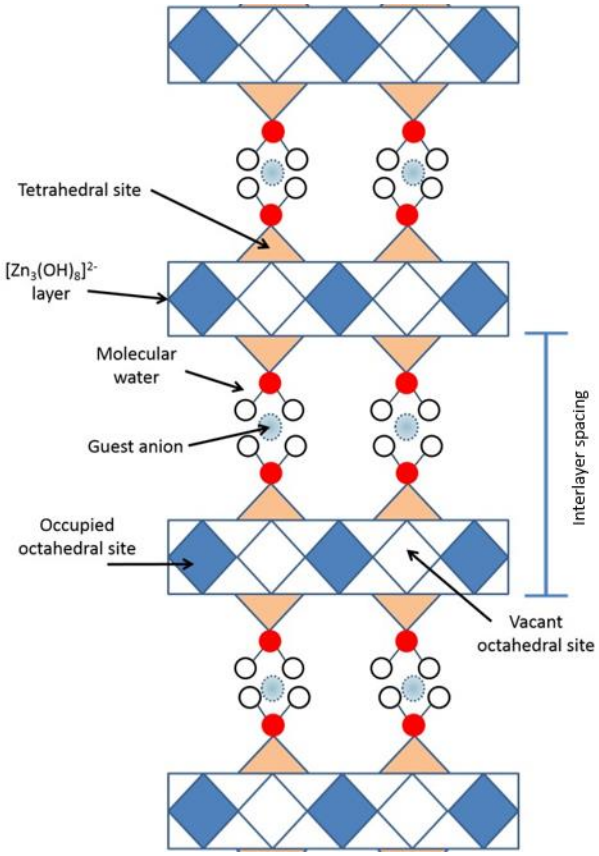

Figure 7.1: ***A schematic depicting the Type IIb structure of HDS materials, highlighting the position of inter-lamellar anions and water molecules with respect to the hydroxide layers. Adapted from [8].***

7.1.2 Synthesis Protocols

There are a variety of different preparation routes that have been described in the literature, but the most commonly reported ones for HDS materials, such as zinc hydroxy nitrate, are (i) thermal decomposition of zinc nitrate hexahydrate [11], (ii) reaction between zinc oxide and zinc nitrate hexahydrate [2] and (iii) the reaction of zinc nitrate hexahydrate with sodium hydroxide [12]. Both the physical and chemical properties of the resultant HDS material can be dependent on the chosen synthesis route.

7.1.3 Aims

HDS materials have been reported as drug delivery systems [13, 14] and preliminary data indicated that they have adjuvant properties [15]. However, a systematic exploration of HDSs as adjuvants has never been performed. Therefore, the main aim of this work was to assess these materials' potential to elicit varied immune responses and determine if there is a way to predict this response from the physicochemical properties of the materials or *in silico* using parameters deduced from simulating the structures.

7.2 Materials and Methods

7.2.1 HDS Synthesis

All materials were procured from Sigma Aldrich UK and were used as supplied. Zinc hydroxynitrate, $[Zn_5(OH)_8](NO_3)_2{\cdot}yH_2O$ (HDS-Nitrate), was prepared through reaction of 4.2 g zinc oxide and 24.1 g zinc nitrate hexahydrate in 60 mL deionised water. The reaction mixture was stirred for 7 days at room temperature and pressure. The resultant white powder was recovered by vacuum filtration, washed with copious amounts of deionised water and a small volume of acetone, then left to dry under vacuum for approximately 30 minutes.

Other HDS materials were prepared using an analogous procedure. Zinc hydroxychloride, $[Zn_5(OH)_8]Cl_2{\cdot}yH_2O$ (HDS-Chloride) was synthesised with 3.0 g ZnO and 7.26 g zinc chloride in 18 mL deionised water. Zinc hydroxyacetate ($[Zn_5(OH)_8](CH_3COO)_2{\cdot}yH_2O$; HDS-Acetate) was prepared from 3.0 g ZnO and 8.05 g zinc acetate di-hydrate in 18 mL deionised water. Cobalt zinc hydroxynitrate ($Zn_{3.8}Co_{1.2}(OH)_8](NO_3)_2{\cdot}yH_2O$; HDS-Cobalt/Nitrate) was generated from 3.0 g ZnO and 8.73 g cobalt (II) nitrate hexahydrate in 18 mL deionised water. Nickel zinc hydroxynitrate ($[Zn_3Ni_2(OH)_8](NO_3)_2{\cdot}yH_2O$; HDS-Nickel/Nitrate) was prepared using 3.0 g ZnO and 8.73 g nickel (II) nitrate hexahydrate in 18 mL deionised water. In all cases, the reactions were stirred at room temperature for 1 week. All four HDS materials were recovered by the vacuum filtration method described above. The Zn-materials were white powders, whilst the $[Zn_{3.8}Co_{1.2}(OH)_8](NO_3)_2{\cdot}yH_2O$ was pink in colour and the $[Zn_3Ni_2(OH)_8](NO_3)_2{\cdot}yH_2O$ material was a blue-green powder.

7.2.2 Materials Characterisation

7.2.2.1 Powder X-ray Diffraction

See **Section 3.3.1**.

7.2.2.2 Scanning Electron Microscopy

See **Section 3.3.2**.

7.2.2.3 Fourier Transform Infra-Red Spectroscopy

See **Section 3.3.3**.

7.2.2.4 Thermogravimetric Analysis

Thermogravimetric analysis of the HDS materials was conducted in a Discovery TGA (TA Instruments) using the automated pan arrangement. Approximately 10 mg of each sample was heated in an aluminium TGA pan to 400 °C under a flowing stream of nitrogen, at a heating rate of 10 ^{o}C min^{-1}. The nitrogen flow rate was 25 mL min^{-1}.

7.2.2.5 Surface Area and Pore Volume Analysis

See **Section 4.3.4.**

7.2.2.6 Zeta Potential Measurements

See **Section 3.3.6**.

7.2.2.7 In silico Simulation Codes

A static energy minimisation code was implemented for calculations using GULP (General Utility Lattice Program) Version 4.0 [16], alongside the scientific visualisation code GDIS (Graphical Display Interface for Structures [17]) to generate structural depictions of the optimised hydroxy double salt structures.

7.2.3 Immunoassay Experiments

See **Section 3.3.7**.

7.2.3.1 Alamar Blue Assay

See **Section 3.3.7.1**.

7.2.3.2 Enzyme-Linked Immuno-Sorbent Assay

See **Section 3.3.7.2**.

7.2.3.3 Fluorescence and Confocal Microscopy

See **Section 3.3.7.3**.

7.3 Results and Discussion

7.3.1 Materials Characterisation

P-XRD patterns of the HDS materials are shown in **Figure 7.2**. All detectable reflections can be assigned by their positions to Bragg reflections of the published HDS structures in the case of HDS-Chloride and HDS-Nitrate (see **Figure 7.2A**) [2, 19]. No impurities were detected.

There are no published structures for the HDS-Acetate, HDS-Cobalt/Nitrate or HDS–Nickel/Nitrate, but the unit cells were predicted using the HDS-Nitrate material [2]. The observed patterns can be indexed using unit cells very similar to those reported in the literature using Celref [20]. Diffraction patterns are presented in **Figure 7.2B** and comparisons between the predicted and observed reflection positions are given in **Table 7.1**, and the refined unit cell details for each material listed in **Table 7.2**. It is clear that the patterns obtained for these materials also agree well with the literature.

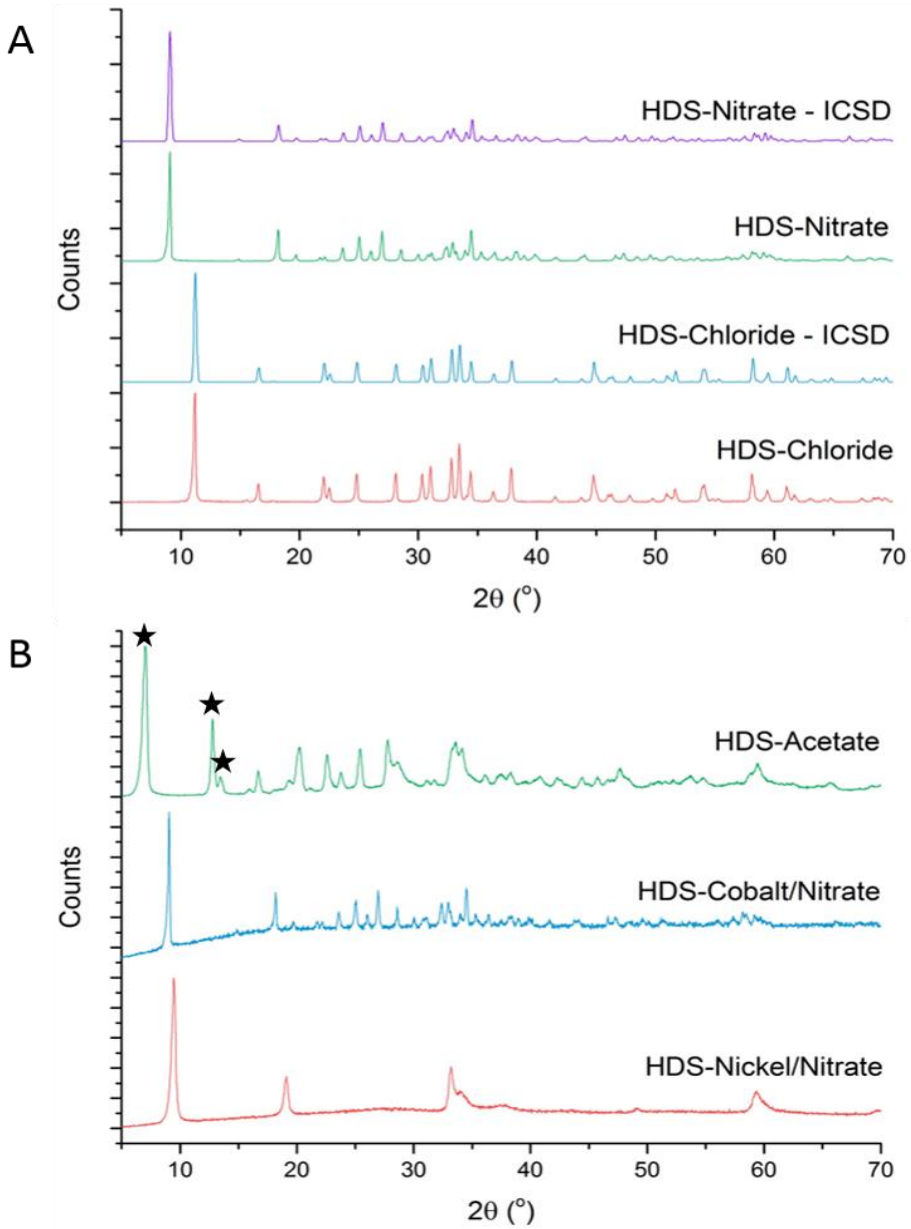

Figure 7.2: ***P-XRD patterns for the hydroxy double salt materials. (a) HDS-Nitrate and HDS-Chloride alongside their reference patterns obtained from [2] and [19], and (b) the remaining HDS materials synthesised with reflections not being able to be indexed using the HDS unit cell being labelled with a *.***

Table 7.1: ***Predicted and observed reflection positions in the P-XRD patterns for the (A) HDS-Acetate, (B) -Cobalt/Nitrate, and (C) –Nickel/Nitrate samples with indexed reflections and the difference between the predicted and observed values.***

(A) HDS-Acetate

Reflection index	Predicted peak positions / 2θ	Observed peak positions / 2θ	Difference
110	14.8955	13.6433	-1.2522
001	16.1801	16.8998	0.7197
310	19.7465	20.2227	0.4762
111	22.2464	22.5487	0.3023
-401	23.8109	23.8115	0.0006
401	25.1633	25.4729	0.3096
600	27.5507	27.7990	0.2483
020	28.5758	28.5965	0.0207
-601	31.3142	31.3213	0.0071
511	32.3202	31.7865	-0.5337
-202	33.5033	33.5808	0.0775
420	34.1280	34.1790	0.0510
112	36.3402	36.2392	-0.101
-312	37.8055	37.5683	-0.2372
-711	38.3579	38.2329	-0.1250
-602	42.0262	42.2204	0.1942
-222	44.5989	44.4135	-0.1854
-712	47.6326	47.5371	-0.0955
1110	53.9562	53.9171	-0.0391
313	54.9909	54.914	-0.0769
040	59.1535	59.4331	0.2796

(B) HDS-Nickel/Nitrate

Reflection index	Predicted peak positions / 2θ	Observed peak positions / 2θ	Difference
200	9.0014	9.3900	0.3886
310	19.3476	19.0265	-0.3211
-202	33.2319	33.1821	-0.0498
202	34.3690	34.1125	-0.2565
223	59.2249	59.4331	0.2082

(C) HDS-Cobalt/Nitrate

Reflection index	Predicted peak positions / 2θ	Observed peak positions / 2θ	Difference
200	9.0884	9.0577	-0.0307
400	18.2347	18.2954	0.0607
-111	21.813	21.9506	0.1376
111	22.2101	22.1500	-0.0601
-401	23.702	23.6785	-0.0235
-311	25.0565	25.0077	-0.0488
311	26.0908	25.9381	-0.1527
510	26.9874	27.0679	0.0805
020	28.5641	28.5965	0.0324
220	30.034	29.9256	-0.1084
-601	31.1878	31.1219	-0.0659
511	32.2977	32.3181	0.0204
601	32.8715	32.8498	-0.0217
-221	34.0042	33.9131	-0.0911
221	34.5328	34.5777	0.0449
710	35.3354	35.3752	0.0398
112	36.2429	36.3721	0.1292
-312	37.6461	37.7012	0.0551
-711	38.2291	38.1000	-0.1291
402	38.5489	38.4987	-0.0502
312	39.0847	39.0304	-0.0543
801	41.4605	41.5558	0.0953
-131	46.7670	46.8060	0.039
-422	47.0674	47.2048	0.1374
023	58.3776	58.3033	-0.0743

***Table 7.2:** Refined unit cell parameters for the HDS-Acetate, -Cobalt/Nitrate, and -Nickel/Nitrate samples, with standard errors.*

Unit Cell Parameter	HDS-Acetate	HDS-Cobalt/Nitrate	HDS-Nickel/Nitrate
Volume / Å³	665.9	669.9	697.1
a / Å	19.46 ± 0.137	19.49 ± 0.030	19.69 ± 1.49
b / Å	6.25 ± 0.034	6.25 ± 0.008	6.43 ± 0.317
c / Å	5.49 ± 0.035	5.51 ± 0.008	5.52 ± 0.200
α / °	90.00 ± 0.000	90.00 ± 0.000	90.00 ± 0.000
β / °	93.14 ± 1.337	93.35 ± 0.279	93.60 ± 22.39
γ / °	90.00 ± 0.000	90.00 ± 0.000	90.00 ± 0.000

Mean crystallite size data are presented in **Table 7.3**, calculated using all reflections in the P-XRD patterns and using a K value of 1 in the Scherrer equation.

Table 7.3: ***Mean crystallite size of the HDS materials deduced via application of the Scherrer equation to P-XRD patterns; mean ± standard deviation.***

HDS material	Mean crystallite size / nm
HDS-Nitrate	36.72 ± 5.93
HDS-Chloride	33.95 ± 9.68
HDS-Acetate	15.01 ± 6.52
HDS-Cobalt/Nitrate	40.86 ± 8.34
HDS-Nickel/Nitrate	13.66 ± 7.95

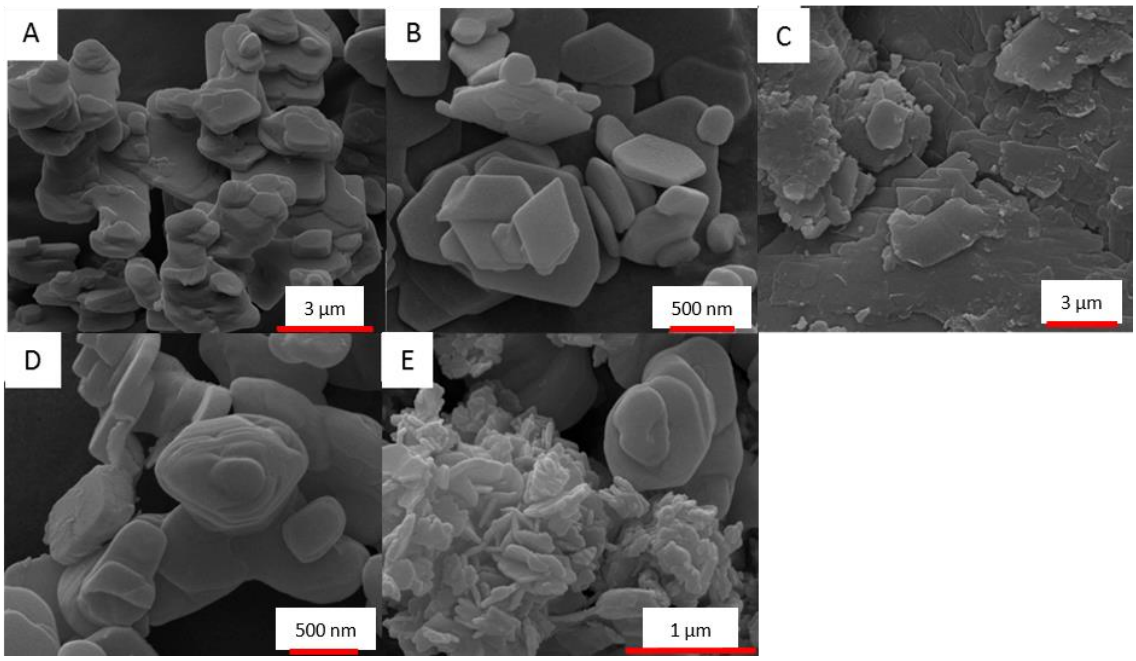

Figure 7.3: ***Scanning electron micrographs of (A) HDS-Nitrate, (B) HDS-Chloride, (C) HDS-Acetate, (D) HDS-Cobalt/Nitrate and (E) HDS-Nickel/Nitrate.***

SEM analysis shows the reaction products are composed of microparticles of platelet morphology (**Figure 7.3**). Size analysis was performed using these images and the mean particle size data are presented in **Table 7.4**. The particles are calculated to be much larger than the crystallite size determined by the Scherrer equation; this is to be expected because particles are composed of many crystallites.

***Table 7.4:** Particle size data for the HDS materials, determined from SEM images, mean ± standard deviation.*

HDS sample	Mean particle size / µm
HDS-Nitrate	1.77 ± 0.84
HDS-Chloride	0.56 ± 0.28
HDS-Acetate	0.91 ± 0.34
HDS-Cobalt/Nitrate	0.38 ± 0.24
HDS-Nickel/Nitrate	0.70 ± 0.27

IR spectra were recorded, and are presented in **Figure 7.4**. All the HDS samples' infra-red spectra contain a broad band *ca*. 3400 cm^{-1}, which is attributed to the O-H vibrational absorption modes (see **Table 7.5**) of both the hydroxyl layer and the weakly hydrogen-bonded water molecules of the interlayer [21]. The breadth of this band varies with the nature of the interlayer anion, which can be attributed to differences in the interactions between the OH groups in the layers and the guest. H-bonding interactions will be possible in the case of nitrate and acetate species, while when Cl^- ions are present between the layers only weaker dipole-dipole interactions will exist. As a result, the OH band is sharper in the latter case.

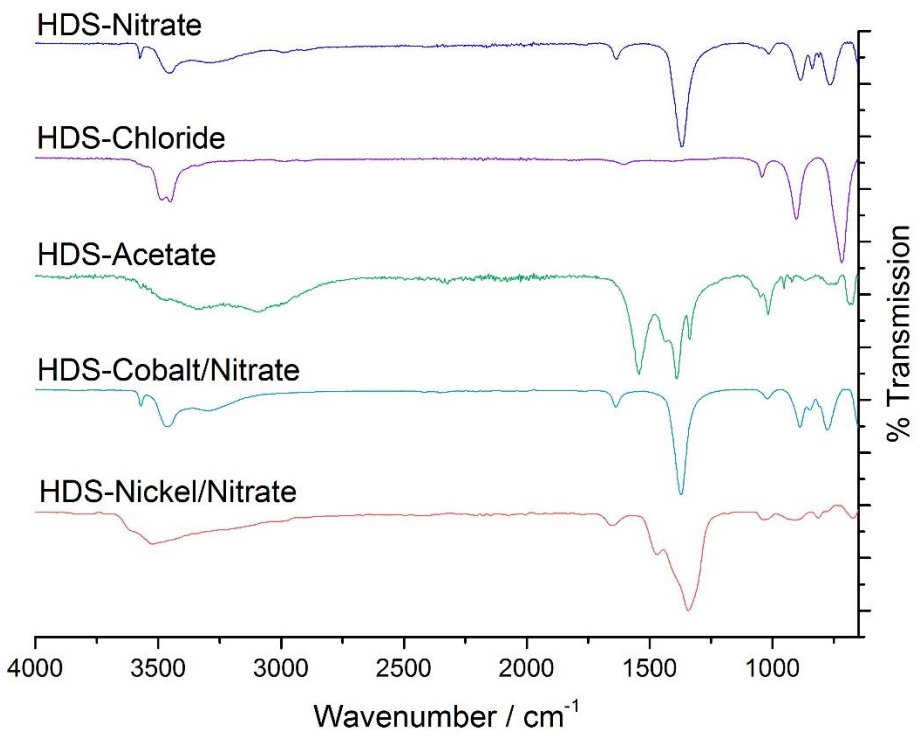

***Figure 7.4:** FTIR spectra for the HDS materials (A) HDS-Nitrate, (B) HDS-Chloride, (C) HDS-Acetate, (D) HDS-Cobalt/Nitrate and (E) HDS-Nickel/Nitrate.*

The peak present at *ca*. 1630 cm^{-1} is attributed to the δ-bend of water; the low intensity of this peak is associated with the small amount of water residing in the interlayer or adsorbed to the surface [12, 22]. Metal-oxygen (M-O) vibrations of the HDS layers occur below 1000 cm^{-1} [23-25].

For the HDS-Acetate material, a broad shoulder to the OH band, at *ca*. 2900 – 3050 cm^{-1}, indicates the presence of the symmetric and asymmetric bands of C-H bonds in the acetate moiety. Furthermore, bands at *ca*. 1560 and 1390 cm^{-1} can be attributed to the v_{as} and v_s vibrational modes of the carboxylate component of the acetate, respectively. In the literature, these two peaks suggest a bidentate co-ordination of the acetate anion [26, 27]. These data are in agreement with literature values [12, 22-27], supporting P-XRD data to confirm the successful synthesis of HDS materials. A full assignment of all the bands observed may be found in **Table 7.5**.

Table 7.5: FTIR assignments for HDS materials.

Wavenumber / cm^{-1}	Assignment
3550	O-H stretch
3445	(Co)O-H stretch
3400	v_{OH} absorptions of OH-layers and co-intercalated water
3200 - 3540	Broad peak attributed to OH^- groups involved in H-bonding [28]
2900 - 3040	v_s and v_{as} (C-H) in acetate moiety
1630	Deformation of water
1560	v_{as} (COO^-) vibrational mode of carboxylate
1450	v_{as} nitrate anion
1390	v_s (COO^-) vibrational mode of carboxylate
1360	N-O stretch
1352	v_s nitrate anion
1050	v_{as} nitrate anion
1000	Zn-O vibrational modes

7.3.2 Thermogravimetric Analysis

Thermogravimetric analysis (TGA) was undertaken to deduce the water content in each of the five synthesised materials. Exemplar data are shown in **Figure 7.5**.

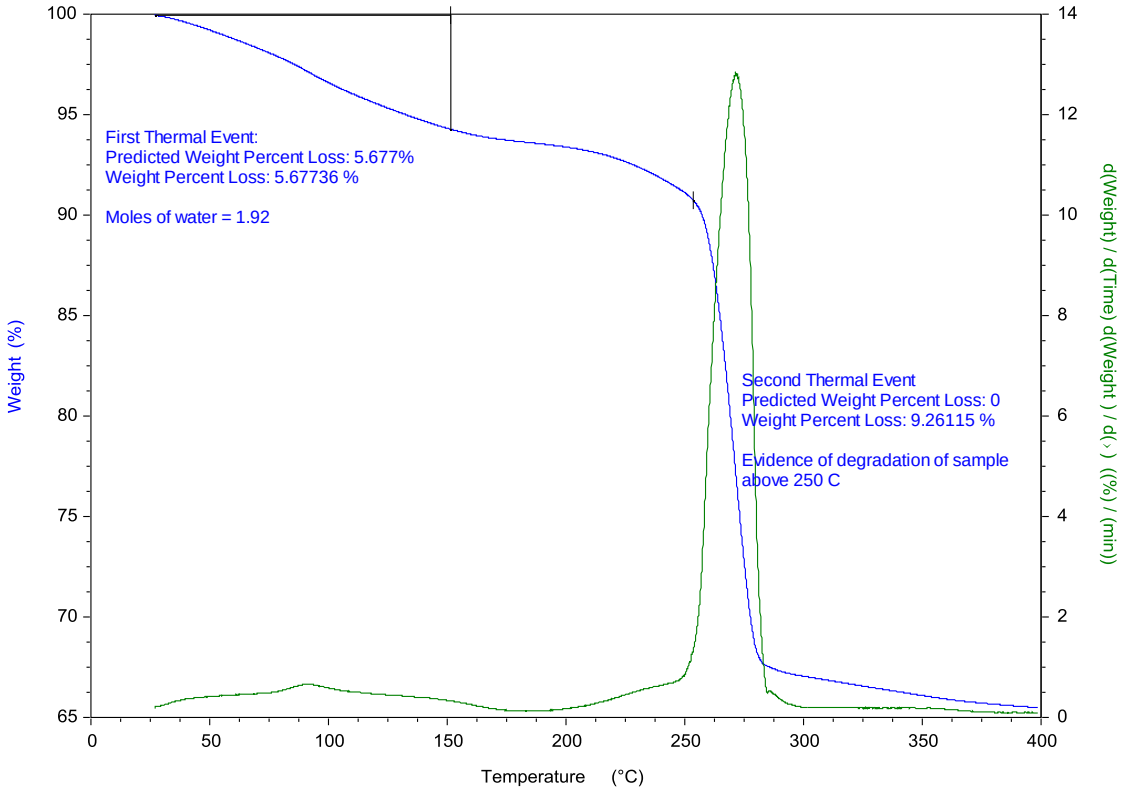

***Figure 7.5:* TGA data for the HDS-Nickel/Nitrate sample.**

Decomposition of the HDS materials exhibit two thermal events, with the first at 50 – 150 °C being assigned to the loss of adsorbed and interlayer water, and the second (at 250 – 285 °C) to the release of water from decomposition of the layers. The first thermal event can be used to determine the molar water content of the sample whilst the second provides information of the chemical composition. The water content values calculated are given in **Table 7.6.** The values observed concur with those recorded in the literature [2, 19].

***Table 7.6:* Details of the expected water loss from each HDS material and the observed value, as deduced from the TGA curves, with the chemical composition deduced using the moles of water per formula unit.**

Material	Expected water loss / %	Observed water loss / %	Moles of water per formula unit	Chemical composition
HDS-Nitrate	5.78	5.78	2.00	$[Zn_5(OH)_8](NO_3)_2{\cdot}2H_2O$
HDS-Chloride	3.26	3.38	1.03	$[Zn_5(OH)_8]Cl_2{\cdot}1.03H_2O$
HDS-Acetate	5.84	6.05	2.25	$[Zn_5(OH)_8](CH_3COO)_2{\cdot}2.25H_2O$
HDS-Cobalt/Nitrate	5.85	5.37	1.84	$[Zn_{3.2}Co_{1.2}(OH)_8](NO_3)_2{\cdot}1.84H_2O$
HDS-Nickel/Nitrate	5.91	5.68	1.92	$[Zn_3Ni_2(OH)_8](NO_3)_2{\cdot}1.92H_2O$

7.3.3 Surface Area and Pore Volume

Surface area and pore volume analyses were completed for each of the five HDS samples with the adsorption isotherms presented in **Figure 7.6.** In all cases, the samples were dried at 100 °C under vacuum prior to analysis.

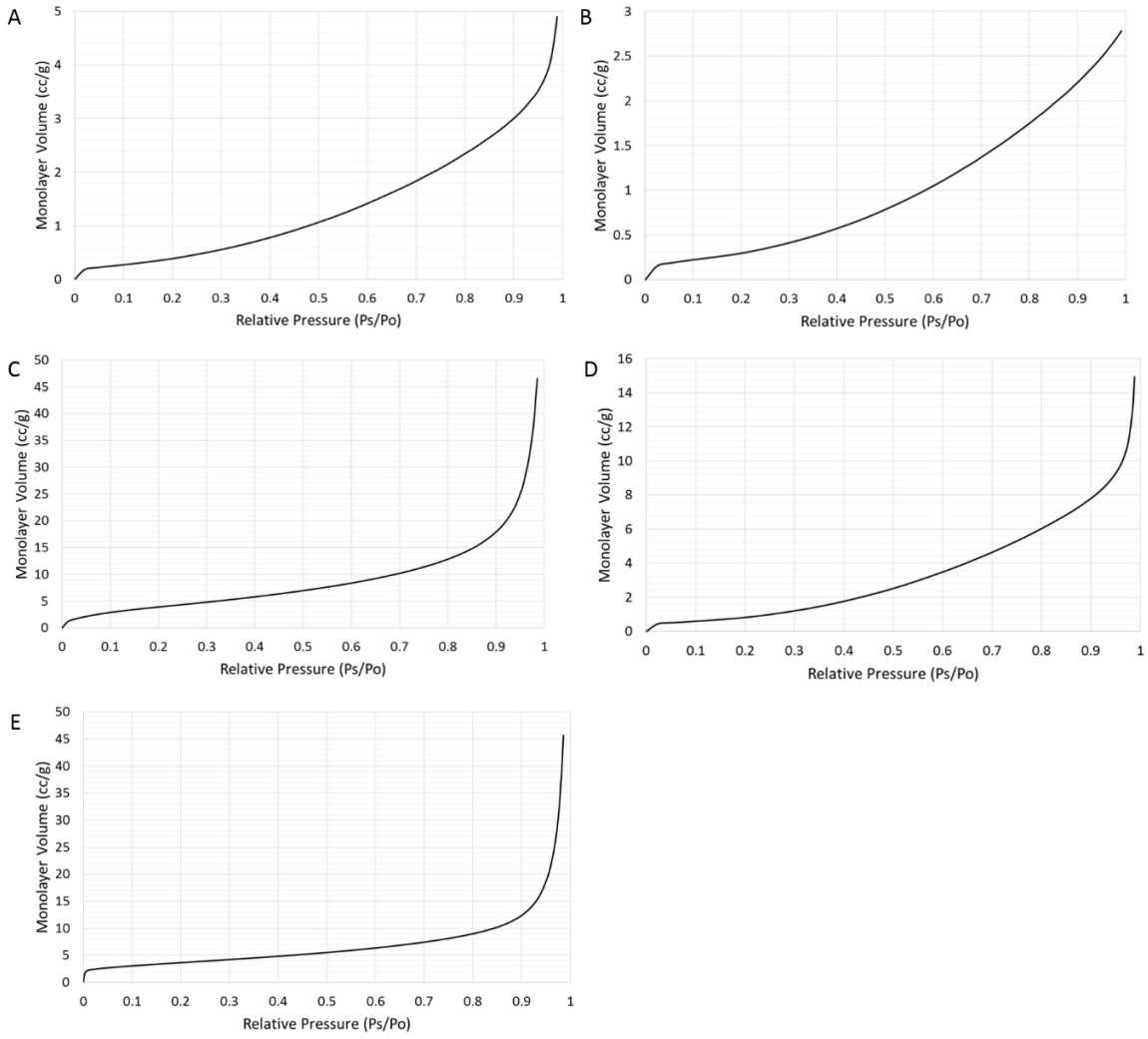

Figure 7.6: ***Adsorption isotherms of the hydroxy double salt materials, (A) HDS-Nitrate, (B) HDS-Chloride, (C) HDS-Acetate, (D) HDS-Cobalt/Nitrate; and (E) HDS-Nickel/Nitrate.***

The isotherms, as presented in **Figure 7.6**, are evidently Type II which is consistent with what has been reported in the literature [29]. This classification of isotherm corresponds to the materials being non-porous, as is supported by all samples having a pore volume less than 0.085 mL g^{-1}, with multiple adsorption layers arising on the adsorbent's surface [30]. The intermediate, plateau portion of the isotherm indicates the formation of a monolayer on the sample surfaces. A full adsorption/desorption program was run between 0 and 1 relative pressures to confirm the absence of any mesopores. Mesoporous materials would exhibit a plateau in the isotherm *ca*. 0.9 Ps/Po [30]; as this is absent from the isotherms in **Figure 7.6**, it is evident that the HDS materials are not mesoporous. Surface area and pore volume data for the five HDS materials are summarised in **Table 7.7**.

Table 7.7: ***Surface area and pore volume data.***

Sample ID	Surface Area / m^2 g^{-1}	Pore Volume / mL g^{-1}
HDS-Nitrate	1.544	0.0078
HDS-Chloride	0.912	0.0043
HDS-Acetate	16.013	0.0810
HDS-Cobalt/Nitrate	3.141	0.0248
HDS-Nickel/Nitrate	13.212	0.0829

Increasing the size of the anion in the HDS interlayer region appears to cause an increase in the surface area of the sample (**Table 7.7**) which may arise due to the interlayer space expanding to accommodate the larger guest anions. Comparing the three nitrate species (HDS-Nitrate, HDS-Cobalt/Nitrate and HDS-Nickel/Nitrate) there is a change in the surface area with the composition of the layer. This follows the inverse trend to the particle size data (for size, HDS-Nitrate > HDS-Nickel/Nitrate > HDS-Cobalt/Nitrate), and thus may be attributed to a reduction is particle size of these materials.

7.3.4 Zeta Potential Measurements

As mentioned in previous chapters, the zeta potential has been shown to be an important physicochemical property in determining the magnitude of the immune response to LDH adjuvants; therefore, this was also investigated for the HDS materials. Data are presented in **Table 7.8** and **Table 7.9.** It is evident that changing the dispersion medium causes a change in the zeta potential: negative readings are generally recorded when PBS is used as the dispersant due to negative phosphate anions within the PBS solution being adsorbed to the surface of the particles and altering the charge at the slipping plane. Positive readings are obtained when UP-water was used as the dispersant.

Unexpected results for HDS-Nitrate and HDS-Cobalt/Nitrate are obtained when PBS is the dispersant, with pronounced changes in the zeta potential in the 10 minutes after the suspension was prepared. These measurements have been repeated and the outcomes were reproducible, however. It is not certain why this occurs, but it may arise due to sedimentation of a fraction of the particles and/or aggregation. Whilst it is not possible to determine the long-term stability of HDS dispersions from their zeta potential measurements alone, the data presented in **Table 7.9** suggests that UP-water may lead to stable suspensions, with readings generally above +30 mV [31].

***Table 7.8:** Mean zeta potential measurements for the HDS materials, when dispersed in 0.01 M phosphate buffered saline solution (PBS) at pH 7.4; mean ± standard deviation.*

Sample ID	Initial ZP / mV	ZP after 10 minutes / mV
HDS-Nitrate	2.90 ± 2.46	-37.98 ± 1.08
HDS-Chloride	-36.87 ± 1.72	-58.9 ± 8.59
HDS-Acetate	-15.40 ± 3.97	-13.45 ± 2.26
HDS-Cobalt/Nitrate	-45.28 ± 1.69	-0.88 ± 4.54
HDS-Nickel/Nitrate	-29.02 ± 1.44	-30.23 ± 1.07

***Table 7.9:** Mean zeta potential measurements for the HDS materials, when dispersed in ultra-pure water with conductivity of 18.2 mΩ; mean ± standard deviation.*

Sample ID	Initial ZP / mV	ZP after 10 minutes / mV
HDS-Nitrate	60.02 ± 1.52	70.03 ± 2.47
HDS-Chloride	24.47 ± 1.08	27.95 ± 1.99
HDS-Acetate	14.10 ± 1.26	13.37 ± 1.10
HDS-Cobalt/Nitrate	69.97 ± 1.16	75.88 ± 0.38
HDS-Nickel/Nitrate	36.36 ± 1.90	41.05 ± 0.43

7.3.5 Structure/Property Relationships

In previous chapters, clear relationships between the particle size and zeta potential were noted for the alum and LDH materials (**Sections 3.4.8 and 6.5.3**). Therefore, efforts to elucidate similar relationships for the HDS materials were made. A summary of these is presented in **Table 7.10** with representative plots in **Figure 7.7**.

***Table 7.10:** Relationships between zeta potential measurements and the particle size of the HDS materials.*

Experimental parameter / µm (x)	Zeta potential / mV (y)	Equation	R^2 correlation
Particle size	ZP in UP-water	y = 15.711x + 27.432	0.1039
	ZP in UP-water (10 minutes)	y = 19.75x + 28.62	0.1591
	ZP in PBS	y = 29.427x – 50.118	0.7084
	ZP in PBS (10 minutes)	y = -2.1641x – 26.421	0.0027

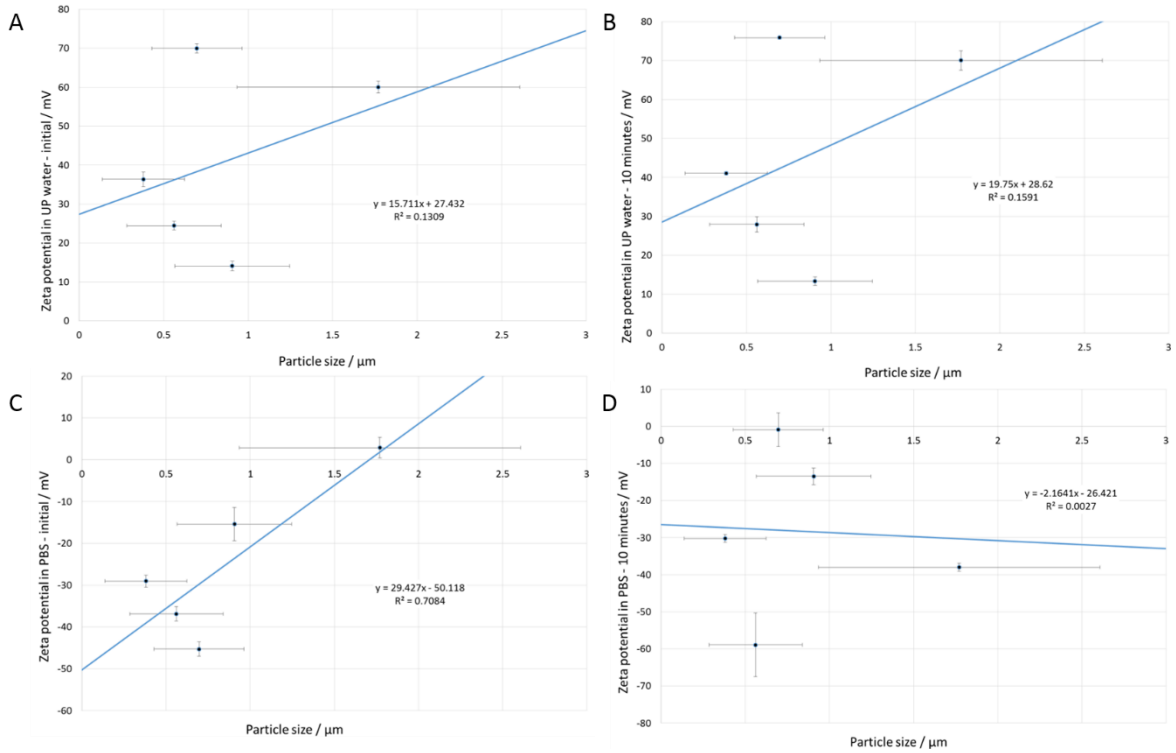

***Figure 7.7:* Graphical representation of the relationships described in Table 7.10. Panels A and B depict plots of zeta potential measurements using UP-water vs. particle size, and panels C and D analogous graphs with zeta potentials measured using PBS.**

It is clear that there are no straightforward relationships here, which is perhaps not surprising given that, as well as a range of sizes, the different materials also have different layer chemistries.

Further correlations were sought in an attempt to elucidate relationships between physicochemical properties of the HDS materials and their zeta potential measurements. These are described in **Table 7.11**. There appear to be no apparent trends between the ionic radii or the electronegativity of the metal cations and the zeta potential measurements, which may be ascribed to the zeta potential being determined by a complex interplay of factors, and thus a single x-variable is not sufficient to determine any correlations. Weighted mean values of either property were implemented for the HDS-Cobalt/Nitrate and HDS-Nickel/Nitrate materials.

***Table 7.11:* Relationships between zeta potential measurements and physicochemical properties of the HDS materials.**

Experimental parameter (x)	Zeta potential / mV (y)	Equation	R^2 correlation
Ionic radius / pm	ZP in UP-water	y = 3.8477x – 296.17	0.0221
	ZP in UP-water (10 minutes)	y = 3.8817x – 294.48	0.0173
	ZP in PBS	y = 1.8642x – 186.51	0.0078
	ZP in PBS (10 minutes)	y = 2.1687x – 218.32	0.0078
Electronegativity	ZP in UP-water	y = 127.26x – 173.05	0.0642
	ZP in UP-water (10 minutes)	y = 135.24x – 181.80	0.0558
	ZP in PBS	y = -179.65x + 277.41	0.1973
	ZP in PBS (10 minutes)	y = 149.07x – 279.00	0.0974

Plots of some of the relationships presented in **Table 7.11** are shown in **Figure 7.8**, with all other plots located in the **Appendix 5.**

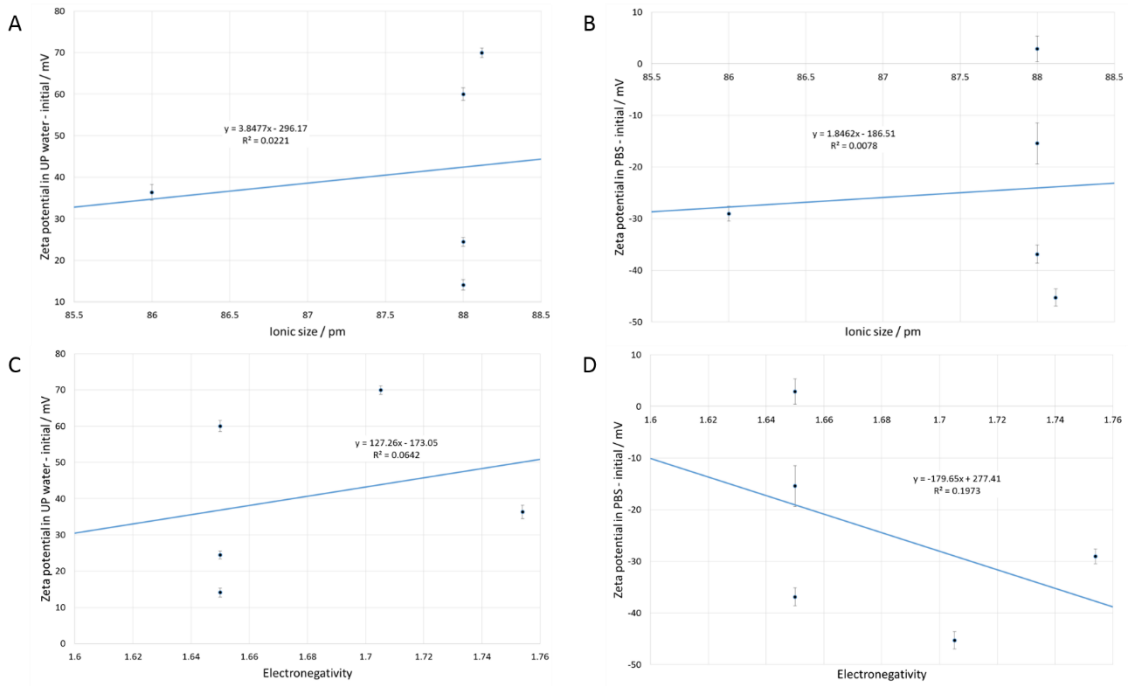

***Figure 7.8:* Graphical representation of the relationships described in Table 7.11. Panels A and C depict plots of zeta potential measurements using UP-water vs. ionic size or electronegativity, and panels B and D analogous graphs with zeta potentials measured using PBS vs. ionic size or electronegativity.**

Subsequent investigations assessed possible relationships between the weighted mean reduction potential of the metal cations (values obtained from [32]) and the zeta potential measurements. No clear linear fits could be obtained, and therefore polynomials were explored; the results are given in **Table 7.12**.

***Table 7.12:* Relationships between zeta potential measurements and physicochemical properties of the HDS materials.**

Experimental parameter / V (x)	Zeta potential / mV (y)	Equation	R^2 correlation
Reduction Potential	ZP in UP-water	$y = 29.82x^2 + 104.04x + 94.812$	0.4773
	ZP in UP-water (10 minutes)	$y = 30.84x^2 + 107.44x + 101.07$	0.3999
	ZP in PBS	$y = -12.25x^2 – 37.239x – 37.716$	0.4491
	ZP in PBS (10 minutes)	$y = 25.341x^2 + 86.643x + 14.522$	0.4841

Representative plots for the data in **Table 7.12** are shown in **Figure 7.9**.

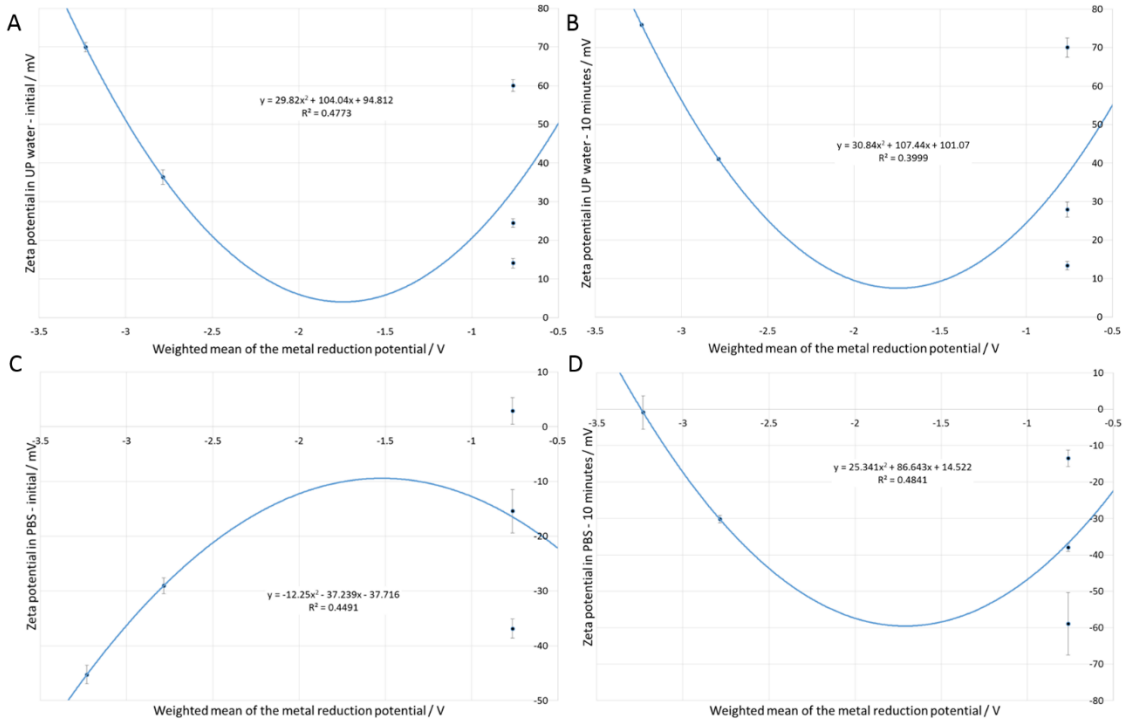

***Figure 7.9:* Graphical representation of the relationships described in Table 7.12. Panels A and B depict plots of zeta potential measurements using UP-water vs. the weighted mean of the metal cation's reduction potential, and panels C and D are analogous graphs with zeta potentials measured using PBS vs. the weighted mean of the metal cation's reduction potential.**

Again the relationships presented here are very weak, indicating that there are no apparent linear or polynomial correlations arising between the physicochemical properties of the HDS materials. As such, this means it does not appear to be possible to tailor the zeta potential through altering the particle size or ionic radius of the cation, for example. In comparison to relationships deduced for the alum and LDH samples, these are poor and highlight the complex nature of the zeta potential of this class of material.

7.3.6 *In Silico* Experiments

There is a published immunological equation for the structurally related LDH materials [33], allowing the immune response to be predicted from the physicochemical properties of the materials. Further, in **Chapter 6** it was shown that simulated properties of LDH structures may be used to make such predictions. A similar means of predicting the immune response was therefore sought for the HDS materials. In order to attempt this, an *in silico* model was first constructed.

In order to optimise the structures, a suitable force field was required. Two pre-existing force fields were investigated (ClayFF and LDH-FF [34, 35]), with limited success. To obtain models of suitable quality a hybrid was developed, containing interatomic potentials from both the ClayFF and LDH-FF. It was also necessary to incorporate the interatomic potential parameters for the nitrate guest anionic species, previously described for the simulation of Li/Al-LDH structures in **Section 6.3.2**, because potentials for these anions were not present in the original LDH-FF force field. The framework parameters are detailed in **Table 7.13** to **Table 7.15**.

***Table 7.13:* HDS framework potential parameters - Coulombic charges.**

Species	Coulombic charge / e
Zn core	2.000
O1 core	-0.9500
H1 core	0.4250
O2 core	-0.8200
H2 core	0.4100
N core	0.4124
$O_{Nitrate}$ core	-0.4708
Cl core	-1.000
Co core	2.000
Ni core	2.000

Table 7.14: ***HDS framework potential parameters - Interatomic potentials for nitrate anions [36].***

Harmonic: $\frac{1}{2}k_2(r-r_0)^2+\frac{1}{2}k_3(r-r_0)^3+\frac{1}{2}k_4(r-r_0)^4$				
Interaction	k_2 / eV Å^{-2}	k_3 / eV Å^{-3}	k_4 / eV Å^{-4}	r_0 / Å
N - O$_{Nitrate}$	50.6370	-408.2327	2779.8844	1.2645
Three-body Harmonic: $\frac{1}{2}k_2(\theta-\theta_0)^2+\frac{1}{6}k_3(\theta-\theta_0)^3+\frac{1}{12}k_4(\theta-\theta_0)^4$				
Interaction	k_2 / eV rad^{-2}	k_3 / eV rad^{-3}	k_4 / eV rad^{-4}	θ_0 / °
O$_{Nitrate}$ - N - O$_{Nitrate}$	10.2547	23.9655	74.9604	120.0
Torsion: $k(1+\cos(nphase(\phi-\phi_0)))$				
Interaction		k / eV	nphase	ϕ_0 / °
O$_{Nitrate}$ – N – O$_{Nitrate}$ - O$_{Nitrate}$		0.623163	+1	0.0
Lennard-Jones: $\frac{A}{r^m}-\frac{B}{r^n}$				
Interaction	A / kcal Å^9	B / kcal Å^6		
H - O$_{Nitrate}$	768.4	40.72		
H – N	888.1	61.30		
O$_{Layer}$ - O$_{Nitrate}$	16442.0	384.8		
O$_{Layer}$ - N	243936.0	84.2		

Table 7.15: ***HDS framework potential parameters - Interatomic potentials.***

Harmonic: $k_{b,2}(b-b_0)^2 + k_{b,3}(b-b_0)^3 + k_{b,4}(b-b_0)^4$

Interaction	b_0 / Å	$k_{b,2}$ / kcal mol^{-1} Å^{-2}	$k_{b,3}$ / kcal mol^{-1} Å^{-3}	$k_{b,4}$ / kcal mol^{-1} Å^{-4}
Co core – O core	2.280	63.0	-162.8	121.5
Ni core – O core	2.310	71.6	-150.6	141.2
Zn core – O core	2.360	60.2	-354.7	137.1
O core – H core	0.965	532.5	-1282.0	2004.0

Three-Body: : $k_{a,2}(\theta-\theta_0)^2 + k_{a,3}(\theta-\theta_0)^3 + k_{a,4}(\theta-\theta_0)^4$

Interaction	θ_0 / °	$k_{a,2}$ / kcal mol^{-1} rad^{-2}	$k_{a,3}$ / kcal mol^{-1} rad^{-3}	$k_{a,4}$ / kcal mol^{-1} rad^{-4}
Ni core – O core – Ni core	102.0	83.9	-113.1	0.0
Zn core – O core – Zn core	107.0	82.2	-101.3	0.0
Co core – O core – Co core	102.0	49.5	-50.0	0.0
O core – Ni core – O core	135.0	-42.2	0.0	34.2
O core – Zn core – O core	135.0	-39.5	0.0	32.1
O core – Co core – O core	135.0	-42.7	0.0	34.7
Ni core – O core – H core	120.0	14.9	-25.6	43.5
Zn core – O core – H core	123.3	4.2	-21.1	61.2
Co core – O core – H core	127.0	5.1	-23.8	10.5

Cross terms: $E_{rr'}(r-r_0)(r'-r'_0)$

Interaction	Bond-Bond kbb' / kcal mol^{-1} Å^{-2}	Bond-Angle kba / kcal mol^{-1} Å^{-2} rad^{-1}	$kb'a$ / kcal mol^{-1} Å^{-2} rad^{-1}
Ni core – O core – Ni core	12.25	-2.560	---
Zn core – O core – Zn core	18.55	-1.675	---
Co core – O core – Co core	14.88	-4.131	---
O core – Ni core – O core	20.25	-3.255	---
O core – Zn core – O core	15.19	0.469	---
O core – Co core – O core	20.63	-3.347	---
Ni core – O core – H core	2.90	1.550	0.1940
Zn core – O core – H core	4.59	0.000	0.2859
Co core – O core – H core	3.05	0.007	-0.1097

Lennard-Jones: $\varepsilon_{ij}\left[2\left(\frac{r_{ij}^0}{r_{ij}}\right)^9 - 3\left(\frac{r_{ij}^0}{r_{ij}}\right)^6\right] + 332.1\left(\frac{q_i q_j}{r_{ij}}\right)$

Interaction	r_i / Å	ε_i / kcal mol^{-1}	q_i / e
Co core	6.235	0.028	0.830
Ni core	6.010	0.036	0.730
Zn core	6.280	0.020	1.070
H core	1.098	0.013	0.460

The outcomes of these simulations are described below. Considering first the HDS-Nitrate system, it can be observed that the unit cell volume is less than 50% of the experimental value (**Table 7.16**). There is also a wide difference in the *a*-parameter and β-angle, with minor differences being recorded for the *b*-parameter and *α*, *γ* angles.

***Table 7.16:* Optimised data obtained from GULP simulations of HDS-Nitrate and the published data.**

	HDS-Nitrate		
Parameter	Published [2]	Optimised	Percentage difference
Volume / Å³	6023.76	2799.79	53.52

There are clear structural differences between the published crystal structure of HDS-Nitrate (**Figure 7.10A**, [2]) and the GULP-optimised one presented in **Figure 7.10B**. The published structure shows an ordered arrangement of atoms whereas the simulated one, using the interatomic potentials listed in **Table 7.13** to **Table 7.15**, is disordered with an apparent collapse in the interlayer space region. This may occur due to partial optimisation of the structure.

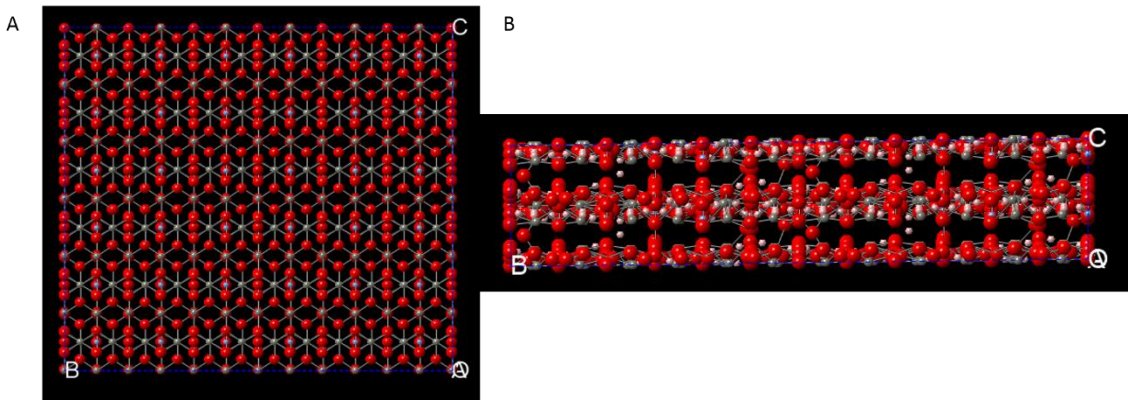

***Figure 7.10:* Visual depictions of (A) the reference HDS-Nitrate material obtained from [2], and (B) the simulated structure in GULP. Zinc is grey, Oxygen is red and Nitrogen is blue.**

Attempts to model the HDS-Chloride material *in silico* also met with limited success. The volume of the optimised structure calculated is more than twice that observed experimentally (**Table 7.17**), with significant differences in all unit cell parameters.

Table 7.17: ***Optimised data obtained from GULP simulations of HDS-Chloride and the published data.***

HDS-Chloride			
Parameter	Published [19]	Optimised	Percentage difference
Volume / Å^3	7410.95	16195.70	118.54

There is a high degree of order in the atomic arrangement in the published structure (**Figure 7.11A**, [19]) which is lost in the GULP-optimised structure shown in **Figure 7.11B**.

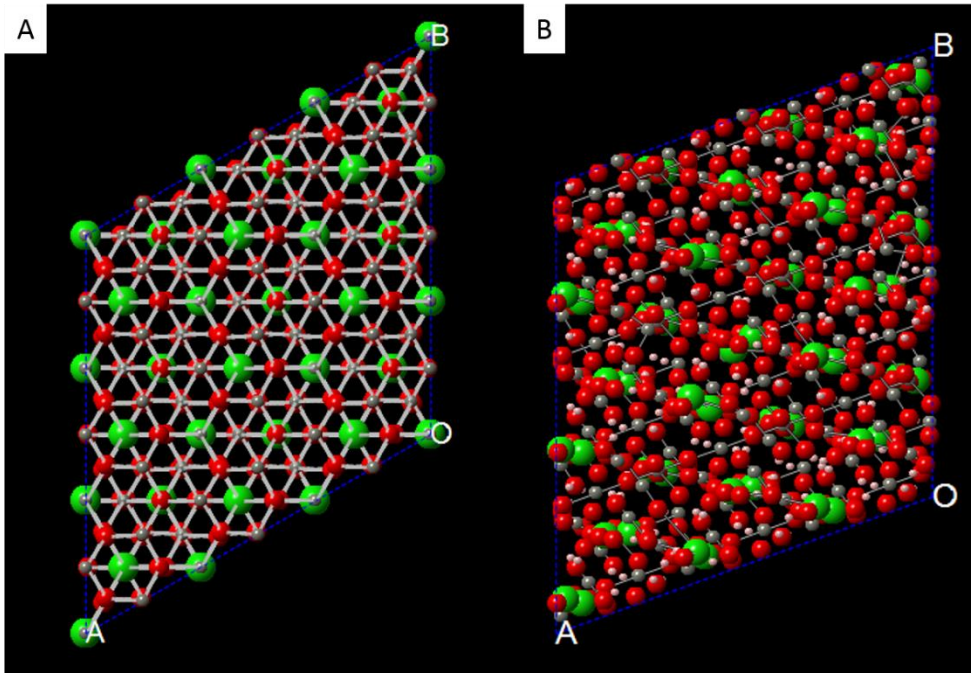

Figure 7.11: ***Visual depictions of (A) the reference HDS-Chloride material obtained from [19], and (B) the simulated structure in GULP. Zinc is grey, Oxygen is red and Chlorine is green.***

Both the HDS-Nitrate and HDS-Chloride materials have been successfully simulated *in silico* using Materials Studio [37], therefore, it is possible that the problems arising with the simulations in GULP are due to problems with the software.

There are no published crystal structures for the mixed metal layer HDS materials (HDS-Cobalt/Nitrate and HDS-Nickel/Nitrate). Both contain nitrate anions intercalated into the interlayer region, however, and therefore attempts were made to produce models using the known structure of the all-Zn HDS-Nitrate as a starting point [2]. Fractional occupancies allowed for compositional changes in the metal layers, with ions inserted according to the ratios in the structural formulae.

The HDS-Nickel/Nitrate structure could not be modelled with the GULP program, with bond lengths within the structure exceeding the limits described in the model during the calculations. However, this was not observed for the HDS-Cobalt/Nitrate structure, for which partial optimisation was achieved. The calculated unit cell volume is given in **Table 7.18** which indicates there is an error in the force field.

***Table 7.18:** Calculated unit cell volume obtained from GULP simulations of the HDS-Cobalt/Nitrate material and the published data of HDS-Nitrate.*

	HDS-Cobalt/Nitrate		
Parameter	Published [2]	Optimised	Percentage difference
Volume / Å^3	6023.76	3183.61	47.15

As for the other structures, large differences between the published and modelled structures were noted. Overall therefore, while extensive effort allowed for partial optimisation of the HDS structures within GULP, none of the materials could be completely optimised. The data presented in **Table 7.16** to **Table 7.18** clearly demonstrate there is a high degree of variation between the published and the calculated data, which we believe arises because of restricted interatomic potentials, limited crystallographic data for the HDS materials and bond length tolerances with the GULP program.

7.3.7 *In Vitro* Experiments

7.3.7.1 Cell Viability

There is very little cytotoxicity recorded following exposure of the RAW264.7 macrophages to the HDS materials (**Figure 7.12**). In all cases, viability is observed to be above 90 %. The HDSs show very similar results to the commercial adjuvant controls. The apparent biocompatibility of these materials is similar to that observed for both zinc oxide and cobalt oxide species in the literature [38-40]. However, nickel oxide has been reported to induce *ca*. 25% cell death of RAW264.7 cells following a 24 hr exposure period [41], which is not observed for the Ni-containing HDS studied here. This suggests that the cytotoxicity of nickel is attenuated by its inclusion into the layer of an HDS.

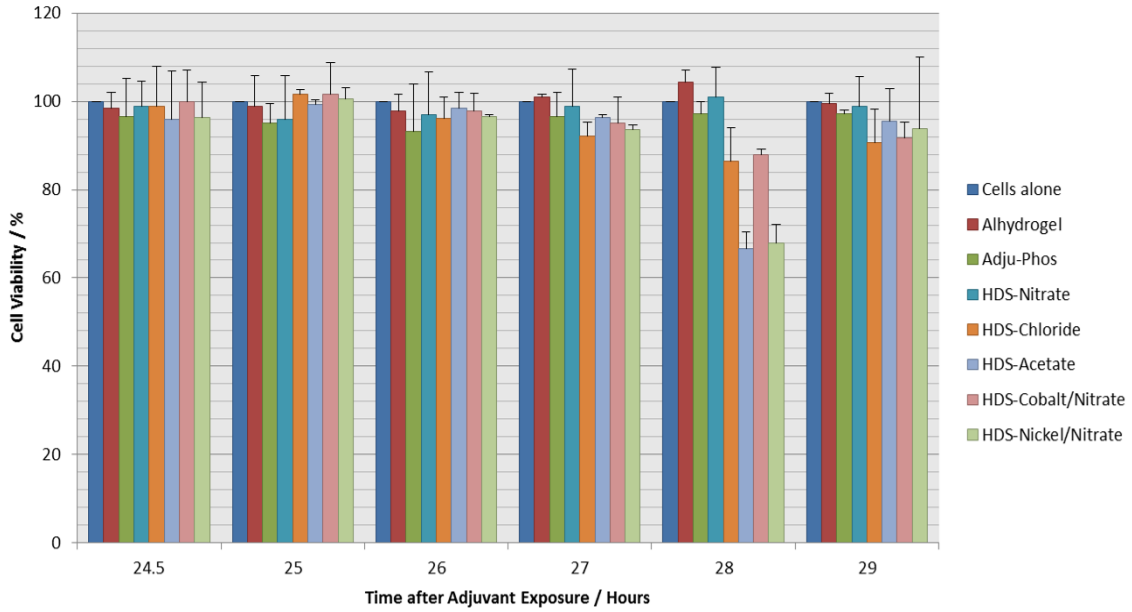

Figure 7.12: ***Cell viability results. RAW264.7 macrophages were exposed to HDS microparticles at 476 µg mL^{-1} for 24 hours. Cells exposed to commercial alums (Alhydrogel® and Adju-Phos®) at the same concentration were used for comparative purposes. Cell viability was quantified by Alamar Blue assays with n=3 with each independent experiment containing nine replicates.***

There is evidence of some cell death at the 28 hours post-adjuvant exposure point (**Figure 7.12**). This might be attributed to the doubling time of the cell line [42]; alternatively, it could be a temporary effect of the adjuvants, but nevertheless the cell numbers recover by the subsequent read point at 29 hours.

7.3.7.2 Immunoassay Experiments

Cytokine concentrations were quantified by means of an ELISA assay on the cell-free supernatants of the RAW264.7 cells. TNF-α concentrations appear to be relatively constant across the five HDS samples with concentrations in the range of *ca.* 50 – 60 pg mL^{-1} (**Figure 7.13**). All the materials perform on par with the commercial Alhydrogel control for TNF-α production, and instigate a greater amount of production than with Adju-Phos. The concentrations recorded lie in a similar range to those recorded for the AlO(OH) and LDH materials reported in **Sections 3.5.2** and **6.7.2**.

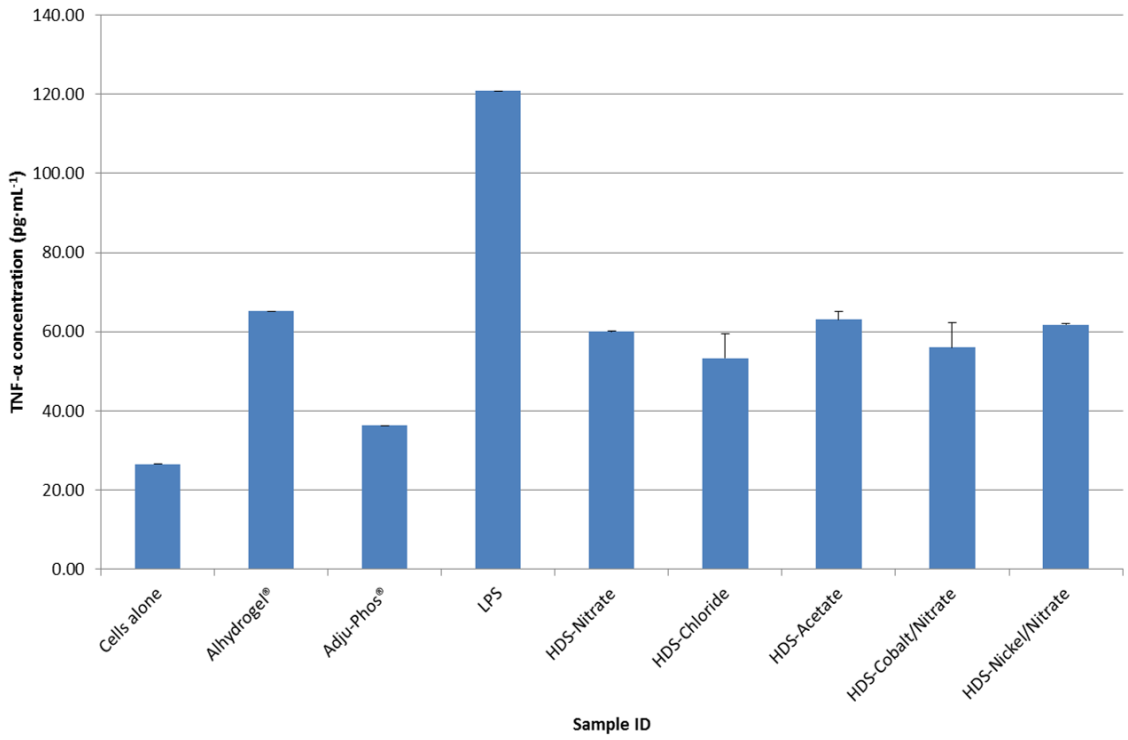

Figure 7.13: ***TNF-α production in response to HDS adjuvants. RAW264.7 macrophages were exposed to HDS microparticles at 476 µg mL^{-1} for 24 hours. Cells exposed to commercial alums (Alhydrogel® and Adju-Phos®) were used for comparative purposes with lipopolysaccharide (LPS) as a positive control. TNF-α cytokine secretions were quantified by ELISA assays with n=3; each independent experiment contained nine replicates.***

There appears however to be some potential for tuning the immune response in terms of IL-6 production (**Figure 7.14**).

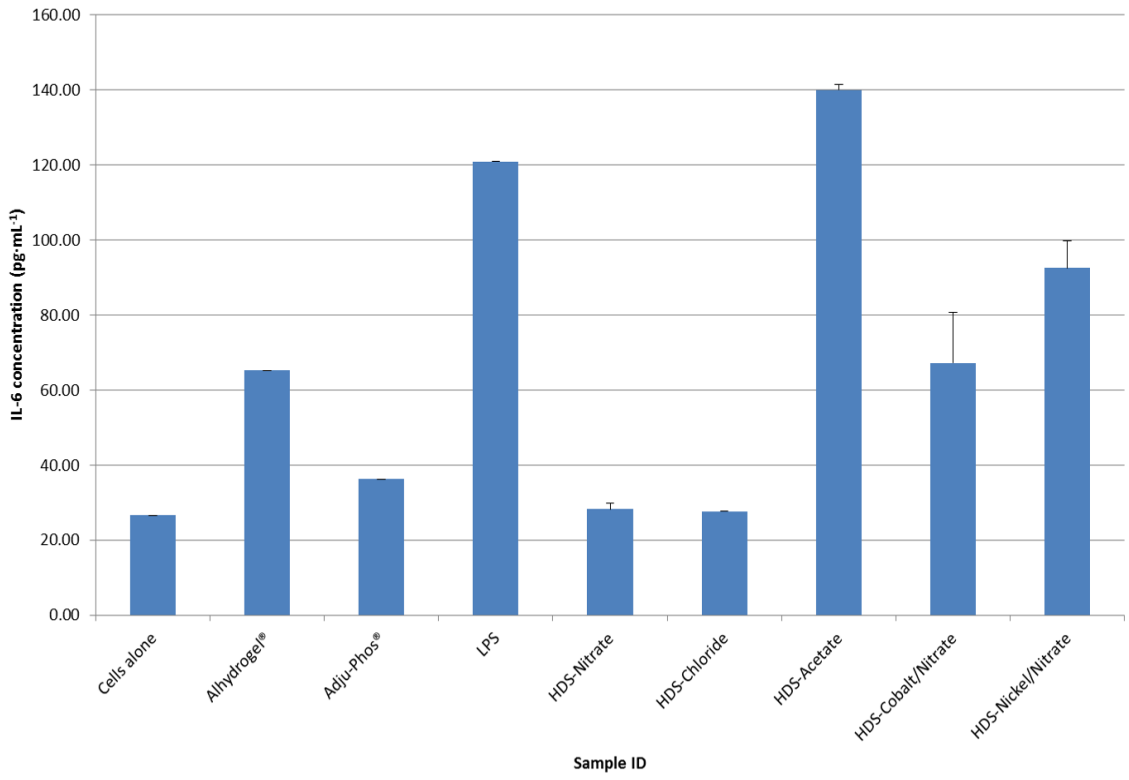

Figure 7.14: ***IL-6 production in response to HDS adjuvants. RAW264.7 macrophages were exposed to HDS microparticles at 476 µg mL^{-1} for 24 hours. Cells exposed to commercial alums (Alhydrogel® and Adju-Phos®) were used for comparative purposes with lipopolysaccharide (LPS) as a positive control. IL-6 cytokine secretions were quantified by ELISA assays with n=3; each independent experiment contained nine replicates.***

The HDS-Nitrate and HDS-Chloride species induce only low concentrations of IL-6, with no increase relative to the untreated cells control. In contrast, the other materials lead to much greater IL-6 production. The HDS-Cobalt/Nitrate material stimulates more IL-6, and appears to lead to approximately equal amounts of both IL-6 and TNF-α being produced; thus, it could be suggested that a balanced immune response may be evoked following application of this material. This is supported by the literature, since cobalt has been shown to induce both Th1- and Th2-type cytokines [43].

Furthermore, the remaining two HDS samples (HDS-Acetate and HDS-Nickel/Nitrate) produce much greater amounts of IL-6, with HDS-Acetate producing even more than the LPS positive control. These materials thus might be Th2-type polarisers (**Figure 7.14**). Overall, there is evidence that the elemental composition of the highly diverse class of HDS materials could provide a means of tailoring the immune response.

7.3.7.3 Fluorescent Microscopy

All HDS materials were labelled with FITC and the RAW264.7 cells with the DAPI nuclear stain; giving rise to green and blue images under the fluorescent microscope, respectively. There is evidence of sample aggregation in the images shown in **Figure 7.15** because no platelet morphology is obvious with most presenting as rod-like or spherical aggregates.

The RAW264.7 macrophages appear to be located around the perimeter of the HDS samples which could suggest that they might elicit their immunogenic effect in a similar way to a proposed mechanism of AlO(OH), *via* lipid membrane disturbances, which would require direct contact of cells with the adjuvant particle [44].

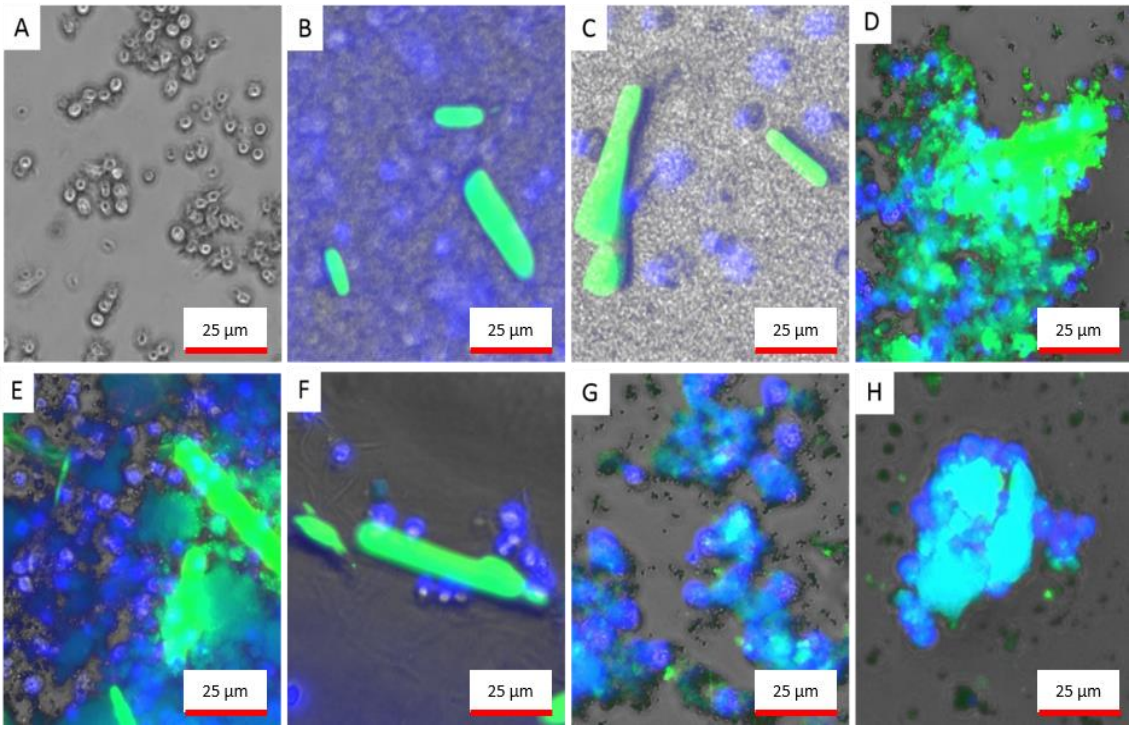

***Figure 7.15:* Fluorescent microscopy with FITC-labelled HDS samples with DAPI nuclear staining; (A) cells alone, (B) Alhydrogel, (C) Adju-Phos, (D) HDS-Nitrate, (E) HDS-Chloride, (F) HDS-Acetate, (G) HDS-Cobalt/Nitrate; and (H) HDS-Nickel/Nitrate.**

Confocal microscopy was undertaken but proved unsuccessful due to the semi-adherent nature of the murine macrophage cell line meaning that the cells ruptured during the transfer stage from the transwell plate, to the microscope slide.

7.4 Structure/property relationships

Since the physicochemical properties of LDHs have been shown to control directly the immune response stimulated, we attempted to deduce similar relationships for the HDS materials. The results of these attempts are summarised in **Table 7.19**.

There are no obvious linear relationships in these data (in contrast to those noted in previous chapters) which means that the physicochemical properties of the HDS materials and the immunological output of the RAW264.7 cells are more complex than such a simple relationship can describe. Therefore, polynomial and exponential plots were also explored to seek links between the two variables. Some plots are presented in **Figure 7.16**, with all others in **Appendix 5**.

***Table 7.19:** Relationships between experimental parameters and immunoassay data of the HDS materials; with particle size being derived by SEM analysis (µm) and zeta potential measurements in mV.*

Experimental parameter (x)	Cytokine concentration / pg mL^{-1} (y)	Equation	R^2 correlation
Particle size	TNF-α	$y = 1.708x + 57.367$	0.0526
	IL-6	$y = -113.28x^2 + 225.83x - 12.708$	0.3232
ZP in UP-water	TNF-α	$y = -0.0418x + 60.554$	0.0595
	IL-6	$y = 0.0624x^2 – 6.2942x + 196.55$	0.4208
ZP in UP-water (10 minutes)	TNF-α	$y = 0.0014x^2 – 0.1652x + 62.677$	0.0805
	IL-6	$y = 0.0456x^2 – 5.1498x + 184.9$	0.4497
ZP in PBS	TNF-α	$y = -0.0073x^2 – 0.1757x + 61.066$	0.5958
	IL-6	$y = -0.1192x^2 – 4.9702x + 55.402$	0.4556
ZP in PBS (10 minutes)	TNF-α	$y = -0.0086x^2 – 0.4402x + 56.664$	0.9034
	IL-6	$y = -0.0368x^2 – 0.8831x + 90.414$	0.4852

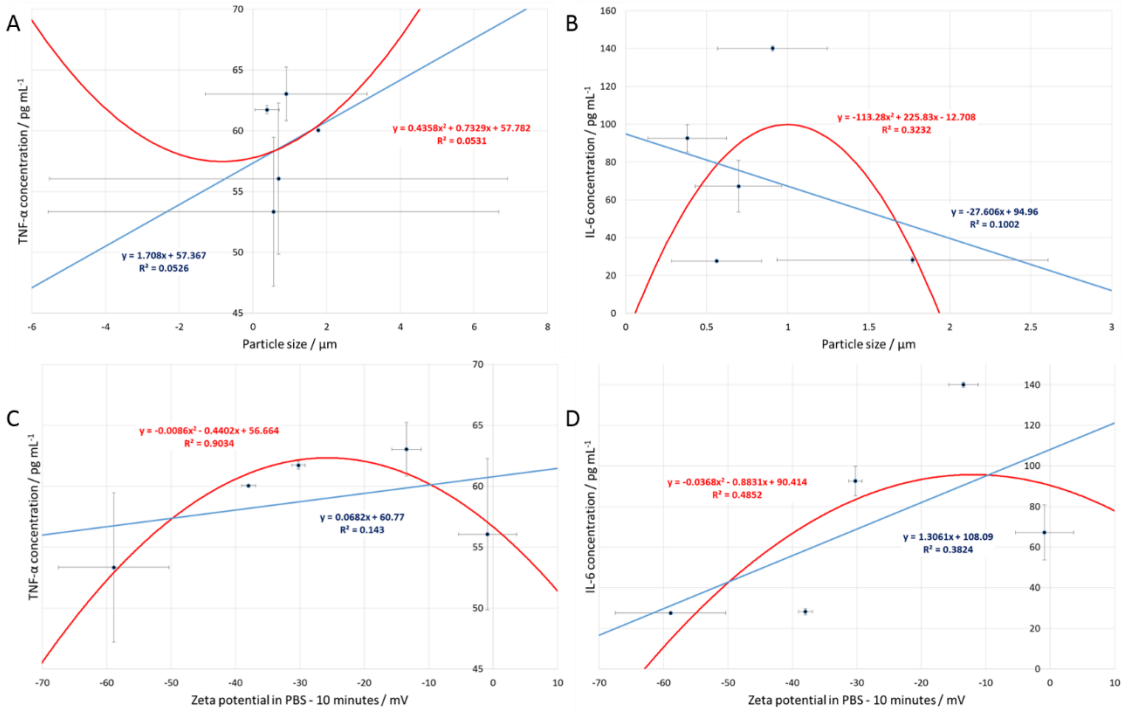

***Figure 7.16:* Graphical representation of the (A) TNF-α and (B) IL-6 cytokine concentrations correlated to particle size; and the (C) TNF-α and (D) IL-6 cytokine concentrations correlated with the zeta potential measurements recorded in PBS (10 minute-time point). With both linear (blue) and polynomial (red) correlations to highlight the differences in correlations.**

However, when altering the relationship type to polynomial, we obtain some degree of correlation, with a very strong relationship between TNF-α and the zeta potential measured in PBS (10 minute time point, see **Figure 7.16**). This finding suggests that it may be possible to tailor the TNF-α production by RAW264.7 cells by tuning the zeta potential of the HDS particles.

Further attempts were made to deduce relationships between the simulated parameters for HDS-Nitrate, HDS-Chloride and HDS-Cobalt/Nitrate and the cytokine concentrations of TNF-α and IL-6, with the outcomes presented in **Table 7.20**. Selected plots are shown in **Figure 7.17**; all other plots are located in the **Appendix 5**.

Table 7.20: ***Relationships between simulated unit cell parameters for HDS-Nitrate, HDS-Chloride and HDS-Cobalt/Nitrate and immunoassay data.***

Simulated parameter (x)	Cytokine concentration / pg mL^{-1} (y)	Equation	R^2 correlation
Volume / Å³	TNF-α	y = -0.0004x + 59.168	0.6736
	IL-6	y = -0.0015x + 51.815	0.2400
a / Å	TNF-α	y = 0.4935x + 42.627	0.9995
	IL-6	y = -0.2456x + 47.942	0.0055
b / Å	TNF-α	y = -0.7506x + 72.769	0.6661
	IL-6	y = -3.0718x + 107.69	0.2468
c / Å	TNF-α	y = -0.1635x + 59.054	0.6453
	IL-6	y = -0.7055x + 52.138	0.2660
α / °	TNF-α	y = 0.1906x + 40.9	0.6510
	IL-6	y = 0.8109x – 25.266	0.2608
β / °	TNF-α	y = -0.1064x + 64.347	0.9993
	IL-6	y = 0.0491x + 37.415	0.0047
γ / °	TNF-α	y = -0.1995x + 75.975	0.6698
	IL-6	y = -0.8088x + 120.06	0.2435

There are no strong linear relationships between the simulated data and the amount of IL-6 produced in response to the samples with R^2 values not exceeding 0.27. However, TNF-α output appears to be correlated to the GULP-simulated values for the *a*-parameter and *β*-angle, with R^2 values of 0.9995 and 0.9993, respectively (**Table 7.20**). The TNF-α concentration range is small, but the relationship nevertheless appears to be clear.

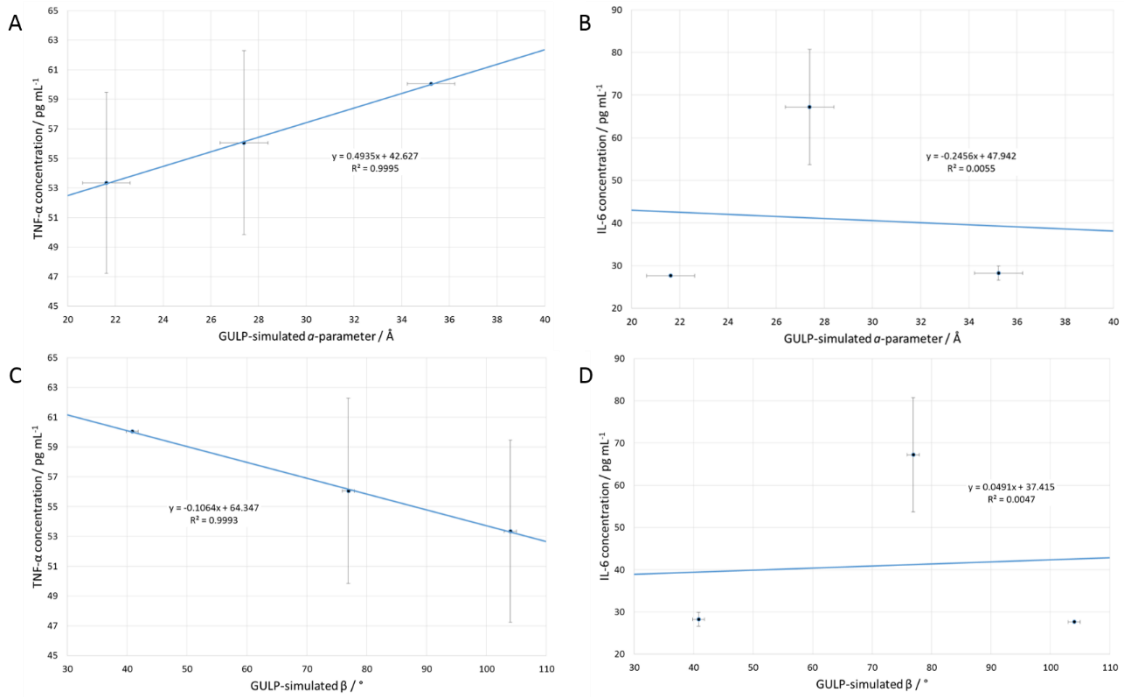

***Figure 7.17:* Graphical representation of the (A) TNF-α and (B) IL-6 cytokine concentrations correlated to the calculated a-parameter; and the (C) TNF-α and (D) IL-6 cytokine concentrations correlated with the calculated β-angle.**

The results presented here show that there is some evidence of tunability of the immune response to HDS materials. The chemical nature of the HDS materials appears to influence IL-6 production, with a range of different concentrations being produced in response to the different chemical compositions and the HDS-Acetate material out-performing LPS for this cytokine. In the literature, it has been reported that both TNF-α and IL-6 cytokine concentrations vary with the HDS material [15] for human dendritic cells, and the findings reported here agree with the previous results, showing that this variation in response occurs across cell lines. Constant TNF-α production, observed here in response to the HDS materials, is not a trait of the RAW264.7 cells, with the literature providing evidence of TNF-α being predominantly produced cytokine over IL-6 [45]. Therefore, it is likely that this response pattern is directly caused by the HDS samples.

The structurally-related class of layered double hydroxide (LDH) compounds has been shown to produce relatively consistent levels of TNF-α in RAW cells, regardless of chemical composition (see **Section 6.7.2**) [46, 47], and thus both families of materials behave the same in this regard (**Figure 7.13**). Some LDH materials have been suggested to exhibit Th1-polarising effects [48]; from the data reported here it is not possible to ascertain whether this is also possible for HDS systems, but it does appear the immune response can be tailored immune through variation of chemical composition.

7.5 Conclusion

A range of hydroxy double salt (HDS) materials were prepared and fully characterised. Simulating the structures of the HDS materials proved to be challenging owing to the need to develop and optimise a new force field that can build every HDS configuration, in addition to a lack of detailed structural information. Nevertheless, partial structure optimisation was achieved for the zinc hydroxynitrate, zinc hydroxychloride and zinc/cobalt hydroxynitrate species, with further work being required to achieve complete structure optimisation.

In vitro and immunoassay investigations indicated the non-toxic nature of the HDS materials, and while all materials caused RAW264.7 cells to produce largely constant amounts of TNF-α, IL-6 production could be modulated through the composition of the HDS. As a result, it appears clear that this class of material might comprise a broad family of tuneable adjuvants.

Attempts were made to seek relationships between physicochemical or simulated parameters of the HDSs and the immunological output of the RAW264.7 cells. The physicochemical properties returned no apparent correlations. However, TNF-α production appears to be highly correlated with two *in silico* parameters (*a*-parameter and β-angle).

7.6 References

1. Majoni, S. and Hossenlopp J.M., *Controlled Release Kinetics in Hydroxy Double Salts: Effect of Host Anion Structure.* Advances in Physical Chemistry, 2014. **2014**: p. 12.
2. Stahlin, W. and Oswald H.R., *Crystal Structure of Zinc Hydroxide Nitrate, Zn5(O H)8(N O3)2. 2 H 2 O.* Acta Crystallographica Section B-Structural Crystallography and Crystal Chemistry, 1970. **B 26**: p. 860-&.

3. Meyn, M., Beneke K., and Lagaly G., *Anion-Exchange Reactions of Hydroxy Double Salts.* Inorganic Chemistry, 1993. **32**(7): p. 1209-1215.
4. Allmann, R., *Double Layer Structures with Layer Ions (Me(Ii)(1-X)Me(Iii)(X)(O H)2)(X+) of Brucite Type.* Chimia, 1970. **24**(3): p. 99-&.
5. Louer, M., Louer D., and Grandjea.D, *Structural Study of Nickel and Zinc Hydroxynitrates .1. Structural Classification.* Acta Crystallographica Section B-Structural Science, 1973. **B 29**(Aug15): p. 1696-1703.
6. Louer, M., Grandjea.D, and Weigel D., *Structural Study of Nickel and Zinc Hydroxynitrates .2. Crystalline-Structure of Basic Zinc Nitrate 2 Zn(O H)2. Zn(N O3)2.* Acta Crystallographica Section B-Structural Science, 1973. **B 29**(Aug15): p. 1703-1706.
7. Louer, M., et al., *Structural Study of Nickel and Zinc Hydroxynitrates .3. Structural Study of Basic Nitrates - Zn(O H)2. Zn(N O3)2. 2 H 2 O and Ni(O H)2. Ni(N O3)2.2 H 2 O.* Acta Crystallographica Section B-Structural Science, 1973. **B 29**(Aug15): p. 1707-1710.
8. Carbajal Arizaga, G.G., Satyanarayana K.G., and Wypych F., *Layered Hydroxide Salts: Synthesis, Properties and Potential Applications.* Solid State Ionics, 2007. **178**(15-18): p. 1143-1162.
9. Brindley, G.W. and Kikkawa S., *Crystal-Chemical Study of Mg,Al and Ni,Al Hydroxy-Perchlorates and Hydroxy-Carbonates.* American Mineralogist, 1979. **64**(7-8): p. 836-843.
10. Stahlin, W. and Oswald H.R., *Topotactic Reaction of Zinc Hydroxide Nitrate with Aqueous Metal Chloride Solutions.* Journal of Solid State Chemistry, 1971. **3**(2): p. 256-&.
11. Biswick, T., et al., *Synthesis, Characterisation and Anion Exchange Properties of Copper, Magnesium, Zinc and Nickel Hydroxy Nitrates.* Journal of Solid State Chemistry, 2006. **179**(1): p. 49-55.
12. Li, P., et al., *Control Preparation of Zinc Hydroxide Nitrate Nanocrystals and Examination of the Chemical and Structural Stability.* Journal of Physical Chemistry C, 2012. **116**(18): p. 10325-10332.
13. Bull, R.M.R., et al., *Hydroxy Double Salts as Versatile Storage and Delivery Matrices.* Journal of Materials Chemistry, 2011. **21**(6): p. 1822-1828.
14. Kaassis, A.Y.A., Wei M., and Williams G.R., *New Biocompatible Hydroxy Double Salts and Their Drug Delivery Properties.* Journal of Materials Chemistry B, 2016. **4**(35): p. 5789-5793.
15. Austyn, J.M., O'hare D., and Williams G.R. *Adjuvants.* 2013. WO2013140136 A1, PCT/GB2013/050636. Application
16. Gale, J.D., *Gulp: A Computer Program for the Symmetry-Adapted Simulation of Solids.* Journal of the Chemical Society-Faraday Transactions, 1997. **93**(4): p. 629-637.
17. Fleming, S. *Graphical Display Interface for Structures (G D I S).* http://gdis.sourceforge.net/
18. *Lipid Maps Thawing and Passage Procedure for Raw264.7*. 2004 08/11/2004; 2:[Available from: http://www.lipidmaps.org/protocols/PP0000000100.pdf.
19. Nowacki, W. and SILVERMAN J.N., *Die Kristallstruktur Von Zinkhydroxychlorid Ii, Zn5 (O H) 8 Cl2. 1 H 2 O.* Zeitschrift für Kristallographie-Crystalline Materials, 1961. **115**(1-6): p. 21-51.
20. Laugier, J., Bochu, B. *Lmgp-Suite, Suite of Programs for the Interpretation of X-Ray Experiments.* BP 46. 38042 Saint Martain d'Hores, France, http://www.inpg.fr/LMGP, http://www.ccp14.ac.uk/tutorial/lmgp
21. Gago, S., et al., *Synthesis and Properties of Zn-Al Layered Double Hydroxides Containing Ferrocenecarboxylate Anions.* European Journal of Inorganic Chemistry, 2004(7): p. 1389-1395.
22. Herrero, M., et al., *Layered Double Hydroxide/Polyethylene Terephthalate Nanocomposites. Influence of the Intercalated L D H Anion and the Type of Polymerization Heating Method.* Journal of Solid State Chemistry, 2011. **184**(11): p. 2862-2869.

23. Williams, G.R., et al., *The Selective Intercalation of Organic Carboxylates and Sulfonates into Hydroxy Double Salts.* Journal of Materials Chemistry, 2012. **22**(27): p. 13600-13611.
24. Kagunya, W., et al., *Vibrational Modes in Layered Double Hydroxides and Their Calcined Derivatives.* Chemical Physics, 1998. **236**(1-3): p. 225-234.
25. Kloprogge, J.T., Frost, R. L., *Infrared and Raman Spectroscopic Studies of Layered Double Hydroxides (L D Hs).* , in *Layered Double Hydroxides: Present and Future*, V. Rives, Editor. 2001, Nova Science Publishers Inc: New York. p. 153-215.
26. Benito, P., et al., *Effect of Post-Synthesis Microwave-Hydrothermal Treatment on the Properties of Layered Double Hydroxides and Related Materials.* Applied Clay Science, 2010. **48**(1-2): p. 218-227.
27. Gago, S., et al., *Zn-Al Layered Double Hydroxide Pillared by Different Dicarboxylate Anions.* Ceramics-Silikaty, 2004. **48**(4): p. 155-158.
28. Biswick, T., et al., *Evidence for the Formation of Anhydrous Zinc Acetate and Acetic Anhydride During the Thermal Degradation of Zinc Hydroxy Acetate, Zn-5(O H)(8)(C H3 C O2)(2).4 H(2) O to Zn O.* Solid State Sciences, 2009. **11**(2): p. 330-335.
29. Zhao, J., et al., *Facile Conversion of Hydroxy Double Salts to Metal-Organic Frameworks Using Metal Oxide Particles and Atomic Layer Deposition Thin-Film Templates.* Journal of the American Chemical Society, 2015. **137**(43): p. 13756-9.
30. Sing, K.S., *Reporting Physisorption Data for Gas/Solid Systems with Special Reference to the Determination of Surface Area and Porosity (Recommendations 1984).* Pure and applied chemistry, 1985. **57**(4): p. 603-619.
31. Malvern, *Zeta Potential Theory, in Zetasizer Nano Series User Manual - Man0317 Issue 1.1*. 2013, Malvern Instruments Ltd: Worcestershire, England. p. 15.2.
32. Vanysek, P., *Electrochemical Series*, in *Crc Handbook of Chemistry and Physics, 94th Edition*, W.M. Haynes, Editor. 2013, Taylor & Francis. p. 5- 80.
33. Williams, G.R., et al., *Immunity Induced by a Broad Class of Inorganic Crystalline Materials Is Directly Controlled by Their Chemistry.* Journal of Experimental Medicine, 2014. **211**(6): p. 1019-1025.
34. Cygan, R.T., Guggenheim S., and van Groos A.F.K., *Molecular Models for the Intercalation of Methane Hydrate Complexes in Montmorillonite Clay.* Journal of Physical Chemistry B, 2004. **108**(39): p. 15141-15149.
35. Zhang, S.T., et al., *Valence Force Field for Layered Double Hydroxide Materials Based on the Parameterization of Octahedrally Coordinated Metal Cations.* Journal of Physical Chemistry C, 2012. **116**(5): p. 3421-3431.
36. Fogg, A.M., et al., *Predicting Guest Orientations in Layered Double Hydroxide Intercalates.* Chemistry of Materials, 1999. **11**(5): p. 1194-1200.
37. Y. A. Kaassis, A., et al., *Hydroxy Double Salts Loaded with Bioactive Ions: Synthesis, Intercalation Mechanisms, and Functional Performance.* Journal of Solid State Chemistry, 2016. **238**: p. 129-138.
38. Roy, R., et al., *Zinc Oxide Nanoparticles Provide an Adjuvant Effect to Ovalbumin Via a Th2 Response in Balb/C Mice.* Int Immunol, 2014. **26**(3): p. 159-72.
39. Matsumura, M., et al., *Adjuvant Effect of Zinc Oxide on Th2 but Not Th1 Immune Responses in Mice.* Immunopharmacology and Immunotoxicology, 2010. **32**(1): p. 56-62.
40. Alinovi, R., et al., *Oxidative and Pro-Inflammatory Effects of Cobalt and Titanium Oxide Nanoparticles on Aortic and Venous Endothelial Cells.* Toxicol In Vitro, 2015. **29**(3): p. 426-37.
41. Cao, Z., et al., *Exposure to Nickel Oxide Nanoparticles Induces Pulmonary Inflammation through Nlrp3 Inflammasome Activation in Rats.* Int J Nanomedicine, 2016. **11**: p. 3331-46.

42. Desimone, J., et al. *Geometrically Engineered Particles and Methods for Modulating Macrophage or Immune Responses.* 2013. US20150037428. WO2013082111 A2, PCT/US2012/066790. Application
43. Minang, J.T., et al., *Nickel, Cobalt, Chromium, Palladium and Gold Induce a Mixed Th1- and Th2-Type Cytokine Response in Vitro in Subjects with Contact Allergy to the Respective Metals.* Clinical and Experimental Immunology, 2006. **146**(3): p. 417-26.
44. Flach, T.L., et al., *Alum Interaction with Dendritic Cell Membrane Lipids Is Essential for Its Adjuvanticity.* Nature Medicine, 2011. **17**(4): p. 479-U121.
45. He, H., et al., *Suppression of Activation and Induction of Apoptosis in Raw264.7 Cells by Amniotic Membrane Extract.* Invest Ophthalmol Vis Sci, 2008. **49**(10): p. 4468-75.
46. Li, A., et al., *Signalling Pathways Involved in the Activation of Dendritic Cells by Layered Double Hydroxide Nanoparticles.* Biomaterials, 2010. **31**(4): p. 748-756.
47. Wang, J., et al., *The Enhanced Immune Response of Hepatitis B Virus D N a Vaccine Using Si O2@ L D H Nanoparticles as an Adjuvant.* Biomaterials, 2014. **35**(1): p. 466-478.
48. Li, A., et al., *The Use of Layered Double Hydroxides as DNA Vaccine Delivery Vector for Enhancement of Anti-Melanoma Immune Response.* Biomaterials, 2011. **32**(2): p. 469-477.

Chapter 8 : Conclusions and Future Work

8.1 Summary of Experimental Findings

The aims of this project were to synthesise an array of different adjuvant candidates and test their adjuvant effect *in vitro*, with structure/property relationships being sought to link physicochemical properties of the samples to the immune response they stimulate.

8.1.1 Particle Engineering of Aluminium Oxyhydroxide

The work performed for this chapter demonstrated that it is possible to synthesise AlO(OH) materials from a variety of different Al-sources using hydrothermal processes. In general, sub-70 °C temperatures in continuous plastic flow synthesis were shown to produce gibbsite [γ-$Al(OH)_3$] whilst temperatures exceeding 80 °C generated boehmite [AlO(OH)]. For reactions using a nitrate Al-source, sub-84 °C temperatures produced $Al(OH)_3$ and above this temperature, phase transition to AlO(OH) occurred. However, although there is some evidence of particle size and morphology control through variation of the experimental parameters, in general the particles produced are largely spherical and fall in the size range 40 to 200 nm. The immunological output of these materials being on par or greater than the cytokine concentrations observed for commercially available alums (TNF-α and IL-6).

Attempts to elucidate relationships between physicochemical properties of the nanoparticles and the immunological output by RAW cells found that the particle size appeared causative of the TNF-α output after exposure to samples synthesised using an Al-chloride source, with some much weaker evidence also found with those generated with an Al-nitrate source and *via* the continuous hydrothermal flow process (CHFS).

8.1.2 Particle Engineering of Hydroxyapatite Nanoparticles

The hydroxyapatite nanoparticles produced were all of a similar size, 150 – 165 nm, but increasing the temperature of the reaction led to an increase in the number of morphologies within the collected sample. The lowest reaction temperature (70 °C) and washing the product with methanol produced solely spherical nanoparticles, while increasing the temperature by 10 – 20 °C led to samples containing spherical and rod-like hydroxyapatite nanoparticles. However, when using deionised water as the cleaning solvent, spherical, rod-like and platelet shaped nanoparticles are obtained at 90 °C.

In vitro experiments suggested an increase in morphology types may induce a weaker IL-6 response from the RAW264.7 cells, with constant TNF-α concentrations. It is therefore possible that there may be potential for tuning the immune response through engineering the hydroxyapatite particles. There were no clear relationships between the physicochemical properties of the particles and the immunological output, however.

8.1.3 Particle Engineering of Zinc Oxide Nanoparticles

Control of the particle size of zinc oxide in the CHFS process requires the addition of Ti(II) salt to the reaction mixture. Increasing the concentration of the Ti(II) salt in the synthetic process corresponds to a decrease in size of the particles from 90 to 42 nm, as well as an increase in the number of particle morphologies present. For the largest sample size only spherical particles are obtained, with rod-like particles additionally being present in the medium-sized material generated in the presence of a small amount of Ti(II). Further, the smallest size material additionally contains platelet-shaped nanoparticles. The particle size was found to be strongly related to the zeta potential measured in phosphate buffered saline.

An increase in ZnO particle size corresponded to an increase in IL-6 production by RAW264.7 cells *in vitro*, with the largest sample being more potent than the positive control. Cytokine production by RAW264.7 cells is strongly correlated to both the particle size and zeta potential of the ZnO materials, and thus particle engineering may provide a means of tailoring the immune response.

8.1.4 The Immunological Properties of Layered Double Hydroxides

A series of LDH materials was generated following literature protocols. All the samples exhibited platelet morphology, and an increase in the radius of the guest anion intercalated into the LDHs' interlayer region appeared to lead to larger particles. It was also possible to synthesise LDH materials with two guest anions intercalated into the interlayer space, and to vary the balance of these depending on the reaction conditions.

In vitro, the LDH materials induced fairly constant concentrations of TNF-α following exposure of RAW cells to these adjuvants, while an increase in the ionic size of the guest seemed to correspond to an increase in IL-6 production. Relationships between physicochemical properties and the immunological output were sought, with strong correlations being obtained for the mono-halide LDH species in terms of their particle size and zeta potential measurements, but weaker ones for the di-halide systems,. Clearly, varying the chemical composition may enable tuning of the immune response.

Dehydrated LDH structures were simulated *in silico*, with the optimised unit cell parameters being found to be predictive of the immunological output of the RAW264.7 cells in some cases: as before, strong correlations were observed for the mono-halide LDHs and weak trends observed for the di-halide systems.

Finally, a suitable proxy for the zeta potential was obtained through computational modelling. The simulated value for the energy of the LDH structures could be used in place of the experimentally derived zeta potential measurements to predict the immune response using the equation previously derived [1]. This opens up the opportunity to undertake *in silico* screening of potentially thousands of LDH structures to identify lead candidates for a given vaccine scenario.

8.1.5 Hydroxy Double Salts as Adjuvants

HDS materials were successfully synthesised following literature protocols; all exhibit platelet morphologies and exist as microparticles. Limited success was obtained with *in silico* modelling of this class of material, with only $[Zn_5(OH)_8](NO_3)_2{\cdot}yH_2O$, $[Zn_5(OH)_8]Cl_2{\cdot}yH_2O$ and $[Zn_{3.8}Co_{1.2}(OH)_8](NO_3)_2{\cdot}yH_2O$ being simulated with any degree of success. Even then, it did not prove possible to fully optimise the structures because of problems arising with the interatomic potential parameters, bond lengths exceeding the maximum cut-offs placed on the system, and a lack of crystallographic insight into the locations of the cobalt and nickel cations in the metal layer.

In vitro the samples vary in terms of the IL-6 concentration they induce in RAW cells, but similar TNF-α concentrations are secreted in response to all the HDS materials. $[Zn_5(OH)_8](CH_3COO)_2{\cdot}yH_2O$ stimulates extremely high IL-6 concentrations, greater than the positive control. Furthermore, the presence of two divalent cations in the layer ($[Zn_{3.8}Co_{1.2}(OH)_8](NO_3)_2{\cdot}yH_2O$ and $[Zn_3Ni_2(OH)_8](NO_3)_2{\cdot}yH_2O$) induces a marked increase in the IL-6 concentration over the single-metal layer system, $[Zn_5(OH)_8](NO_3)_2{\cdot}yH_2O$.

Efforts to correlate the immunological output data to the unit cell parameters calculated *in silico* produced two strong relationships for TNF-α production. These parameters were GULP-simulated values for the *a*-parameter and the β-angle of the HDS unit cell. In contrast, no clear correlations were found between the physicochemical properties of the HDS materials (such as zeta potential measurements and particle size). As noted for the LDH materials, changes in the chemical composition lead to different cytokine concentrations being stimulated *in vitro*, and this offers a route by which the immune response could be tuned.

8.2 Comparison of Systems Explored

There are a variety of different parameters that may affect the ability to tune the immune response. Of the five different materials investigated in this work, it seems that the LDH and HDS materials have the greatest potential as future adjuvants for the reasons set out below.

The two types of layered material (LDH and HDS) possess a high degree of compositional variability due to their capacity to contain a wide variety of metals in the layer, and numerous guest anion species intercalated into the interlayer region. This work has shown that changing the composition of these materials has an impact on the elicited immune response, and therefore there is the potential to fine tune the immune response.

The zinc oxide nanoparticles may lead to some modulation of the immune response, with potent IL-6 concentrations being stimulated in response to large particles. This could provide prophylactic treatment to diseases that would respond to such high cytokine concentrations. However, both the work undertaken here and the literature indicate that a Th2 immune response is overwhelmingly produced in response to ZnO. The existing alum adjuvants also drive a Th2 response, and therefore it is not clear that ZnO offers any major advantages here.

The remaining materials explored (aluminium oxyhydroxide and hydroxyapatite) appear to have less potential for exploitation: it is challenging to control the particle size and shape in the particle engineering approaches applied, and also these materials do not have the same degree of tuneability in the immune response provoked.

8.3 Future Work

8.3.1 Particle Engineering of Aluminium Oxyhydroxide

In order to take this work further, further investigation into synthetic routes for AlO(OH) production, using alternative Al-sources within the continuous plastic hydrothermal flow synthesis (CPFS) process, could be considered. This would allow a broader range of systems to be explored, to determine to what extent the Al-source affects the product generated in terms of particle size and morphology. If it proved possible to tune these over a wider range, further exploration of their adjuvanticity would be warranted.

8.3.2 Particle Engineering of Hydroxyapatite Nanoparticles

Future work for these materials could include a more detailed assessment of the temperature at which the particle morphology changes, by performing reactions at a wider range of temperatures. Investigations into the impact of other solvents on the calcium leaching from the hydroxyapatite nanoparticles would also be interesting to explore. If a greater degree of control over particle size, shape or composition could be obtained, then a further exploration of their adjuvant properties could be considered.

8.3.3 Particle Engineering of Zinc Oxide Nanoparticles

The continuous hydrothermal flow synthesis (CHFS) process used for production of ZnO nanoparticles showed that increasing the concentration of Ti(II) in the reaction mixture resulted in a decrease in the size of the collected ZnO nanoparticles, as well as increasing the number of morphologies contained within each sample size. Therefore, future work could involve exploring a wider range of concentrations to see if the range of sizes/shapes which can be accessed could be expanded. In order to reduce the costs of the process and aid translation to the clinic, attempting to translate this synthetic route to the CPFS reactor and determine the effect of sub-100 °C temperatures has on the obtained products would also be of interest.

8.3.4 The Immunological Properties of Layered Double Hydroxides

There are thousands of LDH systems in existence. The work done to date has shown their physicochemical properties to be causative of the immune response, and that the latter can be predicted *a priori*. However, because of time constraints only a limited number of systems has been used for calibration of the mathematical models developed. To take this work forward, further work is required to expand the range of systems explored, including the intercalation of immunogenic guests such as succinate and malate, and expand the relationships obtained to date across a wider range of structures.

8.3.5 Hydroxy Double Salts as Adjuvants

Future work for the HDS class of layered materials would require detailed crystallographic information about the exact atomic positions of the divalent metal cations, particularly the location of Co^{2+} and Ni^{2+} in the mixed metal species, to allow for simulations of the mixed metal sheet HDS materials to represent the composition of the synthesised sample without using fractional occupancies. Furthermore, extensive research and optimisation of the interatomic potential parameters described in this work would be beneficial, with the aim of refining the input data to successfully simulate the structures.

More broadly, a wider range of systems could be synthesised for exploration, including *via* the intercalation of immunogenic guest species such as succinate and malate, and their *in vitro* effect on RAW cells determined. This might lead to the recognition of relationships between the immunological output and the physicochemical properties or *in silico* data for the HDSs.

8.4 Future Outlook

In this work, the role of inorganic particulate matter as vaccine adjuvants is considered. Given the limitations of alum, in that it can only induce strong humoral (antibody) immune responses but not the cellular immunity required to combat intracellular pathogens or tumours, the development of new adjuvants is vitally important. The use of particle size and shape engineering has tremendous potential to generate adjuvants that can trigger enhanced or bespoke immune responses, as dose chemical composition control.

It should be noted that there will be significant obstacles to moving a research adjuvant into the clinic. Regardless of the promise inorganic adjuvants present, to obtain approval from regulatory authorities, such as the FDA and European Medicines Agency, a range of in-depth studies will be required to ensure safety. Extensive toxicity screening must be undertaken to study both the extent and duration of local inflammation at the site of injection (*e.g.* pain, redness and swelling) and potential systemic issues (*e.g.* anaphylaxis, nausea, diarrhoea and carcinogenicity).

Adjuvants also have the potential to induce autoimmune diseases, such as systemic lupus erythematosus, and even though the risk is incredibly small the impact on an individual would be high. The rate of elimination of the new particulate adjuvants will need to be robustly established. Extensive clinical trials will be required to demonstrate unequivocally the benefits of the proposed adjuvant compared to unadjuvanted immunisation and currently-licensed adjuvants.

Although the hurdles to patients benefiting from the new adjuvant materials being developed are thus high, in my opinion the immense benefit bestowed on humankind by vaccination means that the effort and cost involved in overcoming these will be worthwhile. It is also my view that use of particle engineering and chemical composition control will expand exponentially in the years to come, hopefully leading to the exploration of potent new adjuvant materials in the clinic.

8.5 References

1. Williams, G.R., et al., *Immunity Induced by a Broad Class of Inorganic Crystalline Materials Is Directly Controlled by Their Chemistry.* Journal of Experimental Medicine, 2014. **211**(6): p. 1019-1025.

Appendix 1: Particle Engineering of Aluminium Oxyhydroxide

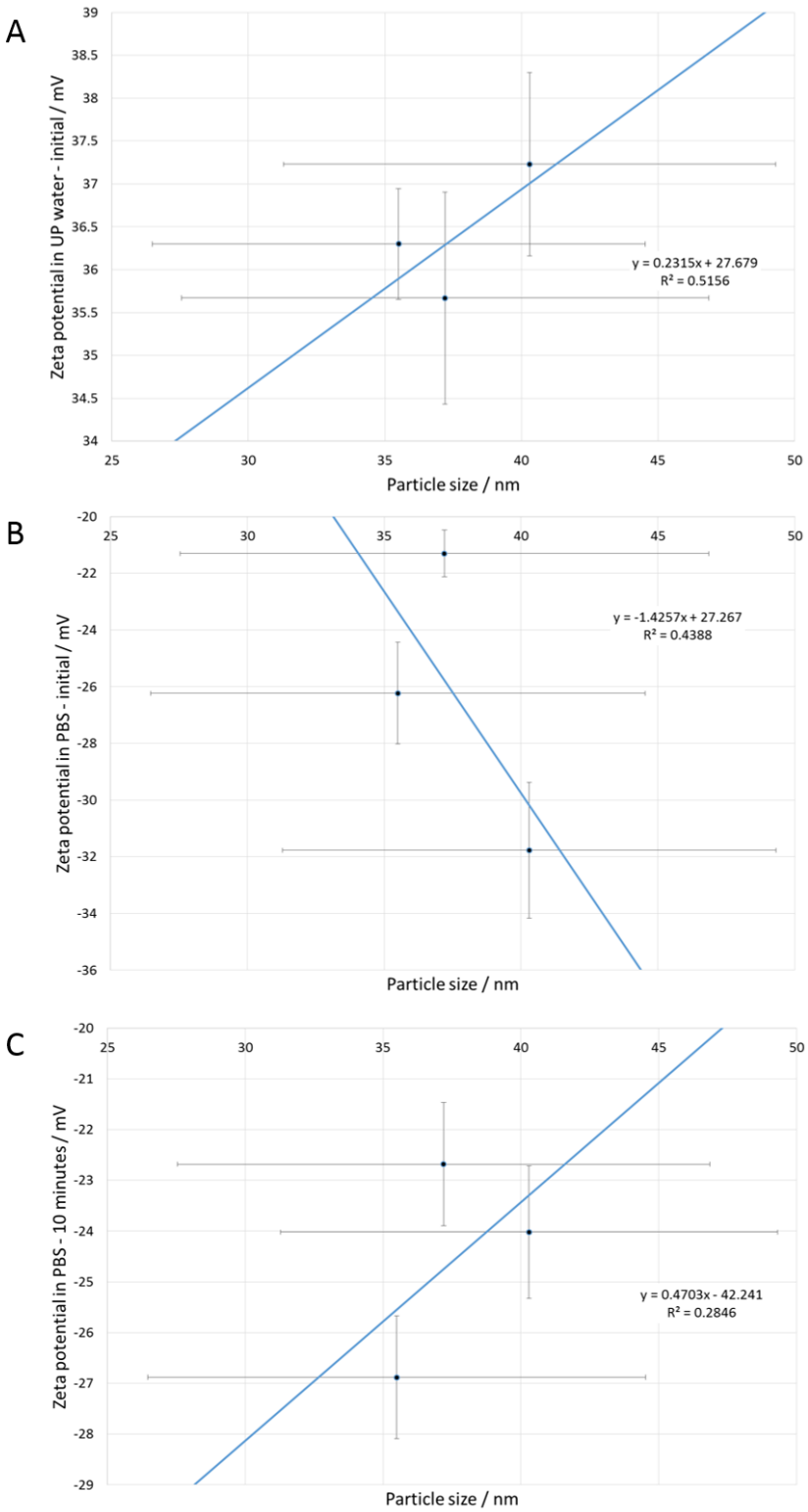

Figure A1.1: ***Graphical representation of the relationships for CPFS-Chloride samples. Plots depict the relationship of zeta potential measurements using (A) UP-water, (B) PBS (initial), and (C) PBS (10 minute time-point) to particle size.***

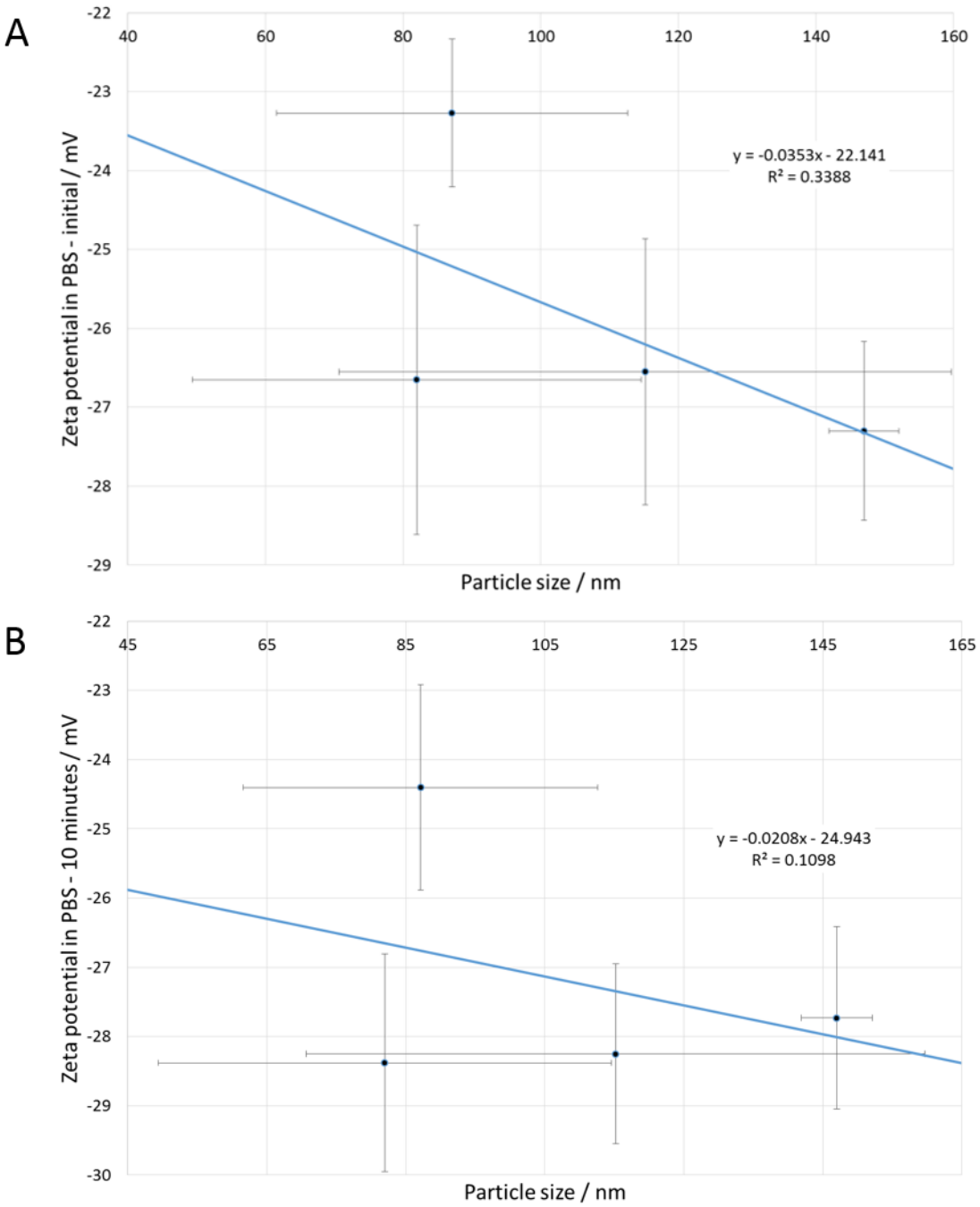

Figure A1.2: ***Graphical representation of the relationships for CPFS-Nitrate samples. Plots depict the relationship of zeta potential measurements using (A) PBS (initial), and (B) PBS (10 minute time-point) to particle size.***

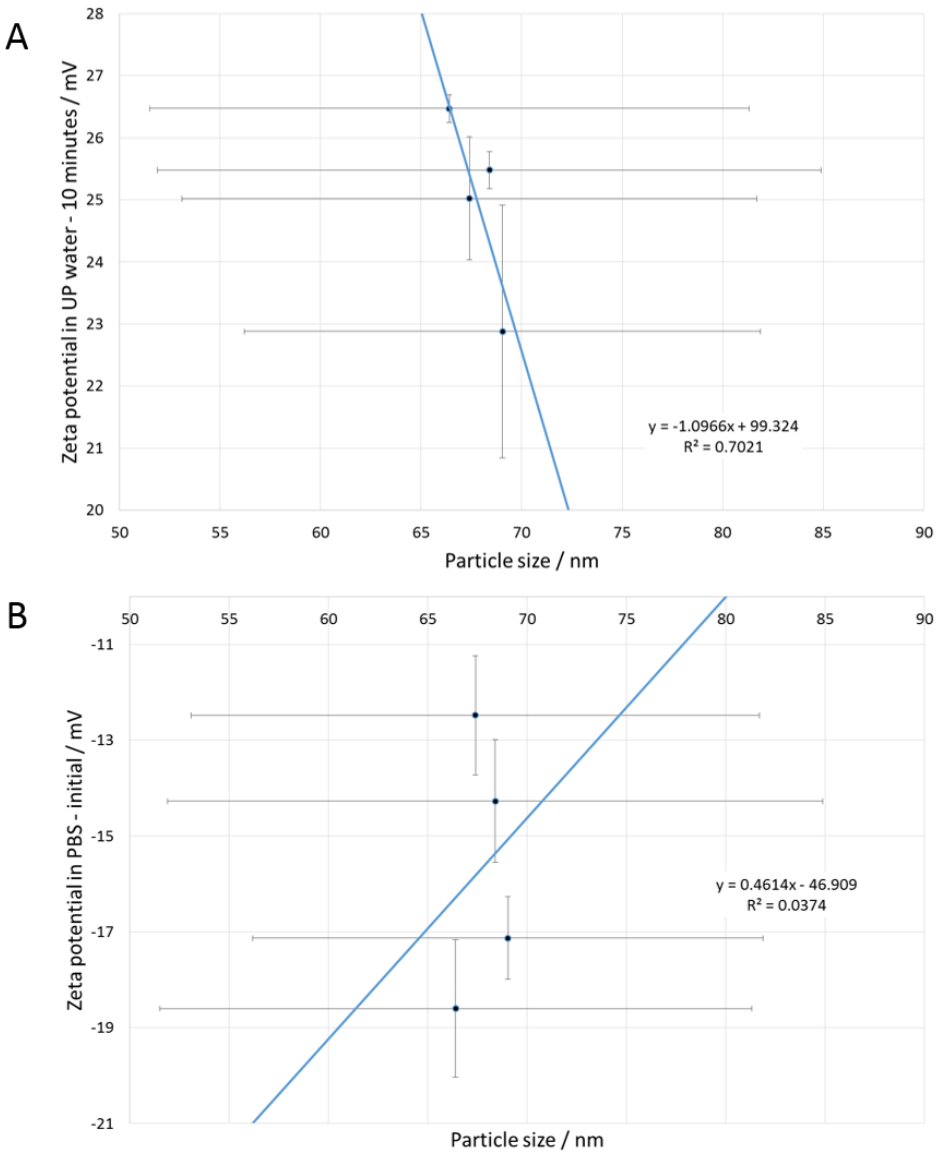

***Figure A1.3**: Graphical representation of the relationships for CHFS samples. Plots depict the relationship of zeta potential measurements using (A) UP-water (10 minute time-point), and (B) PBS (initial) to particle size.*

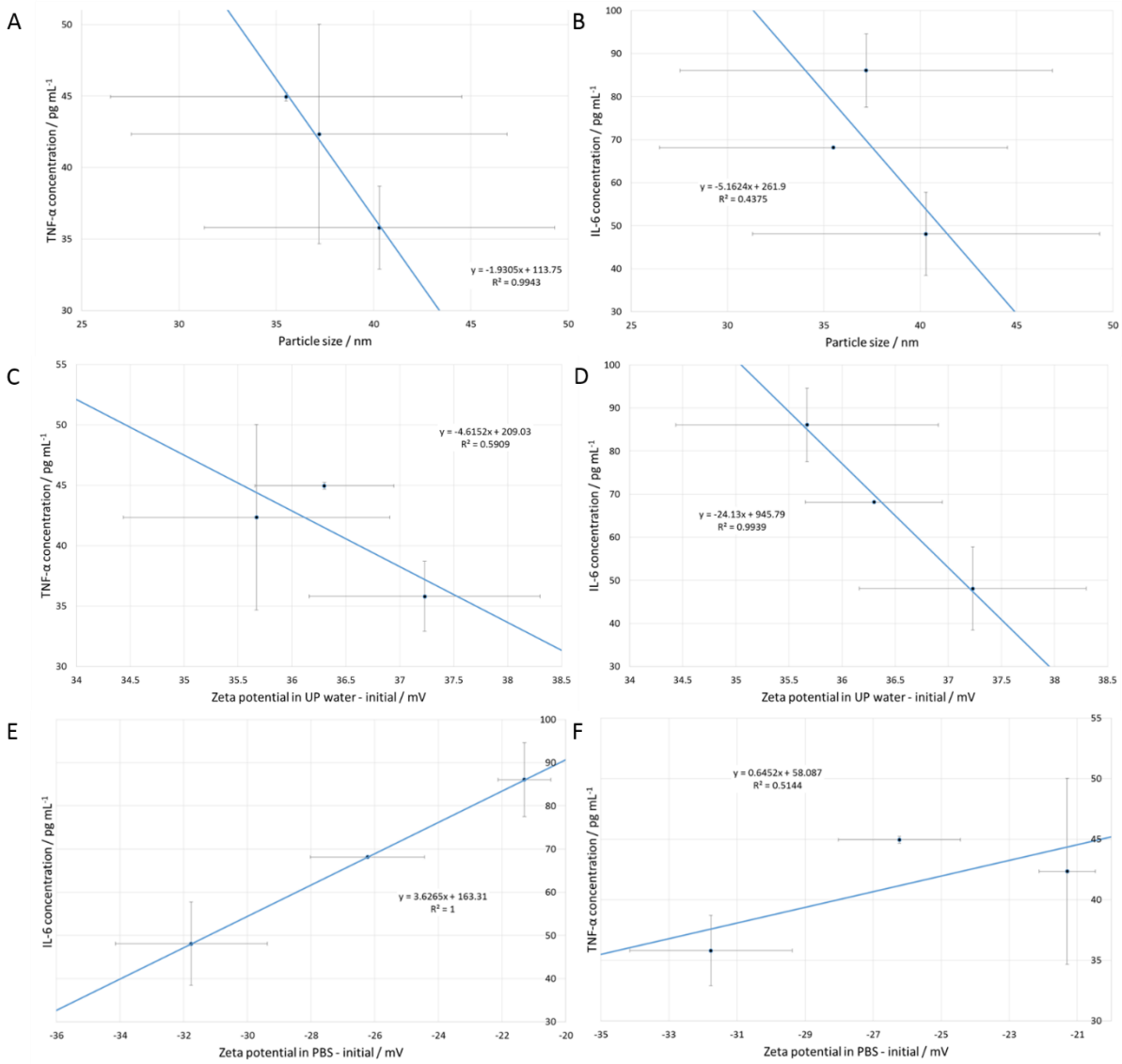

Figure A1.4: ***Graphical representation of relationships for CPFS-Chloride materials with (A and B) particle size, (C and D) zeta potentials measured in UP water (initial), and (E and F) zeta potentials measured in PBS (initial), correlated to TNF α and IL-6 cytokine concentrations.***

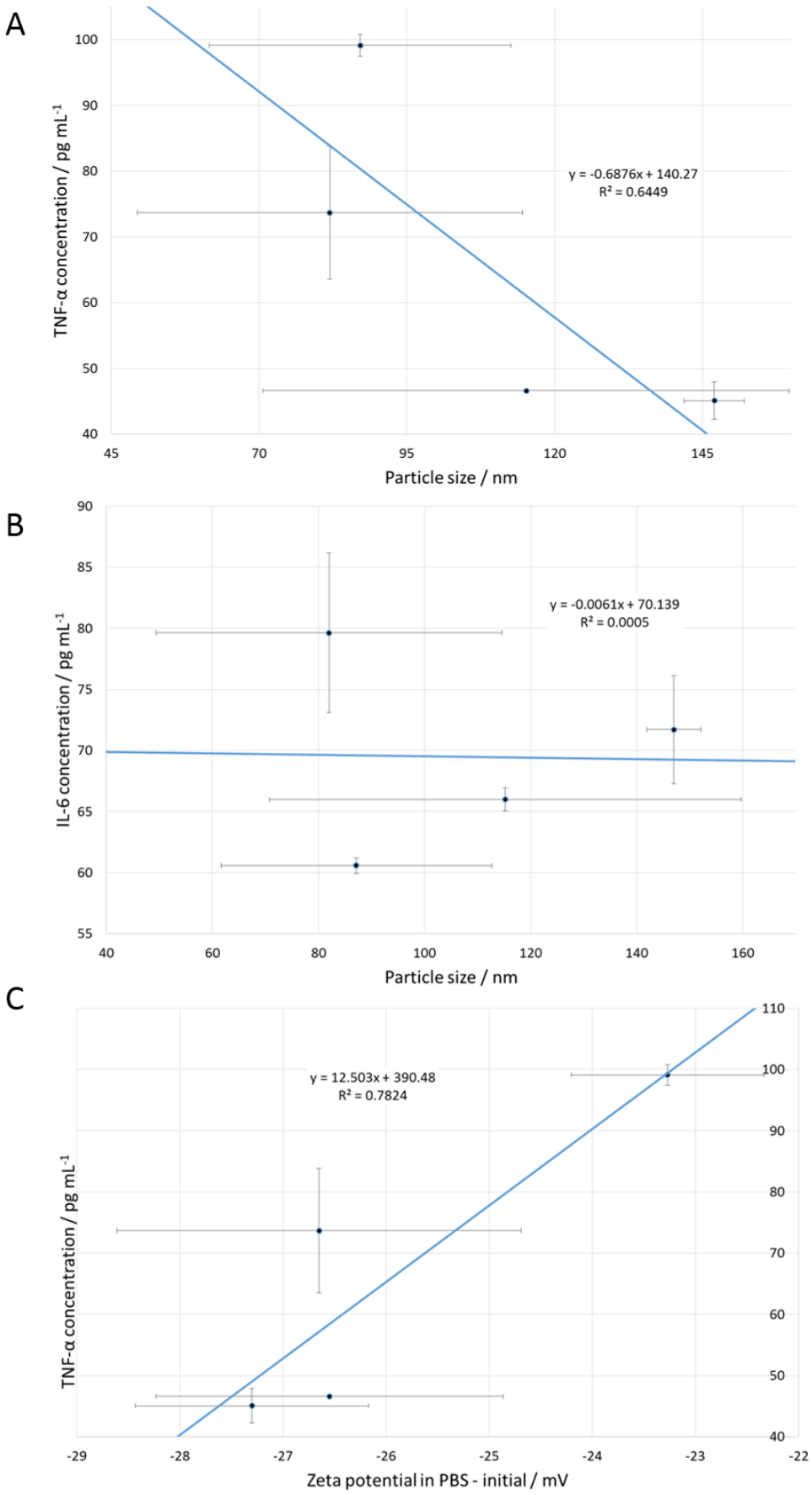

Figure A1.5: ***Graphical representation of relationships for the CPFS-Nitrate samples with (A and B) particle size, (C) zeta potentials measured in PBS (initial), correlated to TNF α and IL-6 cytokine concentrations.***

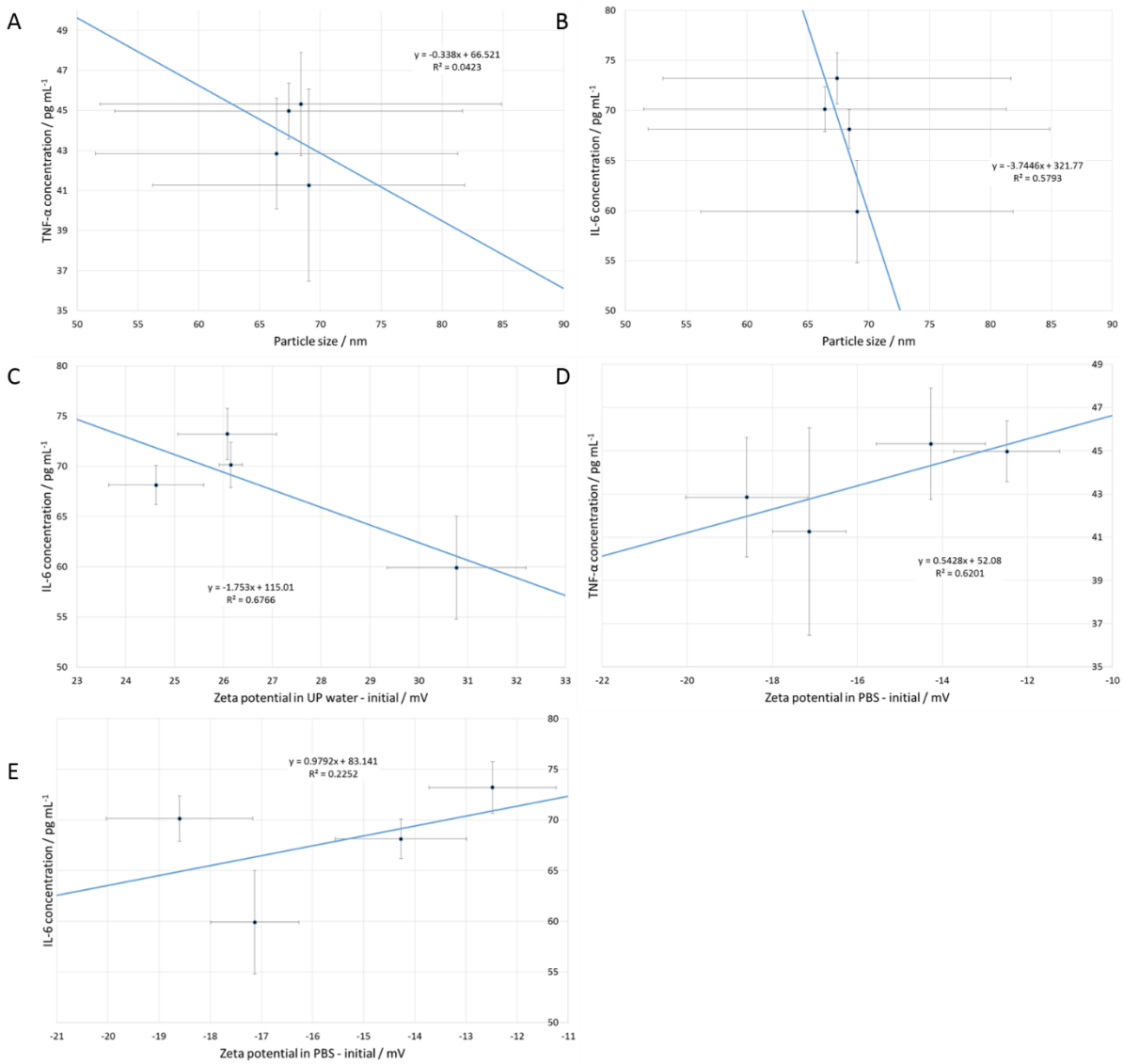

Figure A1.6: ***Graphical representation of CHFS samples with (A and B) particle size, (C) zeta potentials measured in UP water (initial), and (D and E) zeta potentials measured in PBS (initial), correlated to TNF α and IL-6 cytokine concentrations.***

Appendix 2: Particle Engineering of Hydroxyapatite Nanoparticles

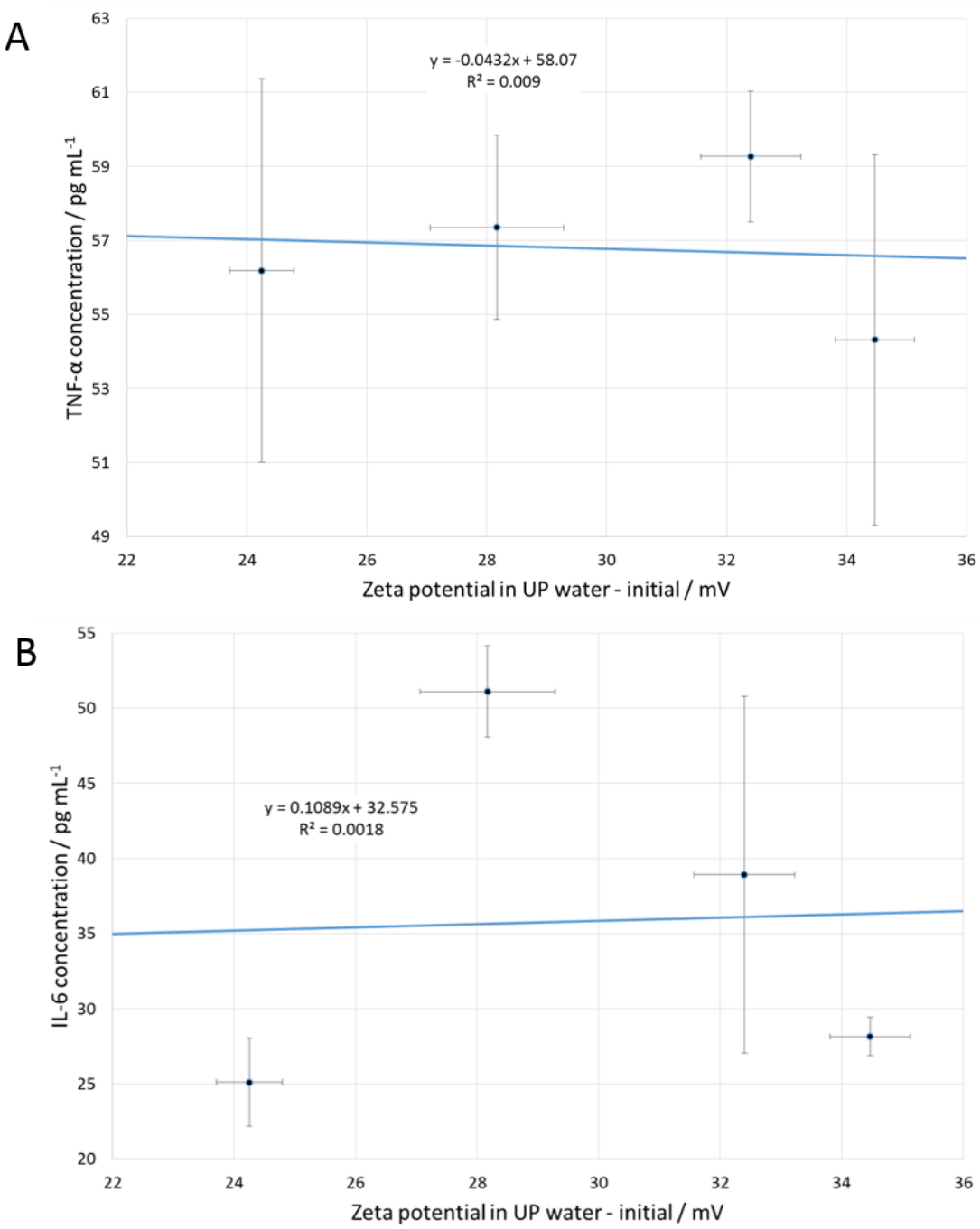

Figure A2.1: ***Graphical representation of the relationships for hydroxyapatite samples. Plots depict the relationship of (A) TNF-α, (B) IL-6 cytokine concentrations with zeta potential measurements in UP water (initial).***

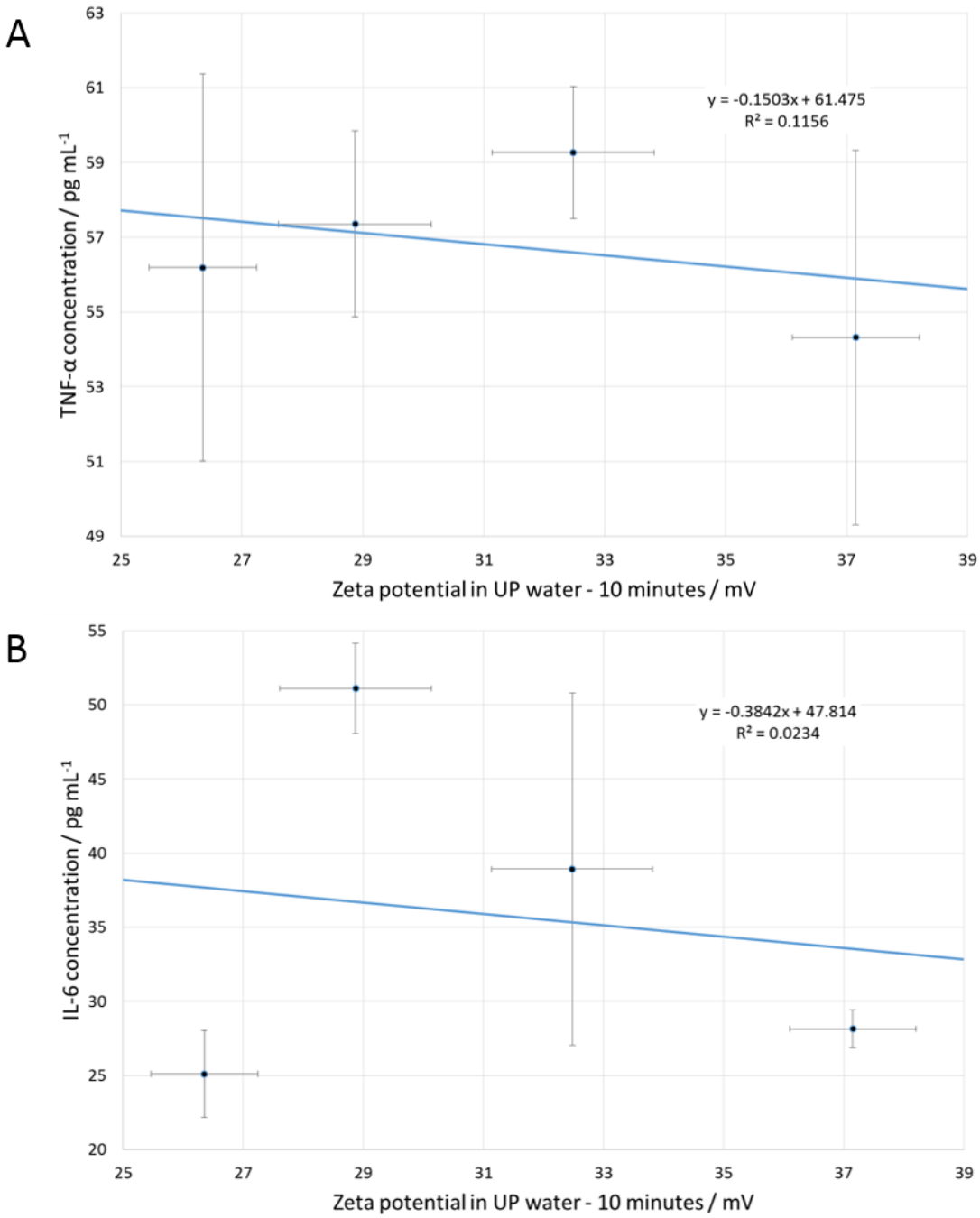

Figure A2.2: ***Graphical representation of the relationships for hydroxyapatite samples. Plots depict the relationship of (A) TNF-α, (B) IL-6 cytokine concentrations with zeta potential measurements in UP water (10 minutes).***

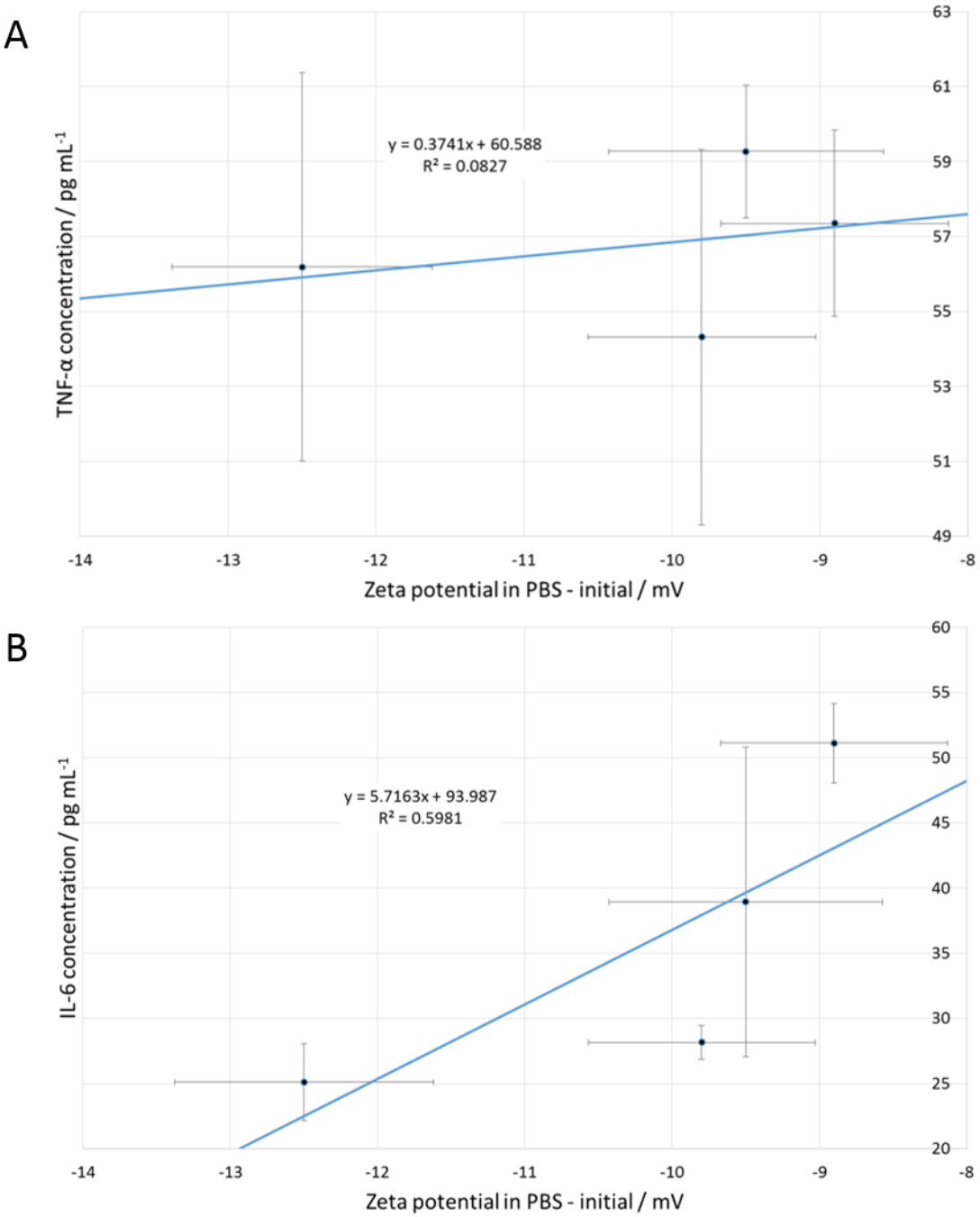

Figure A2.3: ***Graphical representation of the relationships for hydroxyapatite samples. Plots depict the relationship of (A) TNF-α, (B) IL-6 cytokine concentrations with zeta potential measurements in PBS (initial).***

Appendix 3: Particle Engineering of Zinc Oxide Nanoparticles

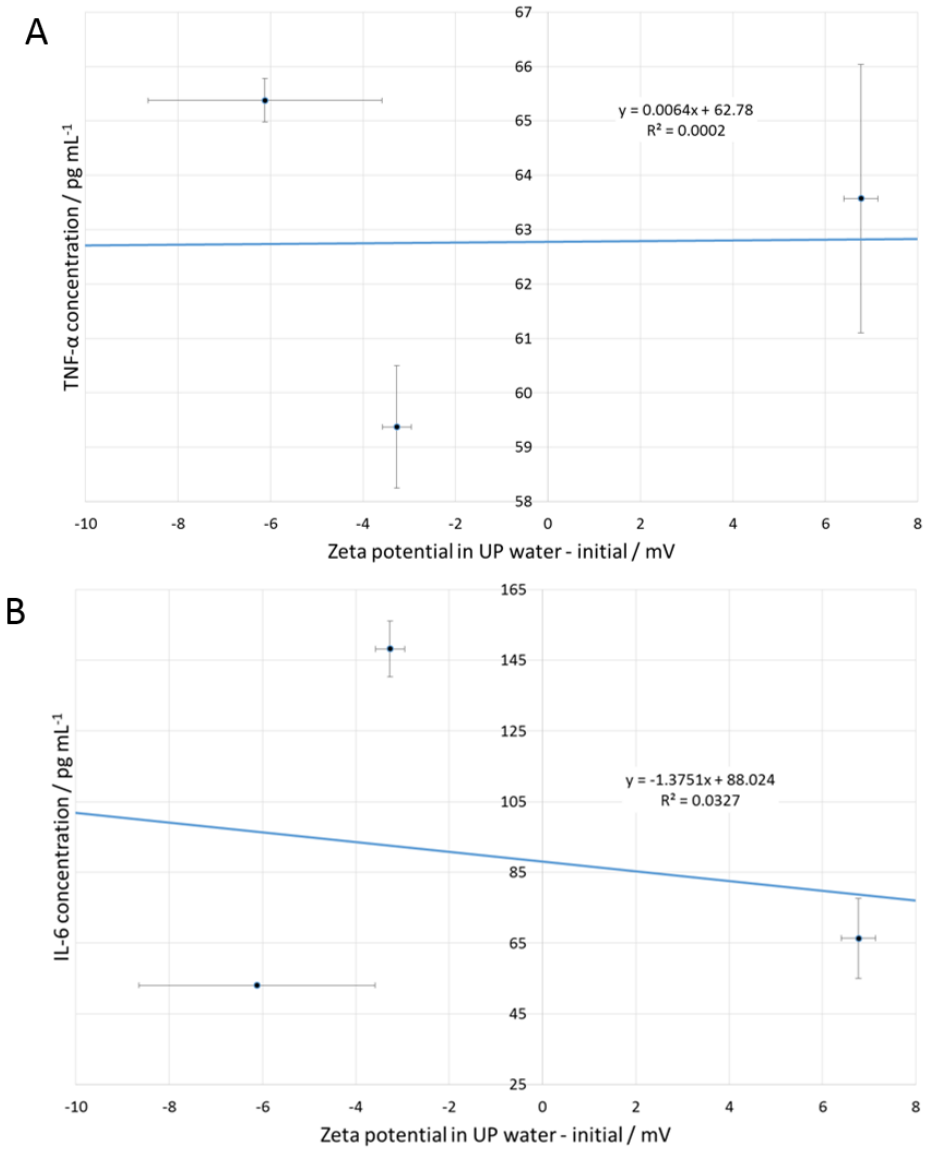

Figure A3.1: ***Graphical representation of the relationships for ZnO samples. Plots depict the relationship of (A) TNF-α, (B) IL-6 cytokine concentrations with zeta potential measurements in UP water (initial).***

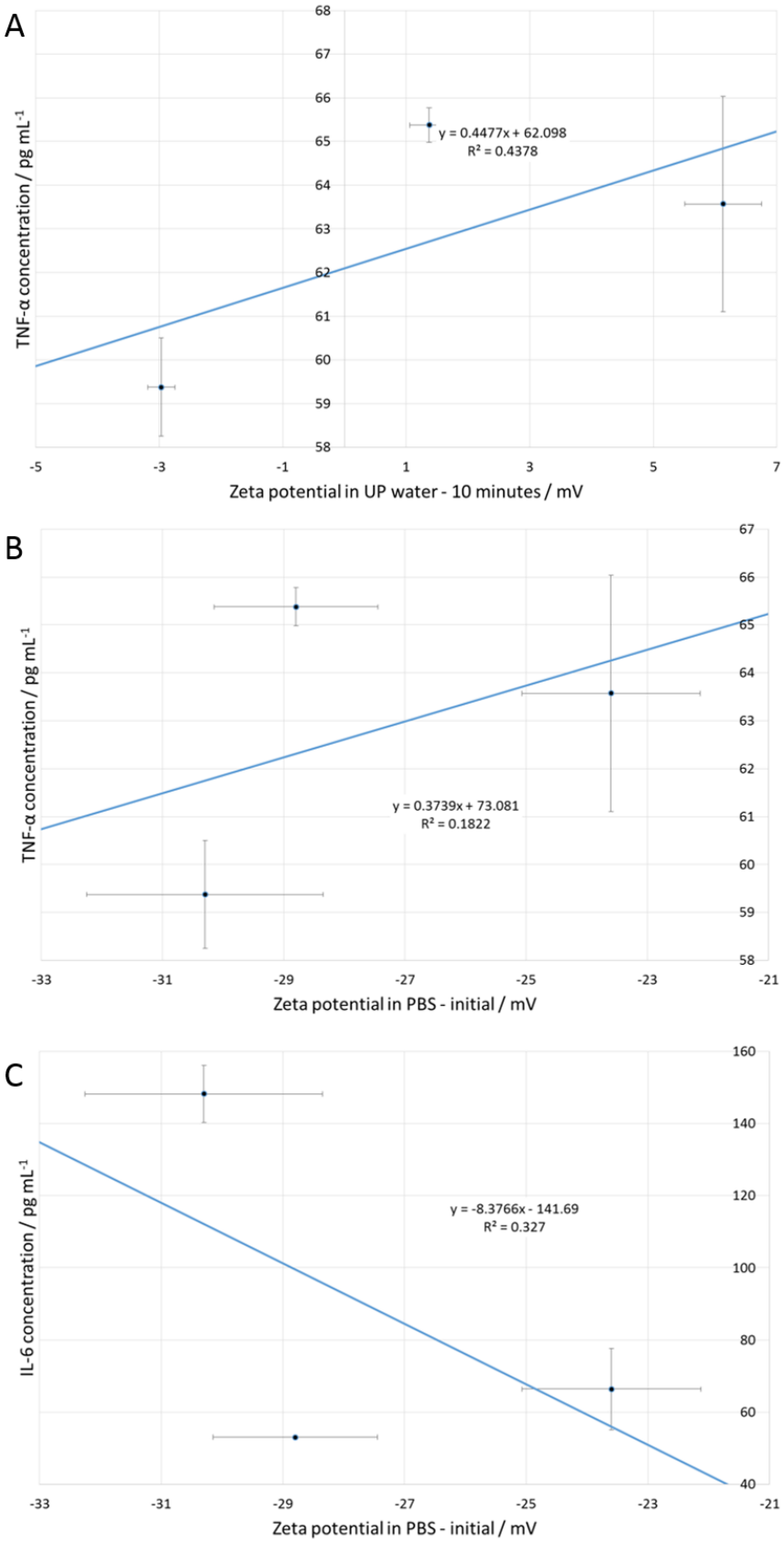

Figure A3.2: ***Graphical representation of the relationships for ZnO samples. Plots depict the relationship of TNF-α and IL-6 cytokine concentrations with zeta potential measurements in (A) UP water (initial), and (B and C) in PBS (initial).***

Appendix 4: The Immunological Properties of Layered Double Hydroxides

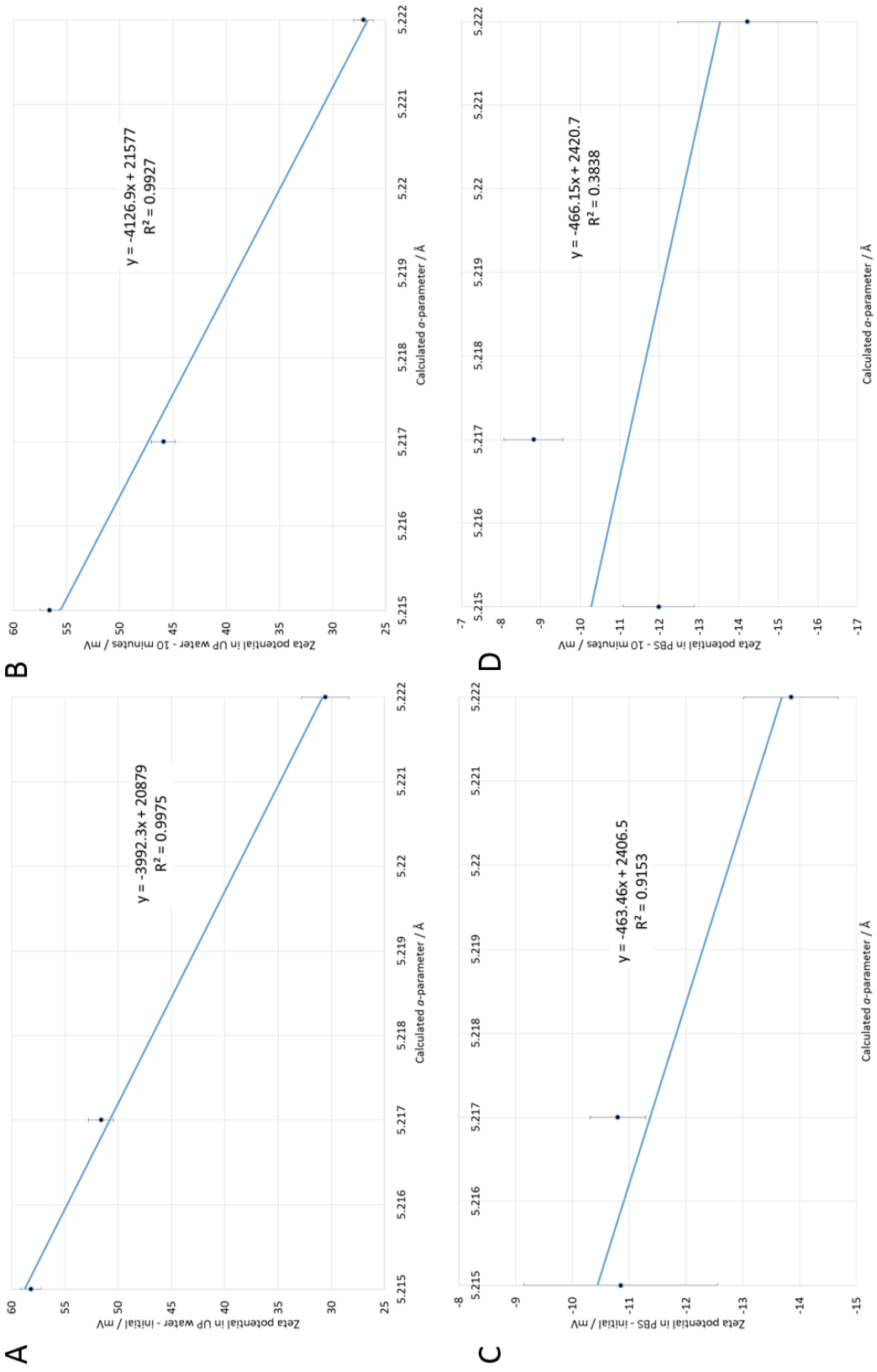

Figure A4.1: ***Graphical representation of the mono-halide LDH materials. The zeta potential measurements recorded in (A) UP water (initial), (B) UP water (10 minutes), (C) PBS (initial) and (D) PBS (10 minutes) are correlated to the calculated lattice a-parameter.***

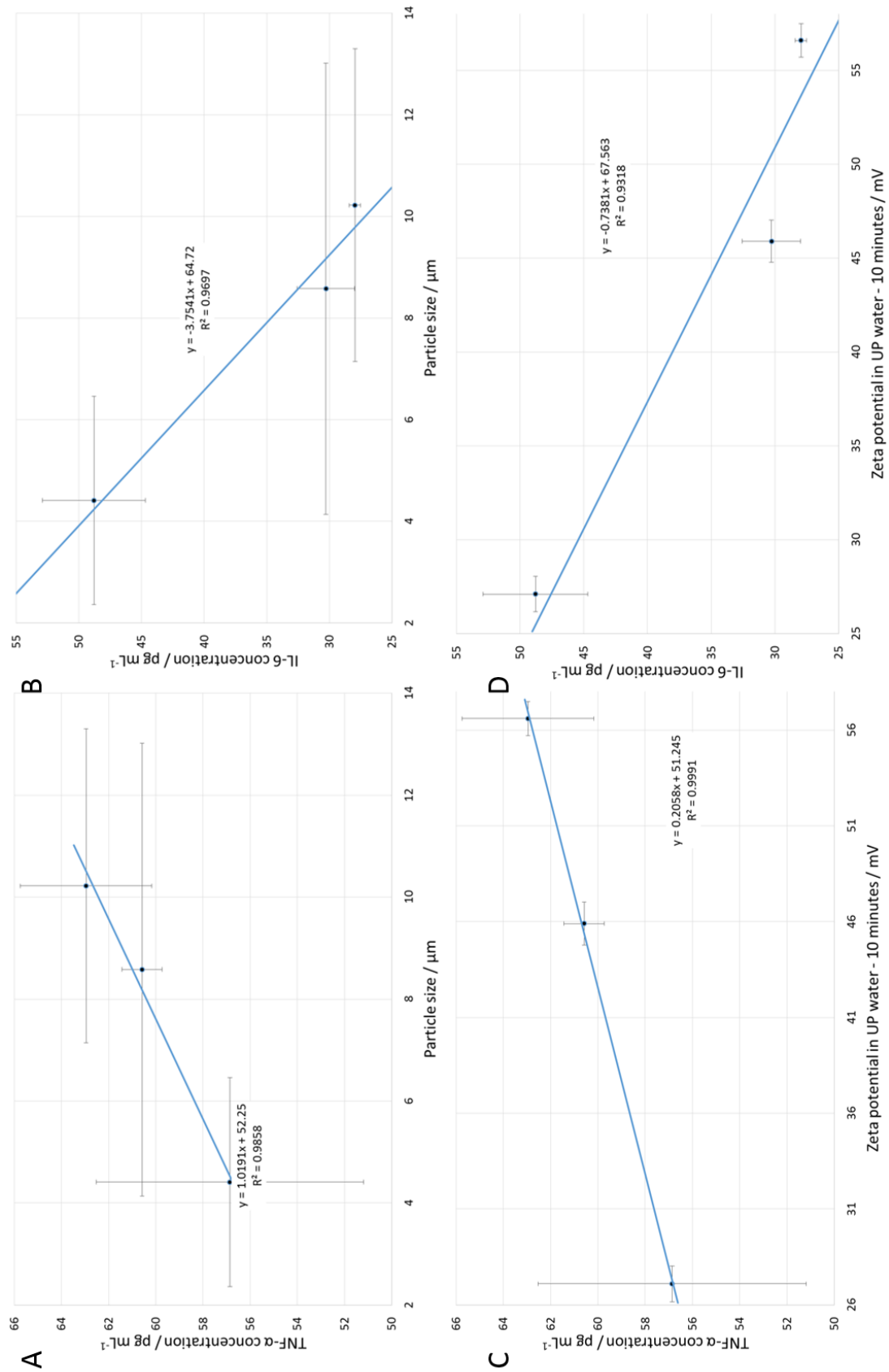

Figure A4.2: ***Graphical representation of the relationships for mono-halide LDH samples. Plots depict the relationship of (A) TNF-α and (B) IL-6 cytokine concentrations with particle size and (C) TNF-α and (D) IL-6 cytokine concentrations with zeta potential measurements in UP water (10 minute time-point).***

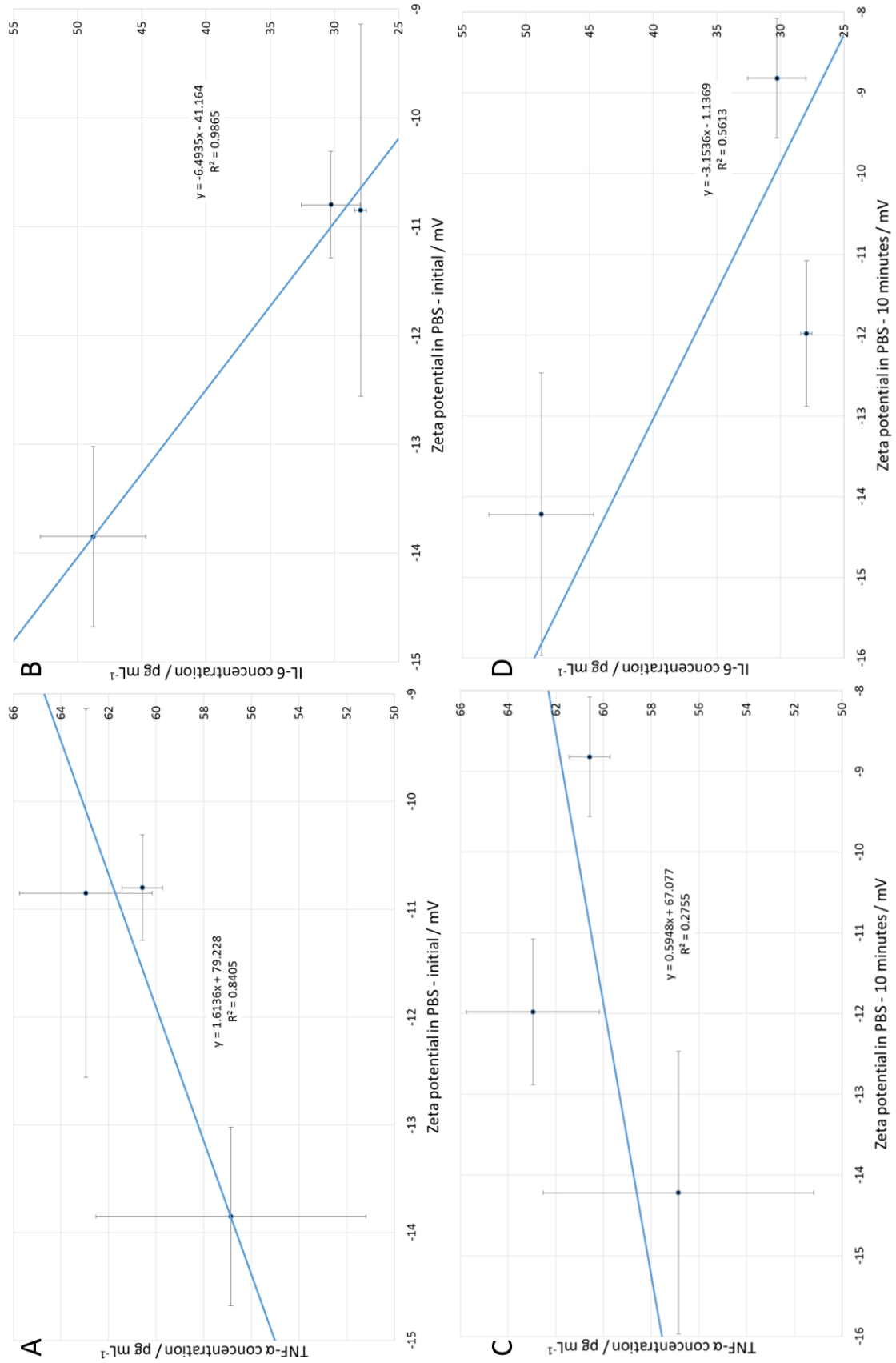

Figure A4.3: ***Graphical representation of the relationships for mono-halide LDH samples. Plots depict the relationship of (A) TNF-α and (B) IL-6 cytokine concentrations with zeta potential measurements in PBS (initial) and (C) TNF-α and (D) IL-6 cytokine concentrations with zeta potential measurements in PBS (10 minute time-point).***

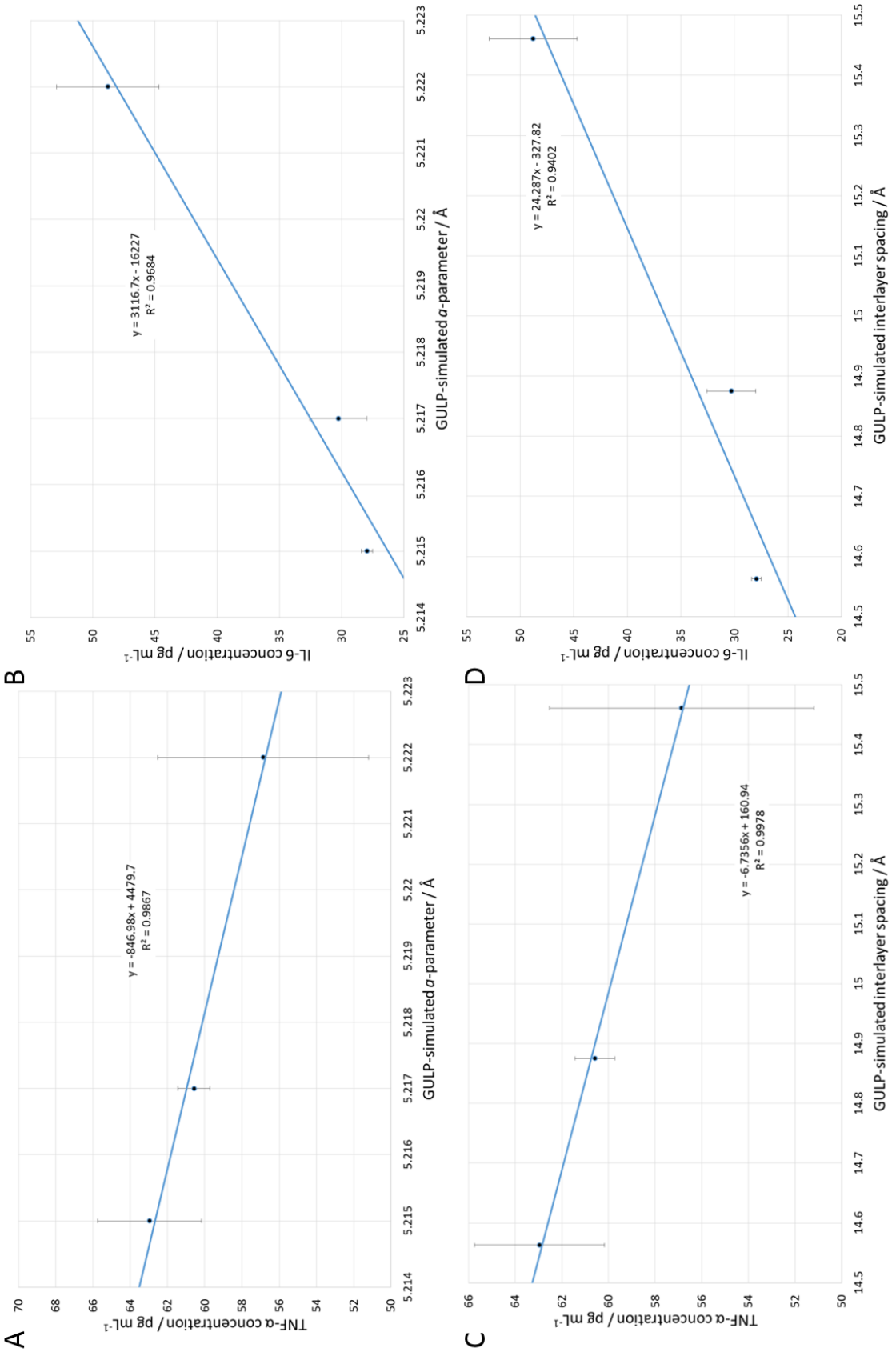

Figure A4.4: ***Graphical representation of the (A) TNF-α and (B) IL-6 cytokine concentrations correlated to calculated unit cell a-parameter; the (C) TNF-α and (D) IL-6 cytokine concentrations correlated with calculated unit cell interlayer spacing-parameter.***

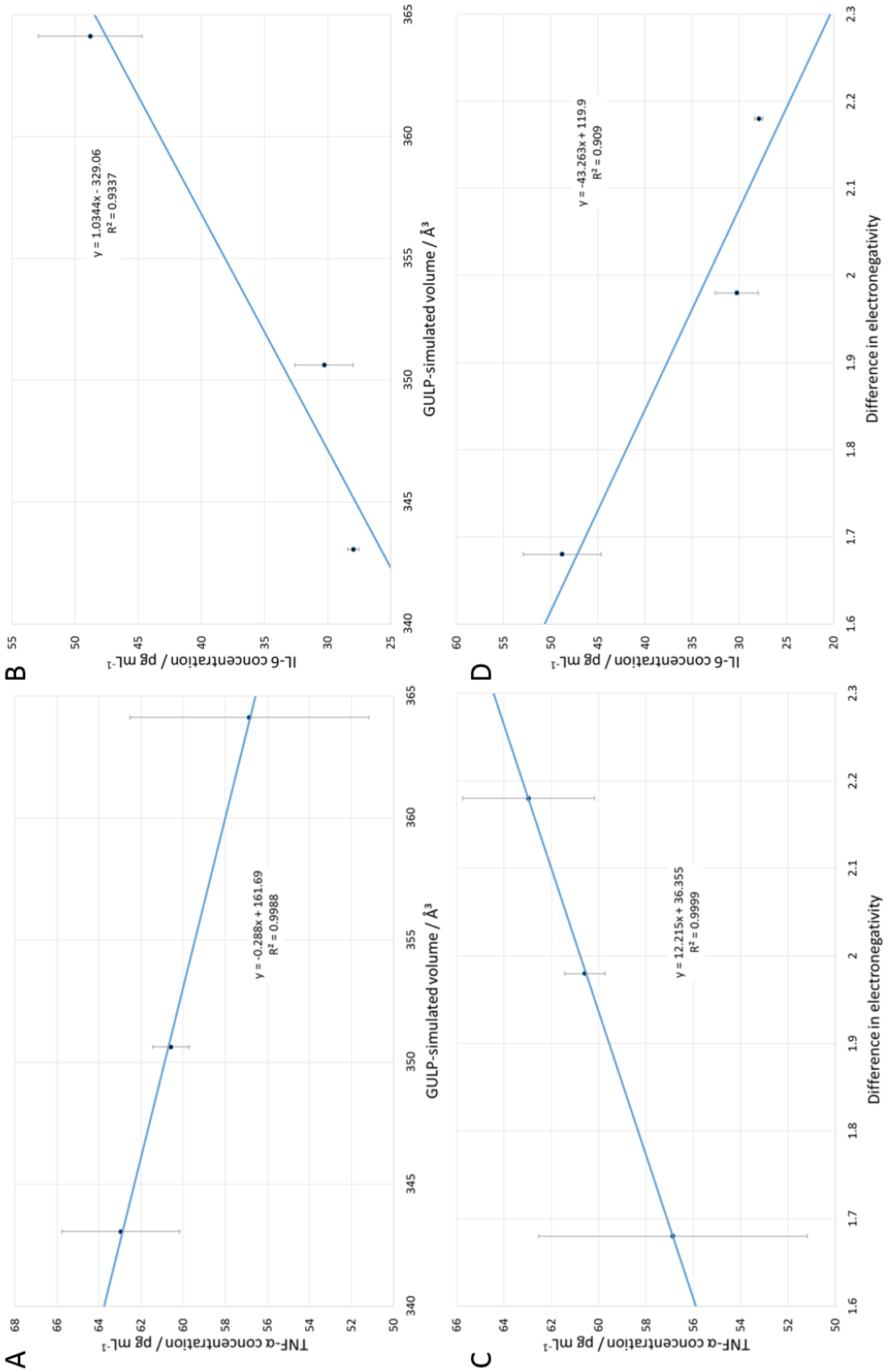

Figure A4.5: ***Graphical representation of the (A) TNF-α and (B) IL-6 cytokine concentrations correlated to calculated unit cell volume-parameter; the (C) TNF-α and (D) IL-6 cytokine concentrations correlated with difference in electronegativity.***

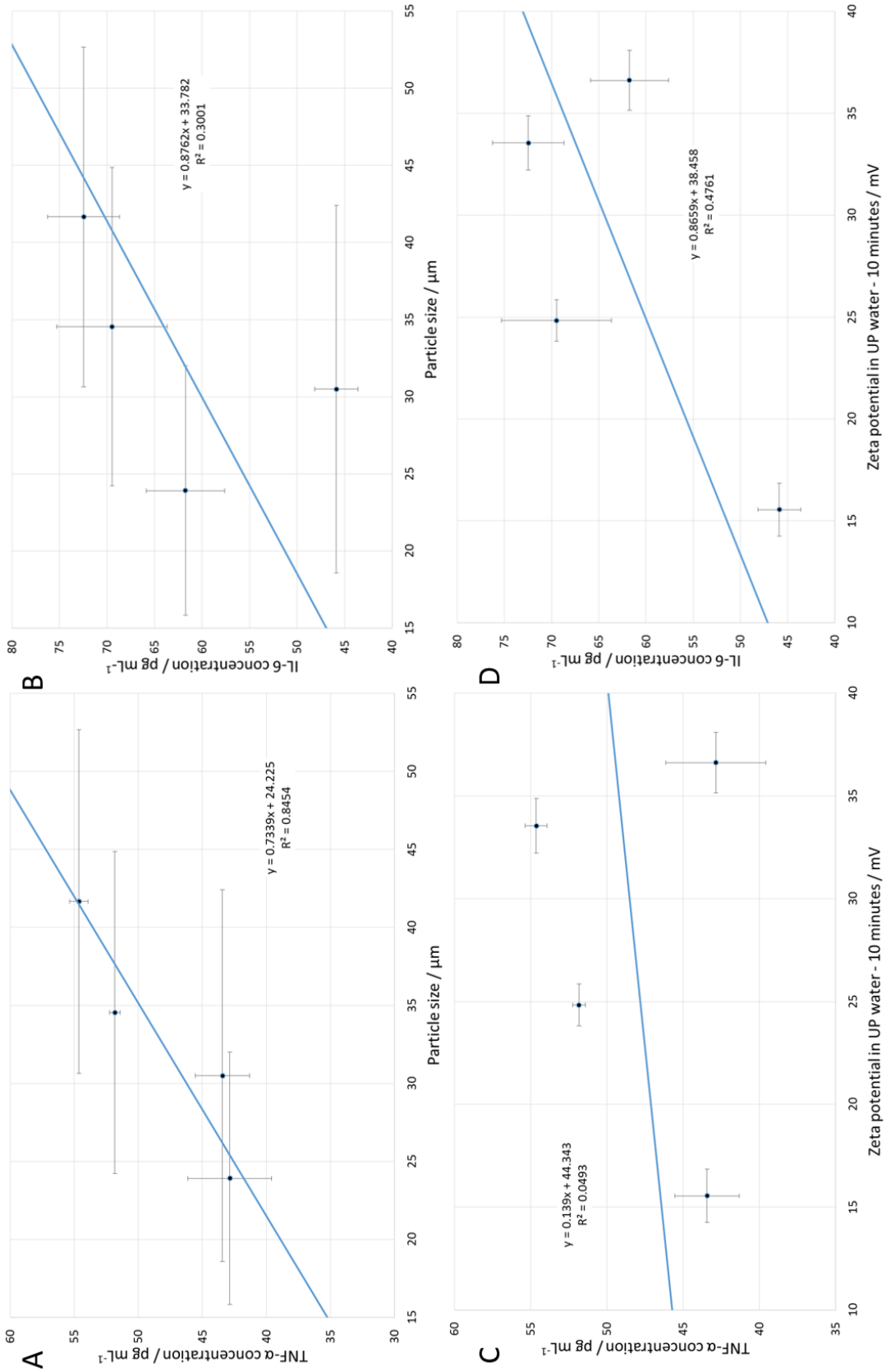

Figure A4.6: ***Graphical representation of the relationships for di-halide LDH samples. Plots depict the relationship of (A) TNF-α and (B) IL-6 cytokine concentrations with particle size and (C) TNF-α and (D) IL-6 cytokine concentrations with zeta potential measurements in UP water (10 minute time-point).***

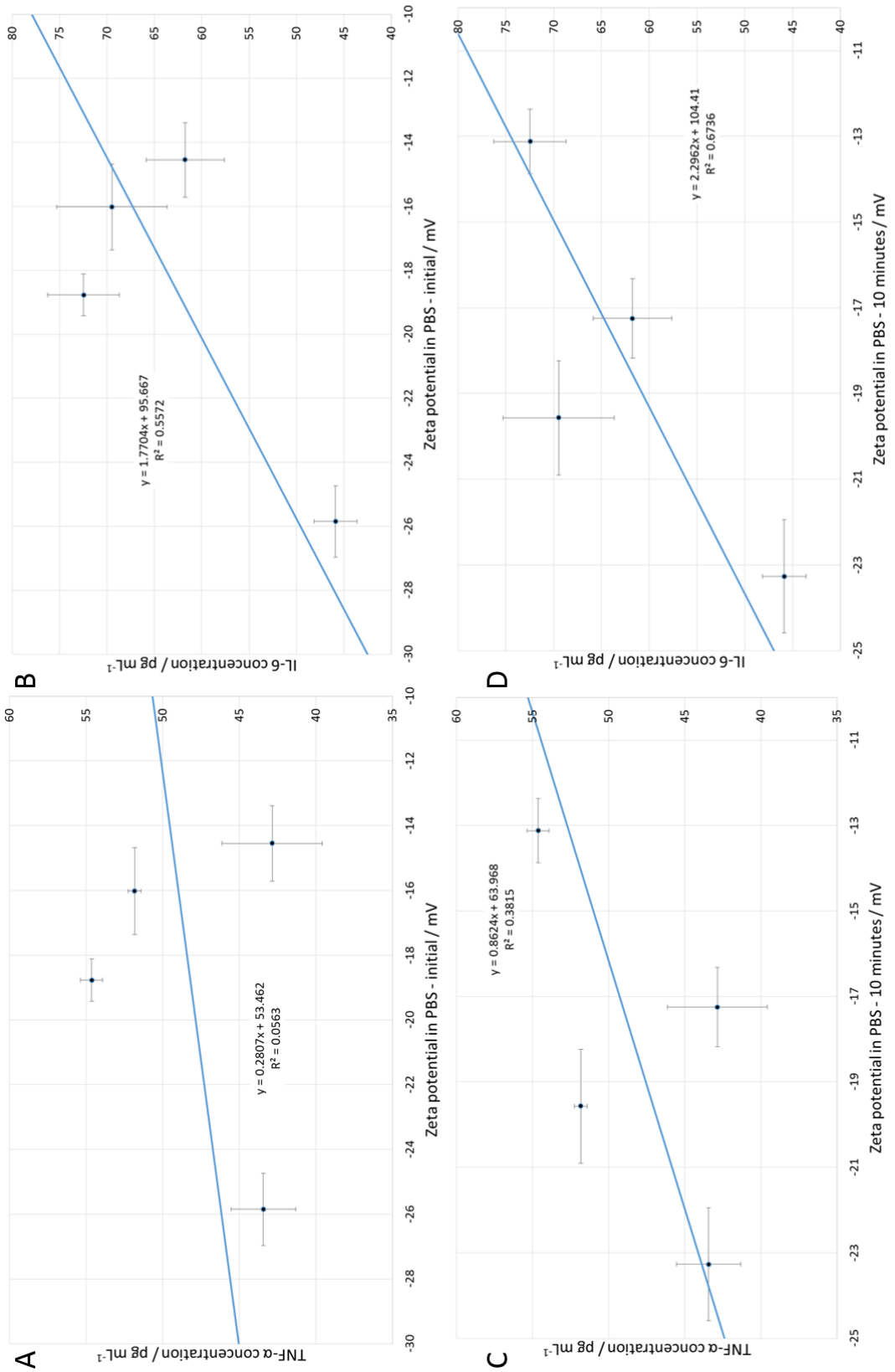

Figure A4.7: ***Graphical representation of the relationships for di-halide LDH samples. Plots depict the relationship of (A) TNF-α and (B) IL-6 cytokine concentrations with zeta potential measurements in PBS (initial) and (C) TNF-α and (D) IL-6 cytokine concentrations with zeta potential measurements in PBS (10 minute time-point).***

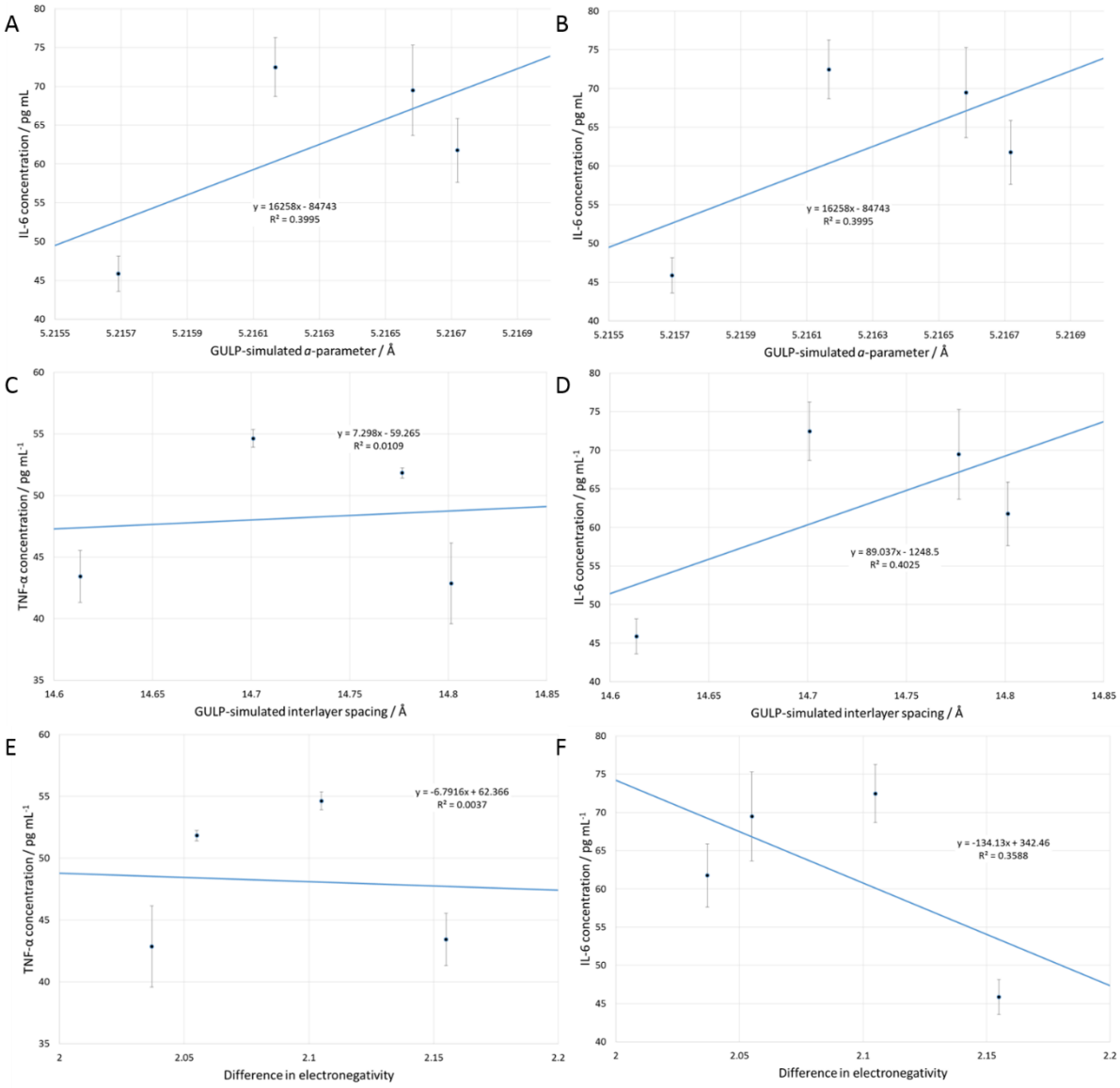

Figure A4.8: ***Graphical representation of the di-halide LDH materials' (A) TNF-α and (B) IL-6 cytokine concentrations correlated to calculated unit cell a-parameter; the (C) TNF-α and (D) IL-6 cytokine concentrations correlated with calculated unit cell interlayer spacing-parameter, and the (E) TNF-α and (F) IL-6 cytokine concentrations correlated to difference in electronegativity.***

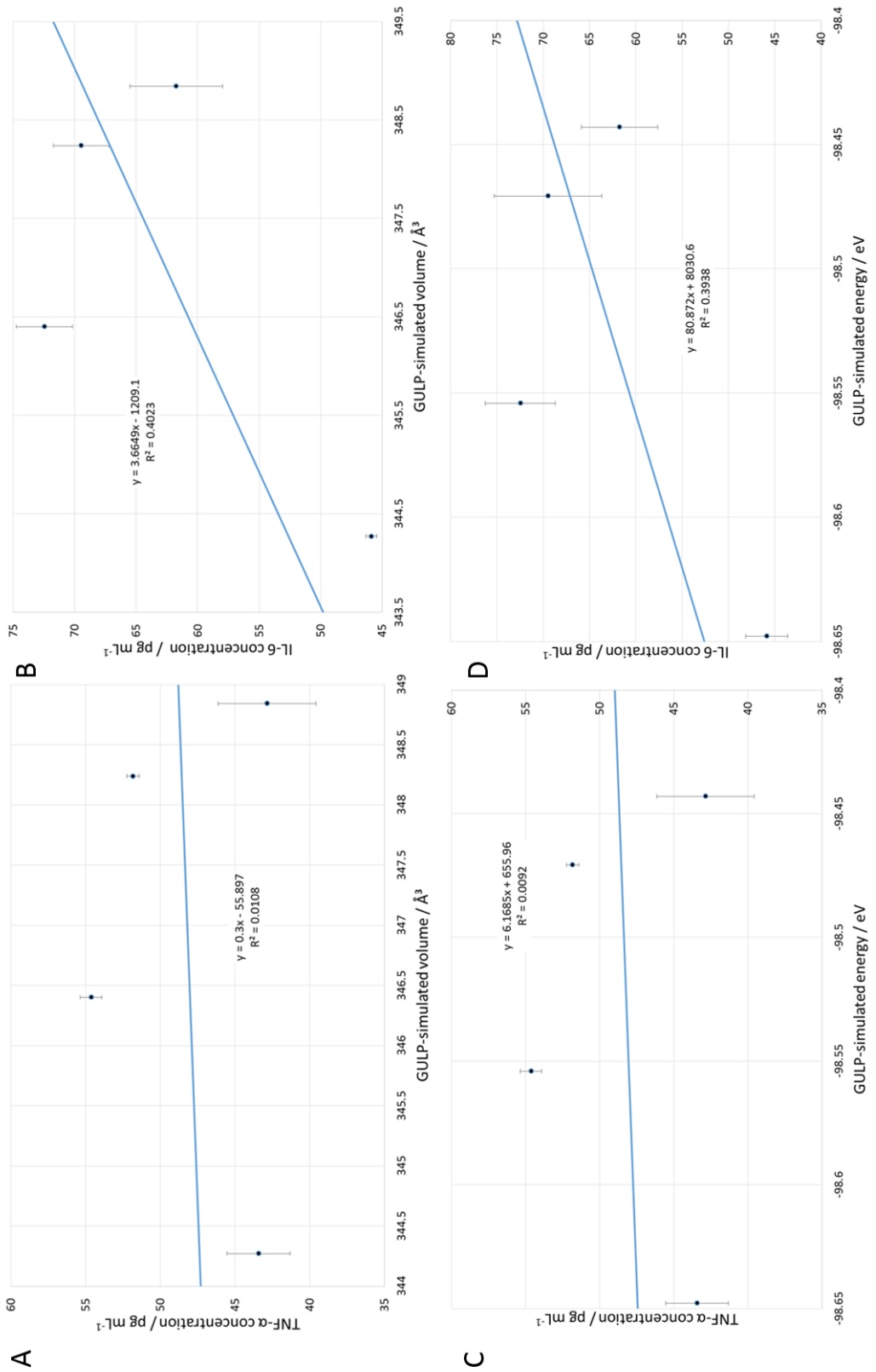

Figure A4.9: ***Graphical representation of the di-halide LDH materials' (A) TNF-α and (B) IL-6 cytokine concentrations correlated to calculated unit cell volume-parameter; the (C) TNF-α and (D) IL-6 cytokine concentrations correlated with calculated lattice energy-parameter.***

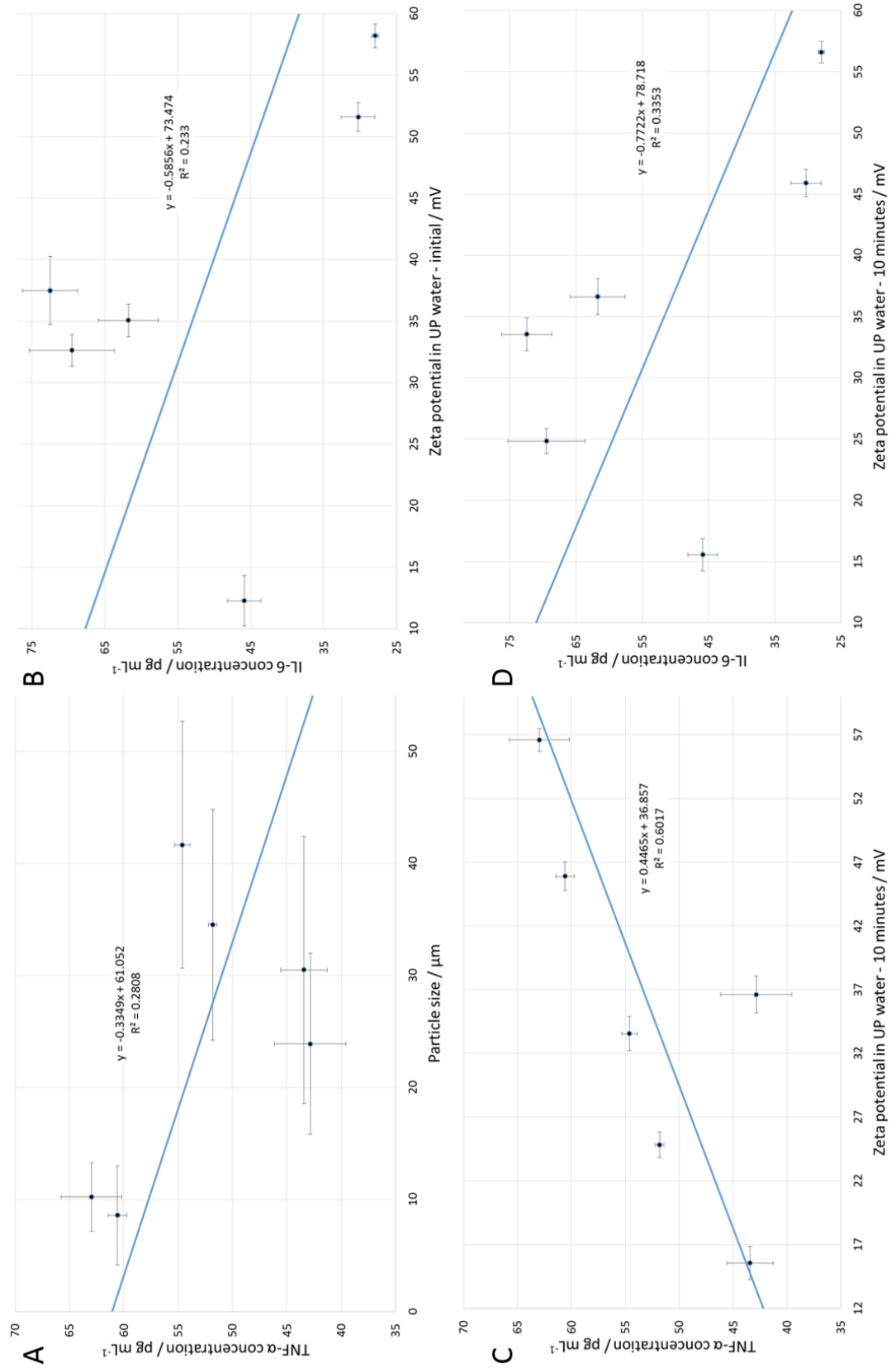

Figure A4.10: ***Graphical representation of the relationships for combined mono- and di-halide LDH samples. Plots depict the relationship of (A) TNF-α cytokine concentrations with particle size, (B) IL-6 cytokine concentrations with the zeta potential measured in UP water (initial), and (C) TNF-α and (D) IL-6 cytokine concentrations with zeta potential measurements in UP water (10 minute time-point).***

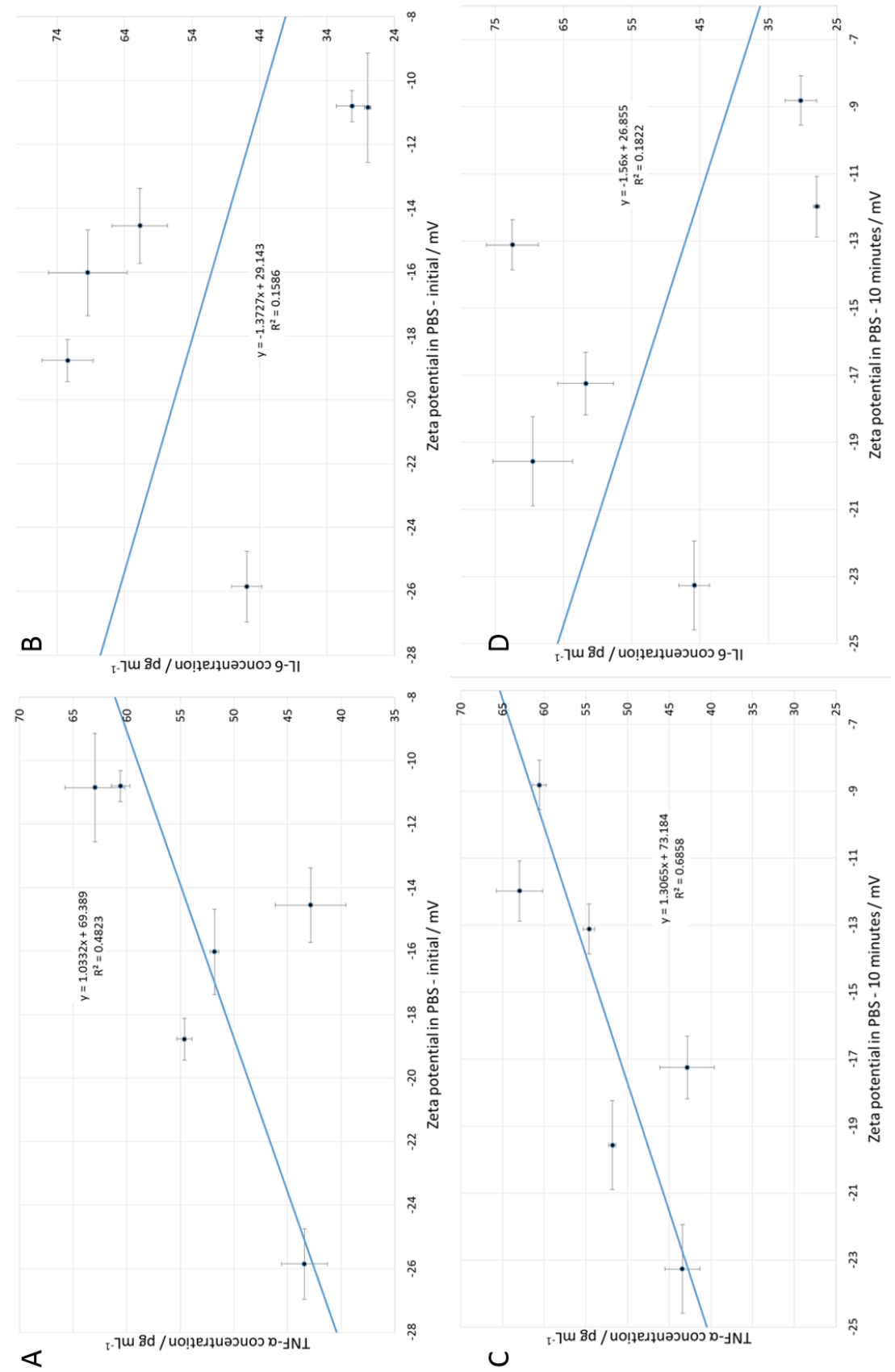

<u>Figure A4.11:</u> Graphical representation of the relationships for combined mono- and di-halide LDH samples. Plots depict the relationship of the (A) TNF-α and (B) IL-6 cytokine concentrations with zeta potential measured in PBS (initial), and (C) TNF-α and (D) IL-6 cytokine concentrations with zeta potential measurements in PBS (10 minute time-point).

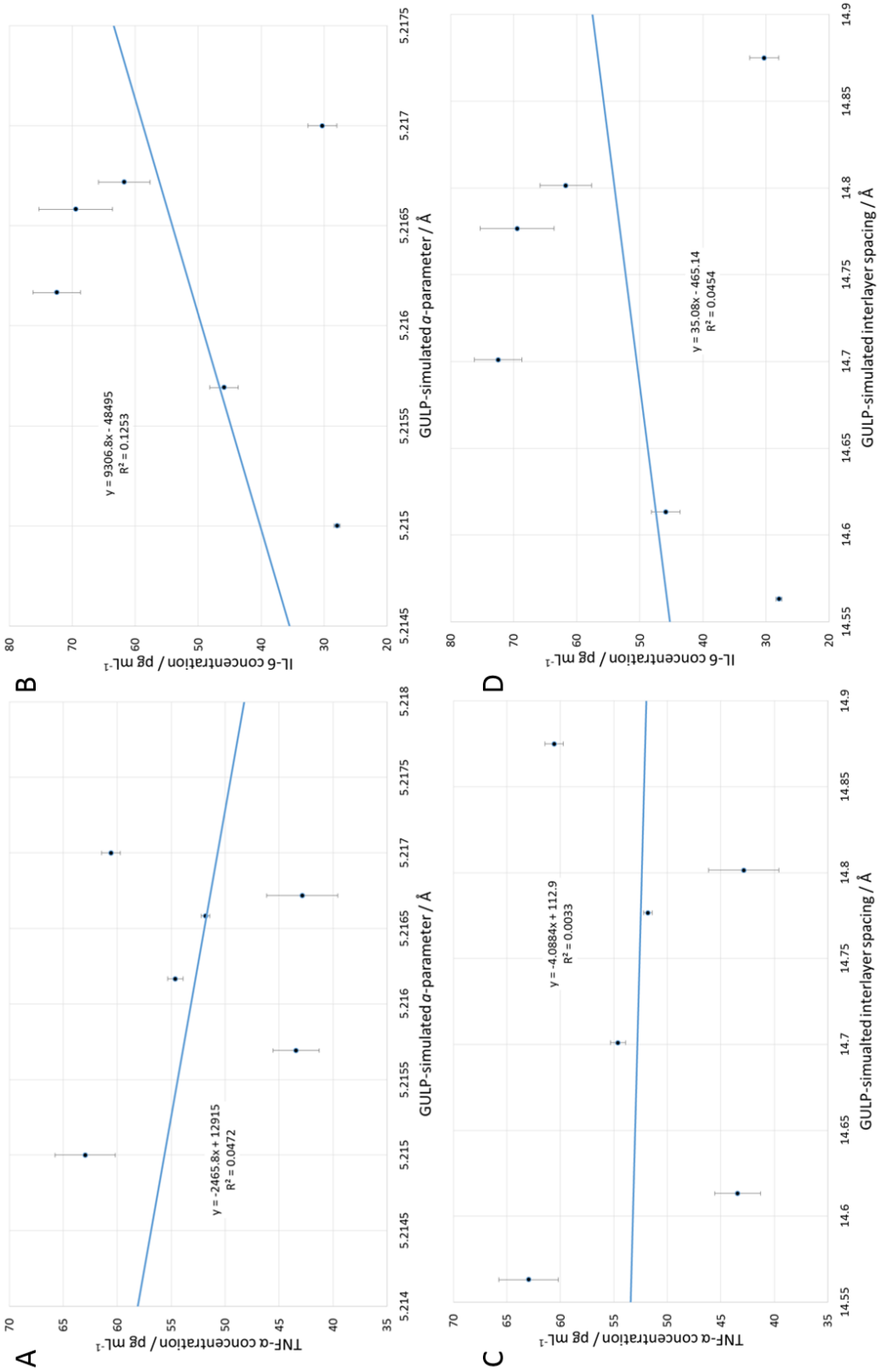

Figure A4.12: ***Graphical representation of the combined mono- and di-halide LDH materials' (A) TNF-α and (B) IL-6 cytokine concentrations correlated to calculated unit cell a-parameter, and (C) TNF-α and (D) IL-6 cytokine concentrations correlated with the calculated unit cell interlayer spacing-parameter.***

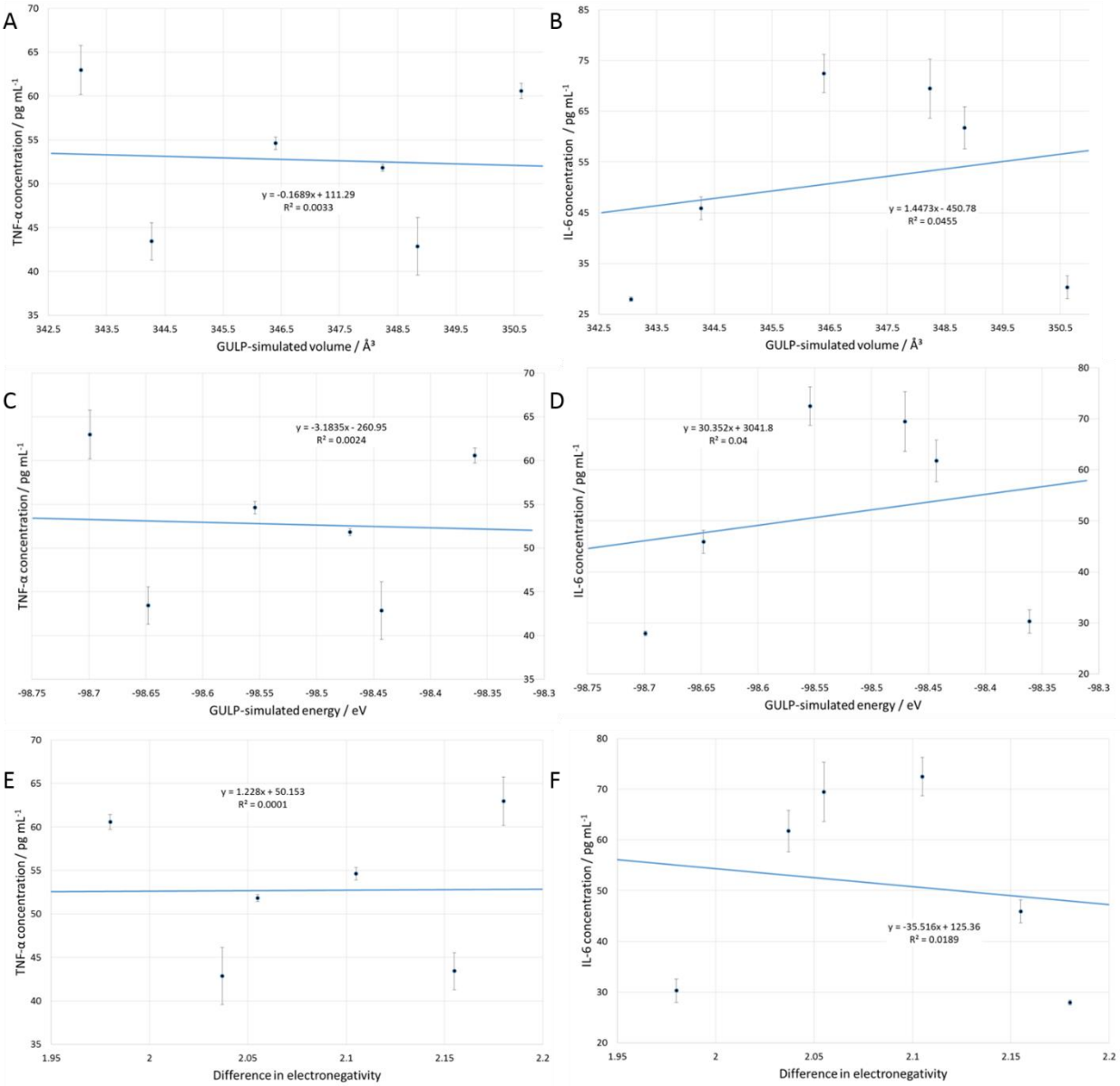

Figure A4.13: ***Graphical representation of the combined mono- and di-halide LDH (A) TNF-α and (B) IL-6 cytokine concentrations correlated to materials' calculated unit cell volume; the (C) TNF-α and (D) IL-6 cytokine concentrations correlated with calculated lattice energy-parameter, and the E) TNF-α and (F) IL-6 cytokine concentrations correlated with difference in electronegativity.***

Appendix 5: Hydroxy Double Salts as Vaccine Adjuvants

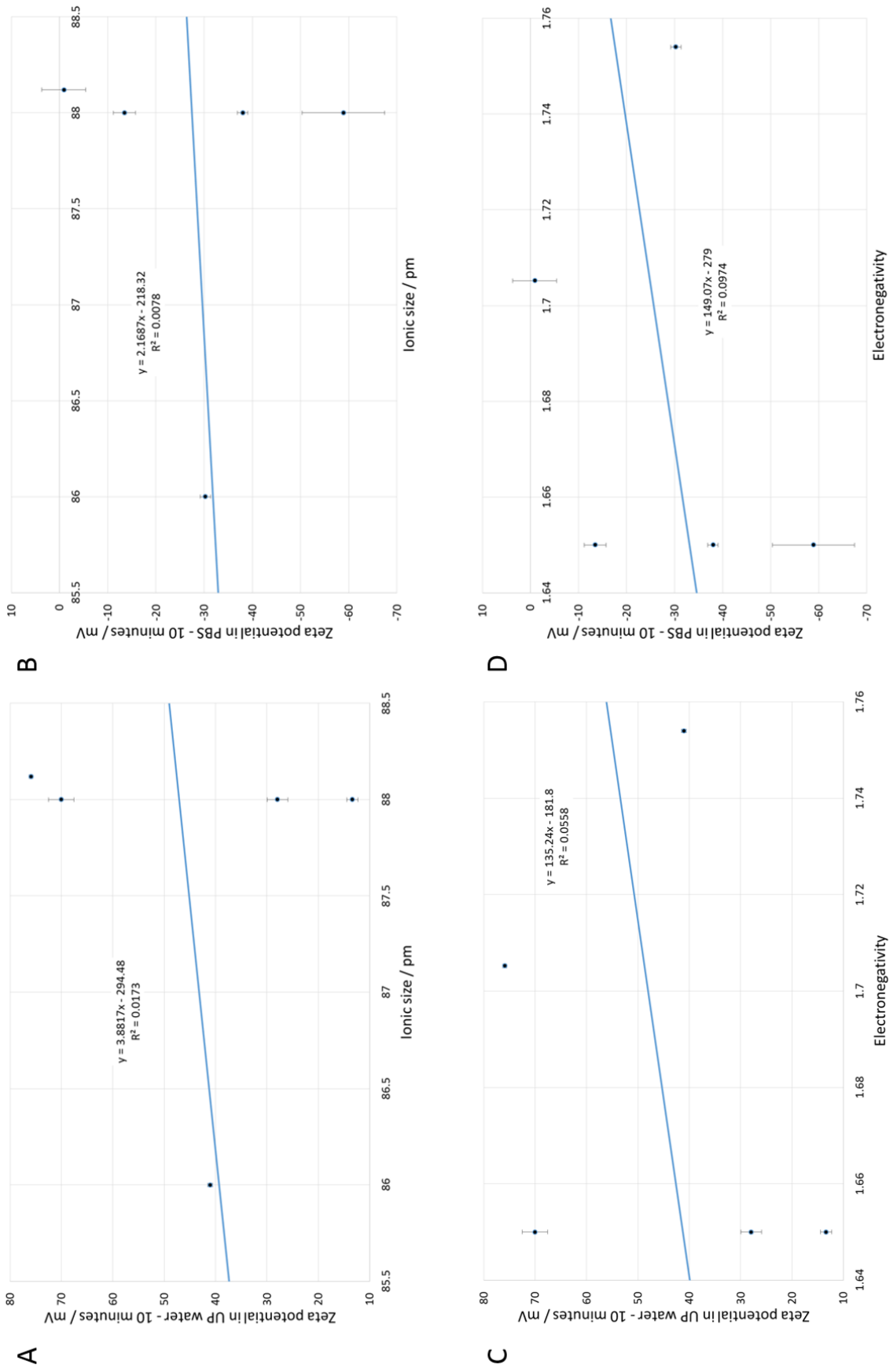

Figure A5.1: ***Graphical representation of the relationships for HDS samples. Plots depict the relationship of zeta potential measurements in UP water (10 minute-point) and PBS (10 minute time-point) with (A and B) ionic size, and (C and D) weighted mean of the metal cation's electronegativity.***

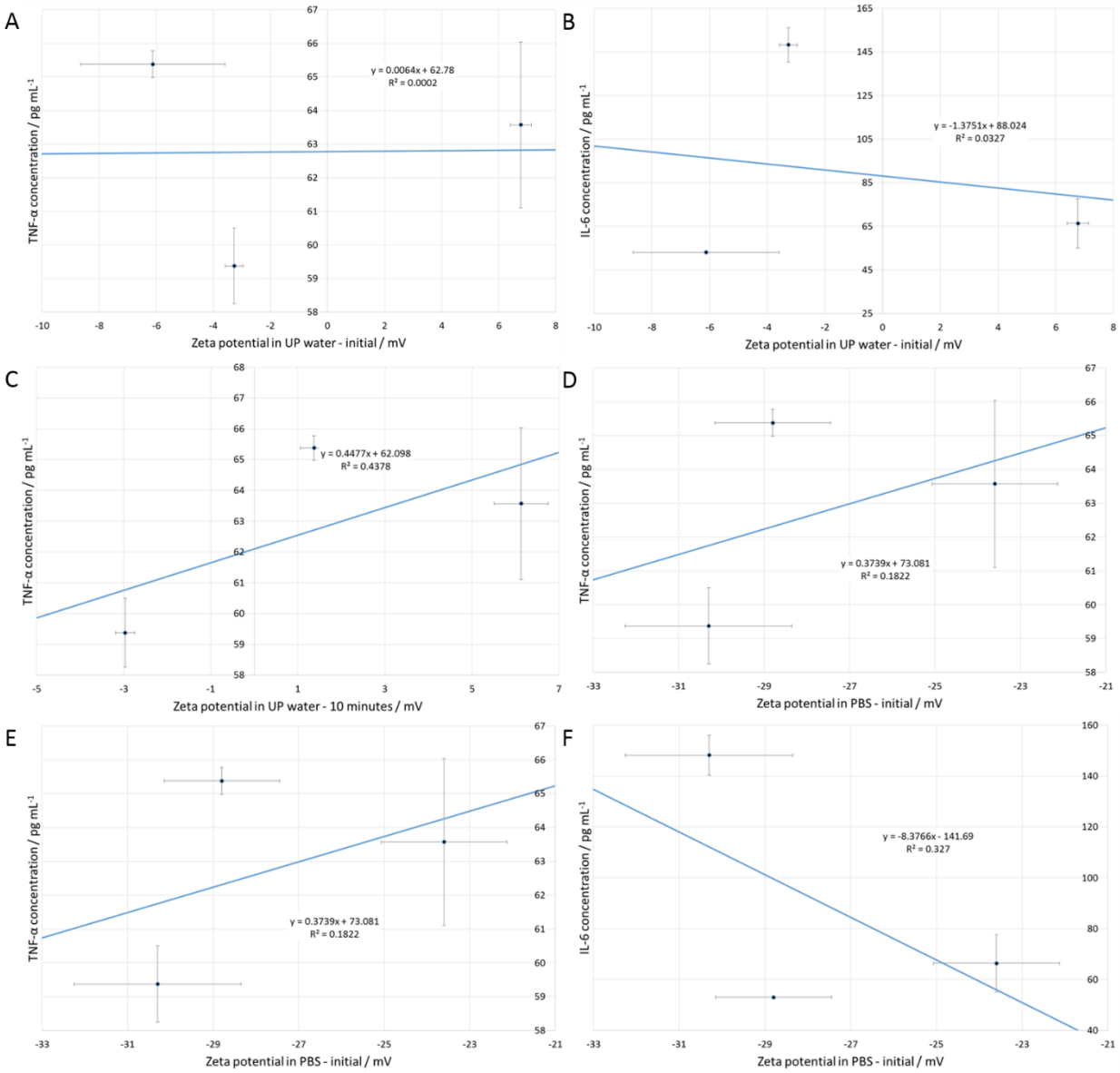

<u>Figure A5.2:</u> Graphical representation of the relationships for HDS samples. Plots depict the relationship of TNF-α and IL-6 cytokine concentrations with zeta potential measurements in (A and B) UP water (initial), (C and D) UP water (10 minute time-point), and (E and F) PBS (initial).

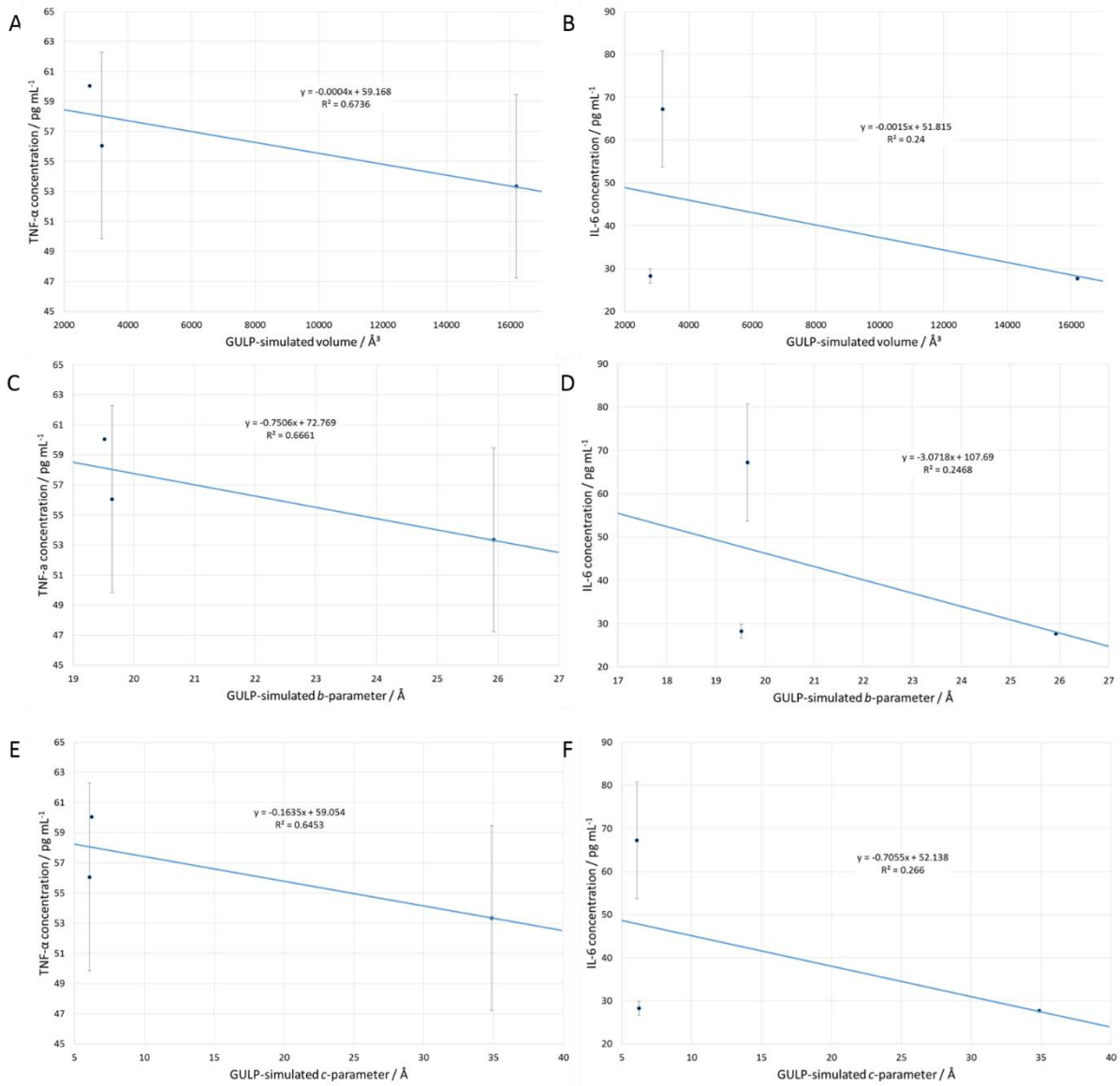

<u>Figure A5.3:</u> Graphical representation of the (A) TNF-α and (B) IL-6 cytokine concentrations correlated to calculated unit cell volume parameter; the (C) TNF-α and (D) IL-6 cytokine concentrations correlated with calculated unit cell* b*-parameter, and the (E) TNF-α and (F) IL-6 cytokine concentrations correlated to calculated unit cell* c*-parameter.

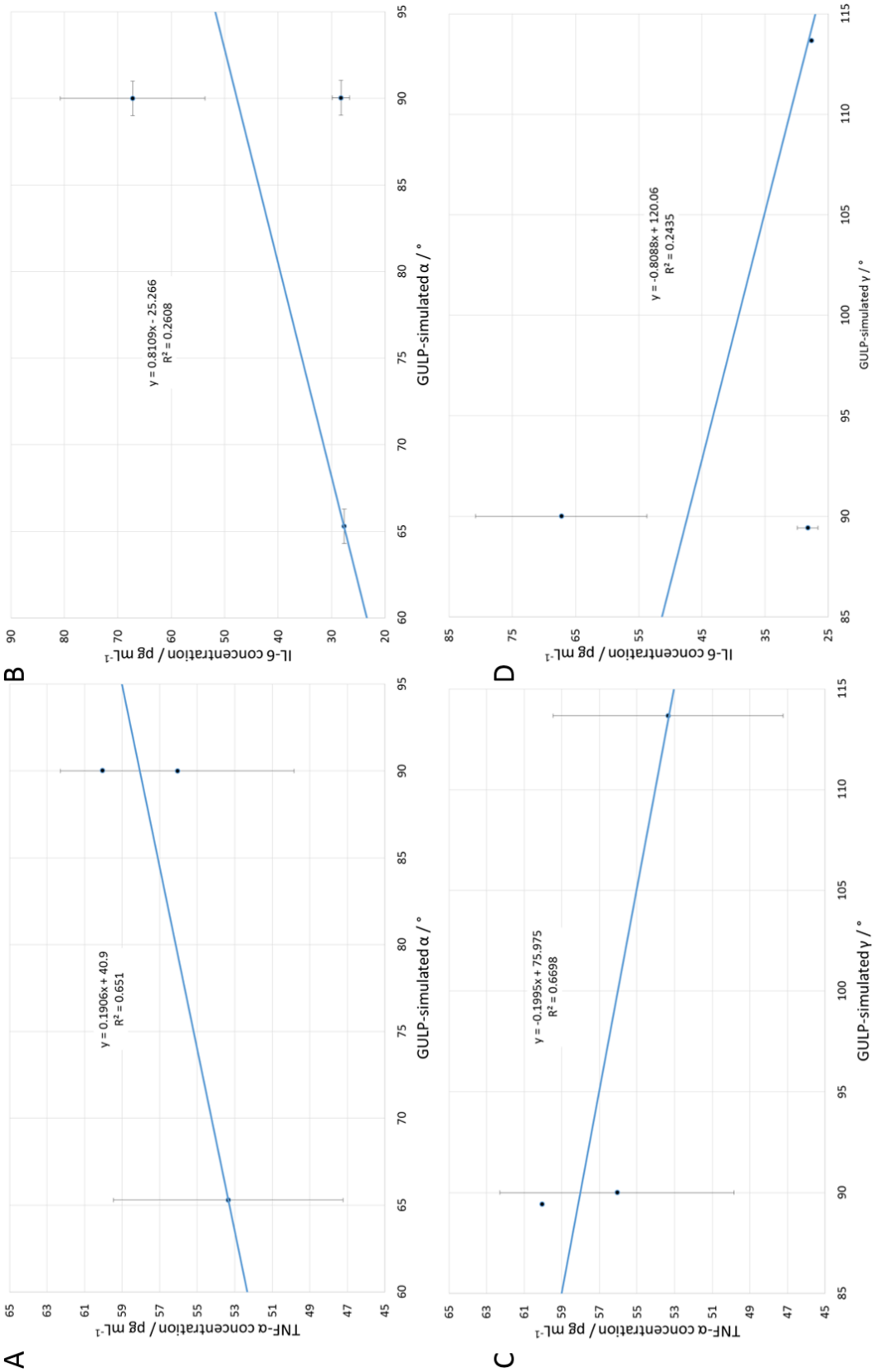

Figure A5.4: ***Graphical representation of the (A) TNF-α and (B) IL-6 cytokine concentrations correlated with calculated unit cell α-angle, and the (C) TNF-α and (D) IL-6 cytokine concentrations correlated to calculated unit cell γ-angle.***